

# **CMOS Circuits for Magnetic Microsensors**



**based on  
Simple  
Sensor Models**

**Christoph Maier**

contains DISS. ETH No. 13532

"Equivalent circuit models and interface circuits  
for CMOS microsensors"

written at  
Physical Electronics Laboratory  
ETH Zürich

---

# **CMOS Circuits for Magnetic Microsensors based on Simple Sensor Models**

Contains the thesis

“EQUIVALENT CIRCUIT MODELS AND INTERFACE CIRCUITS FOR CMOS  
MICROSENSORS”

submitted to the

SWISS FEDERAL INSTITUTE OF TECHNOLOGY ZURICH

for the degree of

Doctor of Technical Sciences

by

Christoph H. Maier

Diplom–Physiker, Ruprecht–Karls–Universität Heidelberg

Born January 6, 1967

German citizen

2000

---

Copyright © 2000 by Christoph Maier

—Unauthorized Extended Version—

All rights reserved. Any part of this book may be distributed, reproduced, stored in a retrieval system, or transmitted, in any form or by any means, electronic, mechanical, photocopying, recording, or otherwise, if referenced by the author's name.

This copyright disclaimer supersedes the copyright notice of the officially authorized thesis if the reference is made to the Unauthorized Extended Version of the thesis.

First of all, I wish to recognize Professor Henry Baltes.

In 1988, Professor Baltes founded the Physical Electronics Laboratory at the Institute of Quantum Electronics of ETH Zürich.

Professor Baltes's highly idiosyncratic leadership makes PEL a very special place. No expenses are spared to provide everything that money can buy to stay on top of the latest trends in microsensor, and lately nanosensor, technology. In more than one way, one can speak of PEL as a Versailles in sensor research.

Professor Baltes is widely known for contributions to each and every aspect of successfully inventing, implementing, and marketing a wide range of micro- and nanosensor systems compatible to industry standard CMOS IC processes, covering the topics of sensor materials characterization, sensor design, sensor modeling, circuit design, and packaging. His institute attracts staff and visitors of highest professional and personal qualification. Due to Professor Baltes's strict focus on industrial needs, he acquires funding from industry in excess of allowances granted by Swiss public authorities. This enables him to use the assets of the institute at his personal discretion to achieve goals which would otherwise be hardly even imaginable.

As his former student, I can think of almost no request which Professor Baltes would not make haste to fulfill in a most graceful and generous manner.



Stand from between me and the sun.

*Diogenes*



---

DISS. ETH No. 13532

# **Equivalent Circuit Models and Interface Circuits for CMOS Microsensors**

A thesis submitted to the

SWISS FEDERAL INSTITUTE OF TECHNOLOGY ZURICH

for the degree of

Doctor of Technical Sciences

presented by

Christoph H. Maier

Diplom–Physiker, Ruprecht–Karls–Universität Heidelberg

Born January 6, 1967

German citizen

accepted on the recommendation of

Prof. Dr. H. Baltes, examiner

Prof. Dr. Shoji Kawahito, co-examiner

Prof. Dr. J. Korvink, co-examiner

2000

---

Copyright © 2000 by Christoph Maier, Physical Electronics Laboratory

All rights reserved. No part of this book may be distributed, reproduced, stored in a retrieval system, or transmitted, in any form or by any means, electronic, mechanical, photocopying, recording, or otherwise, unless legally required by due procedure for submission of a Doctoral Thesis to the Swiss Federal Institute of Technology, Zürich.

---

## **How Flatterers Should Be Avoided**

*I DO NOT wish to leave out an important branch of this subject, for it is a danger from which princes are with difficulty preserved, unless they are very careful and discriminating. It is that of flatterers, of whom courts are full, because men are so self-complacent in their own affairs, and in a way so deceived in them, that they are preserved with difficulty from this pest, and if they wish to defend themselves they run the danger of falling into contempt. Because there is no other way of guarding oneself from flatterers except letting men understand that to tell you the truth does not offend you; but when every one may tell you the truth, respect for you abates.*

*Therefore a wise prince ought to hold a third course by choosing the wise men in his state, and giving to them only the liberty of speaking the truth to him, and then only of those things of which he inquires, and of none others; but he ought to question them upon everything, and listen to their opinions, and afterwards form his own conclusions. With these councillors, separately and collectively, he ought to carry himself in such a way that each of them should know that, the more freely he shall speak, the more he shall be preferred; outside of these, he should listen to no one, pursue the thing resolved on, and be steadfast in his resolutions. He who does otherwise is either overthrown by flatterers, or is so often changed by varying opinions that he falls into contempt.*

[...]

*A prince, therefore, ought always to take counsel, but only when he wishes and not when others wish; he ought rather to discourage every one from offering advice unless he asks it; but, however, he ought to be a constant inquirer, and afterwards a patient listener concerning the things of which he inquired; also, on learning that any one, on any consideration, has not told him the truth, he should let his anger be felt.*

Niccolo Machiavelli, **The Prince**, chapter XXIII

---

*For a successful technology, reality must have precedence over public relations,  
for Nature cannot be fooled.*

Richard Feynman, **Personal Observations on the Reliability of the Shuttle**



<b>Abstract .....</b>	<b>15</b>
<b>Zusammenfassung .....</b>	<b>16</b>
<b>1 Introduction .....</b>	<b>17</b>
1.1 Silicon Microtechnology .....	17
1.2 Microsystem CAD .....	18
1.2.1 CAD for digital circuits .....	18
1.2.2 CAD for analog circuits .....	19
1.2.3 CAD for MEMS .....	19
1.3 Magnetic sensors .....	21
1.3.1 Hall sensor microsystem presented in this thesis .....	23
1.3.2 Fluxgate sensor microsystem presented in this thesis .....	23
1.4 Major Results .....	25
<b>2 Resistive Sensor Models.....</b>	<b>29</b>
2.1 Conductivity relation under influence of non-electrical interactions .....	30
2.1.1 General conductivity relation .....	30
2.1.2 Physical interactions .....	30
2.1.3 Common properties of interactions .....	31
2.1.4 Piezoresistive interaction .....	32
2.1.5 Galvanomagnetic interaction .....	34
2.2 The Framework of Circuit Modeling: Nodal analysis .....	35
2.2.1 Microscopic Formulation of Kirchhoff's Laws .....	36
2.3 The Box Integration Method .....	37
2.3.1 Discretization of flux .....	39
2.3.2 Conservation laws .....	40
2.4 Discretization on a quadrilateral grid .....	42
2.4.1 Defining the grid .....	42
2.4.2 Integration of node currents .....	43
2.5 Translation of the model into SPICE netlist .....	46
2.5.1 Decomposition of the system matrix into basis elements .....	46
2.5.2 Symmetric basis elements and their circuit equivalent .....	47
2.5.3 Antisymmetric basis elements and their circuit equivalent .....	48
2.5.4 Extraction of the basis elements from the admittance matrix .....	49
2.5.5 Translation of the extracted basis elements to SPICE netlist lines .....	50
2.6 Strategies to Compact the Netlist .....	52
2.6.1 Collapsing boundary conditions into terminals .....	53
2.6.2 Schur Complement to eliminate internal nodes .....	53
2.6.3 Inverting the Internal Node System Matrix .....	55
2.7 Direct Translation of Matrix Equations to AHDL .....	55
2.8 Verification of the Box Integration Method .....	56
2.8.1 "Breadboard" Hall sensor .....	57
2.8.2 Cross-shaped Hall sensor .....	60

---

## Table of Contents

---

<b>3 Spinning Current Method For Offset Reduction of Hall Devices.....</b>	<b>65</b>
3.1 The Spinning Current Method .....	65
3.2 Applicability of the Continuous Spinning Current Method .....	70
3.2.1 Device Characterization .....	71
3.2.2 Sensitivity to Nonidealities .....	73
3.3 Magnetic Microsystems Using Offset Compensated Hall Devices .....	77
3.4 Trench Hall sensors .....	80
3.4.1 Equivalent circuit model of the Trench Hall sensors .....	81
3.5 Circuit building blocks .....	83
3.5.1 Hall sensor instrumentation .....	83
3.5.2 Signal accumulator .....	87
3.5.3 Digital spin control .....	92
3.6 Implementation and measurement .....	96
3.6.1 Sensitivity and offset of the Hall devices .....	97
3.6.2 Common mode voltage regulation .....	99
3.6.3 System offset and linearity .....	101
<b>4 Integrated Microfluxgate System.....</b>	<b>105</b>
4.1 The fluxgate measurement principle .....	106
4.1.1 A Theory of Fluxgate Operation Based on Symmetry Principles .....	108
4.1.2 Nonidealities in Fluxgate Operation .....	113
4.1.3 Differential fluxgate arrangement .....	117
4.2 Theory of SD data conversion .....	119
4.3 CMOS compatible fluxgate sensor .....	123
4.4 Circuitry for an integrated microfluxgate system .....	130
4.4.1 SD Modulator Topology .....	133
4.4.2 Fluxgate excitation driver .....	135
4.4.3 Pick-up coil front end amplifier .....	135
4.4.4 Phase shifter and cross-coupled switch .....	136
4.4.5 Anti-aliasing filter .....	139
4.4.6 Sampled-time integrators .....	141
4.4.7 Comparator .....	143
4.4.8 Feedback current source .....	144
4.4.9 Timing generator .....	145
4.4.10 Auxiliary circuit: monitor buffer .....	145
4.5 Measurements .....	146
<b>5 Conclusion.....</b>	<b>153</b>
<b>6 References .....</b>	<b>155</b>
<b>Curriculum vitae .....</b>	<b>165</b>
<b>Quodlibet .....</b>	<b>167</b>
<b>7 A Child's Play .....</b>	<b>169</b>

---

## Table of Contents

---

7.1 Balancing a bridge .....	169
7.2 Balancing magnetic flux .....	174
7.3 Building a scale for magnetic flux .....	176
7.4 Making a model for the flux scale .....	180
7.5 Designing a circuit for the flux scale .....	192
7.6 Putting It All Together .....	220
7.7 Some Notes on the Tools and Equipment Used .....	232
<b>8 References .....</b>	<b>233</b>
<b>Acknowledgments.....</b>	<b>243</b>

## Table of Contents

---

---

# Abstract

This thesis reports on the development of two integrated vector magnetometers for the two-dimensional measurement of magnetic induction.

To integrate Hall sensors into a circuit design environment, a modeling scheme using the Box Integration method to obtain compact SPICE equivalent circuit models of resistive sensors from a discrete mesh representation has been developed. The equivalent circuit model describes the Hall effect as well as sensitivities to other physical quantities, e. g., mechanical stress, by functional relations, allowing to include non-electrical signals in the equivalent circuit description of the microsystem as voltages.

Based on a compact equivalent circuit model of vertical Hall devices generated by this method, a 2-D vector Hall magnetometer to measure magnetic induction in the range of  $\pm 100$  mT has been designed. The offset of the Hall sensors is cancelled by the Spinning Current method to an equivalent offset induction of less than  $50 \mu\text{T}$ , allowing the use of the system design for precise rotary switch applications. Due to the modular design approach, the circuit concept is adaptable to a wide range of applications.

The second 2-D vector magnetometer uses microfluxgate sensors which are implemented by a simple postprocessing sequence fully compatible to industrial CMOS technology to measure magnetic induction in the range of the Earth's magnetic field. The sensors are embedded in a  $\Sigma\Delta$  modulator to obtain digital output. The implemented system has a nonlinearity of less than  $1.5 \mu\text{T}$  in the range of  $\pm 50 \mu\text{T}$ . The angular resolution is better than  $4^\circ$ . This makes the microfluxgate magnetometer suitable for use as a fully integrated magnetic compass.

# Zusammenfassung

Diese Arbeit behandelt die Entwicklung von zwei Magnetometern zur Messung eines zweidimensionalen Vektors der magnetischen Induktion.

Zur Integration von Hallsensoren in eine Entwicklungsumgebung für Schaltungen wurde ein Modellierungsverfahren für die Erzeugung kompakter äquivalenter SPICE–Ersatzschaltungen resistiver Sensoren ausgehend von einer diskretisierten Darstellung der Sensorgeometrie als Gitter entwickelt. Das Modell beschreibt sowohl den Halleffekt als auch die Sensitivität gegenüber anderen physikalischen Größen, z. B. mechanischer Spannung, durch funktionale Beziehungen. Somit können nicht elektrische Signale in der Beschreibung eines Mikrosystems durch ein Ersatzschaltbild als Spannungen dargestellt werden.

Auf der Grundlage eines mit dieser Methode erzeugen kompakten Ersatzschaltbildes für vertikale Hallsensoren wurde ein Hallsensor– Magnetometer für die zweidimensionale Messung des Vektors magnetischer Induktion im Bereich von  $\pm 100$  mT entworfen. Der Offset der Hallsensoren wird durch Drehung der Stromrichtung durch den Hallsensor auf einen Wert von weniger als  $50$   $\mu\text{T}$  reduziert. Das ermöglicht die Verwendung des Systementwurfs für Anwendungen als genaue Winkelsensoren. Die modulare Entwurfsmethode ermöglicht die leichte Anpassung des Schaltungskonzepts für ein breites Spektrum von Anwendungen.

Das zweite Magnetometer zur Messung eines zweidimensionalen Vektors der magnetischen Induktion in der Größenordnung des Erdmagnetfeldes beruht auf Mikrofluxgatesensoren. Die Sensoren wurden mit einem einfachen Postprozessierungsverfahren hergestellt, das mit industrieller Technologie zur Herstellung von CMOS–Schaltungen vollständig kompatibel ist. Das implementierte System zeigt eine Nichtlinearität von weniger als  $1.5$   $\mu\text{T}$  in einem Bereich von  $\pm 50$   $\mu\text{T}$ . Mit einer Winkelauflösung von besser als  $4^\circ$  ist das Mikrofluxgatemagnetometer für die Verwendung als voll integrierter magnetischer Kompass geeignet.

# 1 Introduction

## 1.1 Silicon Microtechnology

In a visionary lecture given in 1959, R. Feynman stated that according to the fundamental laws of nature and the limitations they do *not* impose, it is perfectly possible to build machines down to the size of a few hundred atoms [10]. The invention of the transistor and the integrated circuit has spawned a whole industry dealing with structures on microscopic level. While the main thrust of the semiconductor industry is aimed at digital electronic circuits, the reality of once visionary concepts that “might be just for fun” has been proven by their commercial feasibility [12],[13].

The basis material for the semiconductor industry, silicon, does not only have very favorable electrical properties. The electrical properties of silicon are sensitive to environmental quantities, e. g., temperature, light, magnetic fields, and mechanical stress. These sensitivities have been extensively studied [14],[15],[16]. Whereas the sensitivity of electronic circuits to the environment is usually undesirable, these very effects open an opportunity for the realization of silicon sensors. First devices, e. g., photodiodes and Hall plates, have been introduced in the 1960s [17]. Besides its electrical properties, silicon has outstanding mechanical qualities as well [18], allowing the realization of mechanical devices, such as pressure sensors [19] , acceleration sensors [20] and microfluidics [21]. Mechanical *actuators* based on electrostatic or thermal actuation are also realizable [22]. Using photolithographic methods developed for the definition of structures with a feature size of micrometers in silicon IC technology, materials can be added in post-processing steps to enhance the sensing capabilities of silicon [53].

To obtain cost-efficient and reliable devices, it is advantageous to employ industry standard CMOS process technologies. The advantage is twofold: First, volume production is available from silicon foundries at low cost. For small series production, organizations such as EUROPRACTICE and MOSIS offer foundry service with multi-project wafer (MPW) runs.

Second, industry standard technologies provide well-characterized libraries for electronic devices and circuits. Thus, *smart microsystems* that combine sensors with electronic circuitry for signal calibration and conditioning on the same substrate can be realized [23].

### 1.2 Microsystem CAD

In the fast paced microsystem business, the designer is more often than not confronted to tight deadlines imposed by customers or by management. This is in contrast to the design cycle times for industrial IC technology, which are still in the order of months per iteration. The situation is aggravated by the difficulty of modifications to integrated systems: Properties that are not trimmable by design, which is expensive in terms of area and system complexity, can hardly be modified after fabrication. Moreover, calibration procedures add to the time required for testing and quality control of commercial microsystems. As production in high volumes is one of the inherent advantages of industrial IC fabrication, a small increase in calibration time quickly adds up to a significant factor in overall cost. Therefore, it is necessary to rely extensively on computer simulation for exploring design alternatives and, more important, for design verification.

<b><i>Microsystem CAD tools</i></b>			
	<b><i>System level</i></b>	<b><i>Circuit level</i></b>	<b><i>Device level</i></b>
<b><i>Digital circuits</i></b>	✓	✓	✓
<b><i>Analog circuits</i></b>	under research	✓	✓
<b><i>Microsensors</i></b>	<b><i>... scope of this thesis</i></b>		✓

Tab. 1.1 State of the Art in microsystem CAD tools

#### 1.2.1 CAD for digital circuits

Today, computer-aided design (CAD) of digital electronic circuits can rely on mature design tools. Hardware description languages (HDL), such as Verilog or VHDL [24], allow the design and verification of digital circuits on a level of

abstraction similar to computer software design. The translation from the abstract HDL system description to a circuit layout definition has become a fully automated procedure. Automatic partitioning of the system functionality among hard-wired digital logic, programmable digital logic [25], and microprocessor software is a field of active research.

### 1.2.2 CAD for analog circuits

For analog and mixed-signal circuits, sophisticated simulation tools exist, most of which are derived from the SPICE circuit simulator [26]. SPICE type simulators decompose the analog circuit into a network of circuit elements (resistors, capacitors, transistors, ...), represented by sophisticated device models [27],[28],[29]. While SPICE is an excellent and reliable design verification tool, its use for design synthesis is limited, because it relies on the detailed *numerical* analysis of a complex equivalent circuit network. Analog circuit synthesis begins with the exploration of different circuit topologies to implement a required functionality. For a chosen topology, the device parameters must be optimized in a high-dimensional design space, subject to a multitude of design constraints which are often in conflict with each other. To improve the applicability of analog circuit simulators for design synthesis, two directions are pursued: 1) the abstraction of complex building blocks by a description in an analog hardware description language (ADHL), e. g. SpectreHDL [30], and 2) symbolic analysis methods [31],[32].

### 1.2.3 CAD for MEMS

Compared to the situation for electronic circuitry, the development of CAD tools for integrated microsystems, often summarized under the short if somewhat misleading term “*CAD for MEMS*”<sup>1</sup>, is a relatively new field [33]. The characterization of material properties that can be exploited for the design of sensors is still an area of active research [34]. At the Physical Electronics Laboratory, a database containing the properties of thin film materials used in industrial IC fabrication is built [35].

---

1. CAD for MEMS is *not* restricted to Micro Electro *Mechanical* Systems

*Device* simulators abound that describe one or more of the effects of environmental parameters, such as magnetic fields or mechanical stress—thus principally targeting device designers. System designers require *circuit* level models of coupled behavior: in sensor systems the effect is desired and should be maximized as a system goal; in many systems the effect is unwanted and must be minimized using appropriate circuit techniques.

It has been shown that general device simulation models based on the finite element or box integral method can be coupled with circuit simulation techniques for so-called mixed-mode simulation. Usually, the circuit is moved into the device simulation, thus requiring that the circuit designer learn a new tool (other than the de facto industry standard circuit simulator SPICE). Examples are the DESSIS module in the ISE–TCAD simulation suite [36], which allows the inclusion of circuit elements such as ideal resistors, linear dependent sources, and transistors. The device simulator SIMUL [37] includes a circuit simulator which has been developed independently [38].

### **Contribution of this thesis to the State of the Art**

In this thesis, it is shown that for *resistive* devices the opposite is also possible, i. e., general numerical methods can be used to automatically generate equivalent circuit representations of the coupled sensors that they discretize, thus moving the finite element or box integral method into the equivalent netlist of the circuit. A device designer can develop a netlist representation of a device incorporating the coupled (sense and/or parasitic) effects and pass this on to a circuit system designer.

Of course, netlists which, in terms of nodes, are as large as typical finite element meshes are generally undesirable, especially if the device is instantiated many times in the microsystem. Therefore, a method is devised to compact the netlists, while retaining the coupling fields as parameters to the model, and ensuring that the compacted netlist exhibits identical terminal-to-terminal field-dependent behavior as its discretised origin and thus may be termed equivalent. To speed up computations, an approximate inverse relation is used during compaction that relaxes the above formal equivalence, yet yields accurate results.

The applicability of the equivalent circuit models to the fields of device characterization and the design of integrated microsystems is demonstrated by a Hall sensor magnetometer using the Spinning Current method for offset compensation.

## 1.3 Magnetic sensors

Magnetic field sensors are an enabling technology for a wide range of applications such as data storage devices, automotive sensors, mechatronics, and medical instruments. In most applications, the signal of interest is not the magnetic field itself, but another physical quantity, e. g., mechanical translation or rotation of a permanent magnet, or electrical current. An application of particular interest is the use of integrated magnetic sensors as miniaturized magnetic compass for navigation.

An overview of magnetic field sensors is shown in Figure 1.1. Magnetic sensors can be classified into three categories according to their range of sensitivity [39],[40]:

- **Low-field sensors** detect magnetic fields in the nanotesla range, used, e. g., for medical applications
- **Earth's field sensors** are sensitive in the range of the Earth's magnetic field (100 nT ... 100  $\mu$ T). Their applications encompass the determination of compass heading for navigation, geomagnetic anomaly detection, and spacecraft attitude control.
- **Bias field sensors** are mostly used together with permanent magnets, e. g., for measuring mechanical displacement. Their application includes contactless switches and position sensors in rugged environments, e. g., in automotive applications, where reliability and immunity against dirt and contamination at no maintenance is crucial.

*Low field sensors* include the superconducting quantum interference device (SQUID), fiber optic and optically pumped magnetometers relying on the Zeeman effect, and magnetometers exploiting the precession of the nuclear magnetic dipoles about a magnetic field. Their high sensitivity is paid for by high space and/or power consumption.

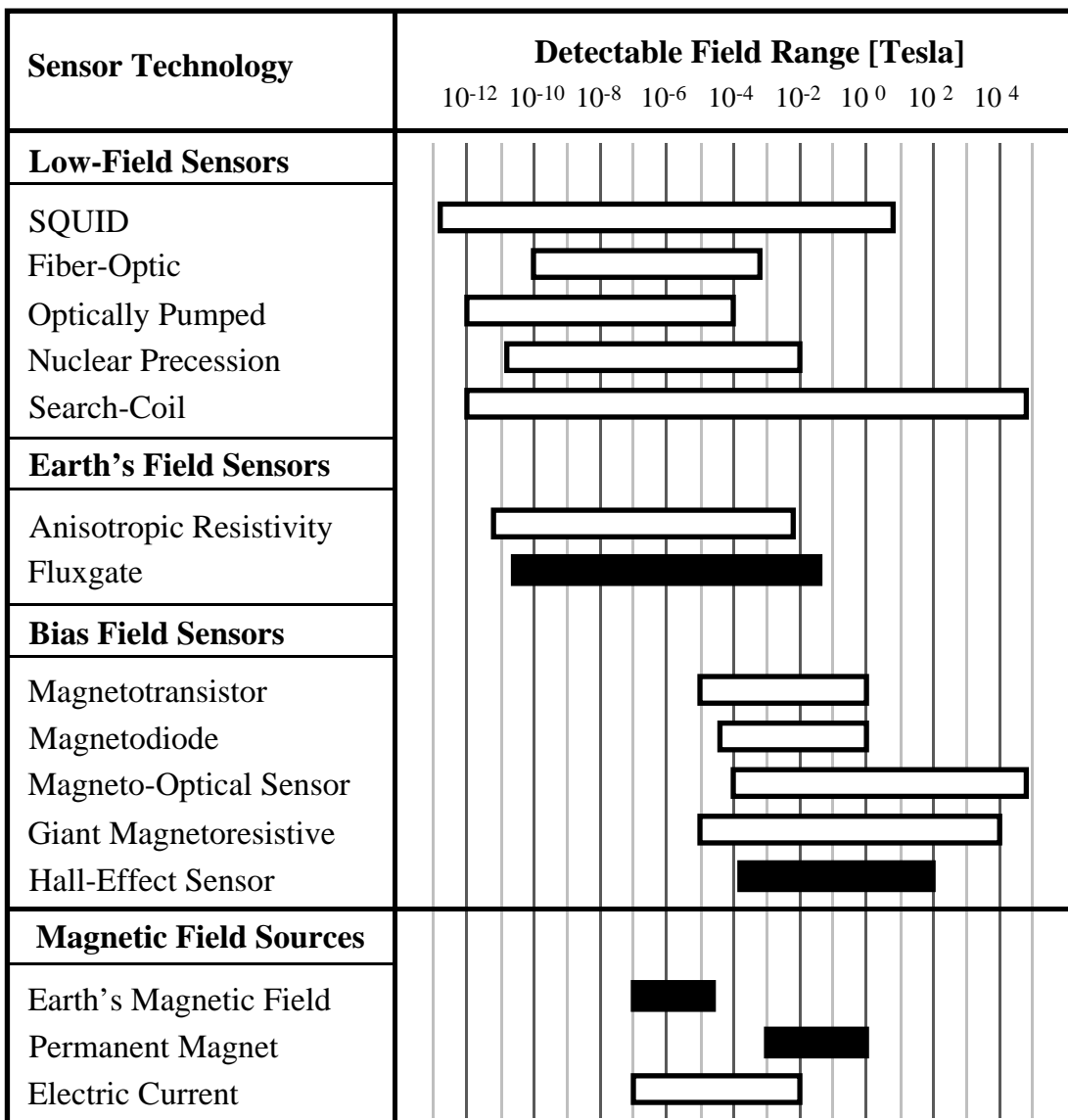


*Fig. 1.1 Comparison of the detection capability of magnetic sensors, adapted from [39] (courtesy of R. Steiner Vanha). The sensors and the magnetic field sources treated in this thesis are shown in black.*

*Earth's field sensors* include magnetoresistive elements, exploiting a large, anisotropic change in resistivity in certain ferromagnetic materials, and the fluxgate magnetometer.

The fluxgate exploits the nonlinear magnetization properties of soft ferromagnetic materials. Developed in the 1920s, a variety of designs have been devised [42] for applications for geomagnetic prospection, submarine detection, and as magnetic compass. More recently, efforts have been made to develop miniaturized sensors

compatible with IC technology [3–7],[43],[44], allowing the implementation of integrated CMOS microfluxgate systems [2],[45],[8].

*Bias field sensors* include the magneto-optical sensor which exploits the change of the polarization of light as it passes through certain magnetic materials (Faraday effect) [46]. Giant magnetoresistive sensors consist of a ferromagnetic/non-ferromagnetic multilayer sandwich. In response to an applied magnetic field, their resistance changes up to 70% [47]. Magnetodiodes rely on the magnetooconcentration or Suhl effect. Dependent on the incident magnetic field, the carriers in a p-i-n diode structure are deflected towards surfaces with different recombination rates, resulting in a change in resistivity [48]. Magnetotransistors are multicollector bipolar transistors whose structures and operating conditions are optimized with respect to the magnetic field-sensitivity of the collector currents. [49].

Hall sensors detect the voltage perpendicular to the flow of current due to the Lorentz force [50]. As they can be made of any resistive material, they are the simplest way to integrate devices sensitive to magnetic fields in standard IC technology [51].

In this thesis, two microsystems for measuring the two-dimensional magnetic induction parallel to the die surface of a CMOS circuit implemented in industrial IC technology are presented.

### **1.3.1 Hall sensor microsystem presented in this thesis**

A magnetometer for measuring magnetic fields in the millitesla range at a rate of up to 125 kSamples/second is presented. It uses two arrays of Trench Hall devices [54] to detect the two orthogonal components of magnetic induction parallel to the die surface. The offset of the Hall devices is cancelled by the Spinning Current method [58]. The Trench Hall sensor magnetometer is implemented in the 0.8  $\mu\text{m}$  CXE technology of Austria Mikrosysteme International AG [55].

### **1.3.2 Fluxgate sensor microsystem presented in this thesis**

A magnetometer for measuring magnetic fields with sufficient sensitivity to measure the Earth's magnetic field (20...50  $\mu\text{T}$ ) is presented. The sensitive elements

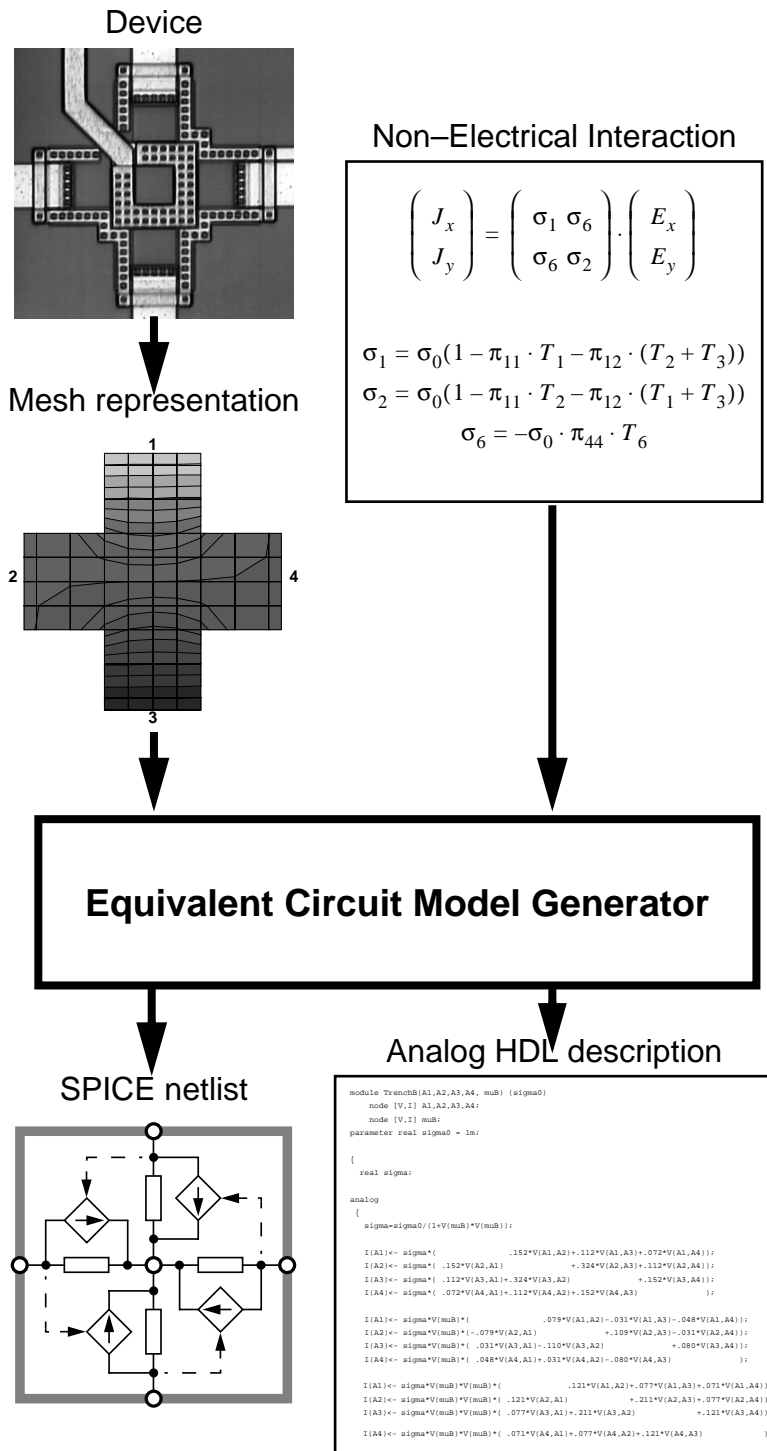
## 1 Introduction

---

are planar microfluxgate sensors implemented by a simple postprocessing sequence fully compatible to standard industrial IC processes [53]. For the readout and digitization of the signal, the sensors are embedded in a  $\Sigma\Delta$  modulator loop. The fluxgate magnetometer is implemented in the 0.8  $\mu\text{m}$  CYE technology of Austria Mikrosysteme International AG [55].

## 1.4 Major Results

### Equivalent Circuit Model for Resistive Structures Subject to Non-Electrical Interaction

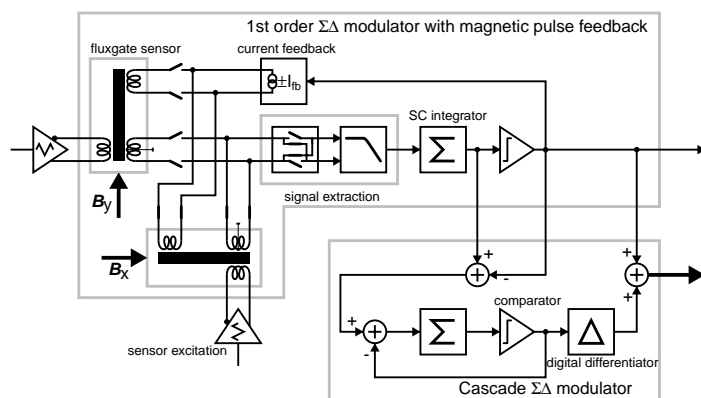


For the design of integrated microsystems including sensors *and* circuits, it is desirable to include the description of the sensor with its sensitivity to non-electrical quantities into a standard circuit design environment, e. g., SPICE.

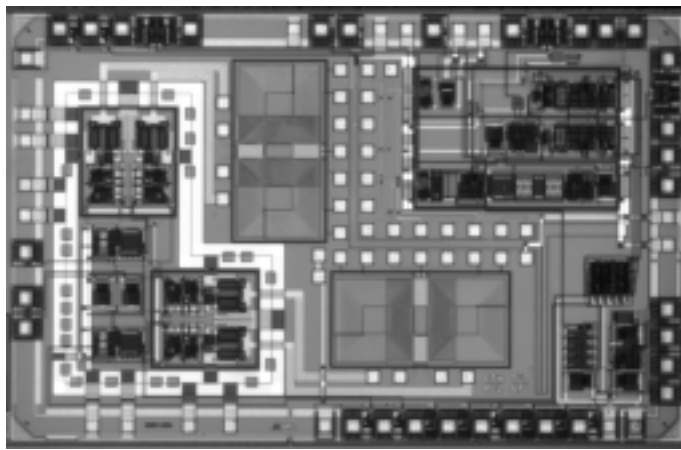
A method has been developed that generates equivalent circuit models of resistive sensors from a mesh representation of the geometry and the microscopic description of the interaction of non-electrical quantities, e. g., magnetic induction or mechanical stress, with the resistivity. The method provides equivalent circuit representations of the sensor with a minimum of equivalent circuit elements. The output format is either standard SPICE or an analog hardware description language, e. g., Spectre HDL.

## Two-dimensional CMOS Microfluxgate Sensor System for Digital Detection of Weak Magnetic Fields

Sensors for the measurement of magnetic induction with a resolution in the range of the Earth's magnetic field ( $20\ldots50\text{ }\mu\text{T}$ ) are an enabling technology for a wide range of applications, notably a magnetic compass. The limited resolution of magnetic sensors that can be implemented using but standard IC processing steps is a major obstacle to low cost, high volume integrated microsystems.



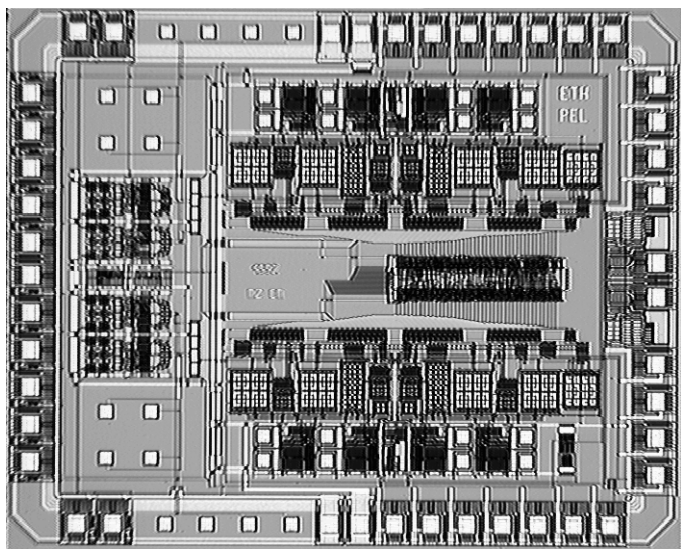
been developed. The planar microfluxgate sensors are embedded in a  $\Sigma\Delta$  modulator that provides a digital output signal.



This obstacle has been overcome by using a method for electroplating ferromagnetic thin films on fully processed standard integrated CMOS circuitry. Based on this method, a fluxgate magnetometer for the measurement of magnetic induction in two dimensions has

The integrated fluxgate magnetometer has been implemented in a standard industrial  $0.8\text{ }\mu\text{m}$  CMOS process. Within the range of  $|B| < 50\text{ }\mu\text{T}$ , the system output signal has a non-linearity of less than  $1.5\text{ }\mu\text{T}$ , corresponding to an equivalent angular resolution of  $4^\circ$  at an induction of  $50\text{ }\mu\text{T}$ .

### Hall sensor microsystem for Detection of Magnetic fields using the Spinning Current Method



Based on the equivalent circuit model of novel Trench Hall devices being developed at Austria Mikrosysteme International AG in collaboration with the Physical Electronics Laboratory, a vector magnetometer for measuring the magnetic induction parallel to the die surface for use with an array of Trench Hall devices has been designed by a systematic and modular approach. The microsystem

uses the Spinning Current method for offset reduction. Measurements of the instrumentation circuitry with one conventional Greek Cross Hall device yielded an equivalent offset induction of the system of  $(43 \pm 7)\mu\text{T}$  at a linear output range of  $\pm 200 \text{ mT}$ .

## 1 Introduction

---

---

## 2 Resistive Sensor Models

In this chapter, an automatic method to produce compact equivalent circuit models of spatially inhomogeneous resistors is developed. Local variations in space of the resistivity due to physical interactions such as magnetic fields and mechanical stress are automatically included. The equivalent circuit model is computed using symbolic algebra, such that the functional relation between the resistivity and the fields interacting with it is included in the circuit design model. Modelling is based on the discretization of the sensor geometry with a mesh of elements and vertex nodes together with the current continuity equation using the box integration method. The resistivity is described by the tensor field of electrical conductivity and functionally depends on the physical interactions to be modelled.

The element inter-node conductivity is mapped to a set of lumped conductances and transconductances (voltage controlled current sources) between the nodes of the discretization mesh. These conductances and transconductances are translated into an equivalent circuit netlist. Optionally, the electrical network representing the sensor is simplified before translation by symbolic linear algebra. Thus, equivalent circuit models consisting of many simple elements can be generated as well as models with only a few, algebraically complicated elements. The method is demonstrated using the public domain circuit simulator SPICE3 [67] for the example of a magnetic Hall sensor, with and without the piezoresistive effect.

This chapter is organised as follows. Section 2.1 outlines the relations governing field-dependent resistance. It shows that all necessary interactions can be described by the linear superposition of a small set of basic forms. A short review of nodal analysis and its relation to Kirchhoff's Laws is given in section 2.2. In section 2.3, the modulated current continuity equation is discretized by the Box Integral method. Thus, a global symbolic algebraic equation system is obtained that governs the flow of current over an arbitrary geometry subject to a field-dependent resistance. Section 2.5 provides a method with which to translate the symbolic algebraic equation system into an equivalent circuit netlist. Strategies to compact symbolic equation systems before netlist generation if they are

linear are shown in section 2.6. An alternative method of directly translating conductivity matrices into analog hardware description language (AHDL) is sketched in section 2.7. The model is verified by comparison to finite element simulation in section 2.8.

## 2.1 Conductivity relation under influence of non-electrical interactions

Ohm's Law is generalized to include interaction with non-electrical fields, and constraints for the proposed generalization are given.

### 2.1.1 General conductivity relation

In all devices which can be described by the model presented, the relation between current density  $\mathbf{j}$  [in ampere/m<sup>2</sup>] and the electrical field strength  $\mathbf{E}$  [in volt/m] is given by Ohm's Law

$$\mathbf{j} = \sigma \cdot \mathbf{E} \quad (2.1)$$

with the specific conductivity  $\sigma$  [in siemens/m]. Unlike ideal isotropic resistors, in which  $\sigma$  is a scalar constant, the conductivity in resistive sensors is a rank 2 tensor with components dependent on variables such as the magnetic field vector  $\mathbf{B}$ , mechanical stress tensor  $\mathbf{T}$ , or spatial position  $\mathbf{x}$ :

$$\sigma(\mathbf{B}, \mathbf{T}, \dots, \mathbf{x}) \quad (2.2)$$

If the geometry of the resistive structure being modeled can be reduced to two dimensions, the current density is replaced by the sheet current density [unit: amperes/m], and the electrical field becomes a two dimensional vector. Consequently, the conductivity becomes a  $2 \times 2$  matrix with unit siemens.

### 2.1.2 Physical interactions

Careful classification of the algebraic form of the constitutive equations for the physical interaction enables the method for netlist generation described here to

remain fairly general and applicable to a wide range of effects. We first look at anisotropic conductivity, then at the piezoresistive and galvanomagnetic interactions.

### 2.1.3 Common properties of interactions

The contributions to the conductivity tensor  $\sigma$  resulting from interactions with external fields can be decomposed into three classes:

1. Isotropic variations. These are scalar quantities which can be cast as multiples of the identity matrix, i.e., in two dimensions, of the matrix

$$\begin{pmatrix} 1 & 0 \\ 0 & 1 \end{pmatrix}. \quad (2.3)$$

2. Symmetric anisotropies (“shear”). These are expressed by symmetric traceless tensors, which in two dimensions can be cast as a linear combination of the matrices

$$\begin{pmatrix} 1 & 0 \\ 0 & -1 \end{pmatrix} \text{ and } \begin{pmatrix} 0 & 1 \\ 1 & 0 \end{pmatrix}. \quad (2.4)$$

3. Antisymmetric anisotropies (“rotation”), which are represented by antisymmetric tensors. In two dimensions, they simply are multiples of the matrix

$$\begin{pmatrix} 0 & -1 \\ 1 & 0 \end{pmatrix}. \quad (2.5)$$

The three classes of interaction are invariant under rotation of the coordinate axes. In three dimensions, the same classes can be found, but the dimensions of the subspaces are 1, 5, and 3, respectively. An example for an anisotropic symmetric interaction is the piezoresitive effect caused by mechanical stress. The Hall effect is caused by the antisymmetric galvanomagnetic interaction.

### 2.1.4 Piezoresistive interaction

The piezoresistive effect is an example for an anisotropic symmetric interaction. Under the effects of mechanical stress, the conductance becomes a symmetric tensor, given by [33]

$$\frac{\sigma_{ij}}{\sigma_0} = -\sum_{kl} \pi_{ijkl} T_{kl} \quad (2.6)$$

with the components  $T_{kl}$  of the  $3 \times 3$  mechanical stress tensor,

$$\mathbf{T} = \begin{pmatrix} T_{11} & T_{12} & T_{13} \\ T_{21} & T_{22} & T_{23} \\ T_{31} & T_{32} & T_{33} \end{pmatrix} = \begin{pmatrix} T_1 & T_6 & T_5 \\ T_6 & T_2 & T_4 \\ T_5 & T_4 & T_3 \end{pmatrix}, \quad (2.7)$$

and the components of the  $3 \times 3 \times 3 \times 3$  piezoresistance tensor  $\pi$

$$\pi_{ijkl} = \begin{cases} \pi_{11} & \text{if } i = j = k = l \\ \pi_{12} & \text{if } i = j \neq k = l \\ \pi_{44} & \text{if } i = k \neq j = l \\ 0 & \text{otherwise} \end{cases} \quad (2.8)$$

for materials with the symmetry properties of crystalline silicon. The indices on the right-hand side of equations (2.7) and (2.8) are assigned according to the *reduced matrix notation*. Numerical values for the piezoresistance coefficients for n-type and p-type silicon are shown in Table 2.1. A good overview of this notation as well as of the transformation properties for arbitrary coordinate orientations is given in [58] and [70]. Note that in the literature, it is common to give the influence of mechanical stress on the specific resistivity, not on the specific conductance. To first order, the relative change in conductance in eqn. (2.1) is equal to the *negative* relative change in resistivity.

Material	Piezoresistance Coefficients ( $10^{11} \text{ Pa}^{-1}$ )			Resistivity ( $\Omega \cdot \text{cm}$ )
	$\pi_{11}$	$\pi_{12}$	$\pi_{44}$	
n-Type Si	-102.2	53.4	-13.6	11.7
p-Type Si	6.6	-1.1	138.1	7.8

Tab. 2.1 Piezoresistance coefficients of n- and p-type silicon (from [80])

To obtain equations applicable to modeling, the geometrical transformations of the  $\pi$  and  $T$  tensors, and hence the conductivity  $\sigma$ , must be carried out explicitly [58]. For two-dimensional conduction in planar structures on (100) silicon wafers, as used for CMOS, the first order expansion of eqn. (2.6) for the effect of 3D mechanical stress on  $\sigma_0$ , the electrical sheet conductivity in absence of mechanical stress, yields the expression

$$\sigma = \begin{pmatrix} \sigma_{xx} & \sigma_{xy} \\ \sigma_{yx} & \sigma_{yy} \end{pmatrix} \quad (2.9)$$

with

$$\begin{aligned} \sigma_{xx} &= \sigma_0(1 - \pi_{11}T_1 - \pi_{12}(T_2 + T_3) - CPT_d - SPT_o) \\ \sigma_{yy} &= \sigma_0(1 - \pi_{11}T_2 - \pi_{12}(T_1 + T_3) + CPT_d + SPT_o) \\ \sigma_{xy} &= \sigma_{yx} = \sigma_0((- \pi_{44}/2 + CP)T_o - SPT_d) \end{aligned} \quad (2.10)$$

and

$$\begin{aligned} T_d &= T_1 - T_2, \quad T_o = 2T_6 \\ P &= \frac{1}{4}(\pi_{44} + \pi_{12} - \pi_{11}) \\ C &= 1 - \cos 4\phi, \quad S = \sin 4\phi \end{aligned} \quad (2.11)$$

where  $\phi$  is the angle of the geometrical coordinates in the  $x-y$  plane (parallel to the die surface) with respect to the crystal orientation, shown in Figure 2.1.

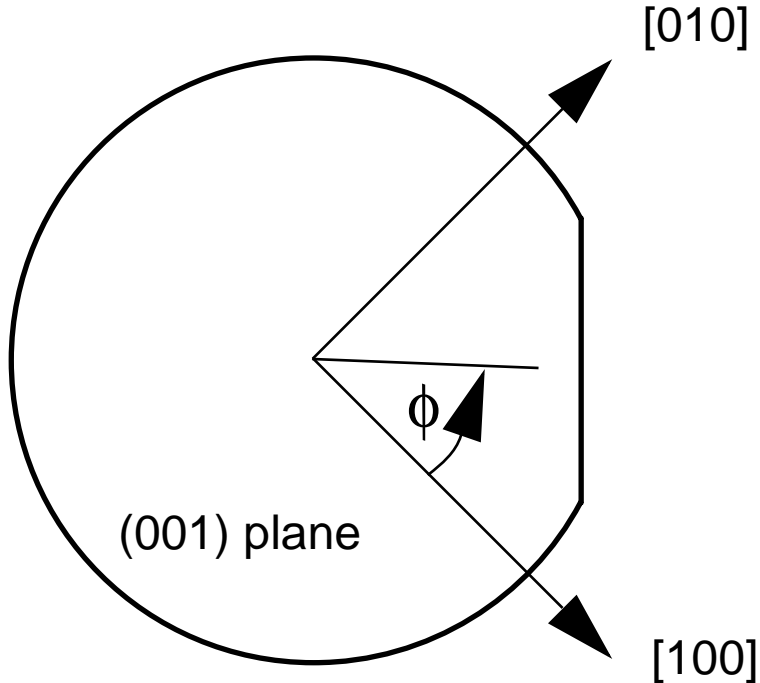


*Fig. 2.1 Geometry of (100) wafer used for CMOS process*

### 2.1.5 Galvanomagnetic interaction

An example for an antisymmetric interaction is the Hall effect. Reduced to two dimensions, as is practical for Hall sensors, the  $x-y$  plane is described by the modulated conductivity

$$\sigma = \frac{\sigma_0}{1 + (\mu B_z)^2} \begin{pmatrix} 1 & -\mu B_z \\ \mu B_z & 1 \end{pmatrix} \quad (2.12)$$

with the Hall mobility  $\mu$ , the conductivity  $\sigma_0$  in the absence of any magnetic fields, and the magnetic field component perpendicular to the  $x-y$  plane  $B_z$ . In addition to the introduction of an antisymmetric component, the conductance is also isotropically scaled by the factor  $1/(1 + (\mu B_z)^2)$ . A good overview of magnetic interactions in silicon is found in [71].

## 2.2 The Framework of Circuit Modeling: Nodal analysis

Circuit simulators such as SPICE [67] are based on nodal analysis [66]. Nodal analysis is a principle by which an *admittance matrix*  $\mathbf{Y}$  relates the voltages  $\mathbf{v}$  of the nodes of an electrical circuit and currents  $\mathbf{i}$  into<sup>1</sup> each node according to the relation (Ohm's Law)

$$\mathbf{i} = \mathbf{Y} \cdot \mathbf{v}. \quad (2.13)$$

A *node* is an idealized electrical interconnection with zero internal resistance and capacitance; therefore it can be assigned a unique voltage  $v_n$  and a unique net current  $i_n$  into the node. Conservation of electrical charge requires that *Kirchhoff's Current Law* be fulfilled, i. e.,

$$\forall n: i_n = 0. \quad (2.14)$$

As Ohm's Law (2.13) is a linear relation, the admittance matrix  $\mathbf{Y}$  can be decomposed to a sum of individual conductances and transconductances. Each group can be represented by *device stamps* corresponding to single resistors and transconductors in an actual circuit:

A resistor with resistance  $R = 1/G$  between nodes  $i$  and  $j$  is inserted to the admittance matrix by setting

$$Y_{ii} += -G, Y_{jj} += -G, Y_{ij} += G, \text{ and } Y_{ji} += G. \quad (2.15)$$

A current source with transconductance  $g_m$  from node  $k$  to node  $l$  controlled by the voltage from node  $i$  to node  $j$  is inserted by setting

$$Y_{ki} += -g_m, Y_{lj} += -g_m, Y_{kj} += g_m, \text{ and } Y_{li} += g_m. \quad (2.16)$$

1. This convention may differ from convention commonly used in the literature.

### 2.2.1 Microscopic Formulation of Kirchhoff's Laws

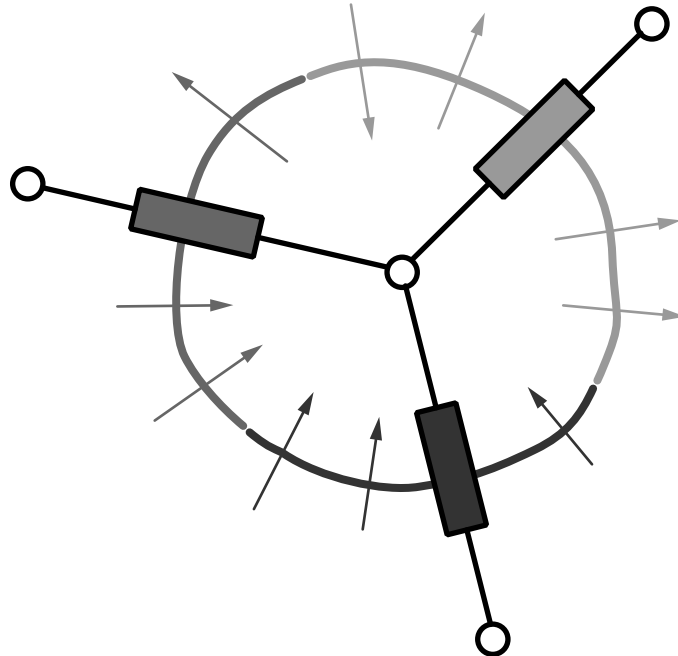


*Fig. 2.2 Discretization of charge conservation: the current through sections of the surface enclosing a node is lumped into impedances between nodes*

Kirchhoff's Current Law is a consequence of charge conservation

$$\nabla \cdot \mathbf{j} + \frac{\partial \rho}{\partial t} = 0. \quad (2.17)$$

Gauß's Law is used to discretize space into finite volumes enclosing nodes,

$$\int_{\Omega_l} \left( \nabla \cdot \mathbf{j} + \frac{\partial \rho}{\partial t} \right) dx = \int_{\partial \Omega_l} \mathbf{n} \cdot \mathbf{j} dS(x) + \frac{dQ_l}{dt}. \quad (2.18)$$

As shown in Figure 2.2, the currents into node  $k$  through sections of the surface of the volume are lumped into a finite sum of currents

$$\int_{\partial \Omega} \mathbf{n} \cdot \mathbf{j} dS(x) = \sum_k \int_{\partial \Omega_l} \mathbf{n} \cdot \mathbf{j} dS(x) = \sum_k i_{kl} \equiv i_l. \quad (2.19)$$

As a node carries no charge *by definition*,  $Q_l = 0$ , Kirchhoff's Current Law (2.14) follows from (2.17).

Kirchhoff's Voltage Law is equivalent with the existence of a uniquely defined potential  $\Phi$ , i. e., any effects of electromagnetic induction are absorbed into the lumped circuit elements connecting the nodes:

$$\sum_{(kl) \in \text{closed loop}} V_l - V_k \equiv \int_{\partial\Omega} \nabla \times \mathbf{E} \, dS(\mathbf{x}) = 0. \quad (2.20)$$

## 2.3 The Box Integration Method

By inserting Ohm's Law (2.1) into the charge conservation equation (2.17), a Poisson-type relation

$$\nabla \cdot (\boldsymbol{\sigma} \cdot \nabla \Phi(\mathbf{x})) - s(\mathbf{x}) = 0 \quad (2.21)$$

with scalar potential  $\Phi$ , scalar source (e. g. current source) density  $s$  and tensor  $\boldsymbol{\sigma}$  (e. g. conductivity) is obtained. This relation is discretized on a grid as follows:  
A potential

$$\Phi(\mathbf{x}) = \sum_k N_k(\mathbf{x}) \Phi_k \quad (2.22)$$

is approximated using the value of the potential  $\Phi_k$  at grid node  $k$  and the node's shape function  $N_k$ . The sum is finite at all locations  $\mathbf{x}$ , so that

$$\sum_k N_k(\mathbf{x}) = 1 \text{ for all } \mathbf{x}. \quad (2.23)$$

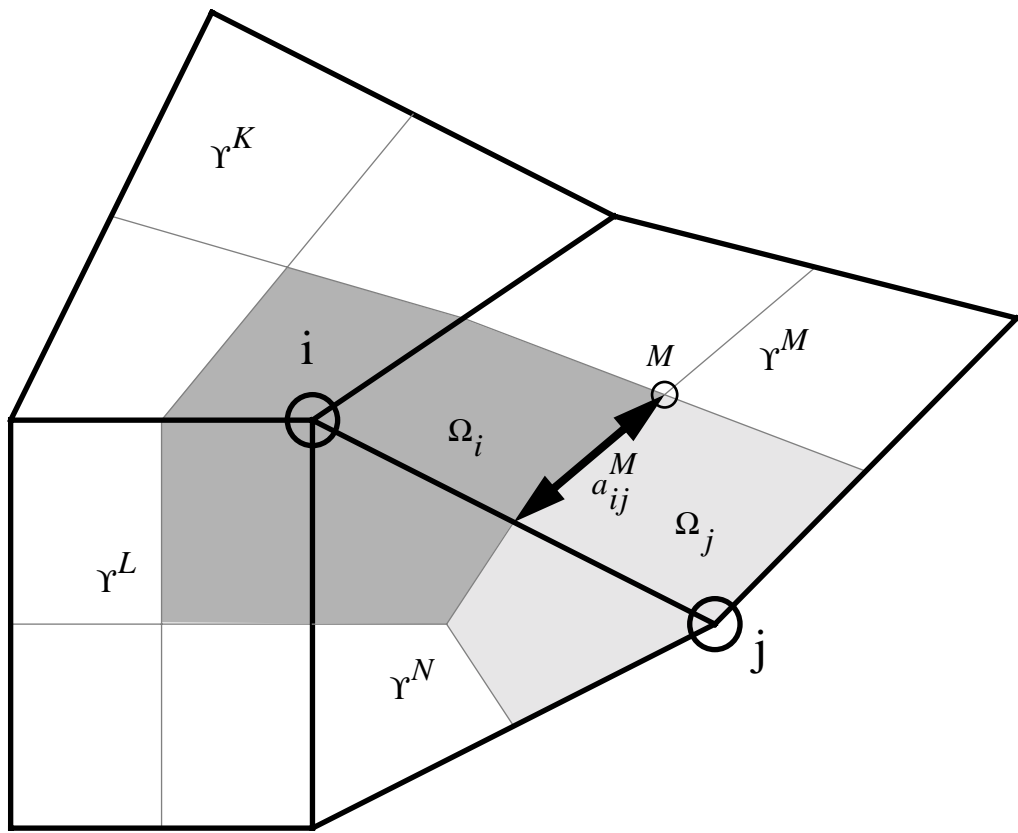


*Fig. 2.3 Box discretization scheme. The darker highlighted area to the left indicates the box or finite volume  $\Omega_i$  about node  $i$ . The lighter highlighted area to the right indicates the box or finite volume  $\Omega_j$  about node  $j$ . The nodes lie on the vertices of mesh elements  $\Upsilon$  whose edges are indicated by the thick black lines. The box edges shown as light-gray lines are constructed by connecting each element's area centroid with its edge centroids, e.g., the edge  $a_{ijM}$  separating nodes  $i$  and  $j$  in mesh element  $M$ , indicated by the arrow.*

The volume is partitioned into nonoverlapping polyhedra  $\Upsilon^M$ , called elements, the vertices of which are the grid nodes. Due to (2.22), the differential operators just act on the shape functions  $N_k(\mathbf{x})$ , so that the Poisson equation (2.21) reads as

$$\sum_k \Phi_k \nabla \cdot (\boldsymbol{\sigma} \cdot \nabla N_k(\mathbf{x})) - s(\mathbf{x}) = 0 \quad (2.24)$$

The differential equation is discretized to volumes of finite size. To this end, the volume is partitioned into another set of nonoverlapping polyhedra  $\Omega_i$ , called

boxes, each of which contains one grid node  $i$  (see figure 2.3). A residual equation is formed by requiring that the integral of equation (2.24) vanish within each box. The integration over a box volume  $\Omega_i$  is performed using Gauss's Theorem:

$$\int_{\Omega_i} \nabla \cdot (\sigma \cdot \nabla \Phi(\mathbf{x})) \, d\mathbf{x} = \int_{\partial\Omega_i} \mathbf{n} \cdot \sigma \cdot \nabla \Phi(\mathbf{x}) \, dS(\mathbf{x}) = \sum_k \left( \Phi_k \int_{\partial\Omega_i} \mathbf{n} \cdot \sigma \cdot \nabla N_k(\mathbf{x}) \, dS(\mathbf{x}) \right) \quad (2.25)$$

### 2.3.1 Discretization of flux

The vertices of the box polyhedra  $\Omega_i$  containing the grid nodes form the nodes of a dual grid. Generally, there is exactly one dual grid node in each element  $\Upsilon^M$ . The boundary  $\partial\Omega_i$  of each of the boxes in  $\Omega_i$  is now split into regions intersecting with different  $\Upsilon^M$ , denoted as  $\partial\Omega_i^M$  (see figure 2.3). Thus, expression (2.25) becomes

$$\sum_M \int_{\Omega_i^M} \nabla \cdot (\sigma \cdot \nabla \Phi(\mathbf{x})) \, d\mathbf{x} = \sum_M \sum_k \left( \Phi_k \int_{\partial\Omega_i^M} \mathbf{n}^M \cdot \sigma \cdot \nabla N_k(\mathbf{x}) \, dS(\mathbf{x}) \right) \quad (2.26)$$

The surface integral is further decomposed into a sum of integrations on surfaces:

$$\int_{\partial\Omega_i^M} \mathbf{n}^M \cdot \sigma \cdot \nabla N_k(\mathbf{x}) \, dS(\mathbf{x}) = \sum_{j \neq i} \int_{a_{ij}^M} \mathbf{n}_{ij}^M \cdot \sigma \cdot \nabla N_k(\mathbf{x}) \, dS(\mathbf{x}) \quad (2.27)$$

with  $a_{ij}^M = \partial\Omega_i \cap \partial\Omega_j \cap \Upsilon^M$  the common boundary of polyhedra  $\Omega_i$  and  $\Omega_j$  within element  $M$ , and  $\mathbf{n}_{ij}^M$  its normal vector **from  $i$  to  $j$** . Substituting everything back into expression (2.25), we get

$$\begin{aligned} \int_{\Omega_i} \nabla \cdot (\boldsymbol{\sigma} \cdot \nabla \Phi(\mathbf{x})) \, d\mathbf{x} &= \sum_M \int_{\Omega_i^M} \nabla \cdot (\boldsymbol{\sigma} \cdot \nabla \Phi(\mathbf{x})) \, d\mathbf{x} = \\ &= \sum_M \sum_k \Phi_k \left( \sum_{\substack{j \\ j \neq i}} \int_{a_{ij}^M} \mathbf{n}_{ij}^M \cdot \boldsymbol{\sigma} \cdot \nabla N_k(\mathbf{x}) \, dS(\mathbf{x}) \right) = \sum_M \sum_k K_{ik}^M \Phi_k \end{aligned} \quad (2.28)$$

We can now collect all the flux  $\boldsymbol{\sigma} \cdot \nabla \Phi$  through the volume  $\Upsilon^M$  at node  $M$  of the second grid.  $\sum_k K_{ik}^M \Phi_k$  is the flux into node  $M$  from volume  $\Omega_i$ . The summation index  $k$  encompasses all the nodes on the primary grid with nonzero shape function  $N_k$  within  $\Upsilon^M$ . This includes node  $i$ .

### 2.3.2 Conservation laws

From equation (2.28) we find that the Poisson equation (2.21), integrated on volume  $\Omega_i^M$ , requires that

$$\sum_k K_{ik}^M \Phi_k = \int_{\Omega_i^M} s(\mathbf{x}) \, d\mathbf{x} \quad (2.29)$$

Because the set  $\{N_k\}_k$  is a partition of unity,

$$\sum_k \nabla N_k(\mathbf{x}) = \mathbf{0} \quad \forall \mathbf{x} \quad (2.30)$$

Consequently, the conductivities into node  $M$  associated with node  $i$  sum to zero:

$$\begin{aligned} \sum_k K_{ik}^M &= \sum_k \sum_{\substack{j \\ j \neq i}} \int_{a_{ij}^M} \mathbf{n}_{ij}^M \cdot \boldsymbol{\sigma} \cdot \nabla N_k(\mathbf{x}) dS(\mathbf{x}) = \\ &\sum_{\substack{j \\ j \neq i}} \int_{a_{ij}^M} \left( \mathbf{n}_{ij}^M \cdot \boldsymbol{\sigma} \cdot \sum_k \nabla N_k(\mathbf{x}) \right) dS(\mathbf{x}) = 0 \end{aligned} \quad (2.31)$$

This relation reflects the fact that there is no current flow in the absence of any potential difference. Due to  $a_{ij}^M = a_{ji}^M$  and  $\mathbf{n}_{ij}^M = -\mathbf{n}_{ji}^M$ , summation of all contributions of flux into node  $M$  proportional to the potential  $\Phi_k$  yields

$$\begin{aligned} \sum_i K_{ik}^M &= \sum_{\substack{i, j \\ i \neq j}} \int_{a_{ij}^M} \mathbf{n}_{ij}^M \cdot \boldsymbol{\sigma} \cdot \nabla N_k(\mathbf{x}) dS(\mathbf{x}) = \\ &\sum_{\substack{i, j \\ i < j}} \int_{a_{ij}^M} (\mathbf{n}_{ij}^M + \mathbf{n}_{ji}^M) \cdot \boldsymbol{\sigma} \cdot \nabla N_k(\mathbf{x}) dS(\mathbf{x}) = 0 \end{aligned} \quad (2.32)$$

This means that the divergence of the flux from node  $M$ , irrespective of the potentials  $\Phi_k$ , is zero. If the flux is an electrical current, this corresponds to Kirchhoff's Current Law. Summing over all contributions involving the volume  $\Omega_i$ , we find

$$K_{ik} \equiv \sum_M K_{ik}^M = \sum_j \int_{a_{ij}} \mathbf{n}_{ij} \cdot \boldsymbol{\sigma} \cdot \nabla N_k(\mathbf{x}) dS(\mathbf{x}) \quad (2.33)$$

with  $a_{ij} = \partial\Omega_i \cap \partial\Omega_j$ . The indices  $i$  and  $k$  in equation (2.33) range over all grid nodes. Thus, the coefficients  $K_{ik}$  form a square matrix, the *system matrix*, with

$$I_i = \sum_k K_{ik} \Phi_k, \quad (2.34)$$

relating the current  $I_i$  emerging from node  $i$  to the potential  $\Phi_k$  at the nodes  $k$ . Charge conservation (2.32) requires that all column sums of the system matrix are

equal to zero. Thus, the system matrix only describes current flows between nodes of the model, irrespective of the applied potentials. External currents must be added separately. Due to relation (2.31), all row sums of the system matrix are equal to zero as well. Thus, at a constant potential, no current flows between the nodes. Consequently, we can replace the potentials  $\Phi_k$  by voltages  $V_k$  with respect to an arbitrary reference potential. In the language of nodal analysis, the system matrix is called the admittance matrix.

## 2.4 Discretization on a quadrilateral grid

In order to represent a resistor by a system matrix as described above, a discretization grid is chosen and the integrals in equation (2.33) are evaluated. As an example, a discretization scheme for quadrilateral discretization grids of two-dimensional structures is implemented.

### 2.4.1 Defining the grid

A possible choice to define the mesh of elements and nodes that represents the discretised geometry of the resistive device is MEMDRAW [72], originally developed in-house, although any other mesh generator could be used. As shown in Figure 2.4, it is important that the mesh file format contain the following information:

- a list of mesh nodes with their geometrical coordinates
- a list of mesh elements, each element with its node reference and material label
- a list of boundary segments with name and associated nodes

This information, used to assemble the admittance matrix representing the device to be modelled, is read into a *Mathematica* [78] program at the start of the model building process.

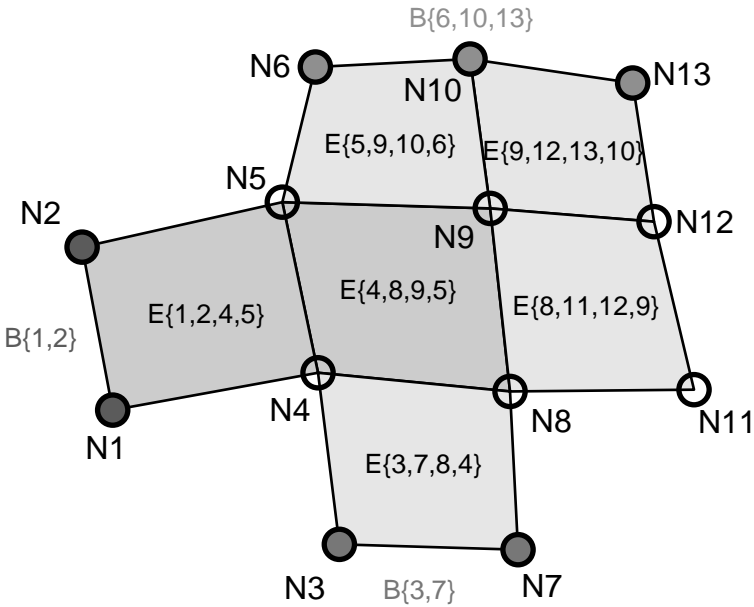


Fig. 2.4 Required mesh information: *Nodes, Elements, and Boundaries*

### 2.4.2 Integration of node currents

In order to determine the conductance  $K_{ik}^M$  out of mesh node  $i$  due to an electric potential at mesh node  $k$  effected by the mesh element  $M$ , line integrals of the form

$$K_{ik}^M = \sum_{\substack{j \\ j \neq i}} \int_{a_{ij}^M} \mathbf{n}_{ij}^M \cdot \boldsymbol{\sigma} \cdot \nabla N_k(\mathbf{x}) \, dS(\mathbf{x}) \quad (2.35)$$

must be evaluated (2.33). The conductivity tensor  $\boldsymbol{\sigma}$  is determined by the interactions being modelled, whereas the shape functions  $N_k$ , normal vectors  $\mathbf{n}_{ij}^M$ , and integration domains  $a_{ij}^M$  are determined by the discretization grids chosen, and in particular, depend on the shape of each individual mesh element.

For each mesh element  $M$ , we choose the integration domain  $a_{ij}^M$  to be the line from the element's centroid to the midpoint of the edge connecting nodes  $i$  and  $j$ , or zero if the nodes do not share a common edge (see figure 2.3). Within element  $M$ , each node has current contributions from only two neighboring nodes, namely, from the two adjacent nodes on the element's edge. Conversely, each

integration domain contributes to the current of two adjacent nodes, once with positive and once with negative sign. This property has been shown in the derivation of charge conservation (2.32). Thus, for each quadrilateral's node  $k$  four integrals of the form (2.35)

$$\mathbf{n}_{ij}^M \cdot \boldsymbol{\sigma} \cdot \int_{a_{ij}^M} \nabla N_k(\mathbf{x}) \, dS(\mathbf{x}) \quad (2.36)$$

with  $ij \in \{12, 23, 24, 41\}$  are evaluated. As the unit normal vectors  $\mathbf{n}_{ij}^M$  are constant on each integration domain and we assume that the conductivity tensor  $\boldsymbol{\sigma}$  is constant within each element, both terms are moved out of the integral.

To simplify the evaluation of the integrals, the quadrilaterals of the discretization mesh are each mapped onto a square with vertices  $(-1, -1)$ ,  $(1, -1)$ ,  $(1, 1)$ , and  $(-1, 1)$  by means of a so-called *isoparametric mapping* [68]. This type of mapping uses the functions  $N_k$  both to map from the square's reference coordinates  $(\xi, \nu)$  to the physical coordinates  $(x, y)$  of the quadrilateral and to interpolate the potential distribution  $\Phi(x, y)$  from the node potentials  $\Phi_k$ . The transformation is shown in more detail in figure 2.5.

The integrals in (2.36) are now evaluated in reference coordinates as

$$\mathbf{w}_{ij} \cdot \boldsymbol{\sigma} \cdot \int_0^1 \boldsymbol{\Xi}(t) \cdot \nabla \bar{N}_k(\eta_{ij}(t)) \, dt \quad (2.37)$$

with the derivative of the shape function  $\nabla \bar{N}_k$  in reference coordinates, transformed to physical coordinates by the inverse Jacobian of the isoparametric mapping function defined on the integration domain  $\eta_{ij}(t)$ ,

$$\boldsymbol{\Xi}(t) \equiv \begin{pmatrix} \frac{\partial x}{\partial \xi} \Big|_{\eta_{ij}(t)} & \frac{\partial x}{\partial \nu} \Big|_{\eta_{ij}(t)} \\ \frac{\partial y}{\partial \xi} \Big|_{\eta_{ij}(t)} & \frac{\partial y}{\partial \nu} \Big|_{\eta_{ij}(t)} \end{pmatrix}^{-1}. \quad (2.38)$$

In this representation, the integration domains and the shape function derivatives  $\nabla \bar{N}_k$  now become equal for all quadrilaterals of the mesh, regardless of their individual shape.  $w_{ij}$  is the vector from the centroid of the element to the midpoint in *physical* (mesh) coordinates between nodes  $i$  and  $j$ , rotated by  $90^\circ$ , hence its length is *not* unity as it also absorbs the integration measure. The integral transformation is detailed in figure 2.5. Note that the functional relation describing the

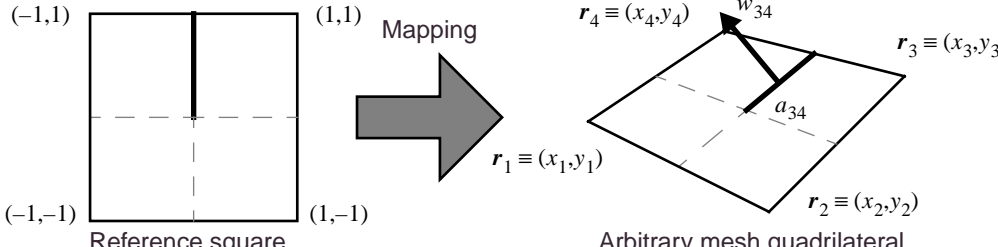
<b>Line integral</b> $\mathbf{w}_{ij} \cdot \boldsymbol{\sigma} \cdot \int_0^1 \begin{pmatrix} \frac{\partial x}{\partial \xi} \Big _{\eta_{ij}(t)} & \frac{\partial x}{\partial v} \Big _{\eta_{ij}(t)} \\ \frac{\partial y}{\partial \xi} \Big _{\eta_{ij}(t)} & \frac{\partial y}{\partial v} \Big _{\eta_{ij}(t)} \end{pmatrix}^{-1} \cdot \nabla \bar{N}_k(\eta_{ij}(t)) dt$			
 <p>Mapping</p> <p>(-1,1) (1,1) (-1,-1) (1,-1)</p> <p>Reference square</p> <p><math>r_4 \equiv (x_4, y_4)</math> <math>w_{34}</math> <math>r_1 \equiv (x_1, y_1)</math> <math>r_2 \equiv (x_2, y_2)</math> <math>r_3 \equiv (x_3, y_3)</math> <math>a_{34}</math></p> <p>Arbitrary mesh quadrilateral</p>			
<b>Normal vectors</b> $w_{34} = \left( \frac{(y_1 + y_2) - (y_3 + y_4)}{4}, \frac{(x_3 + x_4) - (x_1 + x_2)}{4} \right) = -w_{12}$ $w_{41} = \left( \frac{(y_2 + y_3) - (y_4 + y_1)}{4}, \frac{(x_4 + x_1) - (x_2 + x_3)}{4} \right) = -w_{23}$			
<table style="width: 100%; border-collapse: collapse;"> <tr> <td style="width: 33%; padding-right: 10px;"> <b>Jacobian</b>  <math display="block">\begin{pmatrix} \frac{\partial x}{\partial \xi} &amp; \frac{\partial x}{\partial v} \\ \frac{\partial y}{\partial \xi} &amp; \frac{\partial y}{\partial v} \end{pmatrix} = \begin{pmatrix} x_1 &amp; x_2 &amp; x_3 &amp; x_4 \\ y_1 &amp; y_2 &amp; y_3 &amp; y_4 \end{pmatrix} \begin{pmatrix} \frac{\partial}{\partial \xi} \bar{N}_1 &amp; \frac{\partial}{\partial v} \bar{N}_1 \\ \frac{\partial}{\partial \xi} \bar{N}_2 &amp; \frac{\partial}{\partial v} \bar{N}_2 \\ \frac{\partial}{\partial \xi} \bar{N}_3 &amp; \frac{\partial}{\partial v} \bar{N}_3 \\ \frac{\partial}{\partial \xi} \bar{N}_4 &amp; \frac{\partial}{\partial v} \bar{N}_4 \end{pmatrix}</math> </td> <td style="width: 33%; padding-right: 10px;"> <b>Shape function gradients</b>  <math>\nabla \bar{N}_1(\xi, v) = (\frac{v-1}{4}, \frac{\xi-1}{4})</math>  <math>\nabla \bar{N}_2(\xi, v) = (\frac{1-v}{4}, \frac{-\xi-1}{4})</math>  <math>\nabla \bar{N}_3(\xi, v) = (\frac{v+1}{4}, \frac{\xi+1}{4})</math>  <math>\nabla \bar{N}_4(\xi, v) = (\frac{-v-1}{4}, \frac{1-\xi}{4})</math> </td> <td style="width: 33%;"> <b>Integration domains</b>  <math>\eta_{12}(t) = (0, -t)</math>  <math>\eta_{23}(t) = (t, 0)</math>  <math>\eta_{34}(t) = (0, t)</math>  <math>\eta_{41}(t) = (-t, 0)</math> </td> </tr> </table>	<b>Jacobian</b> $\begin{pmatrix} \frac{\partial x}{\partial \xi} & \frac{\partial x}{\partial v} \\ \frac{\partial y}{\partial \xi} & \frac{\partial y}{\partial v} \end{pmatrix} = \begin{pmatrix} x_1 & x_2 & x_3 & x_4 \\ y_1 & y_2 & y_3 & y_4 \end{pmatrix} \begin{pmatrix} \frac{\partial}{\partial \xi} \bar{N}_1 & \frac{\partial}{\partial v} \bar{N}_1 \\ \frac{\partial}{\partial \xi} \bar{N}_2 & \frac{\partial}{\partial v} \bar{N}_2 \\ \frac{\partial}{\partial \xi} \bar{N}_3 & \frac{\partial}{\partial v} \bar{N}_3 \\ \frac{\partial}{\partial \xi} \bar{N}_4 & \frac{\partial}{\partial v} \bar{N}_4 \end{pmatrix}$	<b>Shape function gradients</b> $\nabla \bar{N}_1(\xi, v) = (\frac{v-1}{4}, \frac{\xi-1}{4})$ $\nabla \bar{N}_2(\xi, v) = (\frac{1-v}{4}, \frac{-\xi-1}{4})$ $\nabla \bar{N}_3(\xi, v) = (\frac{v+1}{4}, \frac{\xi+1}{4})$ $\nabla \bar{N}_4(\xi, v) = (\frac{-v-1}{4}, \frac{1-\xi}{4})$	<b>Integration domains</b> $\eta_{12}(t) = (0, -t)$ $\eta_{23}(t) = (t, 0)$ $\eta_{34}(t) = (0, t)$ $\eta_{41}(t) = (-t, 0)$
<b>Jacobian</b> $\begin{pmatrix} \frac{\partial x}{\partial \xi} & \frac{\partial x}{\partial v} \\ \frac{\partial y}{\partial \xi} & \frac{\partial y}{\partial v} \end{pmatrix} = \begin{pmatrix} x_1 & x_2 & x_3 & x_4 \\ y_1 & y_2 & y_3 & y_4 \end{pmatrix} \begin{pmatrix} \frac{\partial}{\partial \xi} \bar{N}_1 & \frac{\partial}{\partial v} \bar{N}_1 \\ \frac{\partial}{\partial \xi} \bar{N}_2 & \frac{\partial}{\partial v} \bar{N}_2 \\ \frac{\partial}{\partial \xi} \bar{N}_3 & \frac{\partial}{\partial v} \bar{N}_3 \\ \frac{\partial}{\partial \xi} \bar{N}_4 & \frac{\partial}{\partial v} \bar{N}_4 \end{pmatrix}$	<b>Shape function gradients</b> $\nabla \bar{N}_1(\xi, v) = (\frac{v-1}{4}, \frac{\xi-1}{4})$ $\nabla \bar{N}_2(\xi, v) = (\frac{1-v}{4}, \frac{-\xi-1}{4})$ $\nabla \bar{N}_3(\xi, v) = (\frac{v+1}{4}, \frac{\xi+1}{4})$ $\nabla \bar{N}_4(\xi, v) = (\frac{-v-1}{4}, \frac{1-\xi}{4})$	<b>Integration domains</b> $\eta_{12}(t) = (0, -t)$ $\eta_{23}(t) = (t, 0)$ $\eta_{34}(t) = (0, t)$ $\eta_{41}(t) = (-t, 0)$	

Fig. 2.5 Isoparametric mapping of reference square to an arbitrary convex quadrilateral and interpolation of potential  $\Phi(x,y)$

coupling of the conductivity to external fields is retained by *symbolic* transforma-

tions, whereas the integrals (2.37) are *numerically* evaluated by Gaussian quadrature [73].

### Assembly of the system matrix

In order to assemble the system matrix  $\mathbf{K}$  from the element matrix contributions  $\mathbf{K}^M$ , the contributions local to an element are simply added up:  $K_{ik} = \sum_M K_{ik}^M$ .

## 2.5 Translation of the model into SPICE netlist

In this section, the translation of the system matrix obtained in the previous section into equivalent circuit elements is demonstrated. To this end, the system matrix is decomposed into a linear combination of basis elements which directly map to equivalent circuit elements. We present methods to extract the circuit elements that ensure charge conservation, which might have been violated by numerical round-off errors.

### 2.5.1 Decomposition of the system matrix into basis elements

The element matrices as well as the complete system matrix satisfy the relations

$$\sum_i K_{ik} = \mathbf{0} \text{ and } \sum_k K_{ik} = \mathbf{0}. \quad (2.39)$$

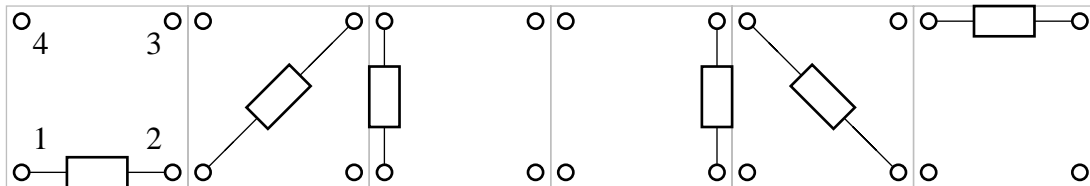
Matrices with these properties can be expanded into a basis which in turn can be directly translated into equivalent circuit elements. The basis for  $4 \times 4$  matrices (corresponding to a basis for a single quadrilateral element) is explicitly given, as well as rules on how to construct a basis for arbitrary  $n \times n$  system matrices. Analogous to the decomposition of the conductivity tensor shown in section 2.1.3, the basis matrices consist of subsets, viz. symmetric and antisymmetric matrices, which translate into conductances and pairs of transconductances (VCCS), respectively.

### 2.5.2 Symmetric basis elements and their circuit equivalent

Any symmetric  $4 \times 4$  matrix with zero column and row sums can be decomposed into a linear combination of basis matrices with four non-zero entries; two diagonal elements and two elements at the intersections of the corresponding rows and columns:

$$\begin{aligned} & \begin{bmatrix} -1 & 1 & 0 & 0 \\ 1 & -1 & 0 & 0 \\ 0 & 0 & 0 & 0 \\ 0 & 0 & 0 & 0 \end{bmatrix}, \begin{bmatrix} -1 & 0 & 1 & 0 \\ 0 & 0 & 0 & 0 \\ 1 & 0 & -1 & 0 \\ 0 & 0 & 0 & 0 \end{bmatrix}, \begin{bmatrix} -1 & 0 & 0 & 1 \\ 0 & 0 & 0 & 0 \\ 0 & 0 & 0 & 0 \\ 1 & 0 & 0 & -1 \end{bmatrix}, \begin{bmatrix} 0 & 0 & 0 & 0 \\ 0 & -1 & 1 & 0 \\ 0 & 1 & -1 & 0 \\ 0 & 0 & 0 & 0 \end{bmatrix}, \\ & \begin{bmatrix} 0 & 0 & 0 & 0 \\ 0 & -1 & 0 & 1 \\ 0 & 0 & 0 & 0 \\ 0 & 1 & 0 & -1 \end{bmatrix}, \begin{bmatrix} 0 & 0 & 0 & 0 \\ 0 & 0 & 0 & 0 \\ 0 & 0 & -1 & 1 \\ 0 & 0 & 1 & -1 \end{bmatrix} \end{aligned} \tag{2.40}$$

The symmetric basis matrices correspond to the device stamps of pure resistances, viz.



For a general  $n \times n$  matrix satisfying relations (2.39), the basis matrices can be constructed by the following rule:

$$\left. \begin{array}{l} B_{ii} = B_{jj} = -1 \\ B_{ij} = B_{ji} = 1 \\ \text{all other } B_{\kappa\lambda} = 0 \end{array} \right\} \text{for indices } i, j \text{ with } i < j. \tag{2.41}$$

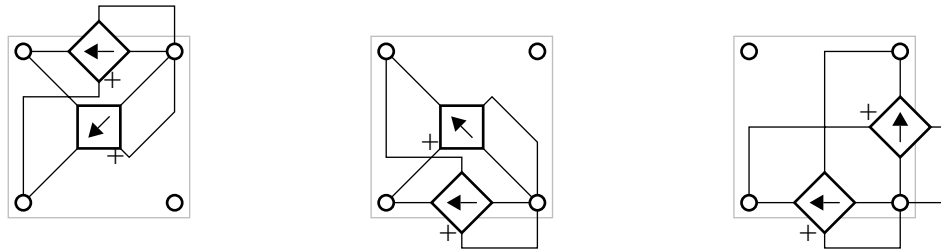
Thus, there are  $\frac{n \cdot (n - 1)}{2}$  symmetric basis matrices for an  $n \times n$  system matrix.

### 2.5.3 Antisymmetric basis elements and their circuit equivalent

Antisymmetric matrices with zero row and column sums can be represented as linear combination of basis matrices with pairs of non-zero entries in three rows and columns. A possible representation of the  $4 \times 4$  antisymmetric basis matrices is:

$$\begin{bmatrix} 0 & 0 & 1 & -1 \\ 0 & 0 & 0 & 0 \\ -1 & 0 & 0 & 1 \\ 1 & 0 & -1 & 0 \end{bmatrix}, \begin{bmatrix} 0 & 1 & 0 & -1 \\ -1 & 0 & 0 & 1 \\ 0 & 0 & 0 & 0 \\ 1 & -1 & 0 & 0 \end{bmatrix}, \begin{bmatrix} 0 & 1 & -1 & 0 \\ -1 & 0 & 1 & 0 \\ 1 & -1 & 0 & 0 \\ 0 & 0 & 0 & 0 \end{bmatrix} \quad (2.42)$$

Every antisymmetric basis matrix can be represented by two voltage controlled current sources, viz.



Each basis matrix corresponds to the device stamps of a pair of voltage controlled current sources (VCCS). The sources can be placed in three different ways, as shown in Table 2.2.

For a general  $n \times n$  matrix satisfying relations (2.39), the basis matrices can be constructed by the following rule:

$$\left. \begin{array}{l} B_{1j} = B_{ji} = B_{i1} = -1 \\ B_{1i} = B_{ij} = B_{j1} = 1 \\ \text{all other } B_{\kappa\lambda} = 0 \end{array} \right\} \text{for indices } i, j \text{ with } 1 < i < j. \quad (2.43)$$

Thus, there are  $(n-1) \cdot (n-2)/2$  antisymmetric basis matrices for an  $n \times n$  system matrix. In total, there are  $(n-1)^2$  basis elements for an  $n \times n$  matrix: Due

<i>Alternative</i>	<i>Source #</i>	<i>I+</i>	<i>I-</i>	<i>V+</i>	<i>V-</i>
A	1	1	i	j	i
	2	i	j	1	i
B	1	1	j	1	i
	2	i	1	1	j
C	1	j	1	i	j
	2	i	j	1	j

Tab. 2.2 Alternatives for representing an antisymmetric basis element by two VCCS

to (2.39), one row and one column depend on the other rows and columns, respectively.

#### 2.5.4 Extraction of the basis elements from the admittance matrix

The decomposition of the admittance matrix representing a resistive device into its basis elements must be performed symbolically to preserve the functional relation of the conductance to the coupling non-electrical fields. Two methods are presented: a least-squares optimal extraction method by forming the pseudoinverse of the vector of basis elements, and a fast, direct extraction method from off-diagonal matrix elements of the symmetrized and antisymmetrized admittance matrices.

##### Extraction by pseudoinverse

Due to the numerical integration of the line integrals as described in section 2.32.4.2, round-off errors may be introduced which cause the row and columns sums of the system matrix to deviate from zero. By reshaping the  $n \times n$  system matrix into a vector  $\mathbf{k}$  of length  $n^2$  and the basis matrices into an  $n^2 \times (n - 1)^2$  matrix  $\mathbf{B}$ , the error

$$\varepsilon = \|\mathbf{k} - \mathbf{B} \cdot \mathbf{c}\|^2 \quad (2.44)$$

is minimized by solving for the vector of the weighting coefficients  $\mathbf{c}$  using the pseudoinverse

$$\mathbf{c} = \mathbf{B}^T \cdot (\mathbf{B} \cdot \mathbf{B}^T)^{-1} \cdot \mathbf{k}. \quad (2.45)$$

Symbolic inversion of the  $n^2 \times n^2$  matrix  $(\mathbf{B} \cdot \mathbf{B}^T)^{-1}$  is prohibitively slow even for moderately sized system matrices.

### Extraction by matrix element read-out

Each symmetrical basis vector is uniquely labelled by an ordered pair of indices  $i, j$  with  $i < j$ . Each antisymmetric basis vector is uniquely identified by an index pair  $i, j$  with  $1 < i < j$ . This follows from the assembly rules (2.40) and (2.42) for the symmetrical and antisymmetrical basis vectors. Thus, the vectors of the expansion coefficients  $c_{ij}^S$  and  $c_{ij}^A$  for the symmetric and antisymmetric basis elements, respectively, can be deduced from the system matrix  $\mathbf{K}$  and its transpose  $\mathbf{K}^T$  as

$$\mathbf{c}^S = \frac{\mathbf{K} + \mathbf{K}^T}{2} \text{ and } \mathbf{c}^A = \frac{\mathbf{K} - \mathbf{K}^T}{2} \quad (2.46)$$

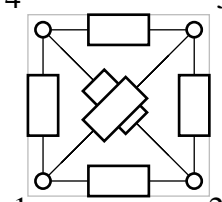
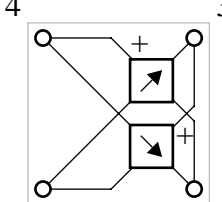
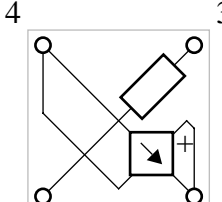
The diagonal elements of the system matrix are not used for element extraction.

### 2.5.5 Translation of the extracted basis elements to SPICE netlist lines

From the expansion coefficients and the equivalent circuit representations for the basis elements, the model, specified by its geometric mesh and the conductivity interaction, can be translated into an equivalent SPICE netlist. As an illustrative example, we explicitly show how the basis matrices of a 2x2 conductivity interaction as given in section 2.1.3 are generated. The representative conductivity interactions, the system matrices for a unit square, and the equivalent schematics

are shown in Table 2.3. Note that the equivalent circuit representation is not

*Tab. 2.3 Equivalent circuit representation of conductivity on a unit square*

<b>Interaction</b>	<b>Element system matrix</b>	<b>Equivalent schematic</b>
$\sigma_{\text{isotropic}} \begin{pmatrix} 1 & 0 \\ 0 & 1 \end{pmatrix}$	$\sigma_{\text{isotropic}} \begin{pmatrix} -\frac{3}{4} & \frac{1}{4} & \frac{1}{4} & \frac{1}{4} \\ \frac{1}{4} & -\frac{3}{4} & \frac{1}{4} & \frac{1}{4} \\ \frac{1}{4} & \frac{1}{4} & -\frac{3}{4} & \frac{1}{4} \\ \frac{1}{4} & \frac{1}{4} & \frac{1}{4} & -\frac{3}{4} \end{pmatrix}$	 <p>All resistances: <math>R = \frac{4}{\sigma_{\text{isotropic}}}</math></p>
$\sigma_{\text{antisymmetric}} \begin{pmatrix} 0 & -1 \\ 1 & 0 \end{pmatrix}$	$\sigma_{\text{antisymmetric}} \begin{pmatrix} 0 & \frac{1}{2} & 0 & -\frac{1}{2} \\ -\frac{1}{2} & 0 & \frac{1}{2} & 0 \\ 0 & -\frac{1}{2} & 0 & \frac{1}{2} \\ \frac{1}{2} & 0 & -\frac{1}{2} & 0 \end{pmatrix}$	 <p>All transconductances:  <math>g_m = \frac{\sigma_{\text{antisymmetric}}}{2}</math></p>
$\sigma_{\text{symmetric}} \begin{pmatrix} 0 & 1 \\ 1 & 0 \end{pmatrix}$	$\sigma_{\text{symmetric}} \begin{pmatrix} -\frac{1}{2} & 0 & \frac{1}{2} & 0 \\ 0 & \frac{1}{2} & 0 & -\frac{1}{2} \\ \frac{1}{2} & 0 & -\frac{1}{2} & 0 \\ 0 & -\frac{1}{2} & 0 & \frac{1}{2} \end{pmatrix}$	 <p>Resistance: <math>R = \frac{2}{\sigma_{\text{symmetric}}}</math>,  transconductance:  <math>g_m = \frac{\sigma_{\text{symmetric}}}{2}</math></p>

Tab. 2.3 Equivalent circuit representation of conductivity on a unit square

<b>Interaction</b>	<b>Element system matrix</b>	<b>Equivalent schematic</b>
$\sigma_{\text{anisotropic}} \begin{pmatrix} 1 & 0 \\ 0 & -1 \end{pmatrix}$	$\sigma_{\text{anisotropic}} \begin{pmatrix} 0 & \frac{1}{2} & 0 & -\frac{1}{2} \\ \frac{1}{2} & 0 & -\frac{1}{2} & 0 \\ 0 & -\frac{1}{2} & 0 & \frac{1}{2} \\ -\frac{1}{2} & 0 & \frac{1}{2} & 0 \end{pmatrix}$	<p>All transconductances:</p> $g_m = \frac{\sigma_{\text{anisotropic}}}{2}$

unique, as there are several possibilities how to represent the antisymmetric basis elements (see section 2.5.3). In general, the conductance and transconductance coefficients extracted from the system matrix depend on physical interactions whose strength depends on external fields. Thus, the equivalent circuit elements must provide additional inputs by which the field strengths can be coupled to the model. SPICE3 [67] provides a nonlinear dependent source element which is best suited for replacing the conductance and transconductance coefficients. Alternatively, a combination of circuit elements provided by SPICE (e.g. JFET) and dependent sources could be used to exploit the advanced models built into SPICE [74]. The external fields coupling to the equivalent circuit elements are modelled as additional nets with voltages proportional to the field strengths.

## 2.6 Strategies to Compact the Netlist

The system matrix obtained by the method described in the previous section can directly be translated to a SPICE netlist. A simulation with this netlist, which can be quite large as all the internal nodes of the discretization mesh are included, provides detailed information about the internal voltage distribution in the modeled resistor. However, for simulating the electrical interaction of the modeled device with surrounding circuitry, only the terminal voltages and currents matter. In this case, it is advantageous to simplify the system matrix, so that it only contains one node per terminal, but the electrical properties of the terminals remain the same.

In this section we show two methods with which to simplify the system matrix prior to translation into a SPICE netlist: we merge shorted nodes belonging to the same terminal, and eliminate nodes without external connection by linear algebra.

### 2.6.1 Collapsing boundary conditions into terminals

In a SPICE-type circuit simulator, boundary conditions are specified by the connection of the circuit nodes to circuit elements external to the model equivalent sub-circuit:

- A terminal connected to a current source corresponds to Neumann boundary conditions. Unconnected terminals can be assumed to be connected to a zero current source. This is equivalent to homogenous Neumann boundary conditions.
- A terminal connected to a voltage source corresponds to Dirichlet boundary conditions.
- A terminal connected to a biased finite resistance corresponds to a mixed boundary condition.

Consequently, there is no need to specify the boundary conditions with the discretization mesh, such as could be specified with MEMDRAW. Instead, the boundary information provided by MEMDRAW is used to specify which nodes of the discretized representation of the structure being modelled are *terminal* nodes that connect to external circuitry. Nodes which belong to one and the same terminal are assumed to be shorted, i. e. their voltage is forced to be the same, and the current can flow unhampered between the nodes. Thus, a set of shorted nodes behaves in every respect as one single node, and the entire set can be mapped to one index in the system matrix. This is equivalent to a floating boundary condition. Compacting the system matrix by collapsing shorted nodes into one node is implemented by a look up table that allows to assign the same matrix index to several nodes of the discretization grid.

### 2.6.2 Schur Complement to eliminate internal nodes

The system matrix obtained by the Box Integration Method contains terminal nodes which connect to external circuitry as well as internal nodes. As the focus of modelling sensors with SPICE lies on simulating the terminal behaviour of the

structure being modelled, it is favourable to eliminate the internal nodes and thus reduce the size of the synthesized netlist. The conductivity equation governed by the system matrix  $\mathbf{K}$  is

$$\mathbf{i} = \mathbf{K} \cdot \mathbf{v} \quad (2.47)$$

Elimination of the internal nodes is accomplished by splitting the system matrix into four blocks:

$$\mathbf{K} = \begin{bmatrix} \mathbf{K}_{TT} & \mathbf{K}_{TI} \\ \mathbf{K}_{IT} & \mathbf{K}_{II} \end{bmatrix} \quad (2.48)$$

with the index sets  $T$  and  $I$  ranging over all terminal and internal nodes, respectively. Partitioning the potential and current vectors consistently with (2.48), equation (2.47) can be decomposed into terminal and internal equations:

$$\begin{aligned} \mathbf{i}_T &= \mathbf{K}_{TT} \cdot \mathbf{v}_T + \mathbf{K}_{TI} \cdot \mathbf{v}_I \\ \mathbf{i}_I &= \mathbf{K}_{IT} \cdot \mathbf{v}_T + \mathbf{K}_{II} \cdot \mathbf{v}_I \end{aligned} \quad . \quad (2.49)$$

In order to eliminate the equations for the non-terminal nodes, we find:

$$\mathbf{v}_I = \mathbf{K}_{II}^{-1} \cdot (\mathbf{i}_I - \mathbf{K}_{IT} \cdot \mathbf{v}_T) \quad (2.50)$$

$$\mathbf{i}_T - \mathbf{K}_{TI} \cdot \mathbf{K}_{II}^{-1} \cdot \mathbf{i}_I = (\mathbf{K}_{TT} - \mathbf{K}_{TI} \cdot \mathbf{K}_{II}^{-1} \cdot \mathbf{K}_{IT}) \cdot \mathbf{v}_T. \quad (2.51)$$

As the net internal currents, i.e the components of  $\mathbf{i}_I$ , are all zero, equation (2.51) reduces to

$$\mathbf{i}_T = (\mathbf{K}_{TT} - \mathbf{K}_{TI} \cdot \mathbf{K}_{II}^{-1} \cdot \mathbf{K}_{IT}) \cdot \mathbf{v}_T \equiv \mathbf{S} \cdot \mathbf{v}_T. \quad (2.52)$$

This procedure is equivalent to calculating the terminal resistances of an  $n$ -port electrical network [75].

### 2.6.3 Inverting the Internal Node System Matrix

Symbolic inversion of the matrix  $\mathbf{K}_{II}$  is prohibitively expensive even for meshes of moderate size. Therefore, it is advantageous to use a method of inverting  $\mathbf{K}_{II}$  which only uses inversions of purely numeric matrices. Many interactions within the scope of our modelling scheme which are relevant in practice are accurately described by a small, linear perturbation of the conductivity  $\sigma_0$  dependent on the coupling fields  $F$

$$\boldsymbol{\sigma}(F) = \boldsymbol{\sigma}_0 + F \cdot \boldsymbol{\sigma}_F. \quad (2.53)$$

which results in a system matrix

$$\mathbf{K}(F) = \mathbf{K}_0 + F \cdot \mathbf{K}_F \quad (2.54)$$

with field-independent matrices  $\mathbf{K}_0$  and  $\mathbf{K}_F$ .

The inverse of the system matrix can be written as an infinite Taylor series in a computationally efficient Horner scheme

$$[\mathbf{K}(F)]^{-1} = [\mathbf{K}_0]^{-1} \cdot (1 - F \cdot \mathbf{K}_F \cdot [\mathbf{K}_0]^{-1} \cdot (1 - F \cdot \mathbf{K}_F \cdot [\mathbf{K}_0]^{-1} \cdot (\dots))) \quad (2.55)$$

Approximating the inverse of non-terminal part of the system matrix results in deviations from the charge conservation conditions (2.39). Translation into circuit elements by multiplying with the pseudoinverse of the basis elements (2.44) or using only off-diagonal elements (2.46) restores charge conservation.

## 2.7 Direct Translation of Matrix Equations to AHDL

State-of-the-art circuit simulators, e. g. Spectre which is included in the Cadence design environment, contain analog hardware description languages (AHDL) which permit the direct inclusion of the matrix equations into a circuit netlist. Figure 2.6 shows the HDL model of the Trench Hall Device modeled by a two-dimensional mesh (B type sensor in Figure 3.9). The Hall effect is represented by a second-order expansion according to (2.55).

## 2 Resistive Sensor Models

---

```

module TrenchB(A1,A2,A3,A4, muB) (sigma0)
// Model derived from Ralph Steiner Vanha's MeshB.grd
node [V,I] A1,A2,A3,A4;
node [V,I] muB;
parameter real sigma0 = 1m;

{
    real sigma;

analog
{
    sigma=sigma0/(1+V(muB)*V(muB));

    I(A1)<- sigma*( .152*V(A1,A2)+.112*V(A1,A3)+.072*V(A1,A4));
    I(A2)<- sigma*( .152*V(A2,A1)           +.324*V(A2,A3)+.112*V(A2,A4));
    I(A3)<- sigma*( .112*V(A3,A1)+.324*V(A3,A2)           +.152*V(A3,A4));
    I(A4)<- sigma*( .072*V(A4,A1)+.112*V(A4,A2)+.152*V(A4,A3)           );

    I(A1)<- sigma*V(muB)*( .079*V(A1,A2)-.031*V(A1,A3)-.048*V(A1,A4));
    I(A2)<- sigma*V(muB)*(-.079*V(A2,A1)           +.109*V(A2,A3)-.031*V(A2,A4));
    I(A3)<- sigma*V(muB)*( .031*V(A3,A1)-.110*V(A3,A2)           +.080*V(A3,A4));
    I(A4)<- sigma*V(muB)*( .048*V(A4,A1)+.031*V(A4,A2)-.080*V(A4,A3)           );

    I(A1)<- sigma*V(muB)*V(muB)*( .121*V(A1,A2)+.077*V(A1,A3)+.071*V(A1,A4));
    I(A2)<- sigma*V(muB)*V(muB)*( .121*V(A2,A1)           +.211*V(A2,A3)+.077*V(A2,A4));
    I(A3)<- sigma*V(muB)*V(muB)*( .077*V(A3,A1)+.211*V(A3,A2)           +.121*V(A3,A4));
    I(A4)<- sigma*V(muB)*V(muB)*( .071*V(A4,A1)+.077*V(A4,A2)+.121*V(A4,A3)           );
}
}

```

*Fig. 2.6 SpectreHDL representation of Trench Hall device shown in Figure 3.9 (version B) with Hall effect up to second order.*

## 2.8 Verification of the Box Integration Method

To demonstrate the accuracy of the modelling scheme, SPICE results for two types of magnetic sensors are compared to finite element simulations which are based on the same discretization grid. The finite element program SOLIDIS [72], used for the numerical comparison, employs a hybrid discretisation scheme that corrects for the overly stiff system matrix resulting from a standard finite element scheme. A less stiff system matrix leads to slightly higher (ca. 2%) voltages, as confirmed by the simulation results.

### 2.8.1 “Breadboard” Hall sensor

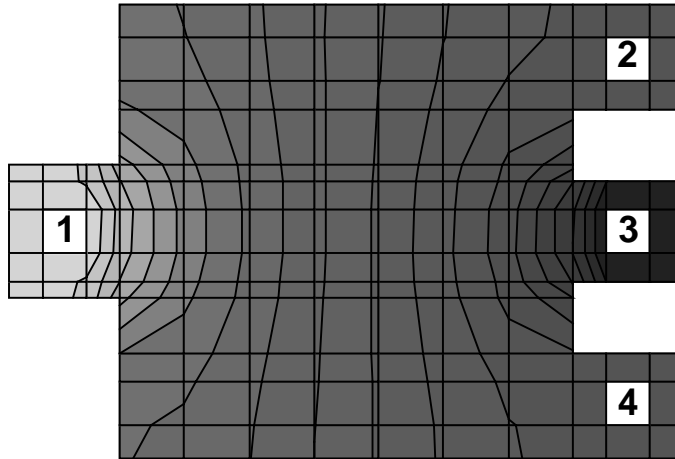


*Fig. 2.7 Layout of magnetic sensitive structure used to validate the compact SPICE model. Voltage levels for voltage mode operation are indicated in gray scale, and were computed using SOLIDIS [72], [76].*

To demonstrate the accuracy of the modelling scheme, SPICE results for two types of magnetic sensors are compared to finite element simulations which are based on the same discretization grid. The finite element program SOLIDIS [72], used for the numerical comparison, employs a hybrid discretisation scheme that corrects for the overly-stiff system matrix resulting from a standard finite element scheme. A less stiff system matrix leads to slightly higher (ca. 2%) voltages, as confirmed by the simulation results.

#### Voltage mode configuration

In this configuration, the structure is operated like a standard Hall device: constant current is driven through two terminals, while the other two terminals serve as high impedance voltage probes (see Figure 2.8). The voltages at the terminals 1, 2, and 4 of the sensor depicted in Figure 2.7 are shown in Figure 2.9.

The results from the SPICE model and from FEM simulation match to an accuracy of 1% for different device geometries. For the Hall effect, the approximation of the  $[K^{II}]^{-1}$  matrix by a quadratic function in  $B$  yields results that are indistinguishable from the results for the full netlist in Figure 2.9.

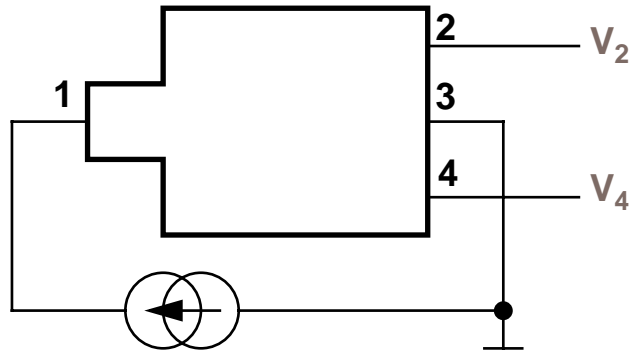


*Fig. 2.8 Schematic for operating the sensor shown in Figure 2.7 in voltage mode: constant current is applied between terminals 1 and 3. Terminals 2 and 4 serve as high impedance voltage outputs.*

--- SPICE, unreduced    --- SPICE, 2<sup>nd</sup> order    - - - SPICE, 1<sup>st</sup> order    ..... FEM (Solidis)

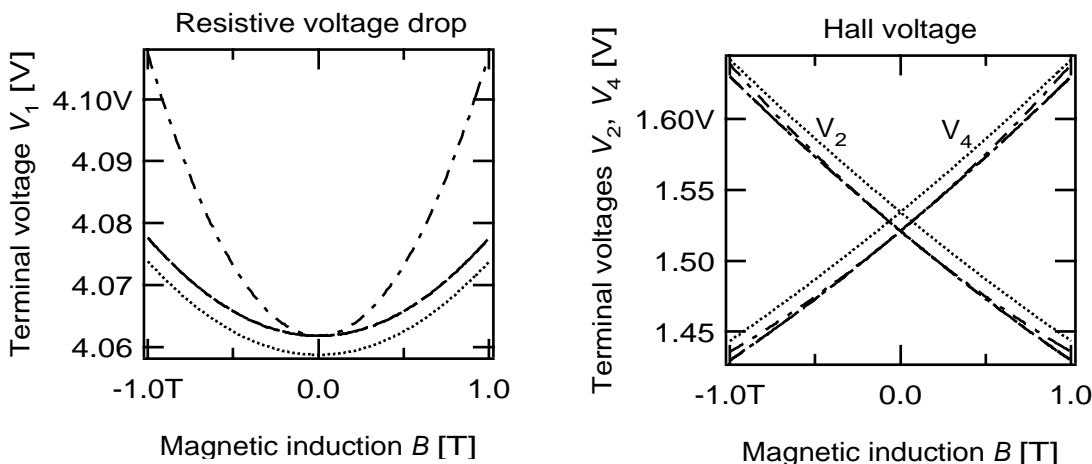


*Fig. 2.9 Terminal voltages (see Figure 2.8) vs. magnetic field for voltage mode operation. The SPICE simulations from full system matrix, reduced system matrix with 2<sup>nd</sup> order expansion and 1<sup>st</sup> order expansion of the inverse non-terminal matrix are drawn as dashed, dash-double dotted, and dash-dotted lines, respectively. The FEM simulation is drawn as dotted line.*

### Current mode configuration

Here, the structure is used as a current mode sensor: the current from the source terminal is allowed to flow into the low impedance sensing terminals. The terminal between the sensing nodes takes a small part of the source current (see

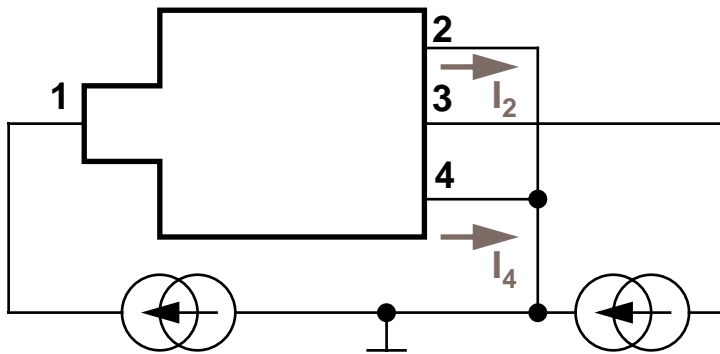


*Fig. 2.10 Schematic for operating the sensor shown in Figure 2.7 in current mode: constant current is supplied to terminal 1. A constant part of the current is sunk from terminal 3. Terminals 2 and 4 serve as low impedance current sinks.*

Figure 2.10). The voltages at the current source and sink terminals 1 and 3 and the currents at the sense terminals 2 and 4 are shown in Figure 2.11.

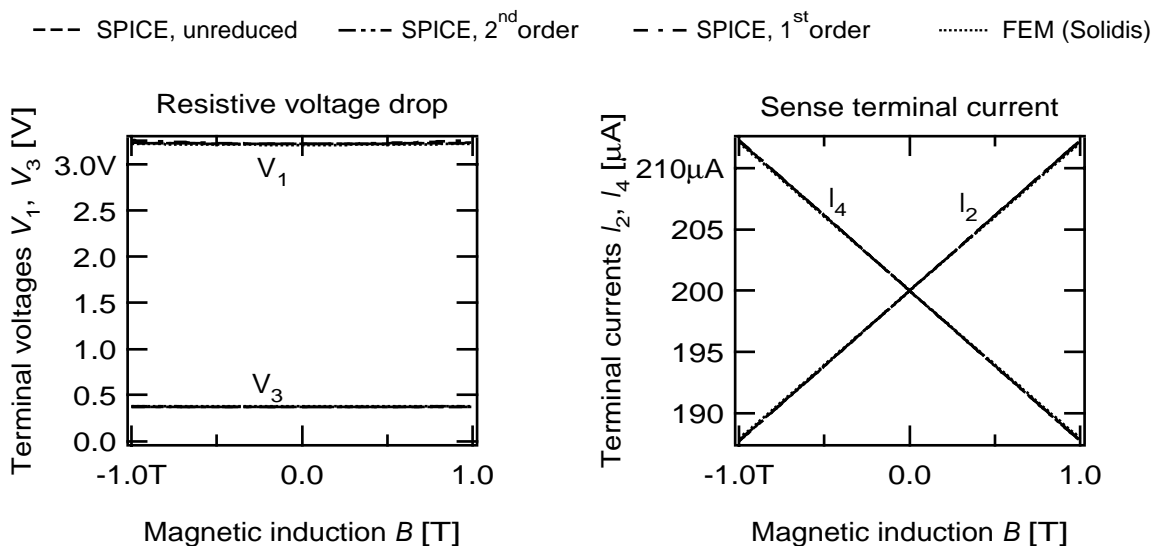


*Fig. 2.11 Terminal voltages (see Figure 2.10) and currents vs. magnetic field for current mode operation. The results from all SPICE models and the FEM simulation are indistinguishable in this diagram.*

In this mode of operation, the results of the SPICE simulation match the results of the FEM simulation within 1% if the non-terminal system matrix is approximated by at least a 2<sup>nd</sup> order expansion in  $B$ .

### 2.8.2 Cross-shaped Hall sensor

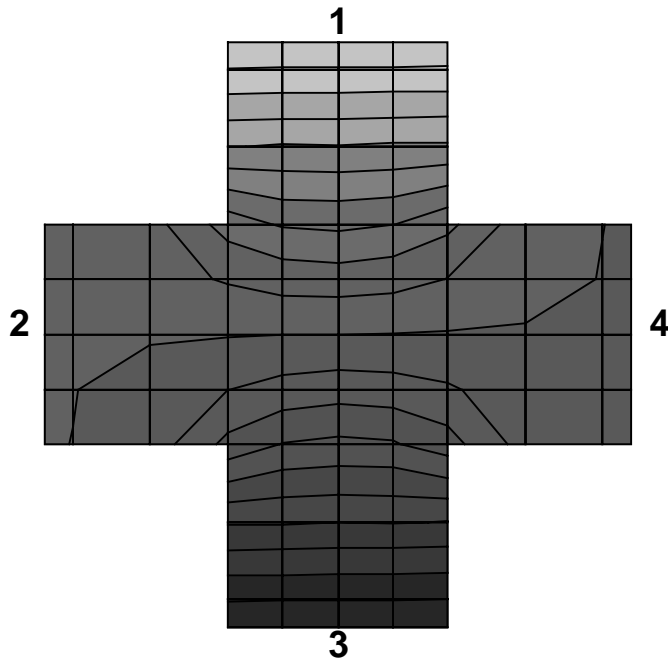


*Fig. 2.12 Layout of cross-shaped magnetic sensitive structure used to compare the compact SPICE model to FEM simulations. The voltage distribution under influence of a perpendicular magnetic field of 200 mT for constant current drive from top to bottom is indicated in gray scale, and was computed using SOLIDIS [72], [76].*

As a second example, we model a cross-shaped Hall sensor. We have compared its equivalent SPICE model to its FEM model under influence of a magnetic field. We have also modelled the influence of mechanical stress on the structure.

#### Hall effect

We have compared the terminal voltages of the SPICE models to an FEM model for voltage mode Hall sensor operation. The terminals are connected as is shown in Figure 2.8. The results agree within a tolerance of 0.5% (see Figure 2.13).

#### Mechanical stress

We have simulated the influence of mechanical stress on the cross-shaped Hall device using the Continuous Spinning Current method [77] (see figure 2.14). A current of constant magnitude which is continuously rotating with respect to the

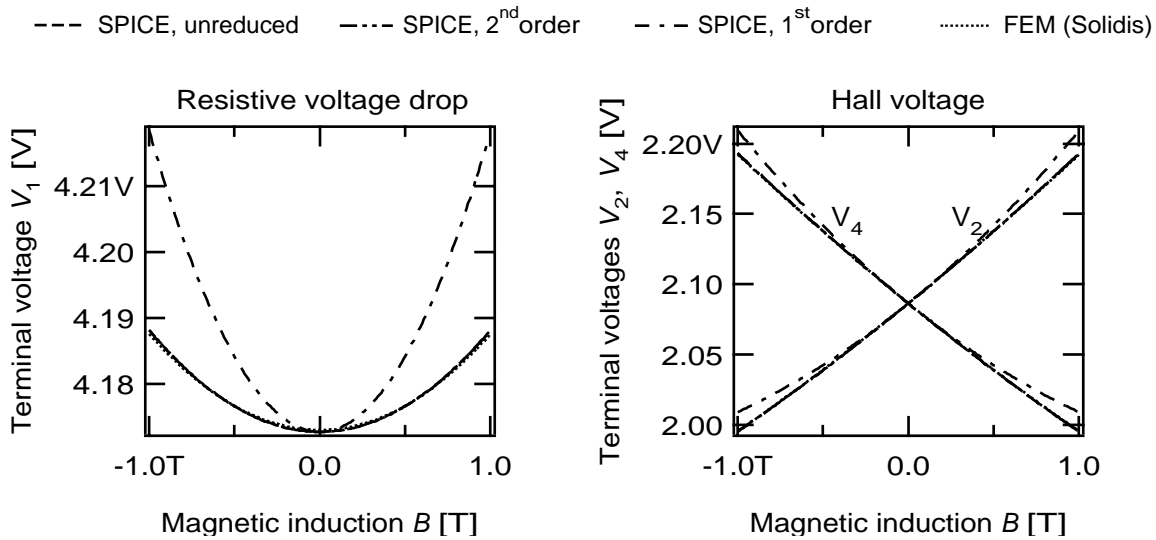


*Fig. 2.13 Terminal voltages (see Figure 2.8) vs. magnetic field for cross-shaped structure. Only the SPICE simulation from the reduced system matrix with 1<sup>st</sup> order expansion of the inverse non-terminal matrix is distinguishable from the FEM simulation.*

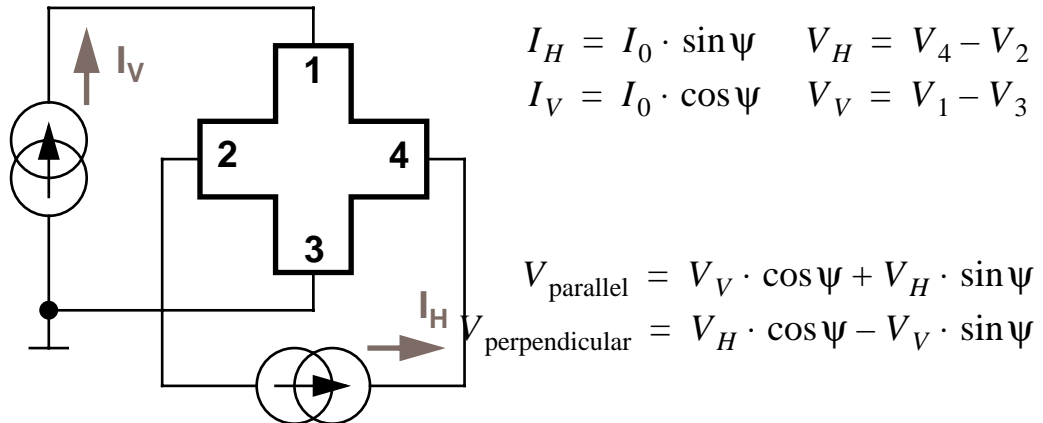


*Fig. 2.14 Schematic for measuring stress with the Continuous Spinning Current method: sinusoidal currents which are 90° out of phase are driven through the terminal pairs 1,3 and 2,4 of the device shown in Figure 2.12, to give a spinning current of constant magnitude. The terminal voltages are decomposed into components parallel and perpendicular to the net drive current.*

sensor's, and hence its stress field's, orientation is generated by superimposing two perpendicular sinusoidal currents which are 90° out of phase. The voltages

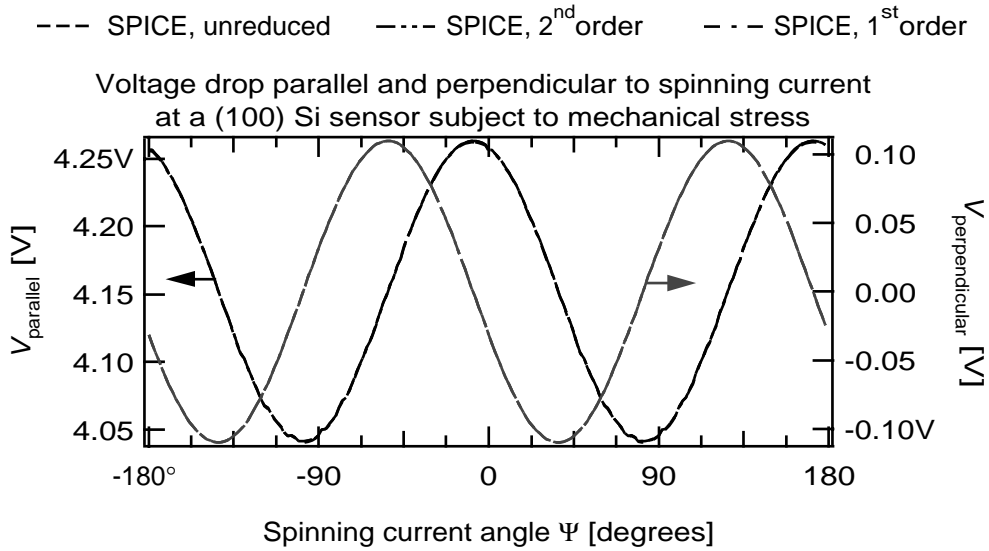


*Fig. 2.15 Voltages parallel (black) and perpendicular (gray) to spinning current vs. angle for cross-shaped structure subject to mechanical stress (see Figure 2.14). The results of the SPICE simulations from full system matrix, reduced system matrix with 2<sup>nd</sup> order expansion and 1<sup>st</sup> order expansion of the inverse non-terminal matrix are indistinguishable in this diagram.*

parallel and perpendicular to the net current are calculated from the terminal voltages. The equivalent circuit model accurately reproduces the dependence of the voltages parallel and perpendicular to the drive current on the second harmonic of the rotation angle which is characteristic for mechanical stress, as is shown in Figure 2.15. For this simulation, a stress distribution as produced by a four-point bending bar setup [34] has been assumed, with a dominant tensile stress component of 121 MPa along one of the cross bars of an n-doped structure oriented in (110) direction in the silicon substrate.

With external circuitry connected for a voltage mode Hall sensor (see Figure 2.8), the stress-induced voltage across the sensing terminals 2 and 4, which mimics a Hall voltage, is predicted by the compact SPICE model [58]. This is shown in Figure 2.16.

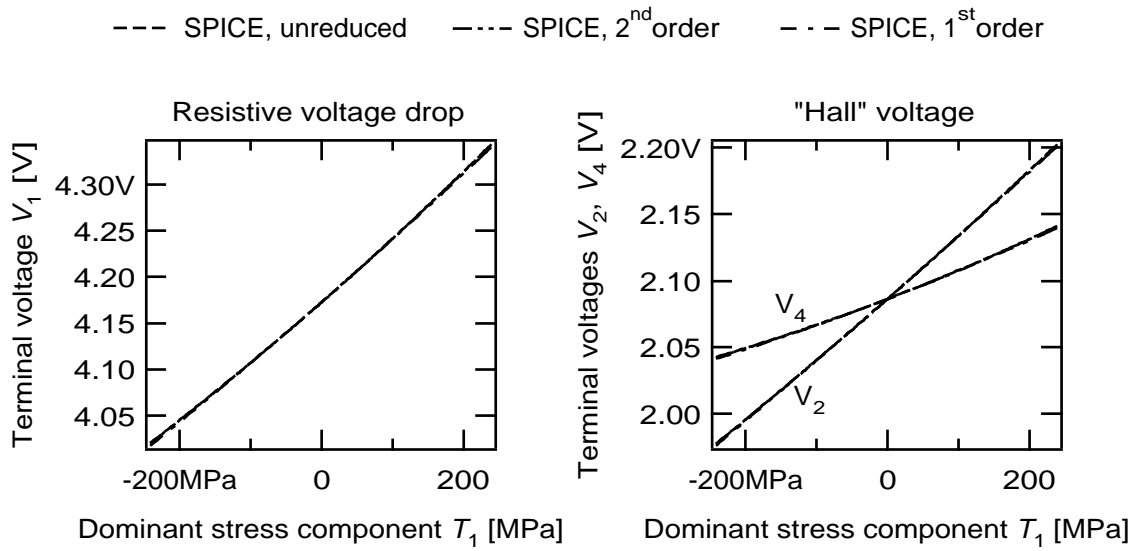


*Fig. 2.16 Terminal voltages (see Figure 2.12) vs. mechanical stress for cross-shaped structure. The ratio of the matrix elements of the mechanical stress applied is according to a four-point bending bar measurement. The results from the different SPICE simulations are indistinguishable from each other in the diagram.*

## 2 Resistive Sensor Models

---

# 3 Spinning Current Method For Offset Reduction of Hall Devices

In this chapter, the applicability of the equivalent circuit device model is demonstrated with a practical design example: A major drawback of silicon galvanomagnetic sensors, such as magnetotransistors [49] and Hall devices [62] is their offset. It has been shown in the previous section that part of the offset can be traced back to cross sensitivities to other physical quantities, e. g., mechanical stress induced by packaging. In general, a signal to be measured can be extracted from undesired offsets and cross sensitivities by exploiting information about the *shape* of the desired signal component. A common method to extract the signal proportional to magnetic induction from Hall sensors is the spinning current method [56][57][58][59].

A general description of the Spinning Current method is given in section 3.1. In section 3.2, the practical applicability of the Continuous Spinning Current Method, which according to theory is optimal, is discussed. Section 3.3 introduces a circuit design example for a class of integrated magnetic microsystems using Hall devices with Spinning Current offset compensation. In Section 3.4, the Trench Hall devices and their description by simple equivalent circuit models are discussed. Section 3.5 presents the circuit blocks used in the design example. The first measurement result obtained by the implemented system is quoted in Section 3.6.

## 3.1 The Spinning Current Method

The spinning current method is based on measuring the Hall voltage of a magnetic sensor for different directions of current and averaging over the measurements. It

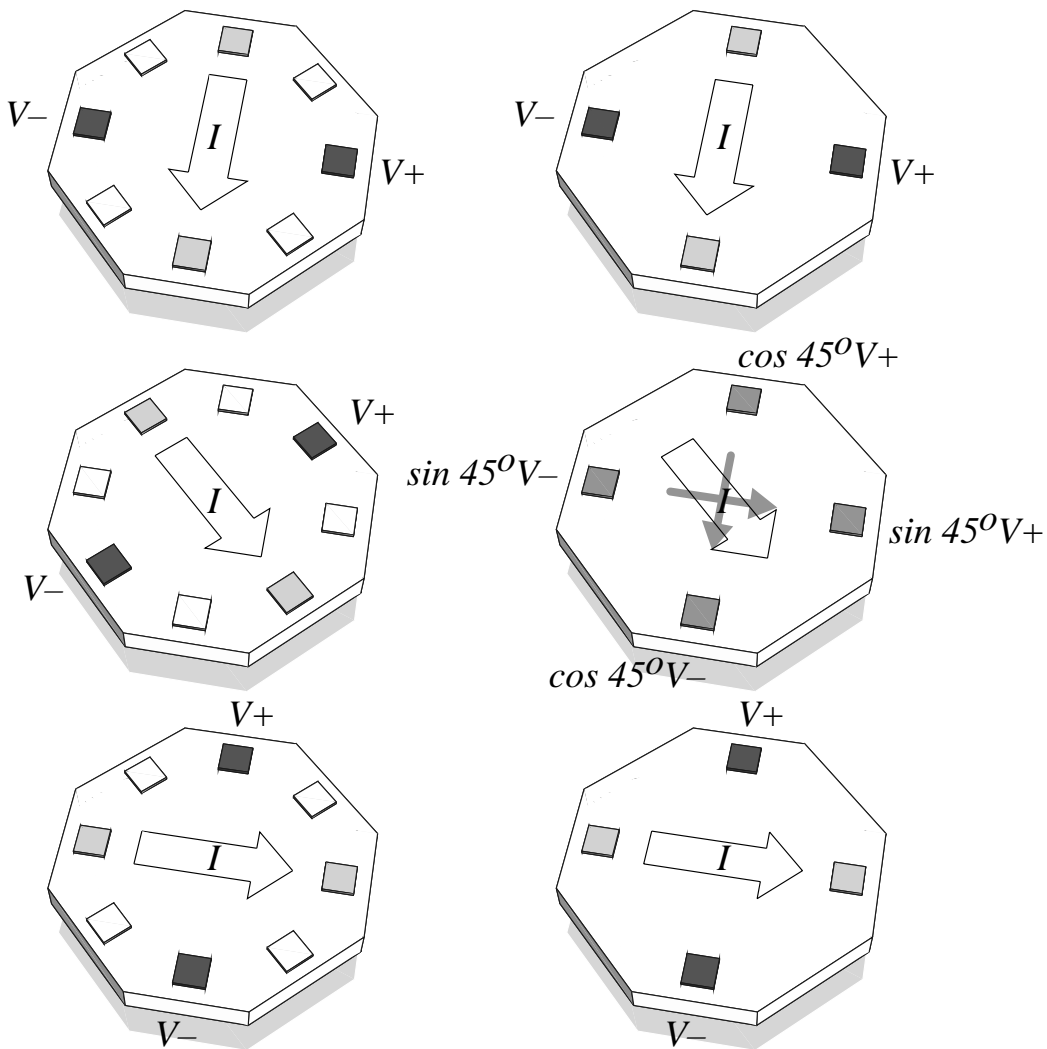


Fig. 3.1 Discrete spinning current method (left) and continuous spinning current method (right)

has first been mentioned by Taranow et. al. [56]. It has been treated extensively by P. J. A. Munter [58] and S. Bellekom [62]. A generalization of the method has been found by R. Steiner Vanha [52].

### Microscopic Description of the Spinning Current Method

To implement the Spinning Current method, a rotating sheet current density  $\mathbf{j}(\psi)$  (unit A/m) is driven through a planar resistive structure. The current density depends on the periodic variable  $\psi$  as

$$\begin{bmatrix} j_x \\ j_y \end{bmatrix} = j_0 \begin{bmatrix} \cos \psi \\ \sin \psi \end{bmatrix}. \quad (3.1)$$

In general, the vector of the electrical field  $\mathbf{E}(\psi)$  is not parallel to the driving current due to anisotropies in the sheet conductivity tensor  $\sigma$ , as discussed in section 2.1. Thus, the vector of the electrical field can be split into components parallel and perpendicular to the sheet current density,

$$E_{\parallel}(\psi) = \begin{bmatrix} \cos \psi & \sin \psi \end{bmatrix} \cdot \begin{bmatrix} E_x \\ E_y \end{bmatrix} \text{ and } E_{\perp}(\psi) = \begin{bmatrix} -\sin \psi & \cos \psi \end{bmatrix} \cdot \begin{bmatrix} E_x \\ E_y \end{bmatrix}. \quad (3.2)$$

Depending on the symmetry properties of the sheet conductivity tensor, the parallel and perpendicular components of the electrical field may vary with the orientation of the current vector  $\mathbf{j}(\psi)$ .

As illustrative examples, the angular dependences of  $E_{\perp}$  caused by the Hall effect and by mechanical stress are considered:

#### *Hall effect*

The electric field  $E_{\text{Hall},\perp}$  perpendicular to the current density caused by magnetic induction can be expressed as a multiple of an antisymmetric anisotropy (2.5):

$$\sigma_{\text{Hall},\perp} = \frac{\mu B \sigma_0}{1 + (\mu B)^2} \begin{bmatrix} 0 & -1 \\ 1 & 0 \end{bmatrix}. \quad (3.3)$$

Instead of applying the transformation rules (3.1) for  $\mathbf{j}$  and (3.2) for  $E_{\perp}$ , the conductivity relation can be transformed according to

$$\begin{bmatrix} \cos\psi & -\sin\psi \\ \sin\psi & \cos\psi \end{bmatrix} \cdot \begin{bmatrix} 0 & -1 \\ 1 & 0 \end{bmatrix} \cdot \begin{bmatrix} \cos\psi & \sin\psi \\ -\sin\psi & \cos\psi \end{bmatrix} = \begin{bmatrix} 0 & -1 \\ 1 & 0 \end{bmatrix}. \quad (3.4)$$

Thus, the perpendicular electric field  $E_{\text{Hall},\perp}$  caused by the Hall effect is invariant under rotation of the current density.

### Piezoresistance

Analogously, the perpendicular component  $E_{\text{Piezo},\perp}$  of the electric field generated by the piezoresistive effect is caused by a linear combination of the anisotropic *symmetric* matrices (2.4)

$$\sigma_{\text{Piezo},\perp} = k_1(\mathbf{T}) \begin{bmatrix} 1 & 0 \\ 0 & -1 \end{bmatrix} + k_2(\mathbf{T}) \begin{bmatrix} 0 & 1 \\ 1 & 0 \end{bmatrix} \quad (3.5)$$

which are transformed according to

$$\begin{bmatrix} 1 & 0 \\ 0 & -1 \end{bmatrix} \rightarrow \begin{bmatrix} \cos 2\psi & \sin 2\psi \\ \sin 2\psi & -\cos 2\psi \end{bmatrix} \text{ and } \begin{bmatrix} 1 & 0 \\ 0 & -1 \end{bmatrix} \rightarrow \begin{bmatrix} -\sin 2\psi & \cos 2\psi \\ \cos 2\psi & \sin 2\psi \end{bmatrix}. \quad (3.6)$$

Unlike the component due to magnetic induction, the perpendicular electric field caused by mechanical stress has a periodicity of  $180^\circ$  with the rotation angle  $\psi$ , as can be seen in Figure 2.15.

The different periodicity with respect to the angle of rotation can be exploited to separate the components of  $E_{\perp}$  by their cause. In the average

$$\langle E_{\perp} \rangle_{90^\circ} = \frac{E_{\perp}(0^\circ) + E_{\perp}(90^\circ)}{2}, \quad (3.7)$$

the component  $E_{\text{Hall},\perp}$  caused by magnetic induction remains unchanged, while the component  $E_{\text{Piezo},\perp}$  due to mechanical stress is canceled. It can be shown [52]

that this result strictly holds for four-terminal devices of arbitrary geometry and for *any* interaction that is characterized by a *symmetrical* conductivity tensor.

While mechanical stress is the dominant source of offset in Hall devices, other effects, such as

- geometrical misalignment,
- local conductivity fluctuations due to doping inhomogeneities or depletion layers with varying thickness, or
- thermal gradients

as well as higher order interactions of these effects result in components of  $E_{\perp}$  with periodicities of  $360^\circ/N$  for different integers  $N$  [61]. Such effects can be cancelled by forming the average

$$\langle E_{\perp} \rangle_{2N} = \frac{1}{2N} \sum_{n=1}^{2N} E_{\perp}(\psi_n) , \text{ with } \psi_n = \frac{360^\circ}{n}. \quad (3.8)$$

### Discrete Spinning Current Method

Conventionally, the spinning current method is implemented by contacting the resistive sensor device at  $2N$  positions located symmetrically at the circumference of the device (see Figure 3.1, left side). For each angular setting, the *entire* current flows through two contacts at diametrically opposite positions. The voltage perpendicular to the current is measured at the contact pair perpendicular to the current driving pair. The conventional spinning current method cannot be extended to an arbitrary number of angular settings, as IC layout rules dictate a minimum contact size and spacing. Thus, sensors with many contacts would become unacceptably large.

### Continuous Spinning Current Method

The requirement of one contact per angle setting can be overcome by *electronically* superimposing two orthogonal currents according to (3.1),

$$\begin{bmatrix} I_x \\ I_y \end{bmatrix} = I_0 \begin{bmatrix} \cos \psi \\ \sin \psi \end{bmatrix}, \quad (3.9)$$

and obtaining the voltage perpendicular to the net current vector by projection from two orthogonal voltages according to (3.2):

$$\begin{bmatrix} V_x \\ V_y \end{bmatrix} = \begin{bmatrix} \cos \psi & -\sin \psi \\ \sin \psi & \cos \psi \end{bmatrix} \cdot \begin{bmatrix} V_{\parallel} \\ V_{\perp} \end{bmatrix}, \text{ and thus } \begin{bmatrix} V_{\parallel} \\ V_{\perp} \end{bmatrix} = \begin{bmatrix} \cos \psi & \sin \psi \\ -\sin \psi & \cos \psi \end{bmatrix} \cdot \begin{bmatrix} V_x \\ V_y \end{bmatrix}. \quad (3.10)$$

The projection of  $V_{\perp}$  is performed by subtracting the voltages  $V_x$  and  $V_y$  scaled by sinusoids with the appropriate phase. This *continuous spinning current* method is shown on the right side of Figure 3.1. Setting  $\psi \equiv \omega t$  and replacing the average (3.8) by

$$\langle V_{\perp} \rangle_{\text{cont}} = \frac{1}{T} \int_0^T V_{\perp}(\omega t) dt \text{ with } T = \frac{2\pi}{\omega}, \quad (3.11)$$

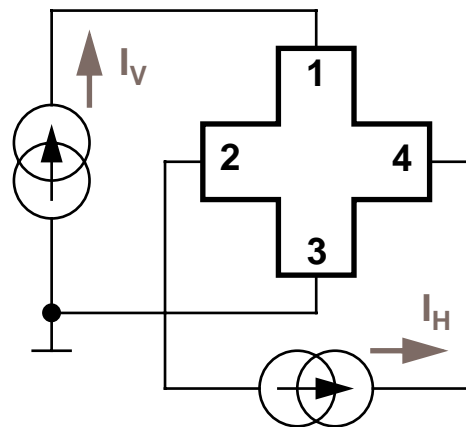
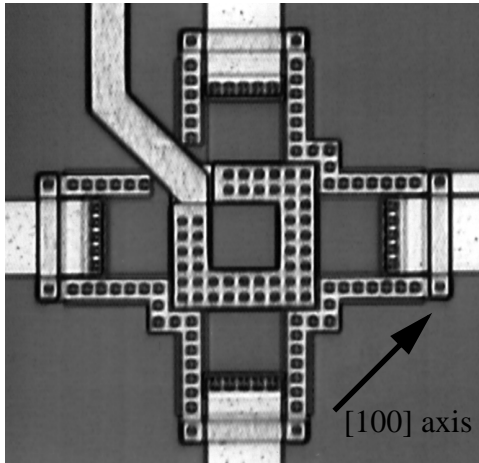
it is principally possible to average the voltage perpendicular to the current over all angles. From this theoretical point of view, the continuous spinning current method is optimal.

## 3.2 Applicability of the Continuous Spinning Current Method

In this section, the practical feasibility of the Continuous Spinning Current method is investigated. Whereas the method proves to be a powerful tool for the characterization of sensor properties, the extreme requirements it imposes on the phase stability, noise margin, common mode rejection, and matching of the read-

out electronics prohibit its use for integrated microsystems with reasonable circuit complexity.

### 3.2.1 Device Characterization



$$I_H = I_0 \cdot \sin \psi \quad V_H = V_4 - V_2$$

$$I_V = I_0 \cdot \cos \psi \quad V_V = V_1 - V_3$$

$$V_{\parallel} = V_V \cdot \cos \psi + V_H \cdot \sin \psi$$

$$V_{\perp} = V_V \cdot \sin \psi - V_H \cdot \cos \psi$$

*Fig. 3.2 n-well Greek cross structure to used to detect mechanical stress (left) using the Continuous Spinning Current method (right).*

As the continuous spinning current method provides the voltages  $V_{\parallel}(\psi)$  and  $V_{\perp}(\psi)$  perpendicular and parallel to the driving current  $I(\psi)$  with unlimited resolution of the angle  $\psi$ , it permits a precise determination of the dependence of the conductivity tensor  $\sigma$  on geometrical orientation.

As an example, the conductivity of a cross shaped Hall sensor, implemented as buried n-well resistor on a (100) CMOS wafer has been measured under different stress conditions. The device was subjected to a well-defined stress distribution obtained with the four-point bending bridge method [34]: A thin steel plate rests on two horizontal rods. Two more rods push the plate downwards, subjecting the device under test mounted to the top of the steel plate to a well-defined bending and, consequently, well-defined mechanical stress (see Figure 3.3 for the principle and Figure 3.4 for the actual experimental apparatus).

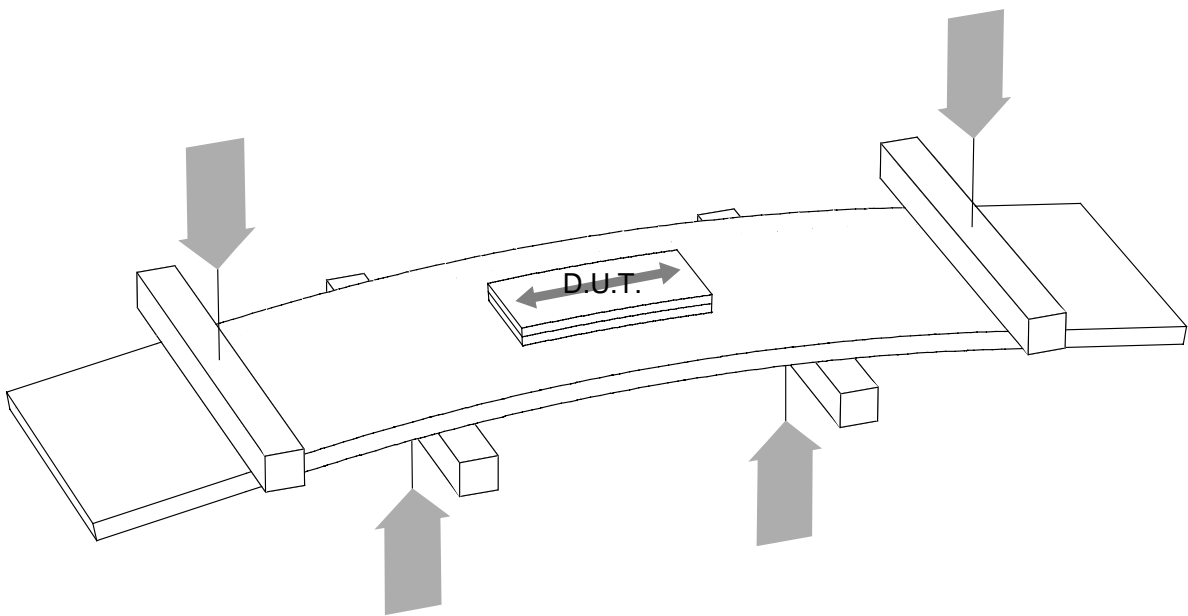


Fig. 3.3 Principle of the four-point bending bridge method to apply defined stress to a device under test.

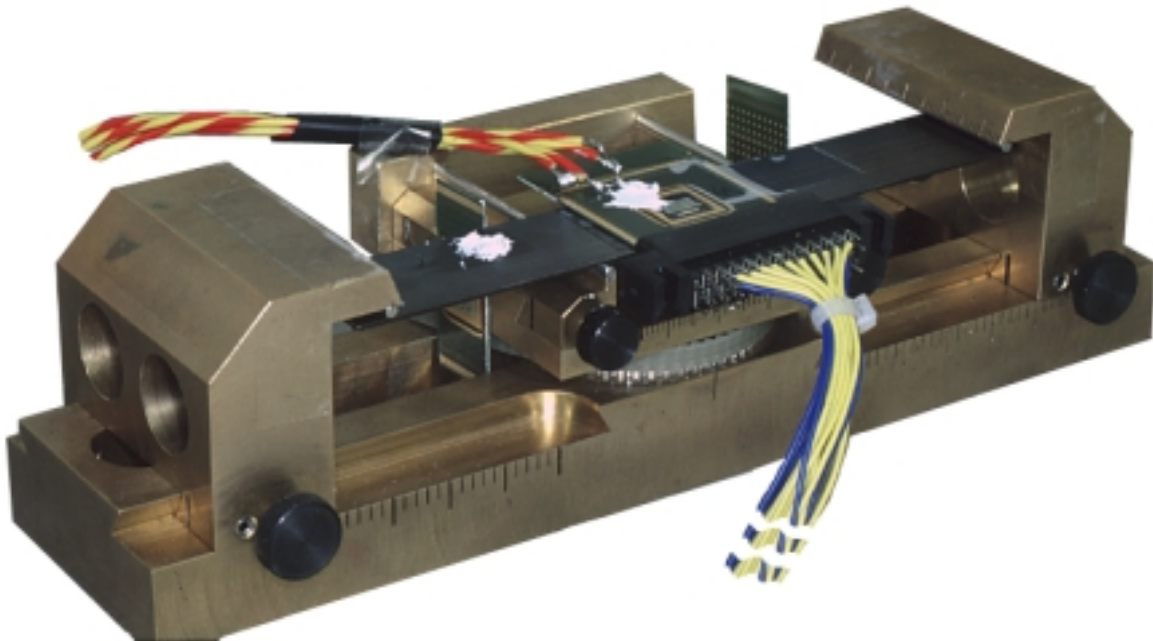


Fig. 3.4 Implementation of four-point bending bridge.

The dominant component of stress thus applied is tensile stress  $T_1$  parallel to the surface of the die. In order to determine the dependence of piezoresistivity on the angle between current, stress, and crystal orientation, the resistance has been mea-

sured with the Continuous Spinning Current method. To this end, sine and cosine currents are applied to the contact pairs of the device under test,

$$I_H = I_0 \cdot \sin \psi \text{ and } I_V = I_0 \cdot \cos \psi, \quad (3.12)$$

and the resulting terminal voltages are translated into components parallel and orthogonal to the current flow,

$$V_{\parallel} = V_H \cdot \sin \psi + V_V \cdot \cos \psi \text{ and } V_{\perp} = V_V \cdot \sin \psi - V_H \cdot \cos \psi. \quad (3.13)$$

Figure 3.5 shows measured and simulated voltages  $V_{\parallel}$  and  $V_{\perp}$  as a function of the angle of the current vector  $\psi$  for different stress distributions.

With increasing tensile stress parallel to the die surface, the average conductivity increases. The component of conductivity proportional to the *second* harmonic of the current rotation frequency increases as well.

In addition to the stress-induced conductivity modulation, there is also a component proportional to the *fourth* harmonic of the current rotation frequency, caused by the cross shape of the device and the well to substrate depletion layer, whose width depends on the voltage from the sensor to the substrate.

### 3.2.2 Sensitivity to Nonidealities

To determine the feasibility of the Continuous Spinning Current method for implementation of microsystems including Hall sensors and instrumentation circuitry, the sensitivities to circuit nonidealities have been systematically investigated.

For the sensitivity analysis, we describe the Hall effect as rotation of the electrical field with respect to the direction of current flow by the *Hall angle*  $\Theta_H$ ,

$$\tan \Theta_H = \mu B = \frac{E_{\perp}}{E_{\parallel}} \approx \frac{V_{\perp}}{V_{\parallel}}. \quad (3.14)$$

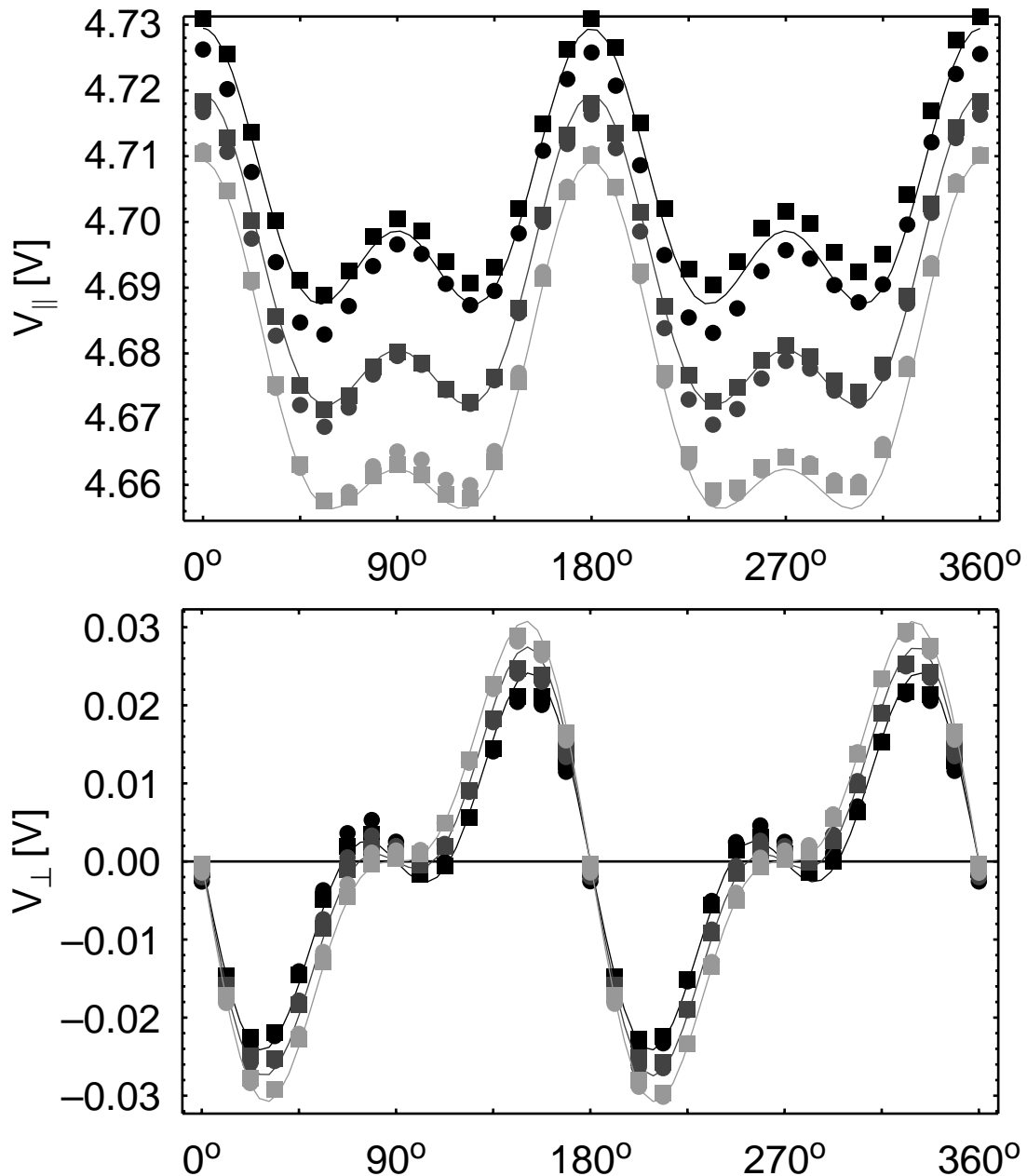


*Fig. 3.5 Measured data of two sensor ICs (circles and squares) for  $V_{\parallel}$  and  $V_{\perp}$  in accordance to equations (3.13), at stress distributions dominated by the tensile stress component  $T_1$  of 90MPa (black), 114MPa (dark grey), and 138MPa (light grey). The solid lines are simulation results from a simple equivalent circuit model describing mechanical stress and the conductivity modulation due to the well to substrate depletion layer [77].*

with the carrier mobility  $\mu$  and the magnetic induction  $B$ . The conductance relation can be put as

$$\begin{bmatrix} V_{\parallel} \\ V_{\perp} \end{bmatrix} = R_{\square} \begin{bmatrix} \cos \Theta_H \\ \sin \Theta_H \end{bmatrix} \cdot I_0 \approx R_{\square} \begin{bmatrix} 1 \\ \Theta_H \end{bmatrix} \cdot I_0 \quad (3.15)$$

with  $R_{\square}$  the sheet resistance of the sensor. With conventional two phase spinning (3.7), offsets equivalent to  $\Theta_H \approx 10^{-5}$  are achievable [62].

### Phase stability

To investigate the sensitivity of the Continuous Spinning Current method to phase errors, let us assume a phase error in one of the driving currents:

$$\begin{bmatrix} I_x \\ I_y \end{bmatrix} = I_0 \begin{bmatrix} \cos \psi \\ \sin(\psi + \varepsilon) \end{bmatrix} \approx I_0 \begin{bmatrix} \cos \psi \\ \sin \psi + \varepsilon \cos \psi \end{bmatrix}. \quad (3.16)$$

The resulting error in the Hall voltage  $V_{\perp}$  is

$$\begin{aligned} V_{\perp} &= R_{\square} I_0 \begin{bmatrix} -\sin \psi & \cos \psi \end{bmatrix} \cdot \begin{bmatrix} \cos \Theta_H & -\sin \Theta_H \\ \sin \Theta_H & \cos \Theta_H \end{bmatrix} \cdot \begin{bmatrix} \cos \psi \\ \sin \psi + \varepsilon \cos \psi \end{bmatrix}, \quad (3.17) \\ &\approx R_{\square} I_0 \Theta_H \left( 1 + \varepsilon \cos \psi \sin \psi + \varepsilon \frac{(\cos \psi)^2}{\Theta_H} \right) \end{aligned}$$

Similar arguments hold for phase errors of the other functions. *Static* phase errors will vanish by averaging over angles. However, any phase fluctuations in the electronic circuit will show up as a relative error of the Hall voltage amplified by  $1/\Theta_H \approx 10^5$ , which is approximately 100dB.

### Noise margin, device matching

Both noise and device mismatch will result in a mismatch of the amplitudes of either the driving currents or the demodulating waveforms. Assuming

$$\begin{bmatrix} I_x \\ I_y \end{bmatrix} = I_0 \begin{bmatrix} \cos \psi \\ (1 + \varepsilon) \sin \psi \end{bmatrix}, \quad (3.18)$$

we get

$$\begin{aligned} V_{\perp} &= R_{\square} I_0 \begin{bmatrix} -\sin \psi & \cos \psi \end{bmatrix} \cdot \begin{bmatrix} \cos \Theta_H & -\sin \Theta_H \\ \sin \Theta_H & \cos \Theta_H \end{bmatrix} \cdot \begin{bmatrix} \cos \psi \\ \sin \psi + \varepsilon \sin \psi \end{bmatrix} . \quad (3.19) \\ &\approx R_{\square} I_0 \Theta_H \left( 1 + \varepsilon (\sin \psi)^2 + \varepsilon \frac{\cos \psi \sin \psi}{\Theta_H} \right) \end{aligned}$$

Again, while static errors are canceled, amplitude noise will get amplified by some 100dB.

### Common mode rejection, Linearity

Even with digital arithmetic, forming the difference of two quantities that are almost equal leads to numerical inaccuracy [73]. Inspection of the equation (3.10) for obtaining the voltage component perpendicular to the current

$$\begin{aligned} V_{\perp} &= R_{\square} I_0 \begin{bmatrix} -\sin \psi & \cos \psi \end{bmatrix} \cdot \begin{bmatrix} V_x \\ V_y \end{bmatrix} \quad (3.20) \\ &= R_{\square} I_0 \begin{bmatrix} -\sin \psi & \cos \psi \end{bmatrix} \cdot \begin{bmatrix} \cos \Theta_H \cos \psi - \sin \Theta_H \sin \psi \\ \cos \Theta_H \sin \psi + \sin \Theta_H \cos \psi \end{bmatrix} \\ &= R_{\square} I_0 \sin \Theta_H \left( \frac{-\sin \psi \cos \psi + \cos \psi \sin \psi}{\tan \Theta_H} + ((\sin \psi)^2 + (\cos \psi)^2) \right) \end{aligned}$$

shows that, in order to separate the Hall voltage  $V_{\perp}$  from the ohmic voltage drop  $V_{\parallel}$  parallel to the current, a difference of two signals approximately  $1/\Theta_H \approx 10^5$  times the Hall voltage must be formed. Thus, the required accuracy of the multiplication and the required common mode rejection ratio of the subtraction operation is 10 parts per million.

#### Conclusion

When using the Continuous Spinning Current method, common circuit nonidealities, e. g., amplitude and phase noise, or common mode sensitivity or nonlinearity in the sensor readout amplifier, are amplified by the ratio  $V_{\parallel}/V_{\perp}$  of the ohmic voltage drop and the Hall voltage. At the offset levels already achievable with conventional current spinning, this ratio is in the order of  $10^5$ . This is in stark contrast to the possible benefit of the Continuous Spinning Current method, which is a reduction in offset of about one order of magnitude.

## 3.3 Magnetic Microsystems Using Offset Compensated Hall Devices

Magnetic microsystems have a wide range of applications, e. g.,

- magnetometers for navigation (compass)
- position encoding (e. g., for brushless motors)
- contactless switches
- dosimetry
- magnetic imaging and pattern recognition.

Dedicated Hall sensor interface circuits have been implemented for specific applications [57].

In the following sections, a modular design concept is presented that is based on building blocks that can be adapted and combined for different applications.

As proof of concept, a microsystem for detecting the magnetic induction in two orthogonal directions *parallel* to the die surface using two arrays of Trench Hall devices [54][81] has been designed. The system uses conventional current spinning for offset compensation. It is composed of three principal building blocks:

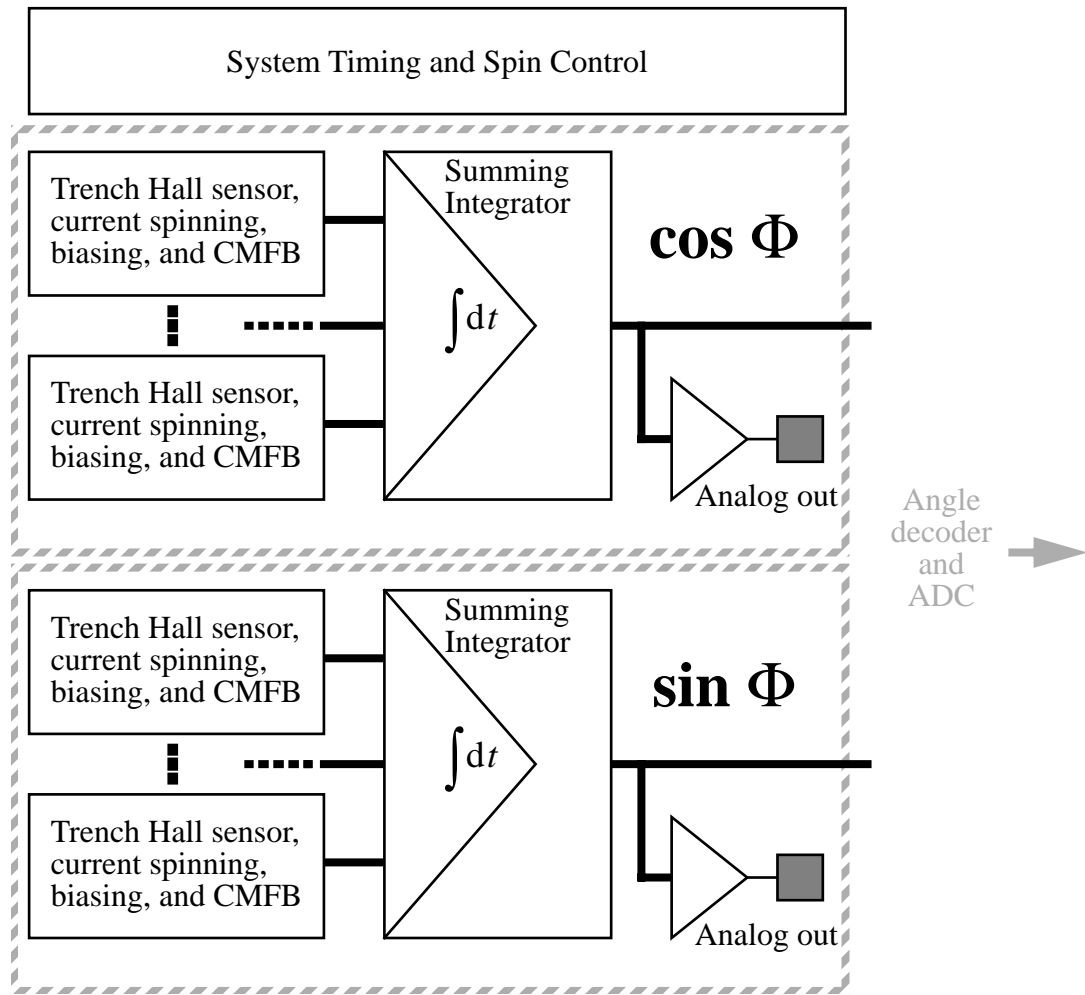


*Fig. 3.6 Block diagram of an angular position sensor using vertical Trench Hall devices with Spinning Current offset compensation*

- a sensor instrumentation block (one per sensor),
- a signal accumulation stage (one per direction)
- a digital master timing and control block (one per system)

The sensor instrumentation blocks are *capacitively* coupled to the integration stage. Thus, linear combinations of the individual signals of an array of sensors can be realized with high precision.

Digital logic derives the control signals for current spinning and signal accumulation from a single-phase clock. As the system is also intended to explore different operating conditions of the newly developed Trench Hall devices, a variety of spinning sequences and gain settings are selectable by static digital control inputs.

### 3.3 Magnetic Microsystems Using Offset Compensated Hall Devices

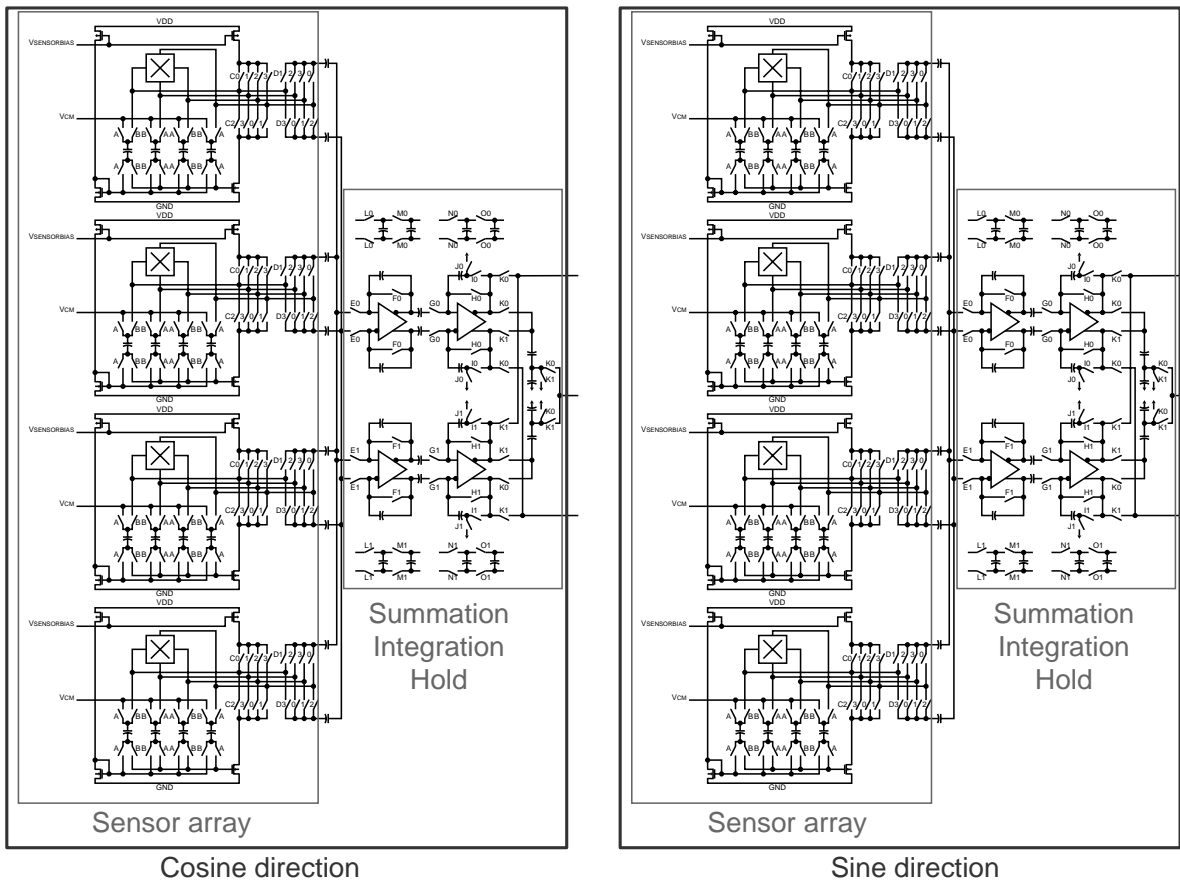


*Fig. 3.7 Conceptual schematic of the Trench Hall sensor interface as shown in Figure 3.6. A sensor bias and common mode feedback block is dedicated to each sensor. A two-branch summator, integrator, and hold stage accumulates the signals of each of the two arrays of sensors measuring orthogonal directions of magnetic induction parallel to the surface of the silicon die. The sensor instrumentation blocks are connected to the summation/integration stages by capacitances.*

The timing sequence is carefully optimized for minimum interference of any digital logic with the acquisition of the analog sensor signals.

A block diagram of the implemented microsystem for angular position detection is shown in Figure 3.6. The conceptual schematic is shown in Figure 3.7.

### 3.4 Trench Hall sensors

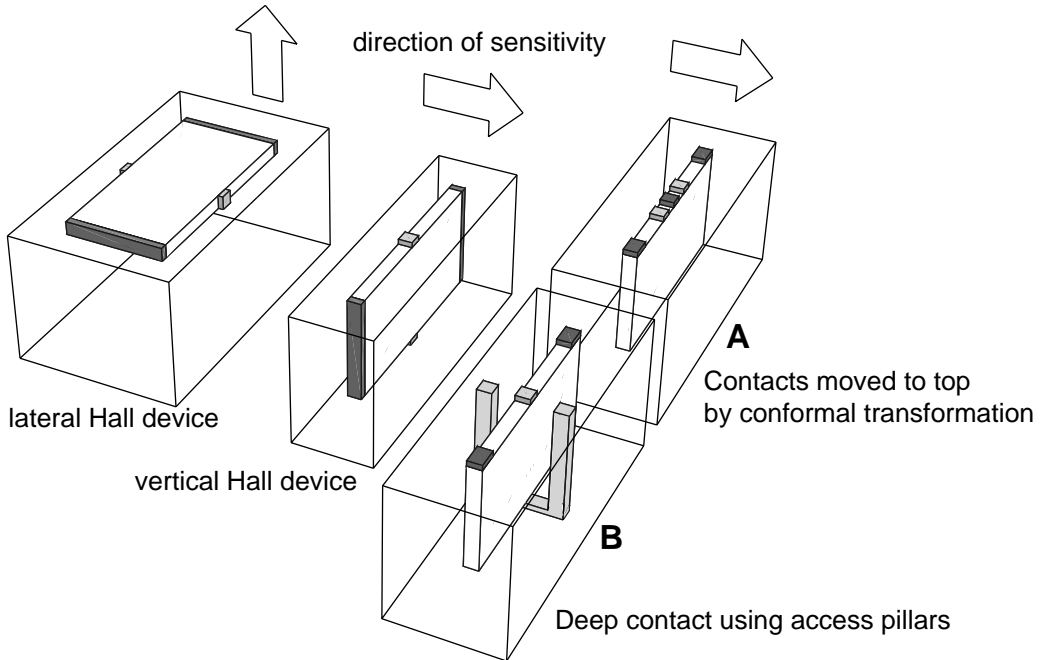


*Fig. 3.8 Transformation of conventional lateral Hall device to vertical Hall device by rotation perpendicular to the die surface. Version A: Trench Hall device with all contacts at the die surface; Version B: Trench Hall device with deep contact*

With a pre-processing sequence using deep trenches followed by the industrial CMOS process of Austria Mikrosysteme International AG, it is possible to implement vertical Hall devices which are sensitive to a component of magnetic induction parallel to the die surface. The system design is targeted on two different types of Trench Hall devices, shown in Figure 3.8. Version A is a Hall plate derived from a symmetric rectangular plate by conformal transformation [52] whose contacts are all at the top side of the structure. Whereas the transformation from a conventional, lateral Hall plate is straightforward, it is not optimal in terms of area consumption. Moreover, the introduction of some asymmetry is inevitable, as the bottom contact must be split. With Version B, the active area is not transformed. The contacts at the buried side of the active area are made accessible by insulated pillars [81]. This approach requires less area. However, a systematic offset and a loss of sensitivity is introduced by the resistance of the deep contact.

The actual geometries of the vertical Hall plates are given by the mesh representations in Figure 3.9.

### 3.4.1 Equivalent circuit model of the Trench Hall sensors

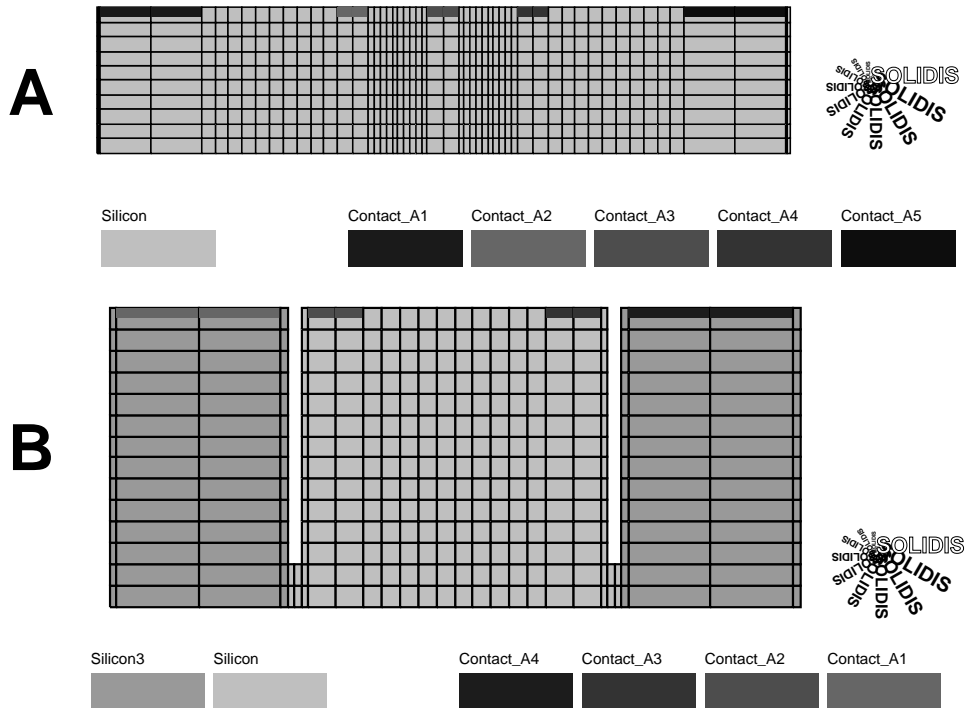


*Fig. 3.9 Two-dimensional mesh representations of Trench Hall sensors version A (top) and version B (bottom). The deep contacts of the version B device are contacted with 3 pillars in parallel. This is modeled by a material “Silicon3” with 3 times the sheet conductance of the Hall plate.*

Equivalent circuit models of both versions of the Trench Hall devices have been generated according to the box integral method described in Chapter 2 from 2-dimensional quadrilateral mesh representations [72], shown in Figure 3.9. The model of the B type sensor is listed in Figure 2.6. The Hall effect is modeled to second order in  $\tan \Theta_H \equiv \mu_{\text{Hall}} B$ , which is provided to the model by a voltage input. With only one fit parameter, namely the sheet conductivity  $\sigma_0$ , the equivalent circuit model derived from a simplified two-dimensional mesh representation matches resistance measurements to within 3%.

### 3 Spinning Current Method For Offset Reduction of Hall Devices

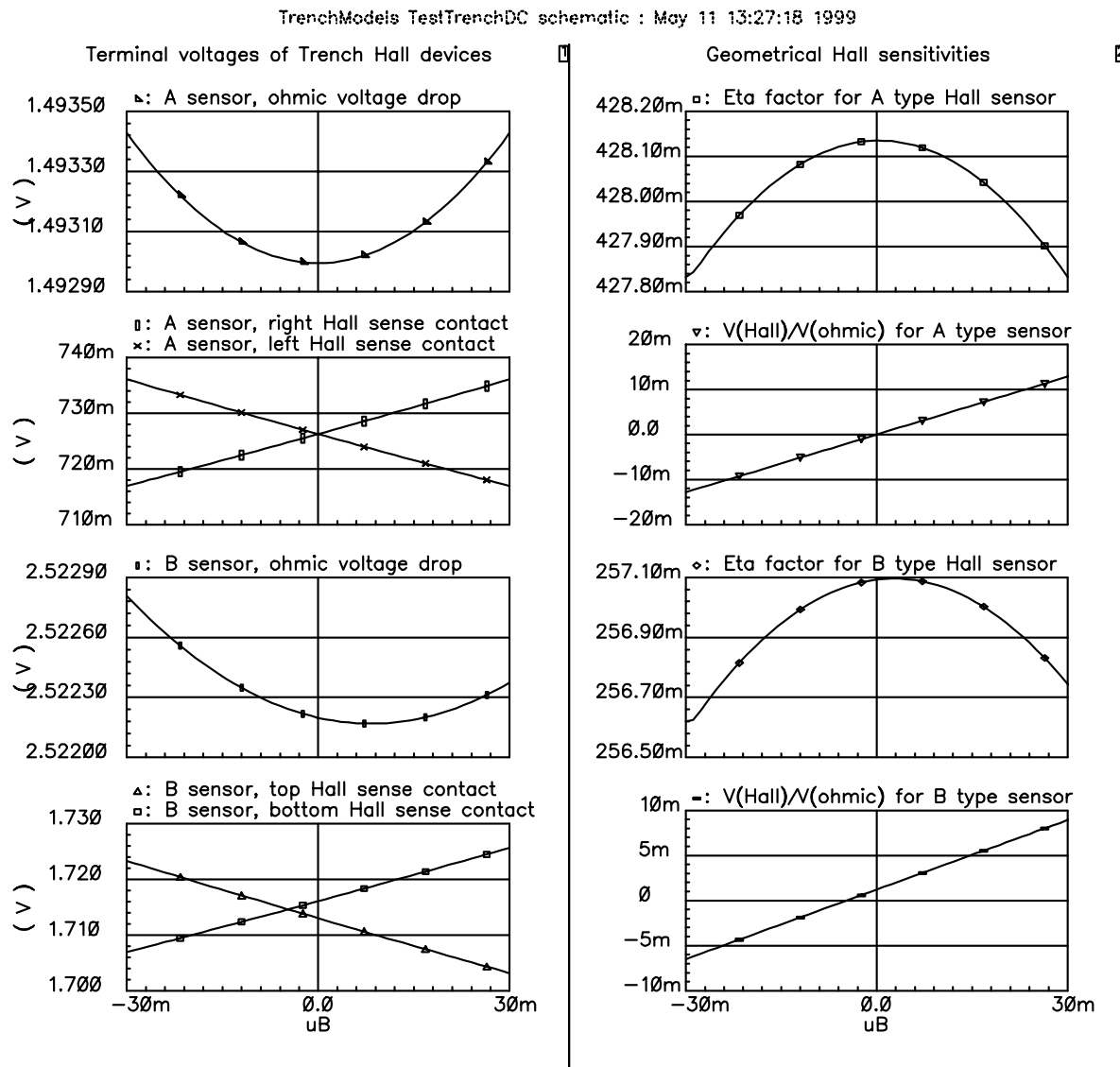


*Fig. 3.10 Simulation of Hall effect on Trench Hall devices using equivalent circuit models. The left column shows the terminal voltages at a bias current of 300  $\mu$ A. The right column shows the quantities  $V_{\text{Hall}}/V_{\text{ohmic}}$  and  $\eta$  (see eqn. 3.21), which depend only on the geometry of the sensor. Note the systematic offset of the B type sensor.*

With the AHDL models, the ohmic voltage drop  $V_{\text{ohmic}}$  parallel to the bias current and the voltages of the Hall sense contacts with respect to the current sink terminal

have been simulated. Figure 3.10 shows the results, together with the dimensionless figures of merit for the sensor geometry,

$$\frac{V_{\text{Hall}}}{V_{\text{ohmic}}} \text{ and } \eta \equiv \frac{V_{\text{Hall}}/V_{\text{ohmic}}}{\mu_{\text{Hall}} B}. \quad (3.21)$$

The second order effect of magnetoresistance and the systematic offset of the deep contact Hall sensor are predicted by the equivalent circuit model.

## 3.5 Circuit building blocks

In this section, the building blocks for assembling Spinnng Current Hall sensor microsystems are described.

### 3.5.1 Hall sensor instrumentation

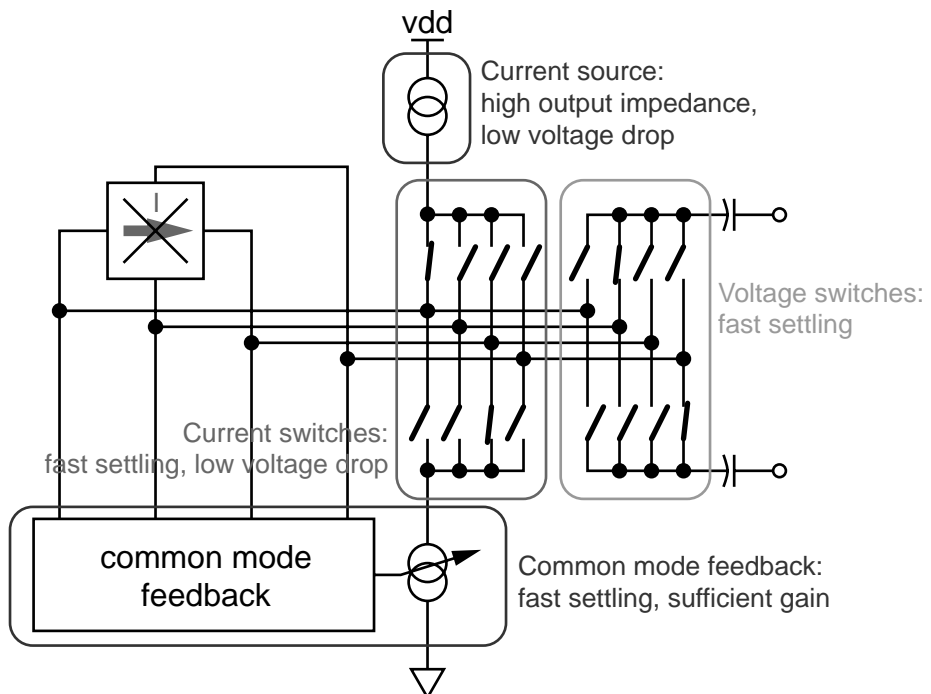


Fig. 3.11 Block diagram of the Hall sensor front end. The key requirements for the sub-blocks are annotated

<i>Quantity</i>	<i>min</i>	<i>typ</i>	<i>max</i>
Sensor bias current		300 $\mu$ A	
Variation of bias current for different spin settings			-70 dB
Variation of Hall terminal common mode voltage			$\pm 20$ mV
Voltage drop across Hall sensor	3 V		
Supply voltage		5 V	
Settling time to 0.1%			300 ns

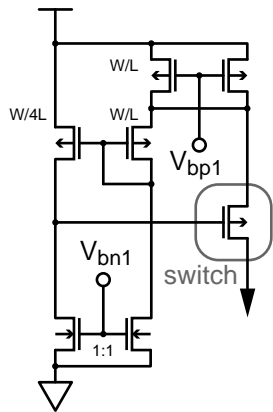
*Tab. 3.1 Specifications for the sensor bias/common mode feedback stage*

The Hall sensor instrumentation block contains the circuitry that is required once for each sensor, viz.

- a stable bias current source
- a variable current sink that regulates the common mode voltage of the voltage sense terminals to a constant value
- current switches for connecting the current sink and source to the terminals of the Hall sensor
- voltage switches for connecting the Hall voltage sense terminals to the coupling capacitances

The sub-blocks of the sensor instrumentation block are shown in Figure 3.11. Quantitative specifications for key parameters are listed in Table 3.1.

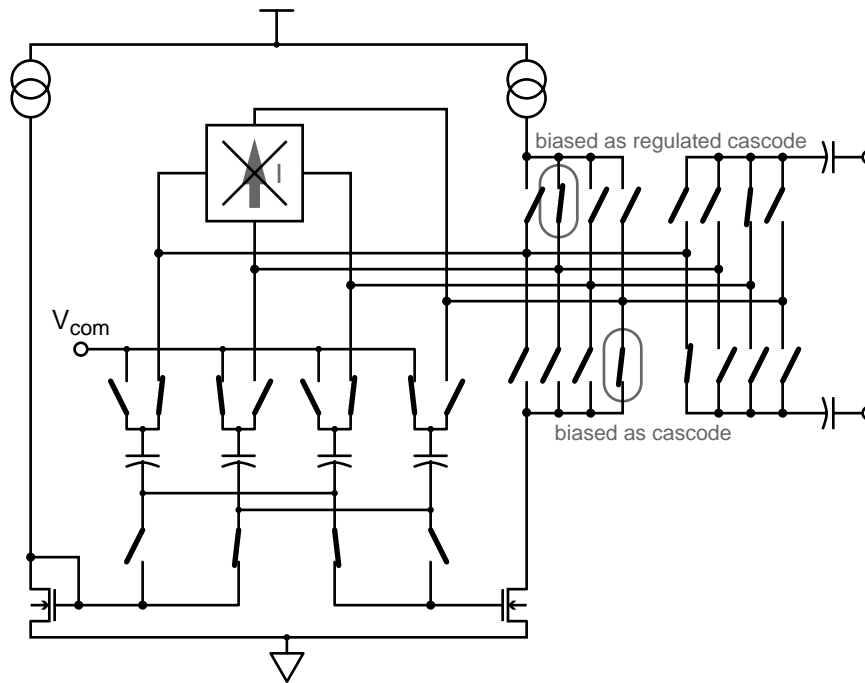
## Constant current source



As the Hall voltage is proportional to the bias current, its stability against variations of the output load must at least match the required system resolution. In order to fully exploit the supply voltage, the voltage drop across the current source must be minimized. Due to the better  $1/f$  noise performance of PMOS transistors, the constant current source connects the Hall device to the positive supply. To achieve a current stability of better than 0.1%, a regulated cascode current source with a low voltage drop of  $2V_{d,sat}$  has been chosen [82].

To reduce the total voltage drop in the current path, the current switch transistors are used as regulated cascode transistors when switched on.

## Regulated current sink with common mode feedback



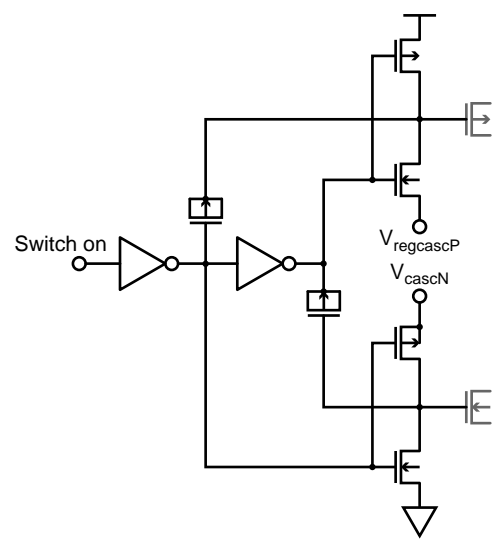
The Hall sensors are insulated from the substrate by a depletion layer. To suppress variations of the sensor characteristics due to the substrate bias, the common mode voltage at the Hall terminal voltages is regulated to a constant voltage by the current sink transistor.

As the function of

each Hall sensor terminal alternates between current sink/source terminal and Hall voltage sense terminal between subsequent current spinning phases, a very simple switched capacitor common mode feedback scheme can be implemented. Compared to conventional switched capacitor (SC) common mode feedback circuits, e.g., the CMFB sub-circuits for the amplifiers sketched in Figures 3.7 and 3.15,

the capacitors permanently connecting the regulated nodes with the gate of the regulating transistor are omitted. Unlike conventional SC CMFB schemes [83], the DC operating point voltage across the feedback capacitors is set in one step. This is possible because the feedback capacitances and the gate capacitance of the current sink transistor form an ideal capacitive divider. Once the DC operating point is set, the feedback loop is closed for *any* frequency. The permanently connected capacitor is included to provide a feedback path at any time, even during switching transients, and to attenuate switch charge injection effects. In this application, the residual error in the common mode voltage is tolerable. Sufficient loop gain and GBW for the common mode feedback regulation is ensured by biasing the switch transistors as cascodes to suppress the Miller capacitance of the current sink transistor.

#### Current switch/cascode driver



The switches for the sensor bias current (shaded in gray in the adjacent schematic diagram) are simple MOS transistors. They are biased as cascode transistors when conducting to increase the output resistance of the current source and the loop gain of the common mode feedback,. To allow settling of the current and the common mode voltage to within 0.1% in 300 ns as required, the gates of the switch transistors are capacitively coupled to the full digital voltage swing. The switch transistors operate as switch during transient and as cascode during settling.

The switch sequence of the current switches is “make before break” to allow the continuous flow of the sensor bias current from the current source to the current sink, Thus, transient voltage excursions during switching are avoided.

#### Output switches

The switches to the coupling capacitors are transmission gates. In the middle of a spinning phase, the polarity of the Hall voltage applied to the capacitors is reversed. Thus, the Hall voltage is doubled and converted to a charge that is

injected to the low impedance summing node of the subsequent charge sensitive accumulating stage. Principally, any charge sensitive amplifier can be used to average over the measurements generated by current spinning from one or several Hall sensor instrumentation building blocks, e. g. the switched capacitor integrators used in the  $\Sigma\Delta$  modulator of the integrated microfluxgate system discussed in Section 4.4.6, with the input capacitances integrated into the Hall sensor instrumentation block.

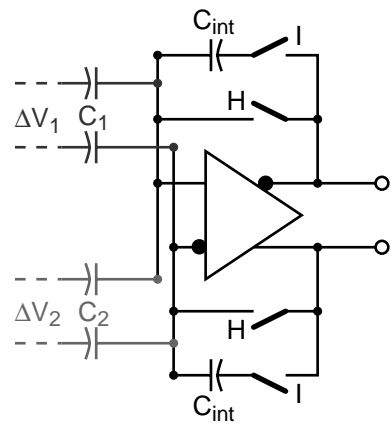
The voltages at the Hall device terminals and the output coupling capacitances as obtained by simulation with SpectreS [30] are shown in Figure 3.12.

### 3.5.2 Signal accumulator

The signal accumulator block contains the circuitry to

- sum the measurements from an array of sensor front ends and
- integrate the measurements made at different current orientations.

#### Basic functionality



The summation of a sequence of measurements from an array of sensor front ends described in Section 3.5.1 is performed by a switched capacitor integrator, e. g., an auto-zeroing integrator [84]. The transition from auto-zero phase (**H** switches closed) to integration phase (**I** switches closed) must occur simultaneously with the reversal of the Hall voltage by the front-end circuit. The input voltage changes  $\Delta V_n$  are added to the differential output voltage  $V_{\text{out}}$  across the integration capacitances according to

$$V_{\text{out}} \rightarrow V_{\text{out}} + \frac{1}{C_{\text{int}}} \sum_n C_n \Delta V_n. \quad (3.1)$$

At the beginning of a new measurement cycle, the integration capacitances are reset by closing both the **H** and **I** switches simultaneously during the auto-zero

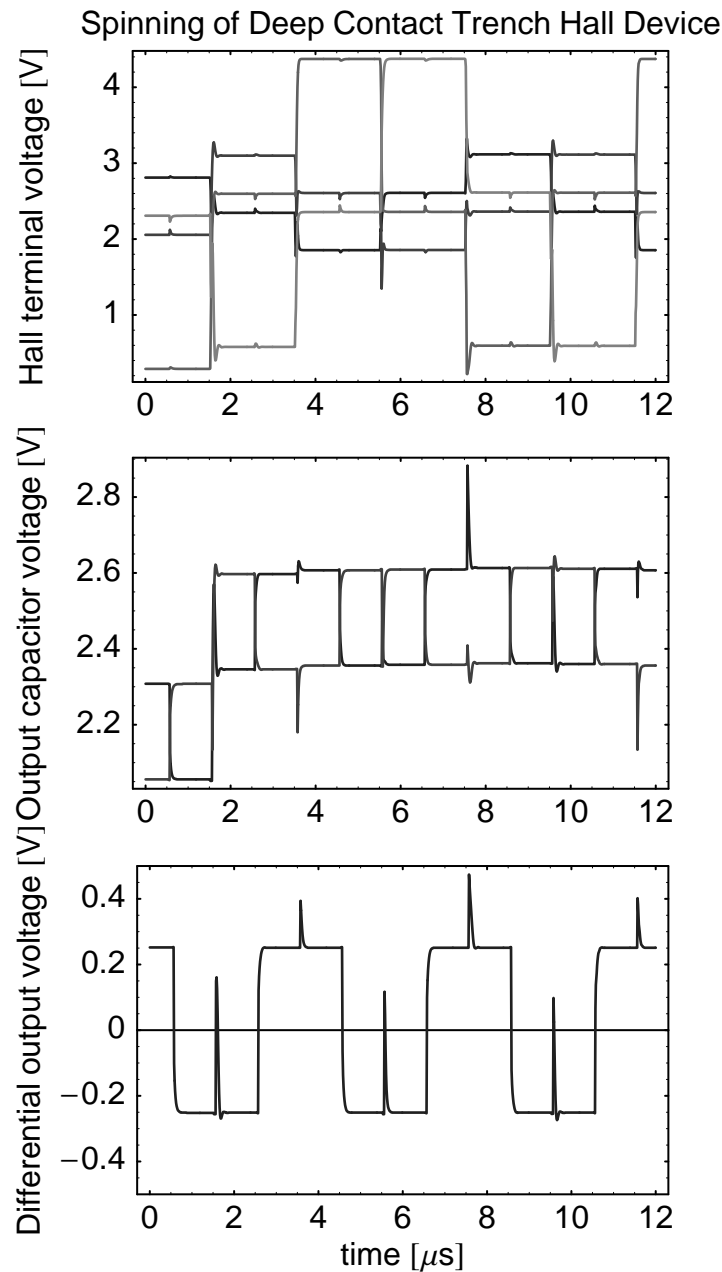


*Fig. 3.12 SpectreS simulation of voltages at B type (deep contact) Trench Hall device (top), and at the output capacitors (middle). The bottom diagram shows the differential voltage at the output capacitors. The output voltage is reversed in the middle of a spinning phase to translate the voltage into a proportional charge. Note the systematic offset due to the resistance of the deep contacts of the Trench Hall device.*

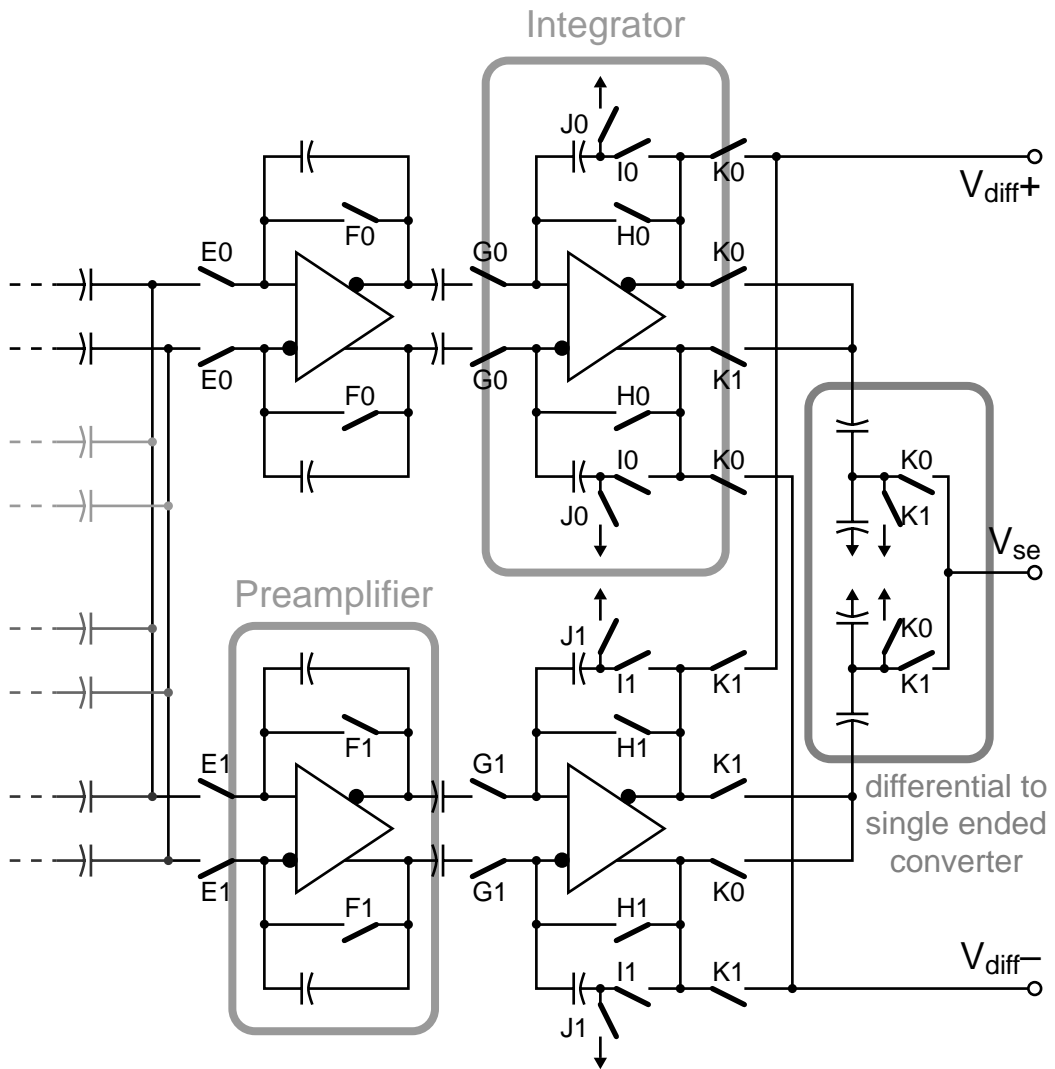


*Fig. 3.13 Schematic of signal accumulator stage and differential to single ended converter. The signal accumulator consists of two identical branches. One branch holds the previous measurement, while the other branch integrates the new measurement. The switches are designated according to the timing diagram in Figure 3.15.*

phase. After the completion of a measurement cycle, its result can be held by keeping the **I** switches closed and the **H** switches opened.

<i>Quantity</i>	<i>min</i>	<i>typ</i>	<i>max</i>
Number of connected sensors $n$	1	4	
Gain per sample	$n \times 0.5$		$n \times 4$
Spinning cycles per measurement	1		8
Sampling phases per measurement	4		32
Overall gain	$n \times 2$	$n \times 16$	$n \times 128$
Dynamic range	60 dB		
Total noise per measurement			1 mV
Supply voltage		5 V	
<i>Continuous</i> analog output		$\pm 2$ V	
Measurement rate			100/ms
Settling time to 0.1%			700 ns
Source capacitance		$n \times 2$ pF	
Output load capacitance			10 pF

Tab. 3.2 Specifications for the signal accumulation stage

### Implemented accumulator stage

The building block presented in this section has added features to fulfill the requirements listed in Table 3.2. The schematic of the accumulator stage is shown in Figure 3.13.

To provide a *continuous* analog output signal as required, the accumulator stage presented here has two identical branches. While one branch accumulates the measurements of the current spinning cycle, the other branch, holding the previous measurement, is connected to the output.

As a Hall sensor magnetometer using the Spinning Current method is inherently a sampled data system, its resolution is limited by the broadband  $kT/C$  noise sampled on the integration capacitors. Therefore, good signal resolution requires large integration capacitances. Measurement frequency is limited by the settling

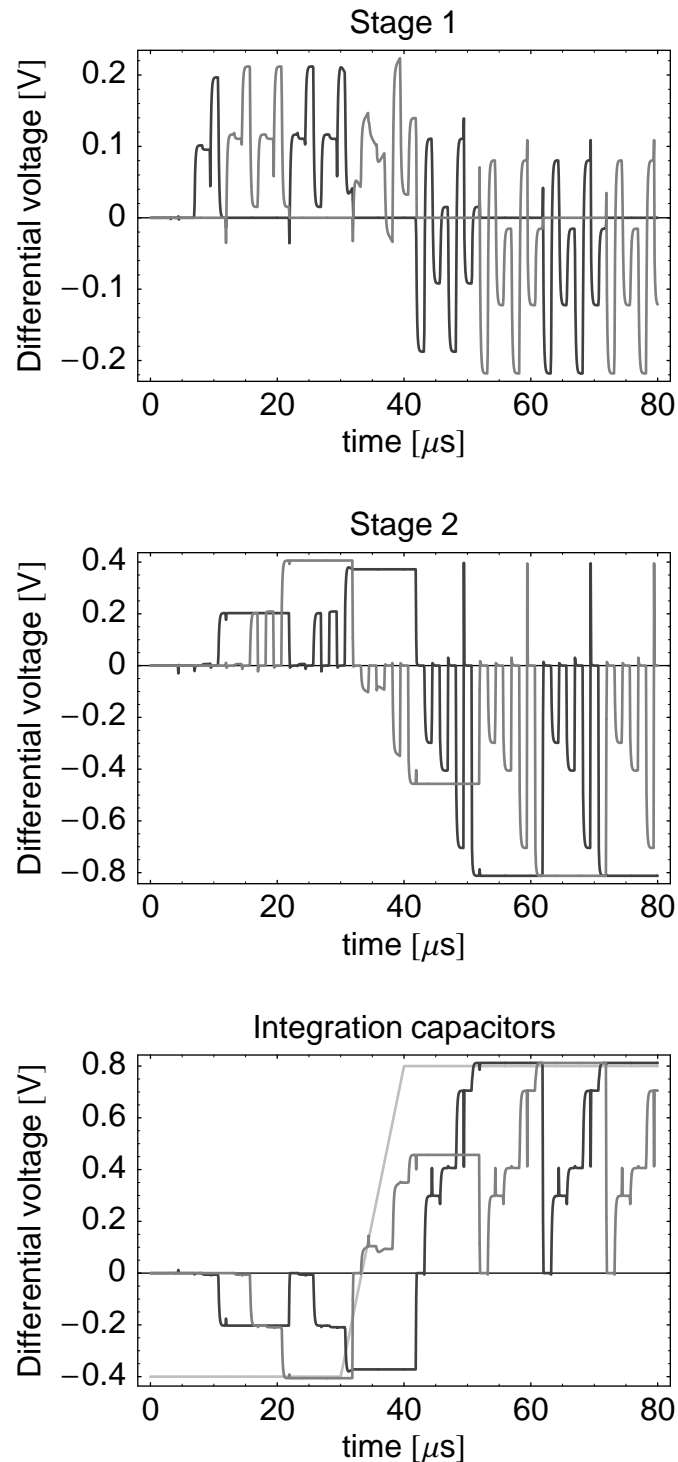


Fig. 3.14 Simulation of differential signals at preamplifiers (top), integrators/hold stages (middle) and integration capacitances (bottom) in response to magnetic field (light gray in bottom diagram, not to scale).

of the Hall voltages, which is determined by the product of the (fixed) source resistance of the Hall device and the coupling capacitances. For a fixed choice of signal gain, determined by the ratio of the coupling capacitances to the integration capacitance (3.1), the requirements of high bandwidth and high resolution are in conflict. The conflict is resolved by a preamplifier providing additional gain. The gain of the preamplifier is precisely set by a ratio of capacitances, changing the gain per sample (3.1) to

$$V_{\text{out}} \rightarrow V_{\text{out}} + \frac{C_{\text{in}, 2}}{C_{\text{int}}} \cdot \frac{1}{C_{\text{fb}, 1}} \sum_n C_n \Delta V_n, \quad (3.2)$$

with  $C_{\text{in}, 2}$  the capacitance coupling the preamplifier with the integrator, and  $C_{\text{fb}, 1}$  the feedback capacitance of the preamplifier. By careful switch timing, detailed in Section 3.5.3, the preamplifier appears as *continuous-time* amplifier during a spinning current measurement cycle despite capacitive feedback. Thus, no additional sampling noise is introduced to the signal. The capacitance values chosen are  $C_n = 2 \text{ pF}$ ,  $C_{\text{fb}, 1} = 0.25 \dots 2 \text{ pF}$ ,  $C_{\text{in}, 2} = 10 \text{ pF}$ , and  $C_{\text{int}} = 10 \text{ pF}$ . The value of the feedback capacitor of the first stage is digitally adjustable for a gain per sample in the range of 0.5...4.

### Differential to single ended converter

The accumulation stage is implemented as fully differential design to reduce the influence of switch charge injection and to double the available signal swing. A continuous single-ended analog output connected to a unity gain output buffer is provided by a simple SC differential to single ended converter.

Simulation results for the analog signals occurring at the preamplifier (stage 1) and the integrator (stage 2) of the signal accumulator in response to a changing input magnetic induction are shown in Figure 3.14. Note the alternation of the two branches between integration and hold cycles.

### 3.5.3 Digital spin control

The switch timing signals necessary for the implementation of current spinning and for signal accumulation are generated by a digital control block. The entire

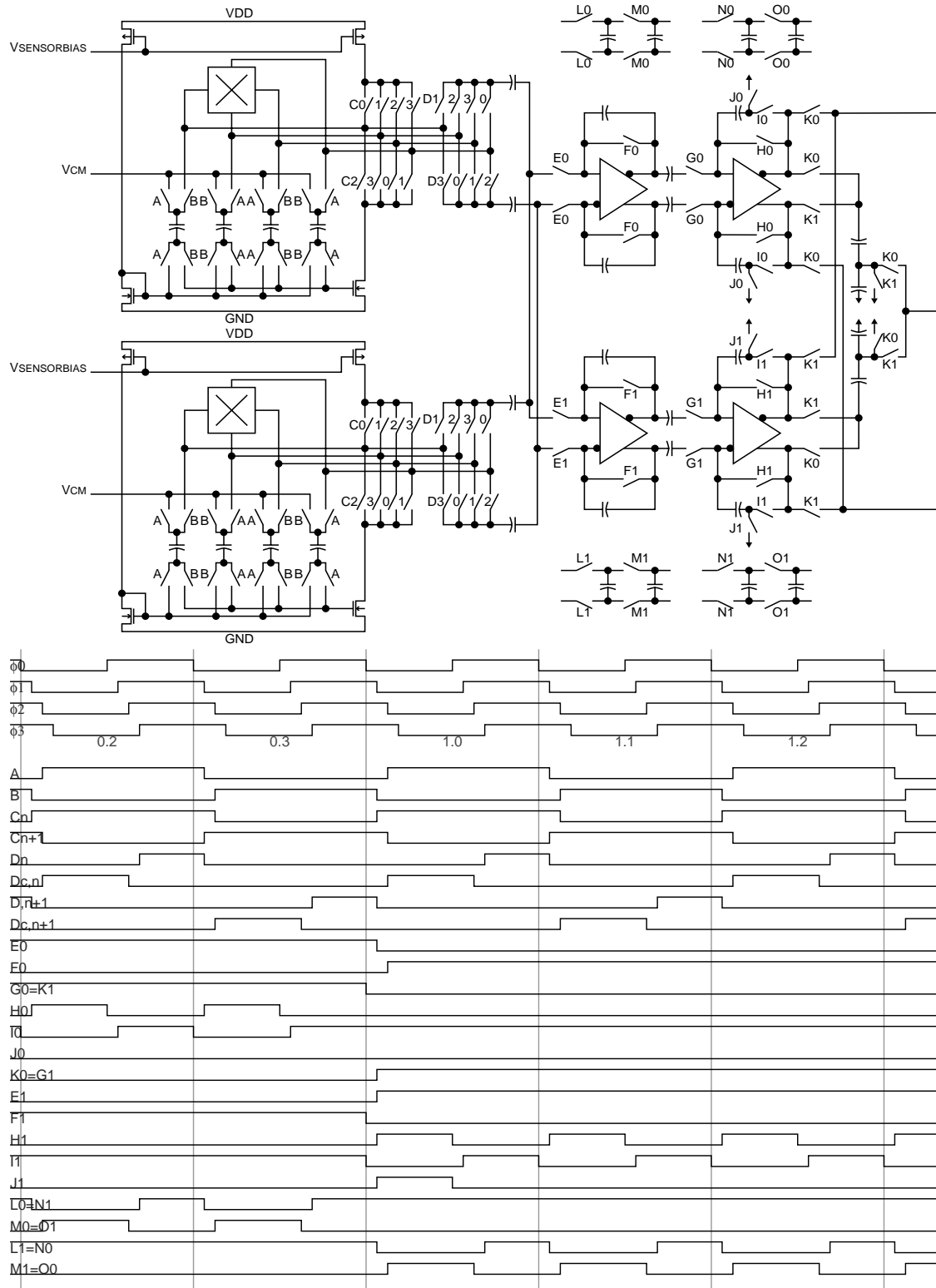
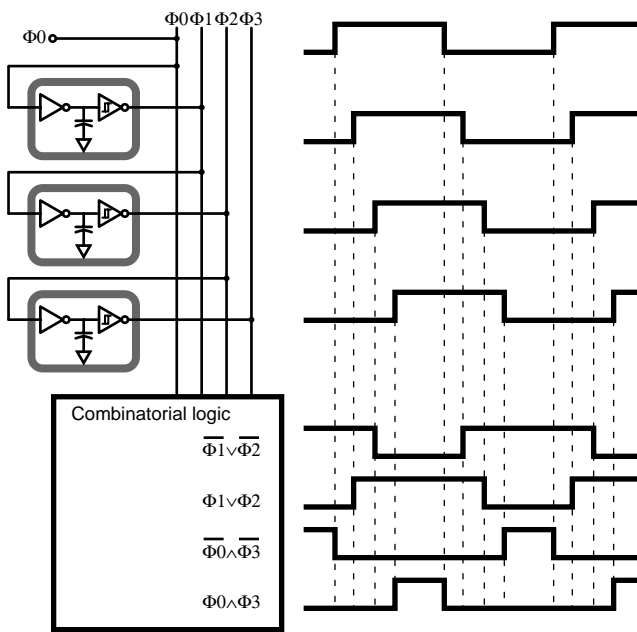


Fig. 3.15 Timing diagram for the switches shown in the schematic. The switch is closed when the signal it is assigned to is in high state.

Timing is derived from a single-phase digital clock. By careful and systematic design of the switching sequence,  $kT/C$  sampling noise and interference from digital transients into the analog signal path is minimized.

#### Systematic implementation of switch timing



In order to derive the complex timing required for current spinning and signal accumulation from a single clock reliably and efficiently, a systematic design approach is used. The clock is delayed several times by digital delay cells. The individual timing signals are derived from the set of delayed clock signals by combinatorial logic. This approach combines the timing flexibility of asynchronous logic with the predictability of synchronous or combinatorial logic and permits the use of standard digital design synthesis tools.

The logic deriving the timing from the delayed clock signals has been synthesized with Verilog HDL. The full timing diagram for the spinning current Hall interface, shown in Figure 3.15, is explained in detail in the following paragraphs.

#### Sensor switch timing

Current spinning is effected by the switches denoted by **C**. To keep the current source and the common mode regulating current sink in saturation, the current flow through the sensor must never be interrupted. This is ensured by closing the switches for the new current setting before opening the switches for the old setting (“make before break”). The Hall voltage sensing terminals are connected to the summation nodes via the **D** switches and coupling capacitances. By reversing the polarity of the Hall voltage applied to the coupling capacitances during the spinning phase, the Hall voltage is transformed to a charge pulse that is summed with

the signals of the other sensors at the input node of the summation/integration block. As a side effect, the Hall voltage is amplified by 2.

### Timing of the accumulation stage

During each spinning phase, only one branch of the summation/integration amplifiers is connected to the summation node by closing the **E** switches, while the other branch serves as hold stage for the previous measurement.

First, the branch holding the value of the previous measurement is considered. The **K** switches of this branch are closed. Thus, the previous measurement, stored as charge on the feedback capacitors of the second stage, is converted to a voltage by closing the feedback path through the **I** switches. The first amplifying stage is completely decoupled by opening the **E** and **G** switches. During a hold cycle, it is auto-zeroed by closing the **F** switches.

In the branch performing the integration of the current measurement, the **E** and **G** switches are closed and the **F** switches are open during the *entire* integration phase. Thus, the first amplifying stage acts like a *continuous-time* amplifier, with its gain defined by a *ratio of capacitors*. The second stage is disconnected from the output by opening the **K** switches. At the beginning of a measurement, the integration capacitors are reset to the amplifier offset by closing the **H** and **J** switches.

The integration of a Hall voltage measurement onto the feedback capacitors of the second stage is performed in two steps. First, the integration capacitances are removed from the feedback loop by opening the **I** switches. The integrator amplifier auto-zeros by closing the **H** switches. The voltage at the output of the first stage (acting as a *continuous-time* amplifier) is set by connecting the Hall voltages of all sensors to their coupling capacitances in reverse polarity by the appropriate set of **D** switches. At the onset of the second integration step, the auto-zero switches **H** are opened, and subsequently the integration capacitances are connected by closing the **I** switches. By reversing the polarity of all Hall voltages to their coupling capacitances by operating the **D** switches, charge proportional to *twice* the sum of all Hall voltages, times the closed-loop gain of the first amplifier stage, is added to the integrating capacitors.

The integration of one measurement is completed by keeping the **I** switches closed and the **H** switches opened, while opening the **G** and **E** switches and connecting the measurement value to the output through the **K** switches.

At the transition between two integrating phases, the differential output signal being held is converted to a single-ended signal.

The switched capacitor common mode feedback (CMFB) of the preamplifiers (switches **L** and **M**) is not operated during an integration cycle, while the CMFB of the integrator amplifier (switches **N** and **O**) is locked during hold phase. This further reduces the interference of digital transients into the analog signal.

#### Timing options

Modifications of the control timing are possible by asserting static digital control signals:

- Two-phase ( $90^\circ$ ) spinning can be selected instead of four-phase ( $360^\circ$ ) spinning to investigate the change in offset reduction
- The signal of multiple spinning phases can be accumulated in one measurement, trading measurement rate for higher gain and resolution

## 3.6 Implementation and measurement

Due to delays in processing the wafers with the non-standard process steps required for Trench Hall devices at the foundry, the fully integrated system could not be implemented in time for the deadline imposed to complete this thesis. However, a test circuit, implemented on a standard multi-project wafer run, has been implemented. It contains one digital control block, two signal accumulation stages, each with two Hall sensor instrumentation blocks. A micrograph of the implemented circuit is shown in Figure 3.16. The functionality of the instrumentation circuitry has been verified with existing Greek Cross and Trench Hall devices:

- The sensitivity and offset of the Hall sensors used for the measurements have been determined.
- The common mode regulation for the sensors has been characterized.

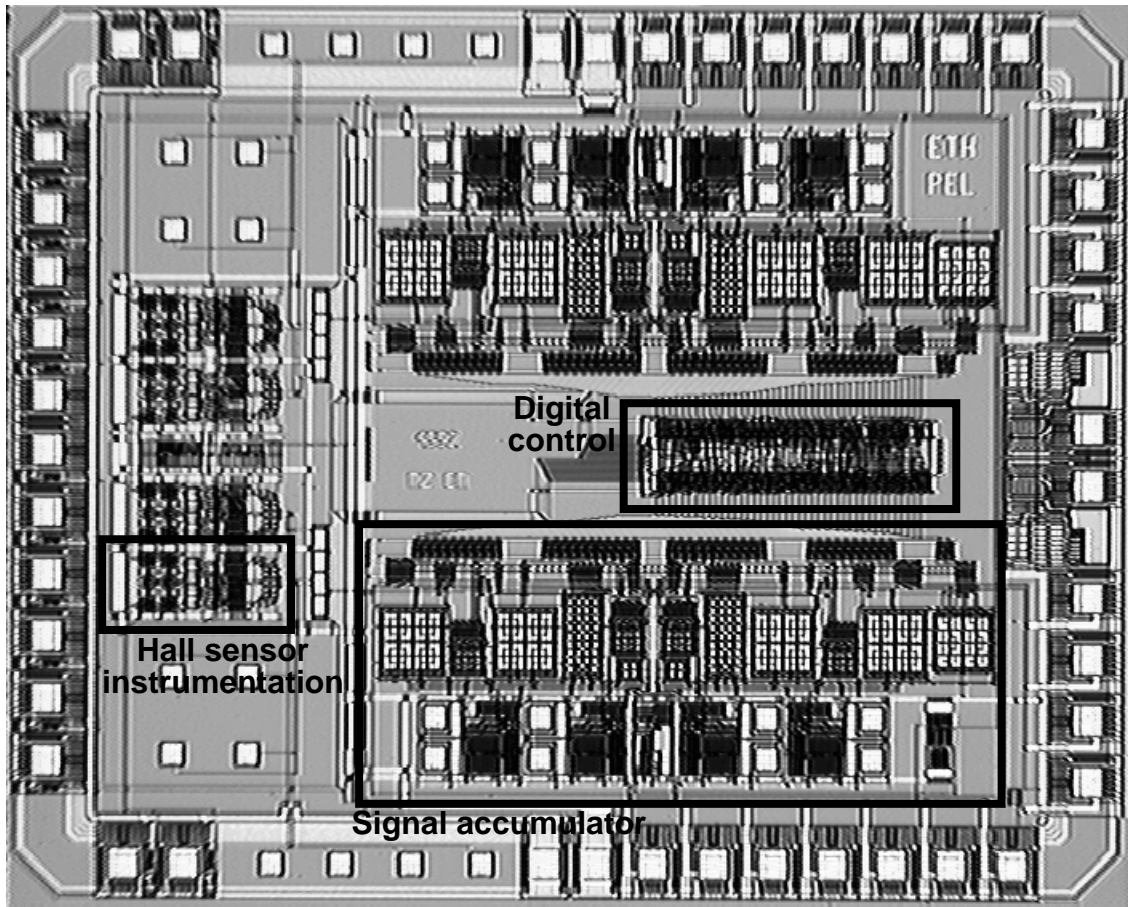


*Fig. 3.16 Micrograph of the implemented test circuit for a Spinning Current Hall sensor interface.*

- The sensitivity, linearity and offset of the system output has been measured.

### 3.6.1 Sensitivity and offset of the Hall devices

A n-well Greek Cross Hall sensor and one of the first, experimental type A Trench Hall sensors have been used to characterize the performance of the Hall sensor interface circuit. The Hall voltage of the Greek Cross sensor is shown in Figure 3.17. At a bias current of  $600 \mu\text{A}$  the sensitivity of the Hall device is  $66 \text{ mV/T}$ , or  $110 \text{ V/(A \cdot T)}$ . The offsets for two perpendicular directions of drive current are:  $3.07 \text{ mT}$  and  $-2.01 \text{ mT}$ , respectively. Figure 3.18 shows the sensitivity and offset of the type A Trench Hall device used for characterization. The sensitivities at bias currents of  $600 \mu\text{A}$  and  $800 \mu\text{A}$  are  $0.16 \text{ V/T}$  and  $0.22 \text{ V/T}$ , respectively, corresponding to a current referred sensitivity of some

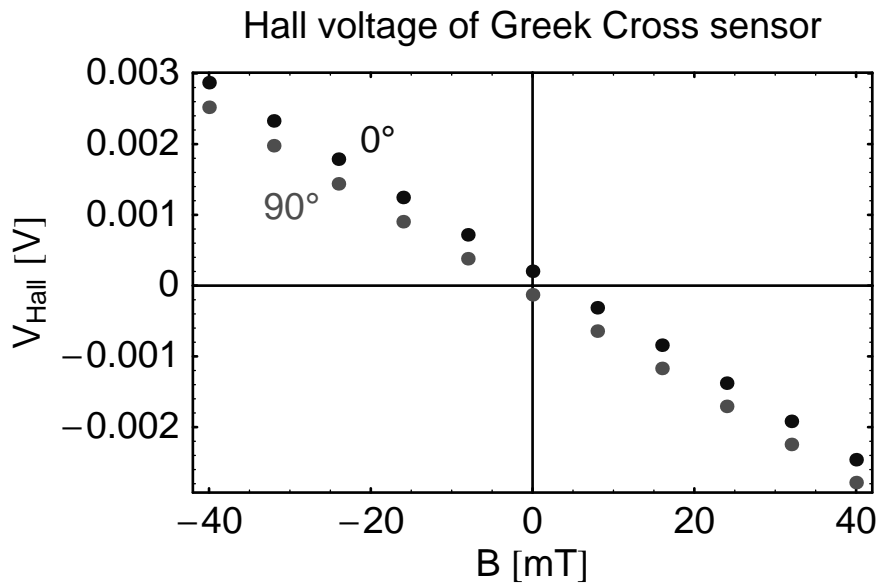


*Fig. 3.17 Measured Hall voltage of a Greek Cross sensor at a drive current of 600  $\mu\text{A}$ , for two perpendicular current directions. The equivalent offset magnetic inductions are 3.07 mT and -2.01 mT, respectively.*

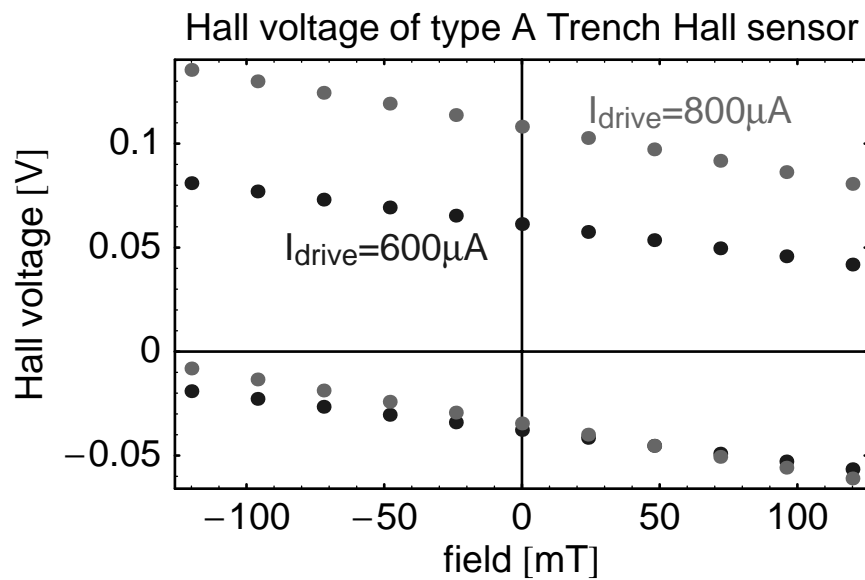


*Fig. 3.18 Measured Hall voltage of the type A Trench Hall sensor used for test of the system, for two perpendicular directions of drive current.*

270 V/(A · T) which slightly increases with the applied current. For a drive current of 600  $\mu\text{A}$ , the offsets for two perpendicular directions of current are

61.4 mV and  $-37.8$  mV, corresponding to magnetic inductions of 377 mT and  $-242$  mT. The offsets for 800  $\mu$ A of drive current are 108 mV and  $-34.6$  mV, corresponding to inductions of 474 mT and  $-157$  mT.

### 3.6.2 Common mode voltage regulation

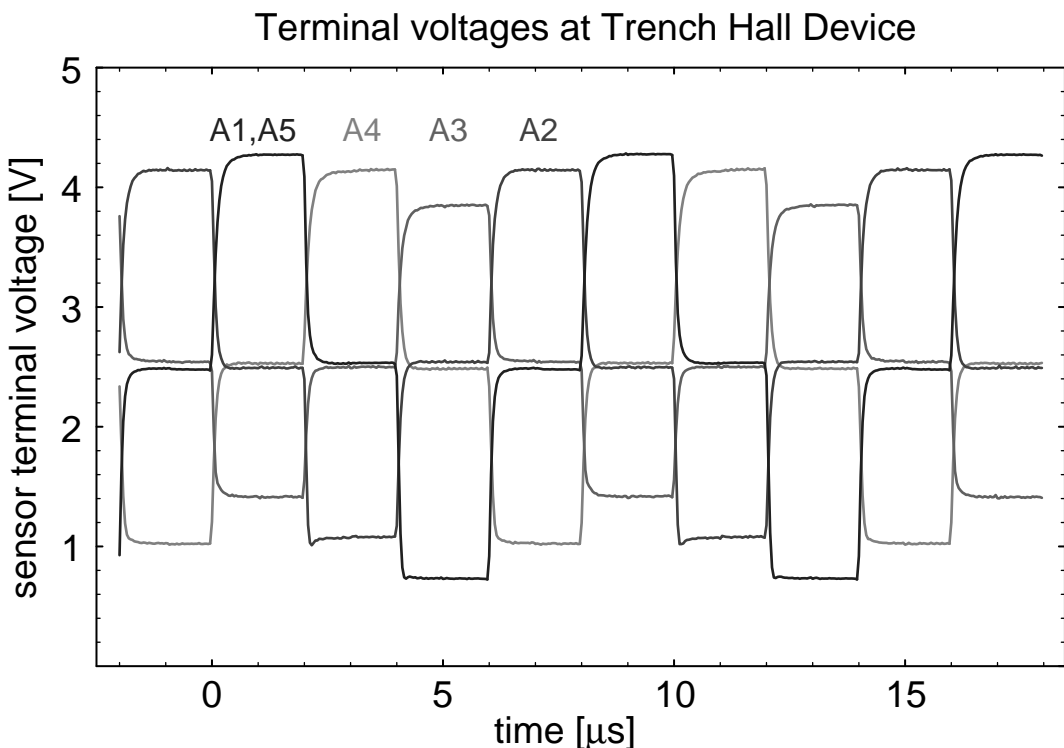


*Fig. 3.19 Measured terminal voltages of type A Trench Hall device at zero magnetic inductance.*

Figure 3.19 shows an oscilloscope of the terminal voltages at the Type A Trench Hall sensor when connected to the interface circuit. The Hall voltage offset can be seen as the distance of the two voltages near the common mode voltage of 2.5 V.

The measured common mode voltage is shown in Figure 3.20. Up to a voltage drop of 3V across the sensor, a deviation from the reference voltage is not detectable with the oscilloscope used for the measurement. With increasing voltage drop across the Hall sensor, the common mode voltage deteriorates because the cascode/switch transistors go out of saturation. For this measurement, the interface circuit is operated at a significantly higher sensor bias current than the design

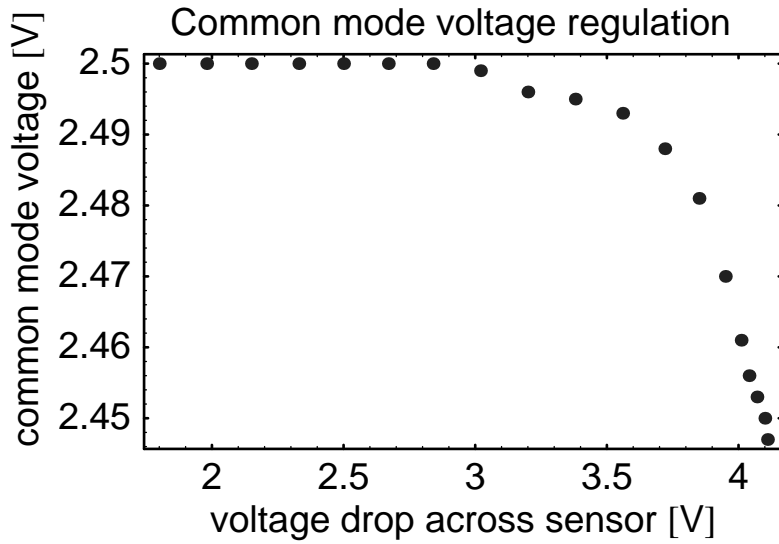


Fig. 3.20 Measured common mode voltage vs. voltage drop across Hall sensor

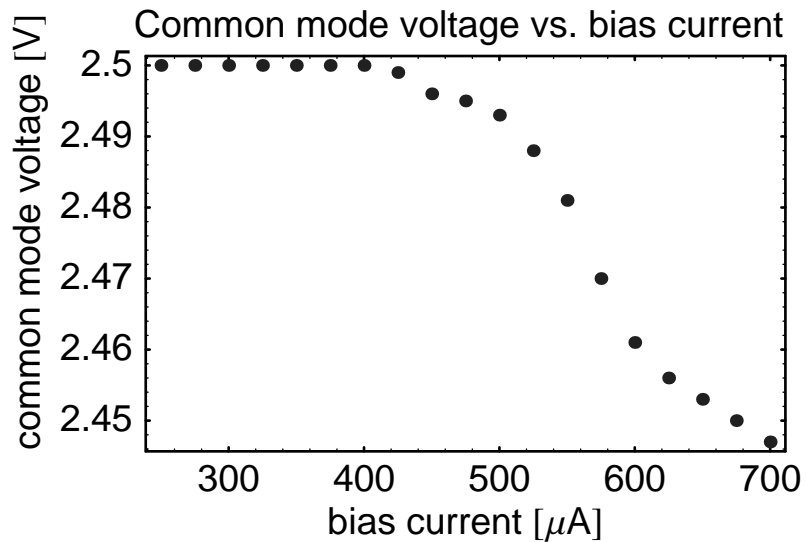
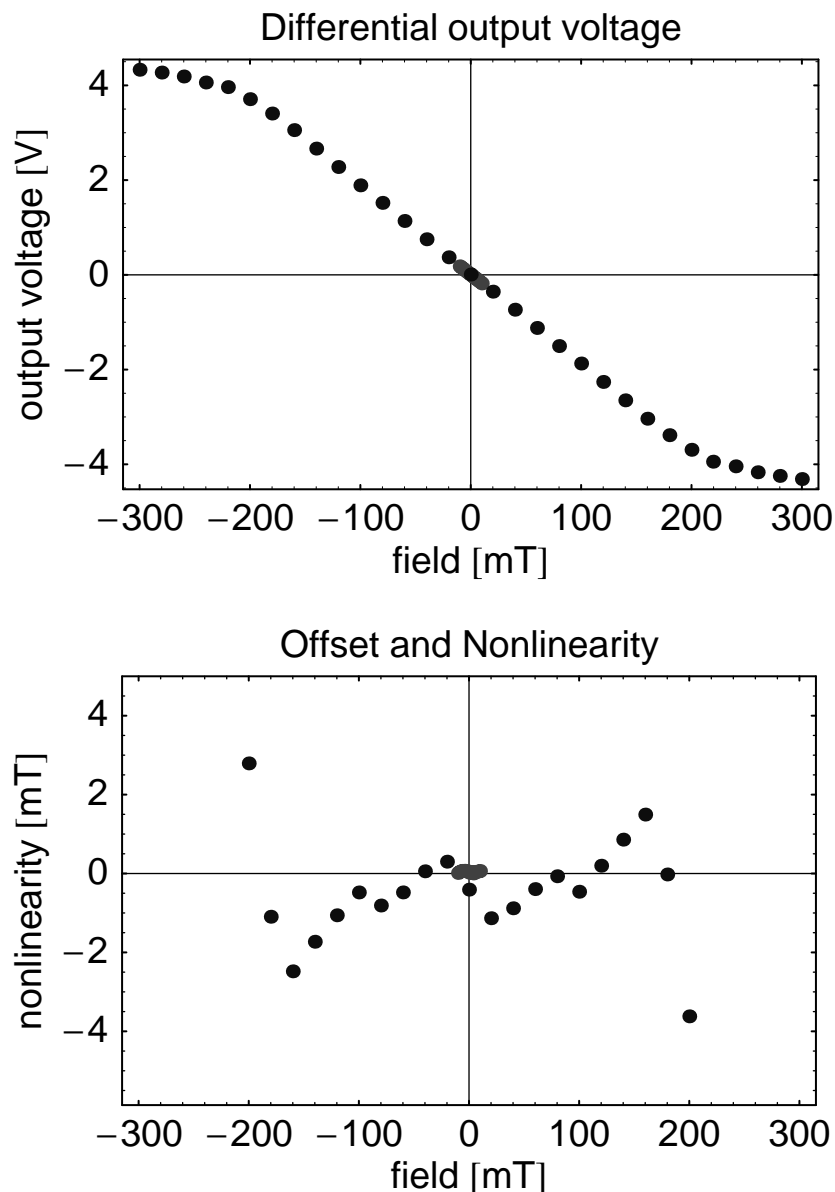


Fig. 3.21 Measured common mode voltage vs. sensor bias current. The circuit is designed for a current of 300  $\mu\text{A}$ .

value of 300  $\mu\text{A}$  (see Figure 3.21). Thus, the sensor voltage drop at which deterioration of the common mode voltage sets in is lower than with a sensor that matches the design specifications.

### 3.6.3 System offset and linearity



*Fig. 3.22 Measured differential output voltage (top) and nonlinearity (bottom) with one Greek Cross Hall device connected to the implemented test circuit. A measurement to determine the offset at zero induction precisely is shown in light gray.*

The differential output of the sensor interface has been measured with both the Greek Cross Hall sensor (Figure 3.22) and the Trench Hall sensor (Figure 3.23).

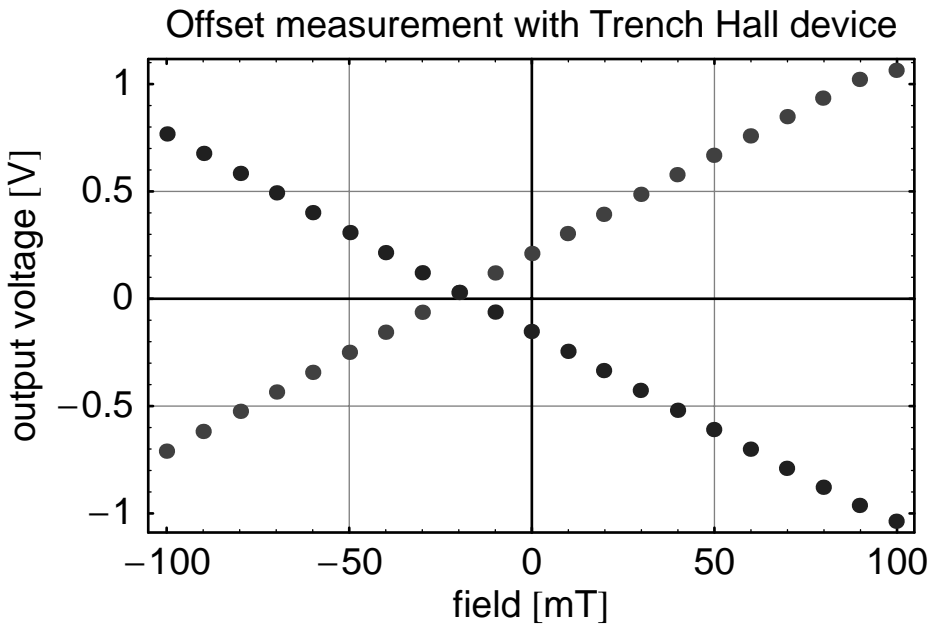


*Fig. 3.23 Measured differential system output with one type A Trench Hall sensor. To separate the offset of the voltmeter from the system offset, the sweep has been performed twice, with the differential output terminals interchanged. The resultant equivalent offset induction is  $-19.8 \text{ mT}$  at a sensitivity of  $9.1 \text{ V/T}$ .*

With one type A Trench Hall sensor at the input, the offset of the Trench Hall device is reduced from several hundred milliteslas to  $-19.8 \text{ mT}$  at a sensitivity setting of  $9.1 \text{ V/T}$ . Clearly, the system offset is dominated by the residual offset of the prototype Trench Hall device which cannot be eliminated by current spinning.

To evaluate the performance of the interface circuitry, the more well-behaved Greek Cross sensor must be used. With one Greek Cross Hall device connected to the input and driven by the nominal bias current of  $300 \mu\text{A}$  and a sensitivity setting of  $18 \text{ V/T}$ , the system has a measured offset voltage of  $780 \mu\text{V}$ , equivalent to an offset induction of  $(43 \pm 7) \mu\text{T}$ .

To determine the offset of the differential system output, the usual methods to obtain a reliable measurement have been carried out:

- The measurement sequences of magnetic induction settings have been randomized to eliminate any systematic remanence effects of the electromagnet gener-

ating the magnetic field.

- To separate the offset of the data acquisition equipment (active differential probe plus voltmeter) from the system offset, the field sweep measurements have been performed twice, with reversed polarity of the differential system output.
- Sensitivities and offsets have been obtained by linear fits to the randomized sequences of measurement samples. In particular, the offset value given for the Hall magnetometer with Greek Cross sensor has been obtained by a linear fit to  $2 \times 11$  measurement points within a range of  $\pm 10$  mT.

The nonlinearity of the system is characterized by measuring the differential output voltage with the Greek Cross device as sensor, shown in Figure 3.22. The piece-wise linear shape of the nonlinearity indicates that the dominant contribution to the relative nonlinearity of approximately 1% is caused by either the gaussmeter or the voltmeter of the measurement setup.



# 4 Integrated Microfluxgate System

This chapter describes an integrated fluxgate magnetometer to perform two-dimensional measurements of magnetic fields that are beyond the resolution of silicon galvanomagnetic sensors, such as Hall devices or magnetotransistors.

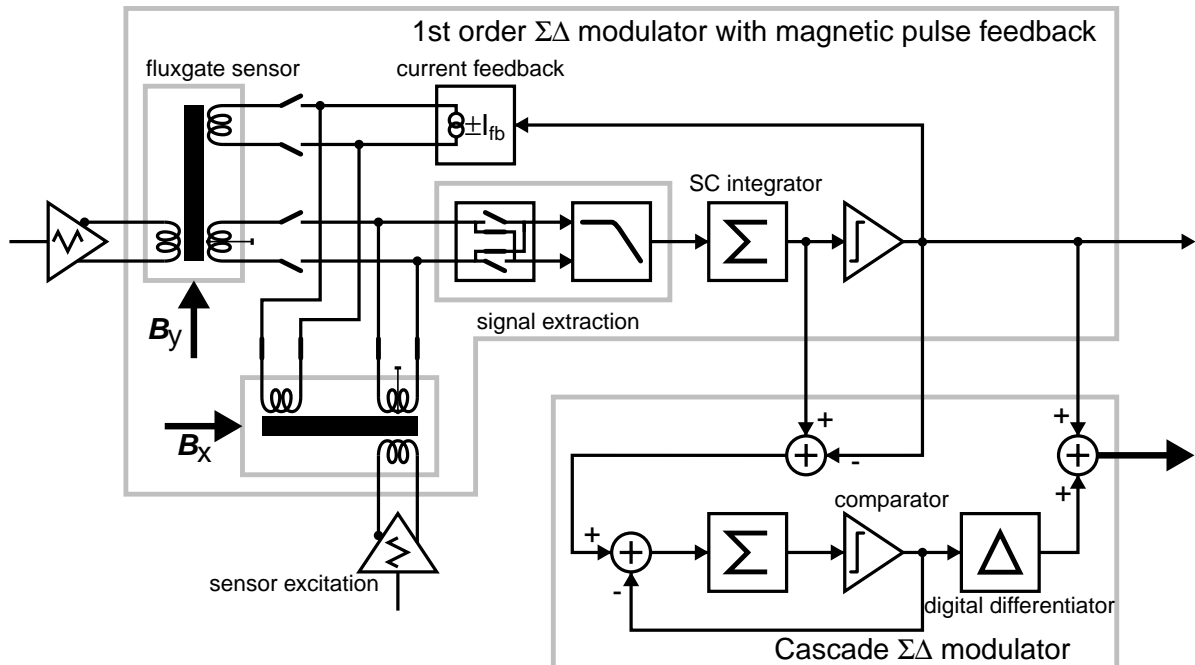


Fig. 4.1 Block diagram of integrated microfluxgate sensor

A block diagram of the integrated microfluxgate system is shown in Figure 4.1. Two microfluxgate sensors for each of the two components of magnetic induction parallel to the die surface of the integrated magnetometer can be selectively excited by a dedicated driver. To provide a digital output for easy interfacing to digital systems, the microfluxgate sensor and its analog readout circuits are embedded in a 1–1 MASH-type  $\Sigma\Delta$  modulator. One feedback loop of the  $\Sigma\Delta$  modulator is closed in the magnetic field domain by means of pulse feedback. Thus,

the system sensitivity is set by the feedback induction. It is independent of variations of the sensor sensitivity due to fabrication tolerances.

This chapter is organized as follows:

Section 4.1 treats the fluxgate principle for measuring weak magnetic fields. A theoretical description based only on elementary symmetry principles is given, and various sources of measurement nonidealities and their remedy is discussed. Section 4.2 outlines the theoretical foundations of the  $\Sigma\Delta$  modulator which is used to convert the measured magnetic induction into a digital output. A description of the planar microfluxgate sensor fully compatible to industrial IC fabrication is given in Section 4.3. Section 4.4 describes the electronic circuitry used to implement the integrated fluxgate magnetometer. Measurement results of the implemented system are presented in Section 4.5.

### 4.1 The fluxgate measurement principle

The fluxgate sensor is based on the properties of ferromagnetic materials. In response to small changes in the externally applied magnetic field, the magnetic dipoles within the ferromagnetic material align themselves in field direction. This results in a very strong relative permeability of up to  $\mu_r = 10^4 \dots 10^6$ . As all the magnetic dipoles in a ferromagnet become aligned with the external magnetic field, the magnetization cannot increase further, and saturation occurs. Saturation introduces nonlinearity in the permeability which is very well defined and symmetrical for opposite directions of magnetization. Even very weak external magnetic fields in the magnitude of nanoteslas result in observable asymmetries in the magnetization when the ferromagnetic core is excited with a periodic magnetic field symmetric about  $H = 0$ .

The excitation magnetic field  $H$  is generated by a periodic current  $I_{\text{exc}}$  that is driven through an *excitation coil*. According to Faraday's Law, the magnetic field is proportional to the line current density through the coil, which is inversely proportional to the pitch  $p_{\text{exc}}$  of the excitation coil. With a geometry factor  $\eta_{\text{exc}}$  accounting for incomplete coupling of the excitation magnetic field into the ferro-

magnetic core, the relation between excitation current and excitation magnetic field is

$$H(t) = \frac{\eta_{\text{exc}}}{p_{\text{exc}}} I_{\text{exc}}(t). \quad (4.1)$$

The excitation field is added to the external magnetic field  $H_{\text{ext}}$  that is to be detected.

If a feedback magnetic field  $H_{\text{fb}}$  is generated by a *feedback coil* to compensate for the external magnetic field, a relation analogous to (4.1) holds between  $H_{\text{fb}}$  and the feedback current:

$$H_{\text{fb}}(t) = \frac{\eta_{\text{fb}}}{p_{\text{fb}}} I_{\text{fb}}(t). \quad (4.2)$$

The ferromagnetic core is magnetized by the total magnetic field  $H_{\Sigma} \equiv H + H_{\text{ext}} + H_{\text{fb}}$ , resulting in a magnetic induction  $B(H_{\Sigma})$  which is a nonlinear function of the magnetic field. This nonlinearity, which is essential for the fluxgate principle, is treated in detail in the following Section 4.1.1. The magnetization of the ferromagnetic core also generates a *demagnetizing field* proportional to the applied magnetic field that counteracts its effect within the core material. Core demagnetization, which depends on the geometry of the ferromagnetic cores, significantly affects the performance of fluxgate sensors. It is discussed in Section 4.3 that describes the design of the microfluxgate sensors.

The time derivative of magnetic flux in the ferromagnetic core is detected by a *pickup coil*, in which a voltage  $U$  is induced according to the Induction Law

$$U(t) = -\eta_{\text{pu}} n_{\text{pu}} A \cdot \frac{dB}{dt}(t), \quad (4.3)$$

with the number of pickup coil windings  $n_{\text{pu}}$  and the effective cross-section  $A$  of the ferromagnetic core. The effect of incomplete coupling of the flux to the pickup coil due to the sensor geometry is described by the factor  $\eta_{\text{pu}}$ .

To simplify the notation, it has been assumed that the both the magnetic field and the magnetic induction are homogeneous throughout the ferromagnetic core and parallel to each other. In general, this is not the case, but effective quantitites can be formed by averaging the *local* magnetic field  $\mathbf{H}(t, \mathbf{x})$  and the *local* magnetic induction  $\mathbf{B}(t, \mathbf{x})$  over the core volume. The linearity and symmetry considerations necessary for the following line of argumentation remain unchanged.

### 4.1.1 A Theory of Fluxgate Operation Based on Symmetry Principles

In this section, the principle of fluxgate operation is derived from elementary symmetry properties of the nonlinear  $B(H)$  relation and of the exciting magnetic field  $H(t)$  only. In contrast to the established treatment of fluxgate operation [85], the use of the Fourier transformation is avoided.

The ferromagnetic core is excited with a symmetric magnetic field of period  $T$ , i. e.,

$$H\left(t \pm \frac{T}{2}\right) = -H(t). \quad (4.4)$$

A direct corollary of this property is

$$\dot{H}\left(t \pm \frac{T}{2}\right) \equiv \frac{dH}{dt}\left(t \pm \frac{T}{2}\right) = -\frac{dH}{dt}(t) \equiv -\dot{H}(t). \quad (4.5)$$

Neglecting hysteresis effects, the magnetization curve of the ferromagnetic core obeys the symmetry relation

$$B(-H) = -B(H), \quad (4.6)$$

and thus

$$B'(-H) \equiv \frac{dB}{dH}(-H) = \frac{dB}{dH}(H) \equiv B'(H) \text{ and} \quad (4.7)$$

$$B''(-H) \equiv \frac{d^2B}{dH^2}(-H) = -\frac{d^2B}{dH^2}(H) \equiv -B''(H). \quad (4.8)$$

To describe the symmetry properties of the signals, the concept of *even* and *odd* functions is introduced:

$$f^{\text{even}}(t) = f^{\text{even}}\left(t \pm \frac{T}{2}\right) \text{ and } f^{\text{odd}}(t) = -f^{\text{odd}}\left(t \pm \frac{T}{2}\right). \quad (4.9)$$

The names “even” and “odd” are chosen because of the property of the products of such functions

<i>Product of functions</i>	<i>even</i>	<i>odd</i>
<i>even</i>	even	odd
<i>odd</i>	odd	even

Linear combinations of all even and all odd signals are even and odd as well, respectively:

<i>Sum of functions</i>	<i>even</i>	<i>odd</i>
<i>even</i>	even	mixed
<i>odd</i>	mixed	odd

According to this definition,  $H(t)$  and  $\dot{H}(t)$  are odd. Any signal with a periodicity of an odd multiple of the excitation frequency  $f \equiv 1/T$  is odd, while any signal with a periodicity of an even multiple of  $f$  is even.

The signal that is extracted from the fluxgate sensor is the induction voltage, which is proportional to  $\frac{dB}{dt}$ . By the chain rule of differentiation,

$$\dot{B}(t) \equiv \frac{dB}{dt}(t) = B'(H(t))\dot{H}(t). \quad (4.10)$$

From these symmetry considerations, the following properties for the induction voltage are found:

*When no external magnetic field is applied, the induction voltage is a purely odd function:*

$$\dot{B}\left(t \pm \frac{T}{2}\right) = B'\left(H\left(t \pm \frac{T}{2}\right)\right)\dot{H}\left(t \pm \frac{T}{2}\right) = B'(-H(t))(-\dot{H}(t)) = -\dot{B}(t) \quad \triangleleft \quad (4.11)$$

*An external magnetic field  $H_{\text{ext}}$  results in a perturbation that is purely even and proportional to  $H_{\text{ext}}$ :*

Assuming that  $H_{\text{ext}} \ll \dot{H}$ ,

$$B'(H + H_{\text{ext}}) = B'(H) + H_{\text{ext}}B''(H) \text{ and} \quad (4.12)$$

$$\dot{B}(t) = [B'(H(t)) + H_{\text{ext}}B''(H(t))]\dot{H}(t) \equiv \dot{B}_0(t) + H_{\text{ext}}\dot{B}_\delta(t). \quad (4.13)$$

As shown in (4.11),  $\dot{B}_0(t)$  is odd. As for  $\dot{B}_\delta(t)$ , we find

$$\dot{B}_\delta\left(t \pm \frac{T}{2}\right) = B''\left(H\left(t \pm \frac{T}{2}\right)\right)\dot{H}\left(t \pm \frac{T}{2}\right) = (-B''(H(t)))(-\dot{H}(t)) = \dot{B}_\delta(t) \quad \triangleleft \quad (4.14)$$

To extract a signal proportional to the external magnetic field, all that has to be done is to extract the even component of the induction voltage. It is convenient to transform this signal component to a DC signal proportional to the external magnetic field  $H_{\text{ext}}$ .

From the multiplication properties of even and odd functions stated above, it is obvious that the extraction of the field-dependent induction voltage component to

DC (which is an even function) is accomplished by multiplying the induction voltage by an appropriately chosen even function  $M(t)$ :

$$v \equiv -\eta_{pu} n_{pu} A \frac{1}{T} \int_0^T U(t) M(t) dt = \frac{1}{T} \int_0^T \dot{B}(t) M(t) dt = H_{ext} \frac{2}{T} \int_0^{\frac{T}{2}} \dot{B}_\delta(t) M(t) dt. \quad (4.15)$$

The simplest even function is a constant. However,

*The mean value of the induction voltage component proportional to the magnetic field  $H_{ext}$  is zero:*

Due to the symmetry properties (4.4) and (4.5) of  $H(t)$  and  $\dot{H}(t)$ , respectively, we find a point  $\hat{H} \equiv H(\tau)$  (e. g. an extremum of  $H(t)$ ) such that

$$H\left(\tau \pm \frac{T}{2}\right) = -\hat{H} \text{ and } \dot{H}(\hat{H}) = \dot{H}(-\hat{H}). \quad (4.16)$$

Consequently, due to (4.7),

$$\begin{aligned} c \int_{\tau-T}^{\tau} \dot{B}(t) dt &= 2c \int_{\tau-\frac{T}{2}}^{\tau} B''(H(t)) \dot{H}(t) dt \\ &= 2c \int_{-\hat{H}}^{\hat{H}} B''(H) dH = 2c[B'(\hat{H}) - B'(-\hat{H})] = 0 \end{aligned} \quad \triangle \quad (4.17)$$

Another even analyzing function  $M(t)$  that is easy to implement electronically is a rectangular wave at twice the excitation frequency:

$$M_\tau(t) = \begin{cases} 1 & \text{if } \tau - \frac{T}{4} < t < \tau \quad \text{or} \quad \tau + \frac{T}{4} < t < \tau + \frac{T}{2} \\ -1 & \text{if } \tau - \frac{T}{2} < t < \tau - \frac{T}{2} \quad \text{or} \quad \tau < t < \tau + \frac{T}{4} \end{cases} \quad (4.18)$$

with a phase shift  $\tau$ . This function can be realized by a cross-coupled switch.

The optimal phase shift  $\tau$  can be deduced from the symmetry properties of the excitation waveform  $H(t)$  and the magnetization curve  $B(H)$  of the ferromagnetic core. The symmetry property (4.8) requires that  $B''(0) = 0$ . Setting  $\tau$  such that  $H(\tau) = 0$ , the sensitivity is

$$\begin{aligned} \frac{v}{H_{\text{ext}}} &= \frac{2}{T} \int_{\tau - \frac{T}{4}}^{\tau + \frac{T}{4}} \dot{B}_\delta(t) M(t) dt = \frac{2}{T} \int_{\tau - \frac{T}{4}}^{\tau + \frac{T}{4}} B''(H(t)) M(t) \dot{H}(t) dt \\ &= \frac{2}{T} \int_{-\hat{H}}^{\hat{H}} B''(H) M(H) dH = \frac{2}{T} \left( \int_0^{\hat{H}} B''(H) M(H) dH + \int_{-\hat{H}}^0 B''(H) M(H) dH \right) \\ &= \frac{2}{T} \left( \int_0^{\hat{H}} B''(H) M(H) dH + \int_0^{\hat{H}} B''(-H) M(-H) dH \right) \end{aligned} \quad (4.19)$$

Inspection of magnetization curves shows that  $B''(H) > 0$  for  $H < 0$  and  $B''(H) < 0$  for  $H > 0$ . Thus, assuming a symmetrical excitation waveform  $H(t)$ , the choice for  $M(t)$  given in (4.18) is optimal, and the mean output signal is

$$v = H_{\text{ext}} \frac{4}{T} \int_{-\hat{H}}^0 B''(H) dH = H_{\text{ext}} \frac{4}{T} [B'(0) - B'(\hat{H})] = H_{\text{ext}} 4f\mu \quad (4.20)$$

with the excitation frequency  $f \equiv T^{-1}$  and the permeability  $\mu \equiv B'(0)$ , assuming that  $B'(\hat{H}) = 0$ , i. e., the ferromagnetic core is driven to saturation.

### 4.1.2 Nonidealities in Fluxgate Operation

In this section, nonidealities of fluxgate operation are discussed:

- Noise of the ferromagnetic cores
- Hysteresis of the ferromagnetic cores
- Effect of finite bandwidth of the front-end amplifier

#### Effects of Noise in the ferromagnetic core

The dominant source of noise in a fluxgate is *Barkhausen noise* [48]. It is due to the change of magnetization of the ferromagnet occurring in discontinuous jumps, resulting in a  $1/f^\alpha$  noise spectrum with  $\alpha \approx 1$  [85],[86]. Barkhausen noise sets a lower limit to the achievable resolution of a fluxgate magnetometer.

#### Effects of Hysteresis in the ferromagnetic core

The *coercitivity*  $H_c$  of the ferromagnetic core results in an offset of the effective excitation magnetic field

$$H_{\text{eff}}(t) = \begin{cases} H(t) - H_c & \text{if } \dot{H}(t) > 0 \\ H(t) + H_c & \text{if } \dot{H}(t) < 0 \end{cases}, \quad (4.21)$$

which does not disturb the symmetry properties of the waveforms involved, but introduces a time lag, which for  $H_{\text{eff}} = 0$  is

$$\tau_c = \frac{H_c}{\dot{H}(H=0)}. \quad (4.22)$$

The phase shift of the demodulating waveform  $M_{(\tau + \tau_c)}(t)$  must be adjusted accordingly.

### Effects of finite bandwidth of a pickup coil amplifier

If an amplifier is connected between the pick-up coil and the demodulator, the signal is distorted and delayed. Following a line of reasoning introduced by C. Menolfi and Q. Huang for the analysis of chopper amplifiers [88, 89], let us assume that the amplifier have first order low-pass characteristics with a time constant of  $RC$ .

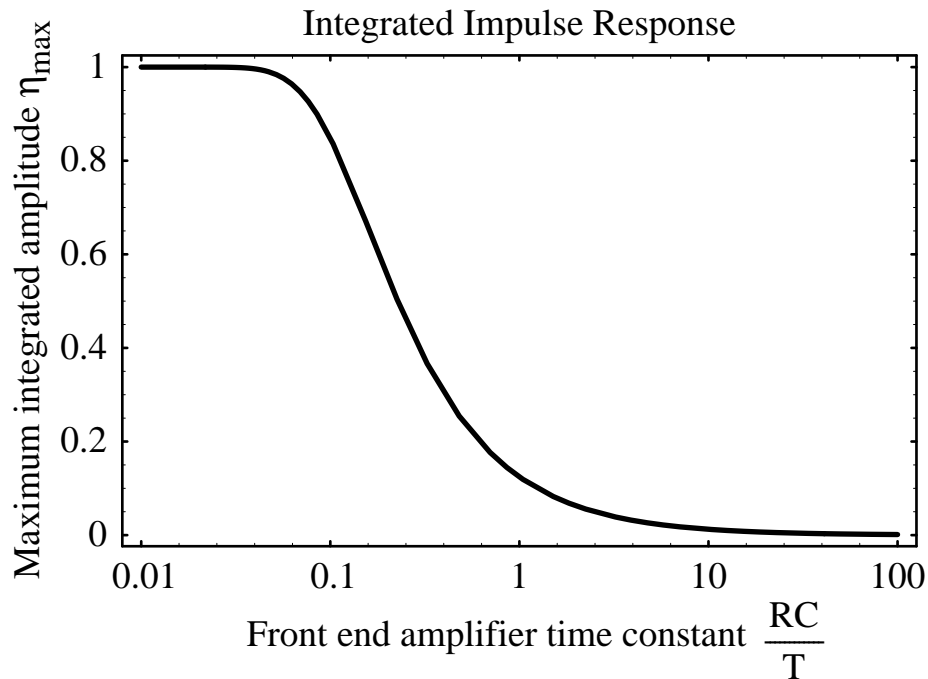


Fig. 4.2 Dependence of the maximum integrated impulse response on the ratio between front-end amplifier filter time constant  $RC$  and excitation signal period  $T$ .

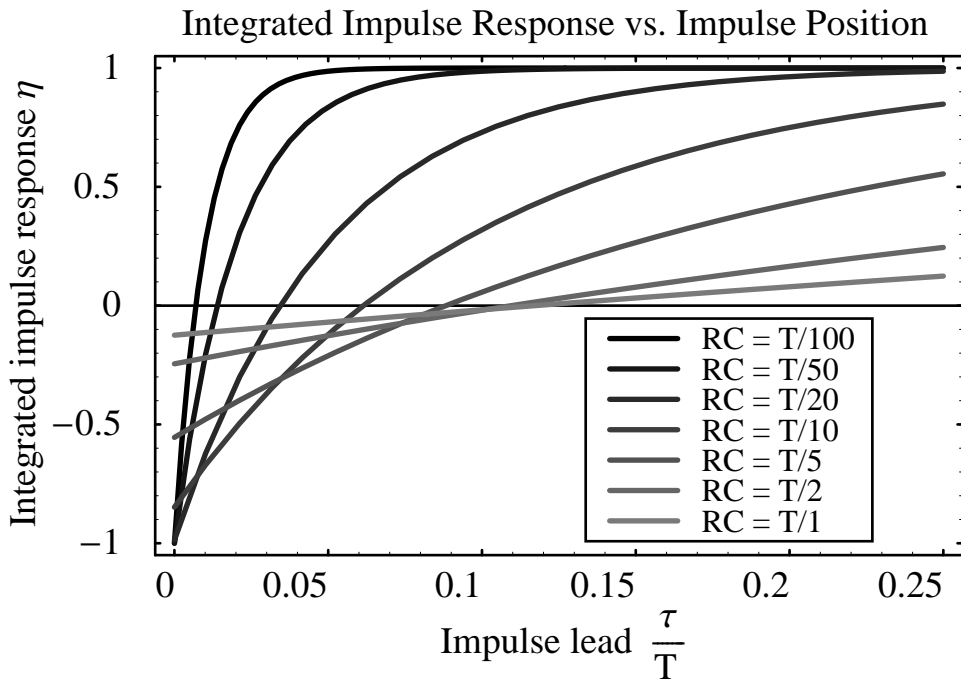


Fig. 4.3 Dependence of the integrated impulse response on the position of the impulse with respect to the switching transient of the demodulating signal.

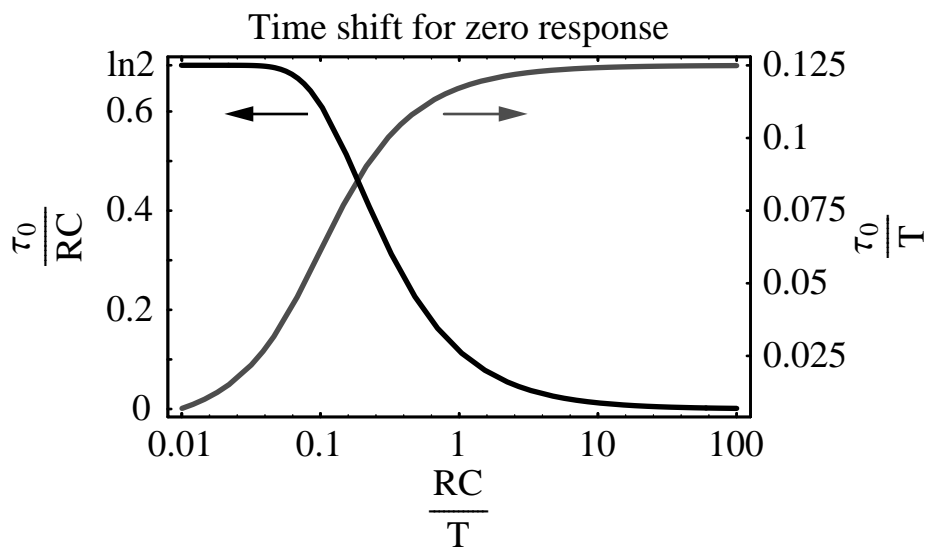


Fig. 4.4 Dependence of the time shift  $\tau_0$  of the demodulating waveform with respect to the generating impulse at which an integrated impulse response of  $\eta = 0$  occurs.

The impulse response of a first order low-pass filter is

$$h(t) = \frac{1}{RC} e^{-\frac{t}{RC}} \quad (4.23)$$

Without subsequent modulation, the contribution to the mean signal is

$$\eta \equiv \int_0^{\infty} h(t) dt = 1. \quad (4.24)$$

However, in the presence of a modulating signal  $M_{\tau}(t)$ , the total contribution to the mean signal becomes

$$\begin{aligned} \eta(\tau) &= \int_0^{\infty} h(t) M_{\tau}(t) dt \\ &= \int_0^{\tau} \frac{e^{-\frac{t}{RC}}}{RC} dt + \sum_{n=0}^{\infty} \left( \int_{\tau + \frac{T}{4} + n\frac{T}{2}}^{\tau + (n+1)\frac{T}{2}} \frac{e^{-\frac{t}{RC}}}{RC} dt - \int_{\tau + n\frac{T}{2}}^{\tau + \frac{T}{4} + n\frac{T}{2}} \frac{e^{-\frac{t}{RC}}}{RC} dt \right) \\ &= 1 - \frac{2e^{-\frac{\tau}{RC}}}{1 + e^{-\frac{T}{4RC}}} . \end{aligned} \quad (4.25)$$

Depending on the time of switching  $\tau$  with respect to the impulse, the amplitude of the integrated impulse response  $\eta(\tau)$  of the impulse to the signal varies within the interval  $\pm(1 - 2/(1 + e^{T/(4RC)}))$ . The maximum amplitude depends on the ratio  $\frac{RC}{T}$  between the time constant and the sampling time. This dependence is shown in Figure 4.2. For a maximum integrated impulse response to the mean signal of 0.9, an amplifier time constant of  $RC < T/12$  is required. The depen-

dence of  $\eta$  on  $\tau$  is shown in Figure 4.3 for different time constants. The time of zero integrated impulse response  $\eta(\tau_0) = 0$  is shown in Figure 4.4. It is given by

$$\tau_0 = \frac{T}{4} - RC \log\left(\frac{1 + e^{\frac{T}{4RC}}}{2}\right). \quad (4.26)$$

For fast amplifiers ( $RC \ll T$ ),  $\tau_0$  tends towards  $\ln 2RC$ , while for slow amplifiers  $\tau_0 \rightarrow T/8$ .

The signal from the fluxgate sensor, after a front-end amplifier with low-pass characteristics and a cross-coupled switch demodulator, assuming that  $H_{\text{eff}}(0) = 0$ , is given by

$$\begin{aligned} \frac{\phi}{H_{\text{ext}}} &= \frac{2}{T} \int_{\tau-\frac{T}{2}}^{\tau} \dot{B}_{\delta}(t) \eta(\tau-t) dt \\ &= \frac{2}{T} \int_{\tau-\frac{T}{2}}^{\tau} B''(H_{\text{eff}}(t)) \left( 1 - \frac{2e^{-\frac{\tau-t}{RC}}}{1 + e^{-\frac{T}{4RC}}} \right) \dot{H}_{\text{eff}}(t) dt \quad . \end{aligned} \quad (4.27)$$

As can be seen from Figure 4.2, the sensitivity increases with the bandwidth of the front-end amplifier.

### 4.1.3 Differential fluxgate arrangement

The finite bandwidth of a front-end amplifier between the fluxgate pickup coil and the demodulating switches reduces the sensitivity, but does not cause coupling of the (odd) excitation signal to the (even) signal proportional to the applied magnetic field  $H_{\text{ext}}$ . However, any deviation in the transfer function  $V_{\text{out}} = A(V_{\text{in}})$  of the amplifier from the symmetry property

$$A(-V_{\text{in}}) = -A(V_{\text{in}}) \quad (4.28)$$

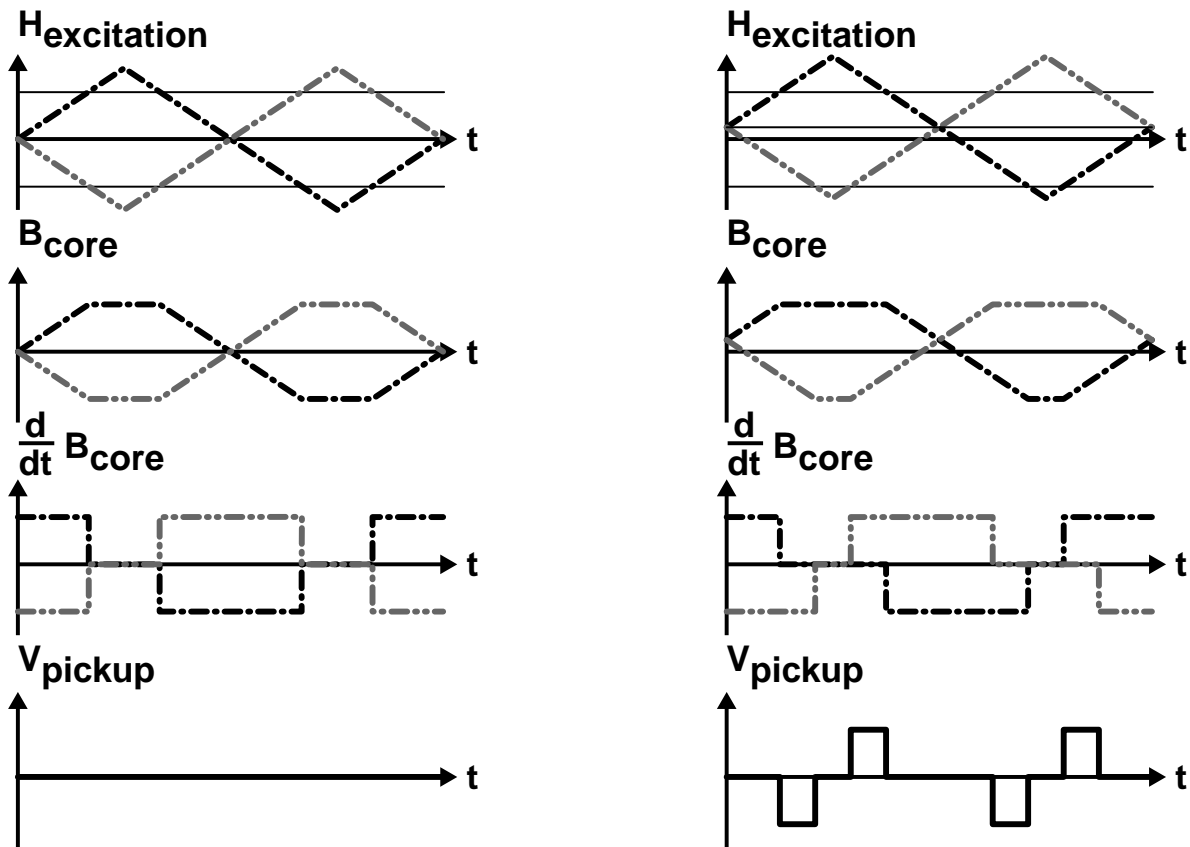


*Fig. 4.5 Waveforms at differential fluxgate sensor without (left) and with (right) external magnetic field.*

*Signals, from top to bottom:*

*Excitation magnetic field*

*Magnetic induction in the ferromagnetic cores*

*Time derivative of the magnetic induction in the ferromagnetic cores*

*Induction voltage in the series-connected pick-up coils*

will lead to intermodulation of odd signal components to the even signal components. This leakage can be avoided by eliminating odd signal components from the pickup signal as early as possible in the signal path. A method to accomplish this is the differential arrangement of sensors [85]: Two equal fluxgate sensors are excited with signals of equal magnitude but opposite signs, and the pick-up wind-

ings are connected in series. The resulting output signal at the series-connected pickup coils is

$$\begin{aligned} U(t) &\sim [B'(H(t)) + H_{\text{ext}}B''(H(t)) - B'(-H(t)) - H_{\text{ext}}B''(-H(t))] \dot{H}(t) \quad (4.29) \\ &= [B'(H(t)) - B'(-H(t)) + H_{\text{ext}}(B''(H(t)) + B''(-H(t)))] \dot{H}(t) = 2H_{\text{ext}}\dot{B}_{\delta}(t) \end{aligned}$$

so, ideally, all odd signal components are eliminated from the sensor readout voltage. A conceptual drawing of the waveforms occurring at the differentially arranged fluxgate sensors is shown in Figure 4.5. An overview of various topologies for differential fluxgate sensors is given in [42].

## 4.2 Theory of $\Sigma\Delta$ data conversion

The fluxgate sensor with its associated signal extraction circuitry is embedded in a first-order  $\Sigma\Delta$  modulator loop. Therefore, in this section, a short overview on the theory of operation of  $\Sigma\Delta$  modulators is given.

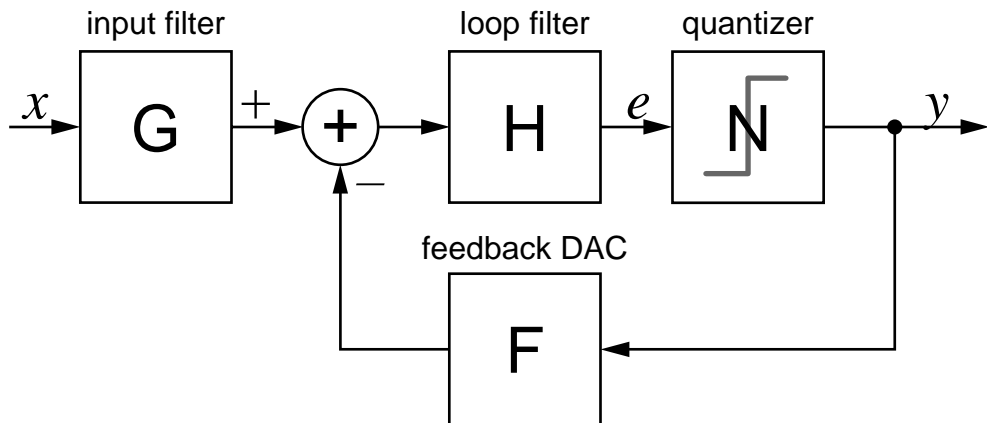


Fig. 4.6 Block diagram of  $\Sigma\Delta$  modulator loop

Figure 4.6 shows the block diagram of a feedback loop with the transfer functions  $G$ ,  $F$ ,  $H$ , and  $N$  for the input, feedback, integrator, and quantizer, respectively. Denoting the input signal with  $x$ , the output signal  $y$  and the signal at the input of the quantizer  $e$ , we get the equations

$$y = N(e) \text{ and } e = H(G(x) - F(y)). \quad (4.30)$$

We can assume the input filter  $G$ , the feedback filter  $F$ , and the loop filter function  $H$  to be linear transfer functions.

The quantizer maps the continuous analog signal  $e$  onto the digital variable  $y$  with a finite number of possible values. Thus, its transfer function  $N$  is inherently nonlinear. Practical implementations of a quantizer sample its input signal  $e$  at discrete points in time. Consequently,  $\Sigma\Delta$  modulators are sampled time systems with a characteristic *sampling frequency*  $f_s$ . A direct consequence of the sampling introduced by the quantizer is a delay of at least  $t_s \equiv 1/f_s$  in the feedback loop.

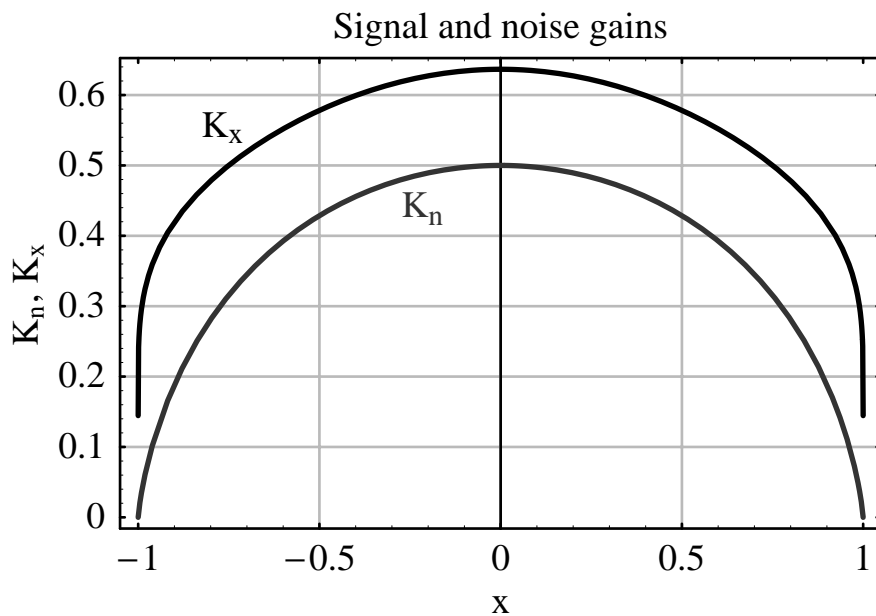


Fig. 4.7 Dependence of signal and noise gains of a single-bit quantizer on the input signal according to [90]

In this context, only single bit quantizers shall be considered, even though multi-bit quantizers are possible as well.

Following the method proposed by Ardalan and Paulos [90], we approximate the quantizer's function by the linear function

$$N(e) \equiv K_x \cdot e_x + K_n \cdot e_n \quad (4.31)$$

with the signal-dependent *quantization gain*  $K_x$  and the *quantization noise*  $e_n$ , which is assumed to be statistically independent from the signal  $e_x$  and to be amplified by the *noise gain*  $K_n$ , with

$$K_x = \frac{E[ye_x]}{E[e_x^2]} \text{ and } K_n = \frac{E[ye_n]}{E[e_n^2]}. \quad (4.32)$$

Solving for the signal and noise components of the output signal  $y$ , we get

$$y_x = \frac{K_x \cdot HG}{1 + K_x \cdot HF} x \text{ and } y_n = \frac{K_n}{1 + K_n \cdot HF} e_n. \quad (4.33)$$

The principle of  $\Sigma\Delta$  modulation is based on a choice of the loop filter function  $H$  with integrating character, such that in the low-frequency limit

$$\lim_{f \rightarrow 0} (H) \gg 1, \quad (4.34)$$

and consequently, the transfer functions for signal and quantization noise become

$$\frac{y_x}{x} = \frac{K_x \cdot HG}{1 + K_x \cdot HF} \rightarrow \frac{G}{F} \text{ and } \frac{y_n}{e_n} = \frac{K_n}{1 + K_n \cdot HF} \rightarrow 0, \quad (4.35)$$

i. e., the output is independent of the loop filter function  $H$  and determined by the ratio of input transfer function and feedback transfer function  $\frac{G}{F}$  only. The particular choice of the loop filter function  $H$  depends on choices and tradeoffs between the transfer function for AC signals and the ease of implementation.

The *order* of a  $\Sigma\Delta$  modulator is equal to the order of its loop filter, i. e., for low-pass loop filters, it is equal to the number of integrators.

### Resolution, frequency response

The resolution and frequency response of the  $\Sigma\Delta$  modulator depend on the choice of the loop filter function  $H$ . For signals that are to include DC, a low-pass function is chosen. With a single-bit quantizer, the achievable resolution, depends on the *oversampling ratio*, the ratio between the sampling frequency and the maxi-

mum signal frequency  $\text{OR} = f_S/f_{\text{Signal,max}}$ . Due to the signal dependent transfer functions, the digital resolution of a  $\Sigma\Delta$  modulator depends on the form of the input signal. For a sinusoidal input, the signal to noise power ratio for an  $n$ th order lowpass filter as loop filter is given in [1] as

$$\text{SNR} \approx 3\pi \frac{2n+1}{2} \left( \frac{\text{OR}}{\pi} \right)^{2n+1}. \quad (4.36)$$

For a first order  $\Sigma\Delta$  modulator, the resolution increases by 1.5 bit per octave of the oversampling ratio; for a second order modulator, the resolution increases by 2.5 bit/octave of oversampling ratio.

## Stability

For the  $\Sigma\Delta$  modulator to be stable, the poles of the  $z$  domain signal and noise transfer functions (4.35) must correspond to damped oscillations, i. e. they must remain within the unit circle for any signal gain  $K_x$  and noise gain  $K_n$  that may occur during operation of the  $\Sigma\Delta$  modulator. Figure 4.7 shows that for signal amplitudes close to the full scale of the converter, the effective gain of the quantizer becomes very small. In general, the resultant large signal amplitudes and changes of the transfer function within the loop filter cause instability.

Stability problems can be avoided by using a first order  $\Sigma\Delta$  modulator. Its transfer function from a state  $i$  to the subsequent state  $(i + 1)$  can be described by the state variable equations

$$e_{i+1} = e_i + G \cdot x_i - F \cdot y_i \text{ and } y_i = \text{sgn}(e_i) \quad (4.37)$$

with the positive constants  $G$  and  $F$ . For input signals with an amplitude of  $|x| < F/G$ , a first order  $\Sigma\Delta$  modulator is always stable.

While a first order integrator is inherently stable, it is prone to *limit cycles*, short cyclic sequences which cause tones at discrete fractions of the sampling frequency. An example of a 4-state limit cycle at half the maximum input range is shown in Figure 4.8. A cascaded, or MASH,  $\Sigma\Delta$  modulator topology of two first order modulators alleviates the issue of limit cycles while retaining their inherent stability.

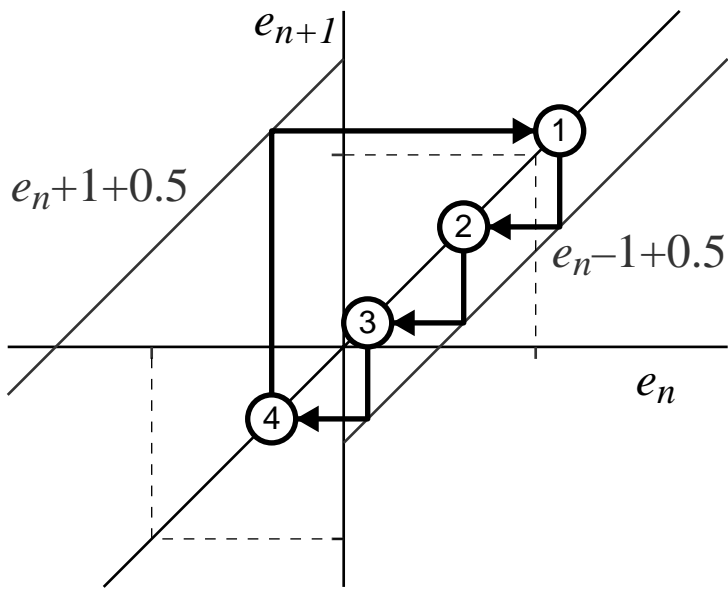


Fig. 4.8 Four state limit cycle in the transfer function of a first-order  $\Sigma\Delta$  modulator, at a constant input of half the maximum feedback amplitude.

### Noise, Distortion

By the very design of a  $\Sigma\Delta$  modulator, the main source of noise, being the quantization noise, is shifted towards high frequencies and subsequently filtered from the signal band. Additional random noise at the input of the quantizer even helps in randomizing the oscillation of the modulator, thereby removing limit cycles. However, noise generated in the input filter  $G$ , the feedback path  $F$ , or at the *input* of the loop filter  $H$ , is indistinguishable from the signal. Eventually, the noise in sampled-time  $\Sigma\Delta$  modulators is dominated by the  $kT/C$  noise at the first stage of the loop filter  $H$ .

Similarly, nonlinearities *within* the forward path of the loop are attenuated by feedback, while nonlinearities in the input filter and the feedback path appear in the filtered output signal. Nonlinearities in the feedback path are eliminated by using single bit feedback with only two possible feedback values.

## 4.3 CMOS compatible fluxgate sensor

The straightforward way to implement coils with ferromagnetic cores is wrapping the coils for excitation, signal pickup, and feedback *around* a ferromagnetic core.

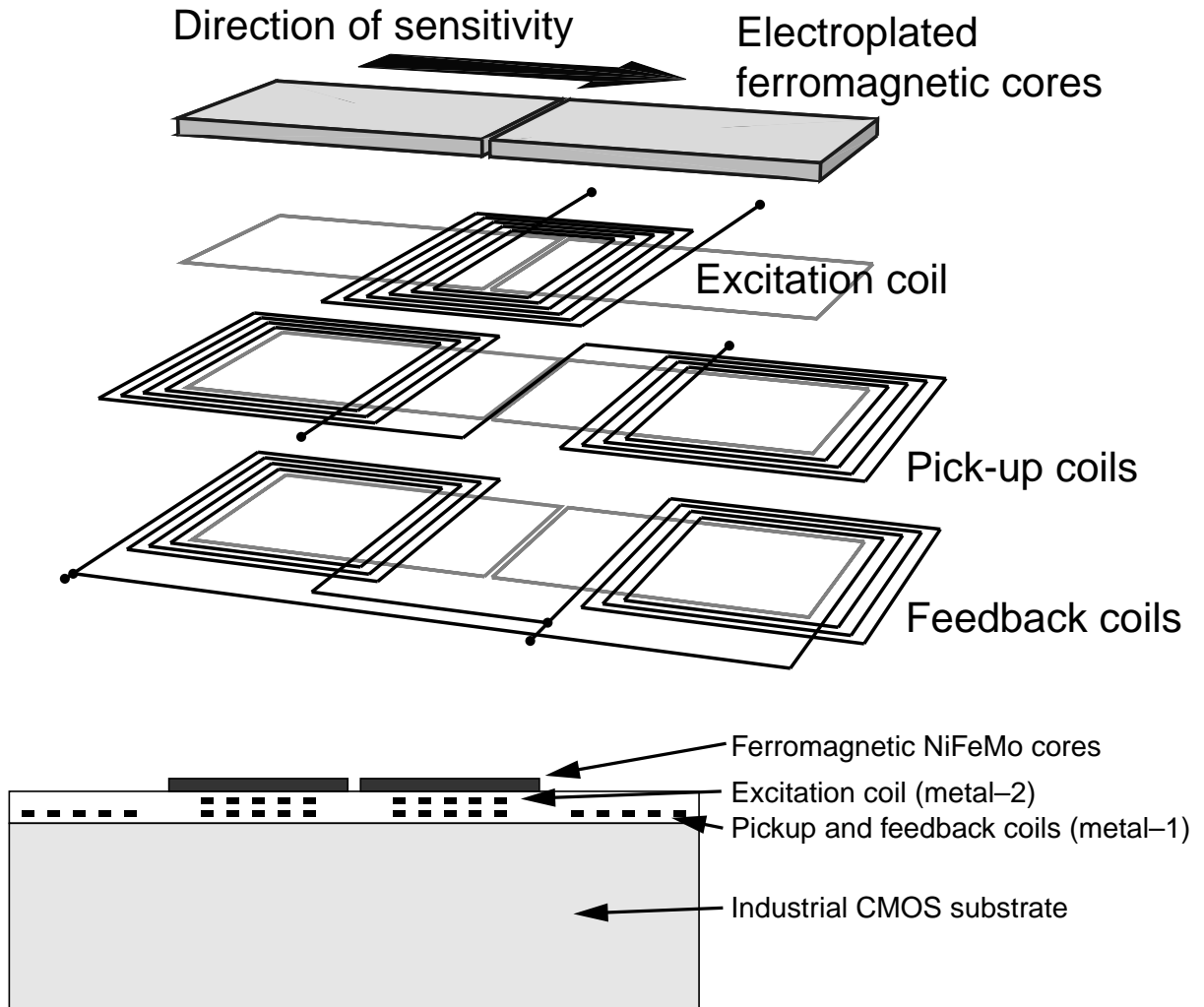


*Fig. 4.9 Exploded view (top) and cross section (bottom) of micro fluxgate sensor compatible to industrial IC fabrication processes*

While this is easily done when dealing with discrete components, i. e., ferrite cores and wire, it cannot easily be transferred to standard IC technology, in which ferromagnetic layers are not available. A process to implement micro-solenoids around ferromagnetic permalloy (NiFe) cores into anisotropically etched grooves has been developed [3][4]. *Planar* fluxgates have been implemented by sputtering a permalloy film on a silicon substrate covered with  $\text{SiO}_2$ , with a planar aluminum pick-up coil on top of the cores, insulated by a polyimide layer [43]. Fully integrated microfluxgate sensors using electrodeposited NiFeIn thin films sandwiched between Al metallization layers have been demonstrated [7].

The microfluxgate sensors of the magnetometer presented in this work use the

metal interconnect layers which are part of the standard IC process for the planar excitation, feedback, and pickup coils. Only the supermalloy (NiFeMo) ferromagnetic cores are electrodeposited on top of the finished circuits in a postprocessing sequence *after* completing the standard process flow [53]. In this way, the ferromagnetic materials, which are intolerable in a standard IC process flow due to potential contamination of the equipment, never enter the foundry, while the necessary postprocessing steps are kept to a minimum. The exploded view and cross-section of the planar fluxgate sensor compatible to any stanard IC technology is shown in Figure 4.9. The implemented planar microfluxgate sensor is shown in Figure 4.10.

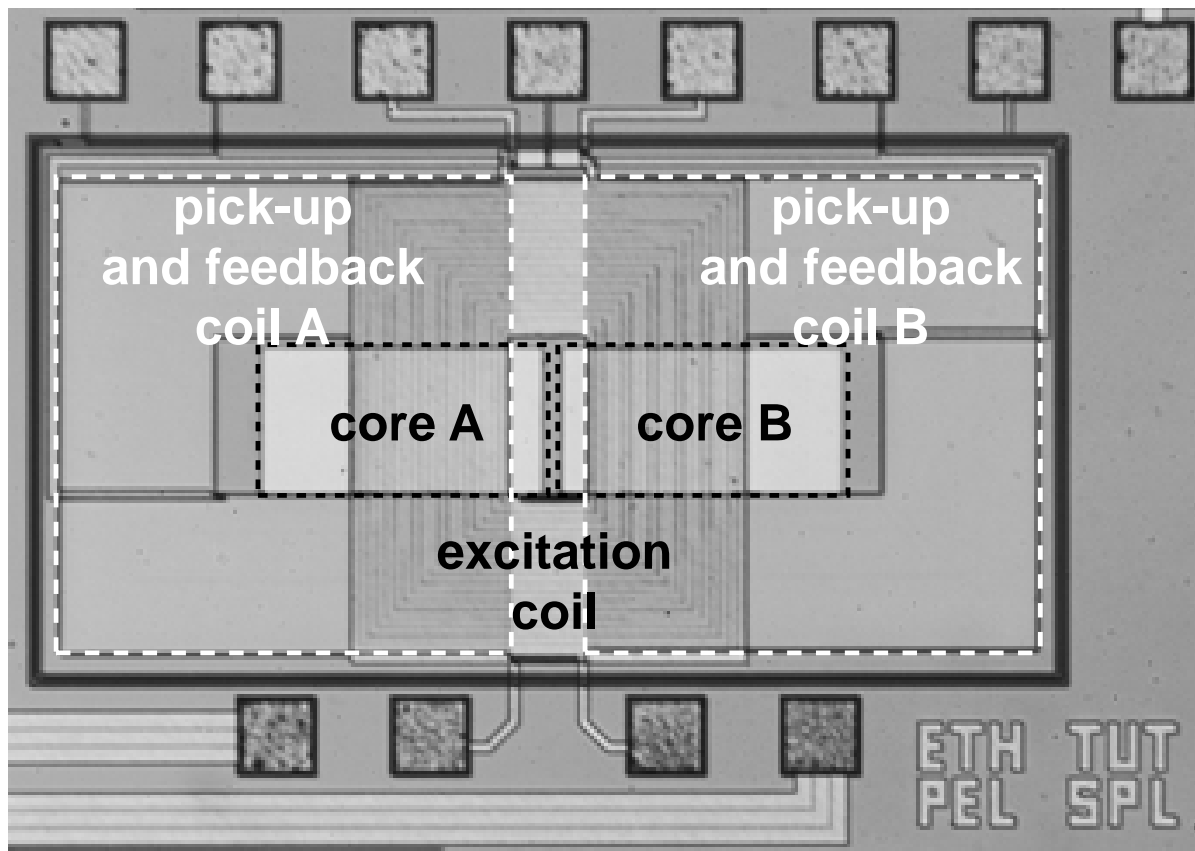


*Fig. 4.10 Micrograph of the implemented planar microfluxgate sensor. The size of each core is  $0.4 \text{ mm} \times 0.2 \text{ mm}$ .The size of the entire sensor is  $1.3 \text{ mm} \times 0.7 \text{ mm}$ .*

## Design parameters for planar fluxgate sensors

Core thickness	$t_{\text{core}} = 2 \mu\text{m}$
Core width	$w_{\text{core}} = 200 \mu\text{m}$
Core length	$l_{\text{core}} = 400 \mu\text{m}$
Excitation coil windings	$N_{\text{exc}} = 18$
Excitation coil pitch	$p_{\text{exc}} = 11.2 \mu\text{m}$
Excitation coil resistance	$R_{\text{exc}} = 99 \Omega$
Pickup coil windings	$N_{\text{pu}} = 41$
Pickup coil pitch	$p_{\text{pu}} = 4.8 \mu\text{m}$
Pickup coil resistance	$R_{\text{pu}} = 6365 \Omega$
Feedback coil windings	$N_{\text{fb}} = 41$
Feedback coil pitch	$p_{\text{fb}} = 4.8 \mu\text{m}$
Feedback coil resistance	$R_{\text{fb}} = 1589 \Omega$
Excitation current	$I_{\text{exc}} = 55 \text{ mA}$
Effective permeability	$\mu_{\text{eff}} \approx 200$

Tab. 4.1 Design parameters of the planar fluxgate sensor

The output signal of the differential fluxgate sensor is the even component of the induction voltage. Hence, according to (4.3), the sensitivity of the fluxgate is proportional to the cross-section perpendicular to the direction of sensitivity, which is the product  $A = w_{\text{core}} \times t_{\text{core}}$  of the width and thickness of the ferromagnetic thin film cores. The length of the cores is important because of their geometry dependent demagnetization. The magnetization  $M$  of the core generates a magnetic field  $H_{\text{demag}} = DM$  counteracting the applied magnetic field. The *demag-*

*netizing factor*  $D$  depends on the core geometry. For rectangular thin film cores with  $l_{\text{core}} \gg w_{\text{core}} \gg t_{\text{core}}$ , it can be approximated by [53]

$$D = \frac{w_{\text{core}} \times t_{\text{core}}}{l_{\text{core}}^2} \cdot \left( \ln \frac{4l_{\text{core}}}{w_{\text{core}} + t_{\text{core}}} - 1 \right). \quad (4.38)$$

This results in a reduction of the relative permeability  $\mu_{\text{rel}}$  to the *effective permeability*

$$\mu_{\text{eff}} = \frac{1}{1/\mu_{\text{rel}} + D} \approx \frac{1}{D} \text{ for high } \mu_{\text{rel}}. \quad (4.39)$$

The sensitivity of the differential fluxgate sensor is

$$S = 2 \cdot 4A\mu_{\text{eff}}f_{\text{exc}} \approx 8 \frac{A}{D} f_{\text{exc}} = 8f_{\text{exc}} \frac{l_{\text{core}}^2}{\ln \frac{4l_{\text{core}}}{w_{\text{core}} + t_{\text{core}}} - 1}. \quad (4.40)$$

Thus, it is advantageous to design a sensor with long cores. However, there is a tradeoff of sensitivity versus power, as the entire core must be driven to saturation with a line current density  $I_{\text{exc}}/p_{\text{exc}} > H_{\text{sat}}$  over the area  $w_{\text{core}} \times l_{\text{core}}$ .

As the sensitivity is proportional to  $f_{\text{exc}}$ , it is advantageous to operate the sensor at a high excitation frequency. The operating frequency is limited by the frequency dependence of the relative permeability  $\mu_{\text{rel}}$ . The frequency dependence of  $\mu_{\text{rel}}$  is significantly improved by premagnetizing the ferromagnetic cores perpendicular to the direction of sensitivity. By this means, the permeability in the direction of sensitivity at low frequencies is reduced, but remains constant to frequencies in the Megahertz range.

Quantitative design considerations are detailed in [53]. A micrograph of the implemented microfluxgate sensor is shown in Figure 4.10. Its design parameters are given in Table 4.1.

### AHDL model of the microfluxgate sensor

```

module flat_ms_fg_7(DRVM, DRVP, FBM, FBP, PUM, PUP, COMPU, Hsig())
    node [V,I] DRVM;
    node [V,I] DRVP;
    node [V,I] FBM;
    node [V,I] FBP;
    node [V,I] PUM;
    node [V,I] PUP;
    node [V,I] COMPU;
    node [V,I] Hsig;

    {
        export real HEXC;
        export real H1;
        export real H2;
        export real HFB;
        export real B1;
        export real B2;
        export real OUT1;
        export real OUT2;
        parameter real KPU = 6.25e-9, KFB = 2500, KEXC=500;
        parameter real REXC = 100,RFB = 2800;

        analog {
            HEXC = KEXC*I(DRVP,DRVM);
            V(DRVP,DRVM) <- REXC*I(DRVP,DRVM);
            HFB = KFB*I(FBP,FBM);
            V(FBP,FBM) <- RFB*I(FBP,FBM);
            H1 = HEXC + V(Hsig) + HFB;
            H2 = -HEXC + V(Hsig) + HFB;
            B1 = 1 - 2/(1+exp(H1/4));
            B2 = 1 - 2/(1+exp(H2/4));
            OUT1 = 0.05*KPU*(dot(B1) + dot(B2));
            OUT2 = -0.05*KPU*(dot(B1) + dot(B2));
            V(PUP) <- OUT1 + V(COMPU);
            V(PUM) <- OUT2 + V(COMPU);
        }
    }
}

```

*Fig. 4.11 AHDL model for the microfluxgate sensor*

For a description within a circuit design environment, a model of the fluxgate sensor has been formulated in the analog hardware description language Spectre-HDL [30]. It is based on the following equations:

- The *excitation coil* is modeled as a purely resistive load:  $V_{\text{drv}} = R_{\text{drv}}I_{\text{drv}}$  due to its negligible inductance of 300nH.  
The current through the coil generates a magnetic field  $H_{\text{exc}} = k_{\text{exc}}I_{\text{drv}}$  in the ferromagnetic cores. The factor  $k_{\text{exc}}$  absorbs the excitation coil winding pitch  $p_{\text{exc}}$  and the efficiency of coupling the magnetic field into the cores.
- The *feedback coil* is also considered a purely resistive load with  $V_{\text{fb}} = R_{\text{fb}}I_{\text{fb}}$ . Its magnetic field in the cores is described by  $H_{\text{fb}} = k_{\text{fb}}I_{\text{fb}}$ .
- The nonlinear *magnetization of the ferromagnetic cores* is described by a sigmoid function for which the saturation induction  $B_{\text{sat}} = 1$  and the zero field permeability  $\mu = B'(H = 0) = 1$  are normalized. For the two cores that are magnetized in opposite directions, the equations are:

$$B_1 = \tanh\left(\frac{H_1}{8}\right) \text{ with } H_1 = H_{\text{sig}} + H_{\text{fb}} + H_{\text{exc}} \text{ and}$$

$$B_2 = \tanh\left(\frac{H_2}{8}\right) \text{ with } H_2 = H_{\text{sig}} + H_{\text{fb}} - H_{\text{exc}}. \quad (4.41)$$

- The *output voltage* induced in the series connected pickup coils is proportional to the time derivative of the magnetic induction in both ferromagnetic cores. The constant of proportionality absorbs the effective permeability  $\mu_{\text{eff}}\mu_0$ , the core cross section, the number of pickup coil windings, and the efficiency of coupling the flux into the pickup coils. The induced voltage is centered around the voltage  $V_{\text{com}}$  at the center tap of the series connected pickup coils:

$$V_{\text{pu+}} = V_{\text{com}} + 0.05k_{\text{pu}}\left(\frac{dB_1}{dt} + \frac{dB_2}{dt}\right) \text{ and}$$

$$V_{\text{pu-}} = V_{\text{com}} - 0.05k_{\text{pu}}\left(\frac{dB_1}{dt} + \frac{dB_2}{dt}\right). \quad (4.42)$$

The source text of the SpectreHDL model of the fluxgate sensor is shown in Figure 4.11.

## 4.4 Circuitry for an integrated microfluxgate system

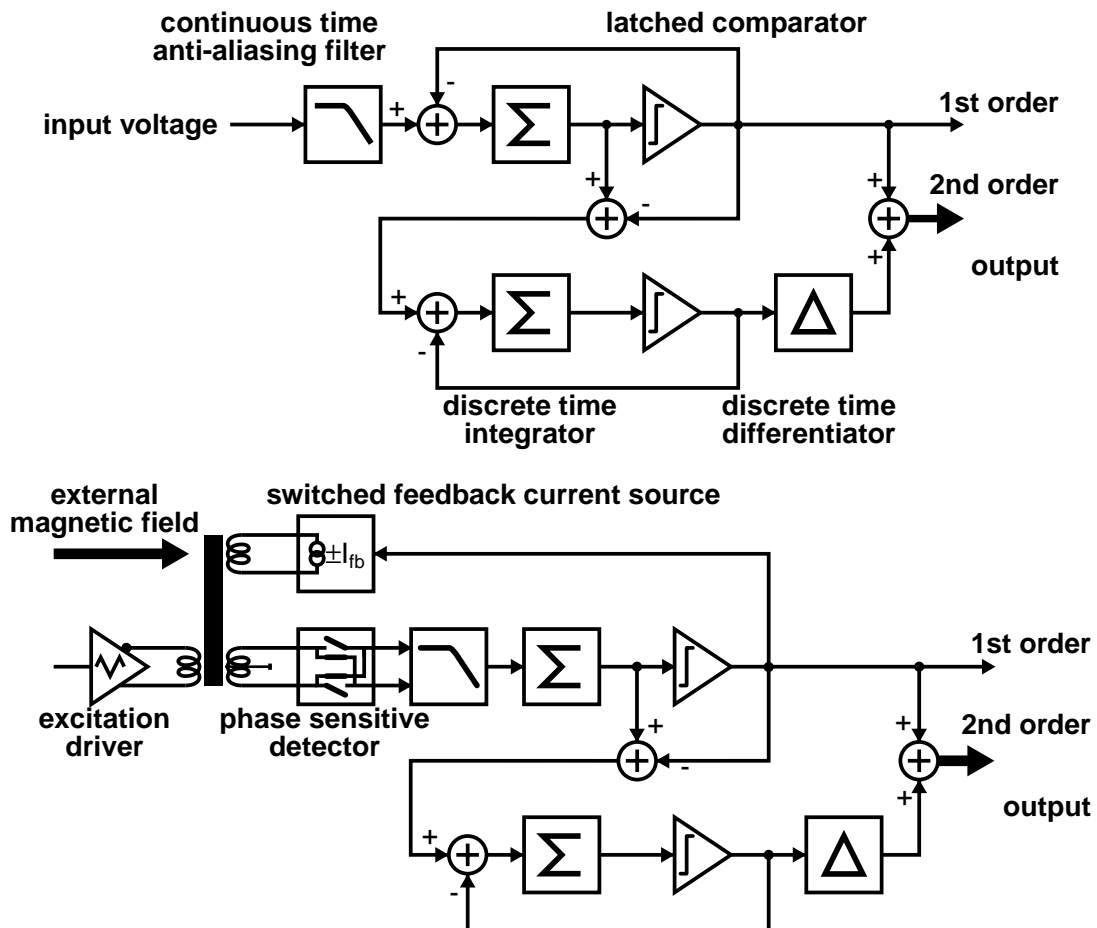
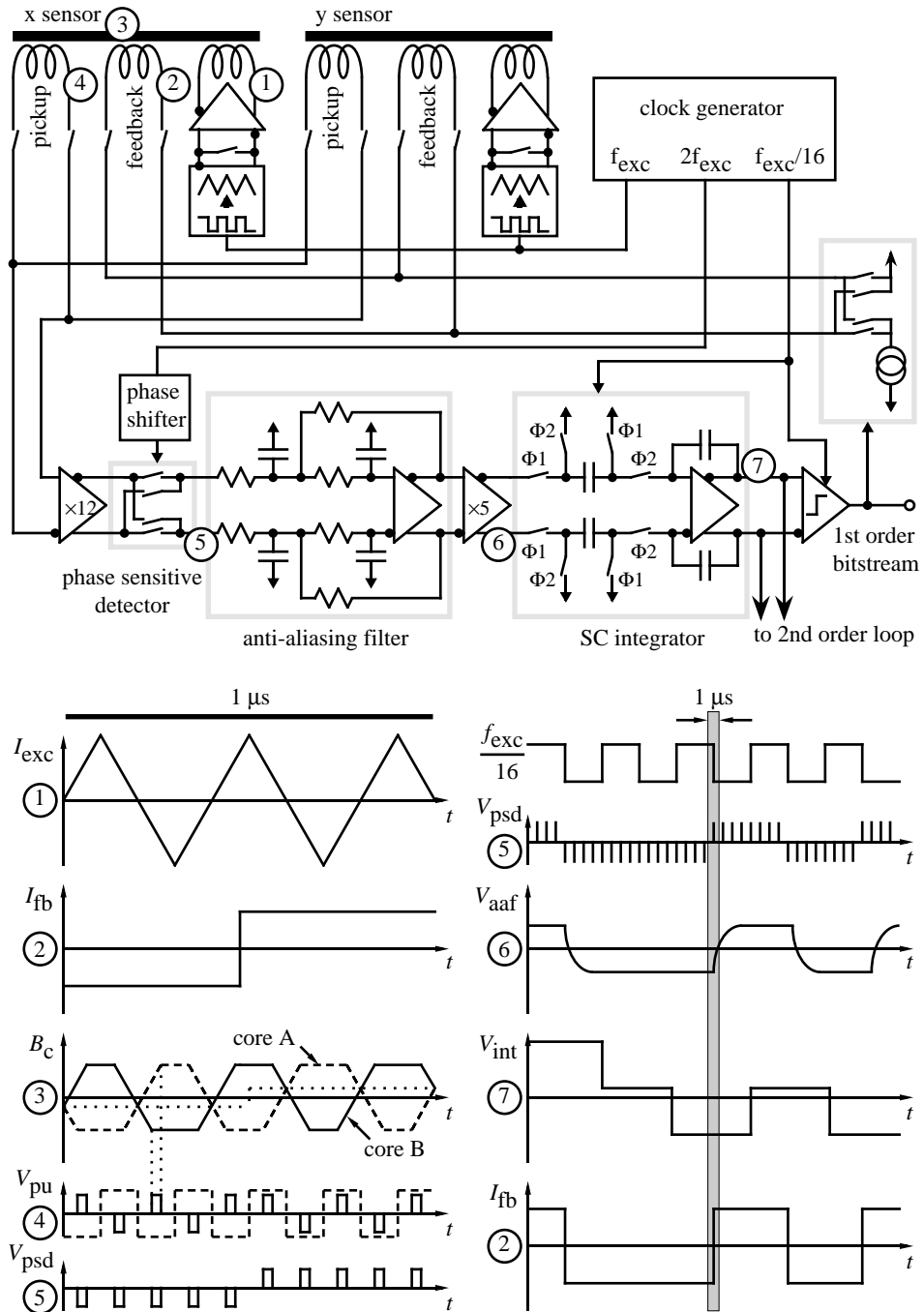


Fig. 4.12 Block diagram of a conventional 1-1 MASH  $\Sigma\Delta$  analog to digital converter (top) and of the integrated microfluxgate system with feedback in the magnetic field domain (bottom)

In the magnetometer that has been implemented, the fluxgate sensor is embedded in a 1-1 cascade  $\Sigma\Delta$  modulator. The feedback of the loop containing the sensor is closed in the magnetic field domain. In conventional analog to digital converters, the analog input signal is filtered outside the feedback loop to avoid aliasing by the sampled-time integrator. For the integrated fluxgate magnetometer, the anti-aliasing filter as well as the extraction circuitry for the signal proportional to the magnetic field are included within the feedback loop. Block diagrams of a conventional analog to digital converter and the fluxgate magnetometer with digital output are shown in Figure 4.12.



*Fig. 4.13 Schematic of the first order  $\Sigma\Delta$  modulator with embedded fluxgate sensors (top) and signals in the loop (bottom).*

A more detailed block diagram of the first order  $\Sigma\Delta$  modulator loop with the embedded fluxgate sensors is shown in Figure 4.13. The fluxgate sensor for the direction of magnetic induction to be measured is selected by connecting the

pickup and feedback coils to the front-end amplifier and the feedback current source of the  $\Sigma\Delta$  modulator loop, respectively, and by activating the excitation driver assigned to the sensor.

A triangular-wave excitation current  $I_{\text{exc}}$  with frequency  $f_{\text{exc}} = 2.5$  MHz is applied to the excitation coil. This current causes a magnetic induction  $B_c$  which periodically saturates the ferromagnetic cores. Due to the differential sensor arrangement, odd signal components from the excitation current to the sensor output voltage  $V_{\text{pu}}$  are suppressed. Any magnetic induction applied to the sensor causes an asymmetry leading to the generation of alternating pulses in the sensor output signal at  $2f_{\text{exc}}$ . Pulse width and sign are a measure of magnitude and direction of the total applied magnetic induction  $B_{\text{tot}}$ , which is composed of the external magnetic induction  $B_{\text{ext}}$  to be measured and the feedback magnetic field  $B_{\text{fb}}$  generated by the feedback coil current  $I_{\text{fb}}$ . A phase sensitive detector operating at frequency  $2f_{\text{exc}}$ , followed by a second order low-pass filter, generates a voltage  $V_{\text{aaf}}$  proportional to the total magnetic induction  $B_{\text{tot}}$  from the sensor output  $V_{\text{pu}}$ .

The low-pass filter serves two purposes:

- it demodulates the field dependent component of the sensor output voltage  $V_{\text{pu}}$ , and
- it prevents aliasing of signal components from harmonics of the sensor excitation frequency  $f_{\text{exc}}$  into the  $\Sigma\Delta$  loop.

To ensure proper operation of the  $\Sigma\Delta$  loop, the delay from feedback current  $I_{\text{fb}}$  to the filter output  $V_{\text{aaf}}$  must be kept small. All these conditions are met by setting the cut-off frequency of the low-pass filter to  $f_{\text{exc}} / 4$ . The demodulated and filtered sensor voltage  $V_{\text{aaf}}$  is sampled and integrated by a switched capacitor integrator. The integrated voltage  $V_{\text{int}}$  is digitized to a bitstream by a latched comparator. The feedback loop is closed by a switched current source providing current  $I_{\text{fb}}$  to the feedback coil.

The excitation and demodulation frequencies for the fluxgate sensors as well as the sampling frequency for the  $\Sigma\Delta$  modulator are derived from a master clock oscillator by a digital divider chain. The fluxgate sensor is excited at 16 times the sampling frequency of the  $\Sigma\Delta$  modulator to allow sufficient settling of the low-pass filtered demodulated sensor signal in response to the feedback magnetic field before it is sampled by the switched capacitor integrator.

#### 4.4.1 $\Sigma\Delta$ Modulator Topology

The  $z$  domain equations for the first order  $\Sigma\Delta$  modulator with the embedded flux-gate sensor are

$$e_1 = \frac{2z^{-1/2}}{1-z^{-1}} \cdot S \cdot (H_{\text{ext}} - F_1 y_1) \text{ and } y_1 = K_1 z^{-1/2} (e_1 + q_1), \quad (4.43)$$

the equations for the cascade  $\Sigma\Delta$  modulator are

$$e_2 = \frac{1}{1-z^{-1}} (z^{-1/2} e_1 - (F_2 \cdot (y_1 + z^{-1/2} y_2))) \text{ and } y_2 = K_2 z^{-1/2} (e_2 + q_2); \quad (4.44)$$

with the sensitivity  $S$  (unit  $\text{V}/\text{Am}^{-1}$ ) of the sensor plus analog signal conditioning, the feedback gains  $F_1$  (unit  $\text{Am}^{-1}$ ) and  $F_2$  (unit  $\text{V}$ ), the quantization gains  $K_1$  and  $K_2$  (units  $\text{V}^{-1}$ ), and the quantization noises  $q_1$  and  $q_2$  (units  $\text{V}$ ).

The transfer functions of the first loop are

$$\begin{aligned} y_1 &= \frac{2K_1 S \cdot z^{-1}}{1 - (2K_1 SF_1 - 1)z^{-1}} H_{\text{ext}} + \frac{K_1 \cdot z^{-1/2} (1 - z^{-1})}{1 - (2K_1 SF_1 - 1)z^{-1}} q_1 \text{ and} \\ e_1 &= \frac{2S \cdot z^{-1/2}}{1 - (2K_1 SF_1 - 1)z^{-1}} H_{\text{ext}} - \frac{2K_1 SF_1 \cdot z^{-1}}{1 - (2K_1 SF_1 - 1)z^{-1}} q_1. \end{aligned} \quad (4.45)$$

For the transfer functions of the second loop, we get

$$\begin{aligned} y_2 &= \frac{K_2 \cdot (z^{-1} e_1 - F_2 \cdot z^{-1/2} y_1)}{1 - (K_2 F_2 - 1)z^{-1}} + \frac{K_2 \cdot z^{-1/2} (1 - z^{-1})}{1 - (K_2 F_2 - 1)z^{-1}} q_2 \text{ and} \\ e_2 &= \frac{z^{-1/2} e_1 - F_2 y_1}{1 - (K_2 F_2 - 1)z^{-1}} + \frac{K_2 F_2 \cdot z^{-1}}{1 - (K_2 F_2 - 1)z^{-1}} q_2. \end{aligned} \quad (4.46)$$

The *total* quantization gains adjust themselves such that the loop gain is unity [93], viz.

$$K_1 = \frac{1}{2SF_1} \text{ and } K_2 = \frac{1}{F_2}. \quad (4.47)$$

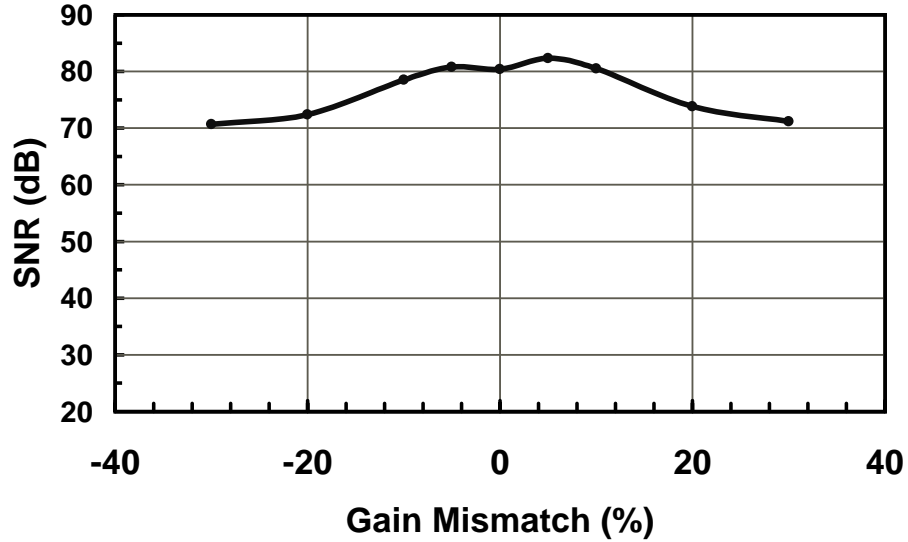


Fig. 4.14 MATLAB simulation result of SNR of filtered second-order bitstream output as a function of gain mismatch of the two  $\Sigma\Delta$  modulator loops.

If the open loop gains in the two  $\Sigma\Delta$  modulators match, i. e.,

$$F_2 = 2SF_1, \quad (4.48)$$

the transfer functions are

$$\begin{aligned} y_1 &= \frac{z^{-1}}{F_1} H_{\text{ext}} + \frac{z^{-1/2}(1-z^{-1})}{2SF_1} q_1, \quad e_1 = 2S \cdot z^{-1/2} H_{\text{ext}} - z^{-1} q_1, \\ y_2 &= -\frac{z^{-1}}{2SF_1} q_1 + \frac{z^{-1/2}(1-z^{-1})}{2SF_1} q_2 \text{ and } e_2 = -z^{-1/2} q_1 - z^{-1} q_2. \end{aligned} \quad (4.49)$$

so that in the sum

$$z^{-1/2}y_1 + (1 - z^{-1})y_2 = \frac{z^{-3/2}}{F_1}H_{\text{ext}} + \frac{z^{-1/2}(1 - z^{-1})^2}{2SF_1}q_2, \quad (4.50)$$

the quantization noise  $q_1$  of the first modulator is cancelled, while the quantization noise  $q_2$  of the cascade modulator is differentiated twice, yielding second order high pass characteristics.

The two cascaded  $\Sigma\Delta$  modulators measure different physical quantities: one measures magnetic induction, while the other measures voltage. For ideal cancellation of the quantization noise  $q_1$  of the first  $\Sigma\Delta$  modulator, (4.48) should hold exactly.

Figure 4.14 shows the influence of gain mismatch to the signal-to-noise ratio (SNR) of a second-order bitstream. The result has been obtained by MATLAB [94] behavioral simulation of the cascaded  $\Sigma\Delta$  modulator and low-pass filtering at 1/100 of the sampling frequency. The simulation shows that the SNR of the digital output is insensitive to open loop gain mismatch of less than 5%.

#### 4.4.2 Fluxgate excitation driver

The excitation coil of the fluxgate can be assumed to be a purely resistive load, as its inductance is negligible. The driving circuit for the excitation coil consists of a rectangle to triangle waveform converter, as shown in Figure 4.15, and a pair of class AB amplifiers according to [95], one of which is shown in Figure 4.16. The class AB amplifier consists of a complementary source follower stage that determines the quiescent current of the amplifier of 8.5 mA, in parallel with a class B stage consisting of output transistors in common source configuration with local feedback.

#### 4.4.3 Pick-up coil front end amplifier

The first stage of the readout circuitry is a fully differential front end amplifier. It amplifies the differential signal from the pickup coils, while common mode components, that might be introduced by asymmetric capacitive coupling from the excitation coils, are suppressed. The topology shown in Figure 4.17 has been

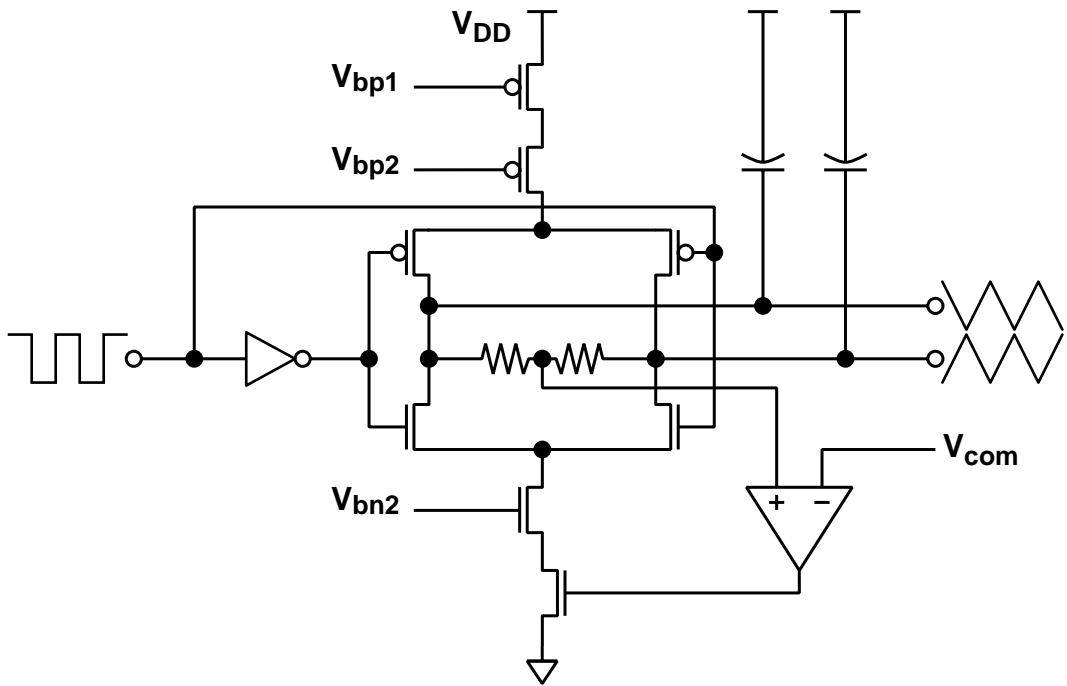


*Fig. 4.15 Rectangle to triangle waveform converter for generation of the fluxgate excitation signal*

implemented. It consists of a fully differential amplifier as shown in Figure 4.18 with a fixed gain of 12 set by resistive feedback. To obtain a high input impedance, two unity gain buffers have been added at the inputs. The entire configuration has a 3 dB bandwidth of 20 MHz, which is accomplished by using a total current of 1 mA for the main amplifier and 250  $\mu$ A for each of the unity gain input buffers.

#### 4.4.4 Phase shifter and cross-coupled switch

The amplified signal from the pickup coils is demodulated by a cross-coupled switch operating at twice the excitation frequency for the microfluxgate sensors. To allow the adjustment of the phase of the demodulator with respect to the excitation waveform for optimal sensitivity, the waveform controlling the cross-coupled switch is delayed by the phase shifter circuit shown in Figure 4.19. The phase shifter consists of a string of inverters whose output current is limited by adjustable current sinks and sources driving capacitances. At the output, standard digital inverters restore the rectangular waveform with rail-to-rail signal swing. The

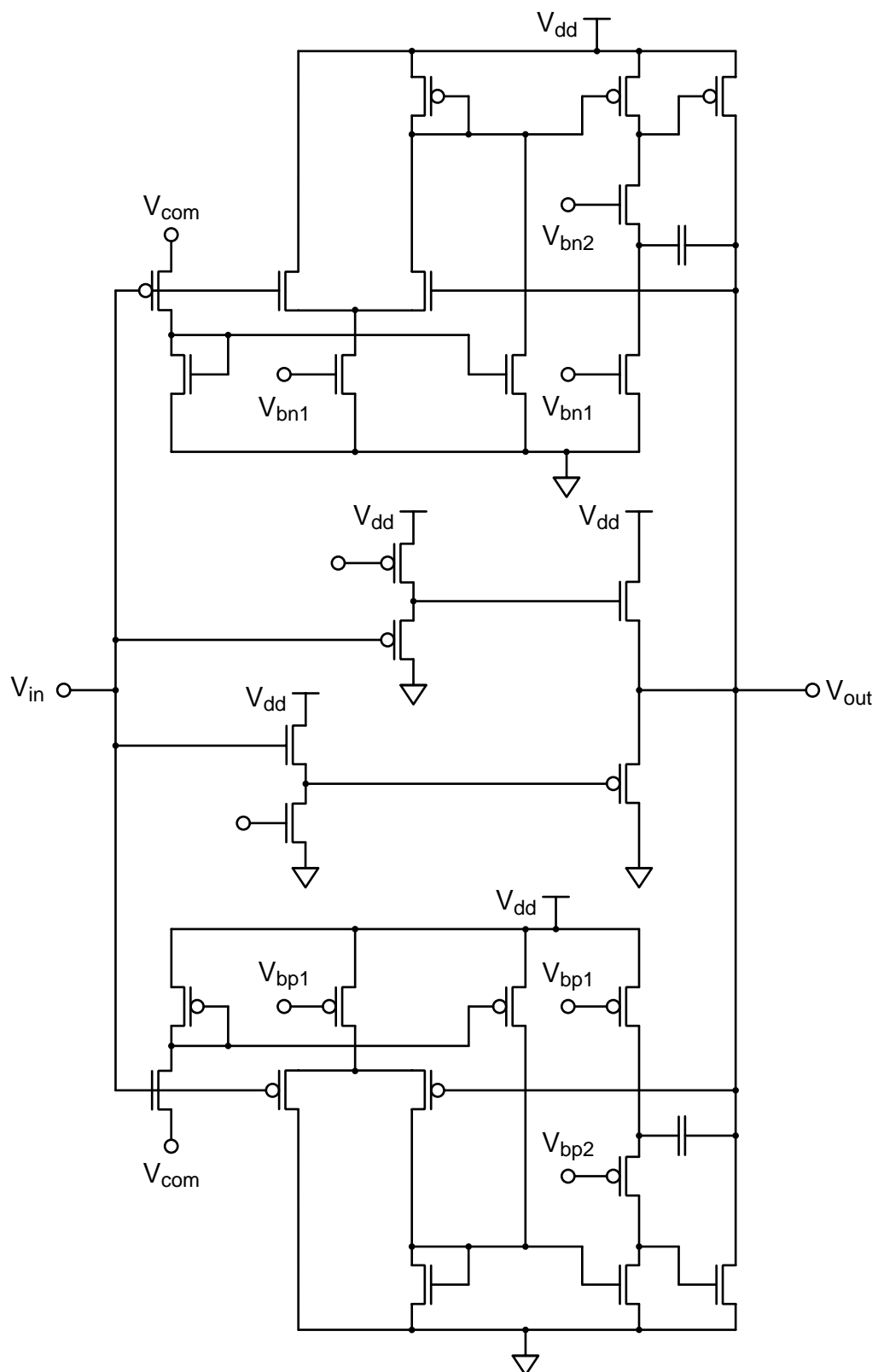


Fig. 4.16 Class AB coil excitation driver (one of two branches)

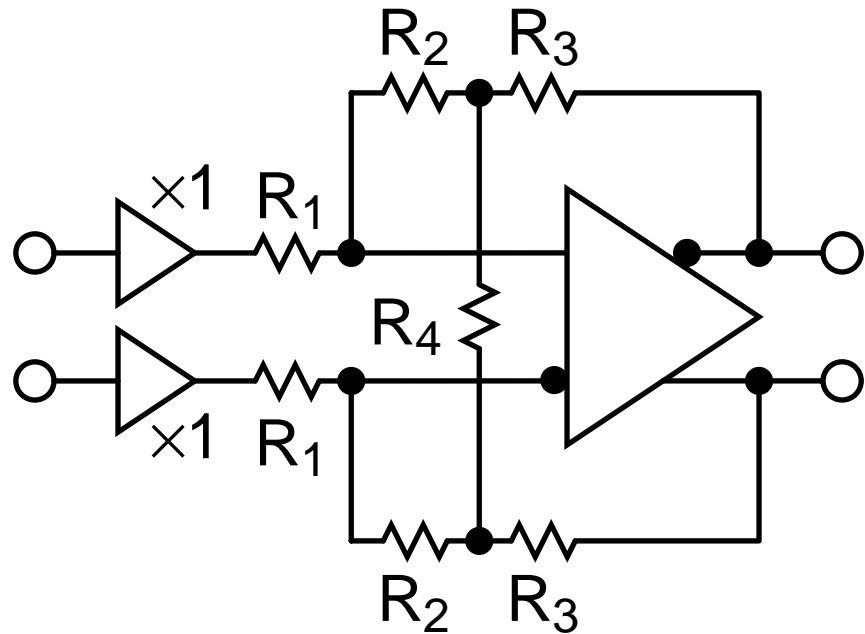


Fig. 4.17 Schematic of front-end amplifier arrangement

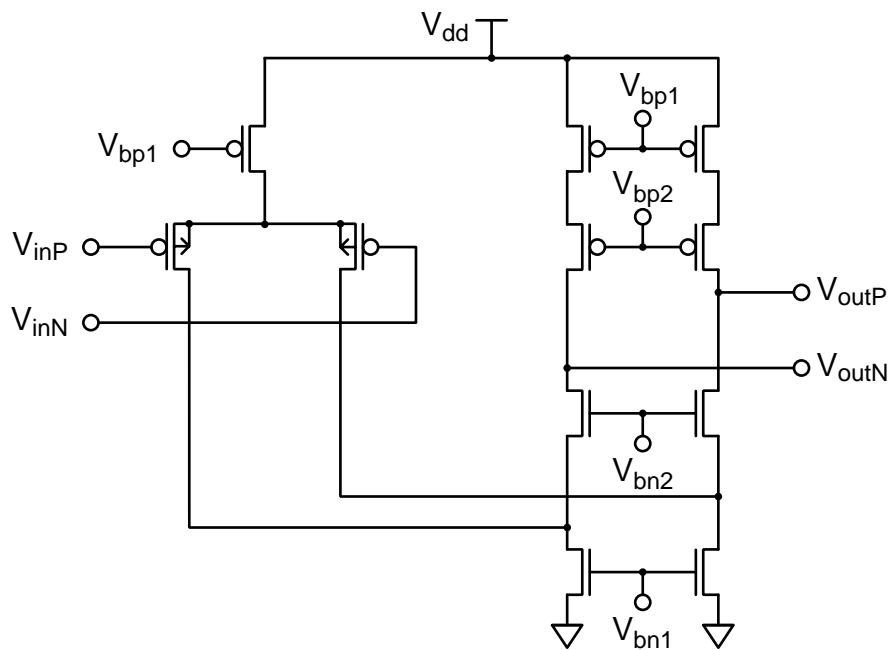
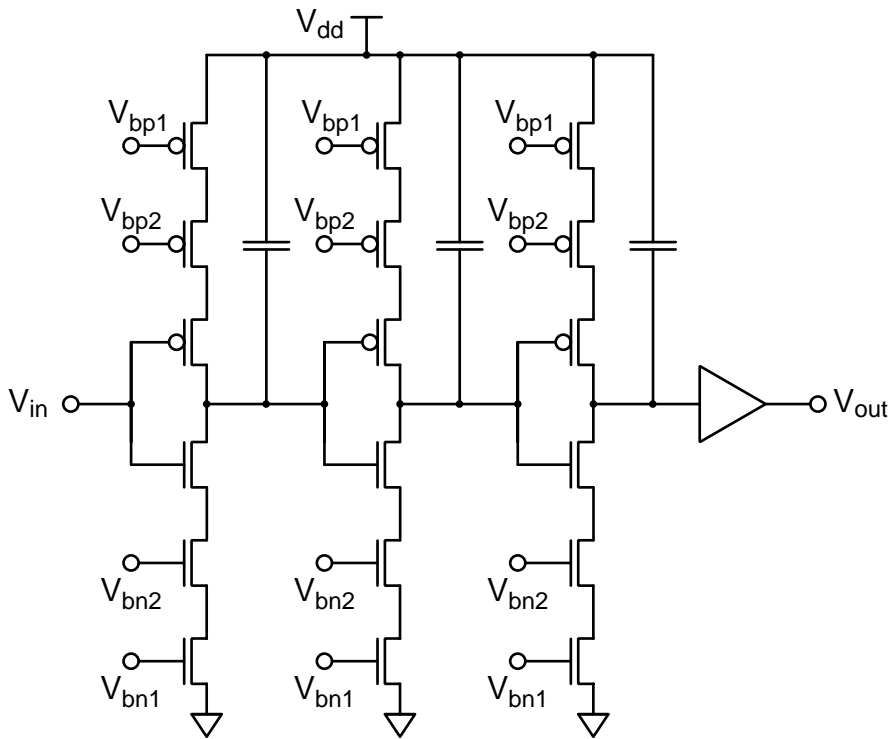


Fig. 4.18 Fully differential folded cascode amplifier used in front end and switched capacitor integrator stages. Common mode feedback is implemented by adjusting  $V_{bn1}$ .



*Fig. 4.19 Phase shifter for delay of the demodulating waveform. The delay can be trimmed by setting the bias voltages of the current sources and sinks.*

phase shifter consists of three delay elements to allow a delay of more than half a period of the demodulating waveform.

#### 4.4.5 Anti-aliasing filter

A continuous-time low-pass filter prevents harmonics of the fluxgate sensor excitation frequency from entering the sampled-time section of the  $\Sigma\Delta$  modulator, where they would cause aliasing. The topology of the second order low-pass filter is shown in Figure 4.20. Its transfer function is

$$\frac{V_{\text{out}}}{V_{\text{in}}} = \frac{A}{A+2} \left( \frac{1}{1 + s \frac{4}{\sqrt{A+2}} \frac{RC}{\sqrt{A+2}} + s^2 \left( \frac{RC}{\sqrt{A+2}} \right)^2} \right). \quad (4.51)$$

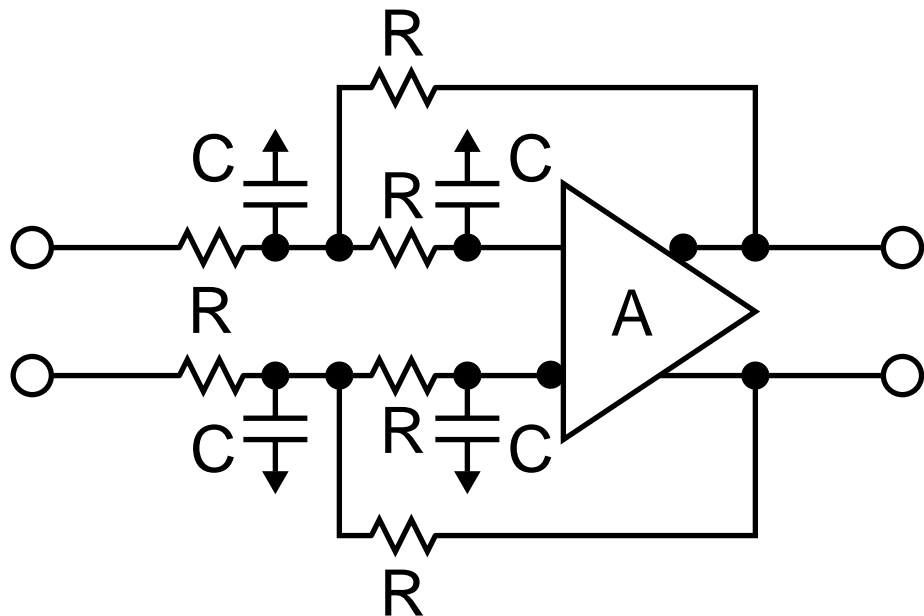


Fig. 4.20 Anti-aliasing filter

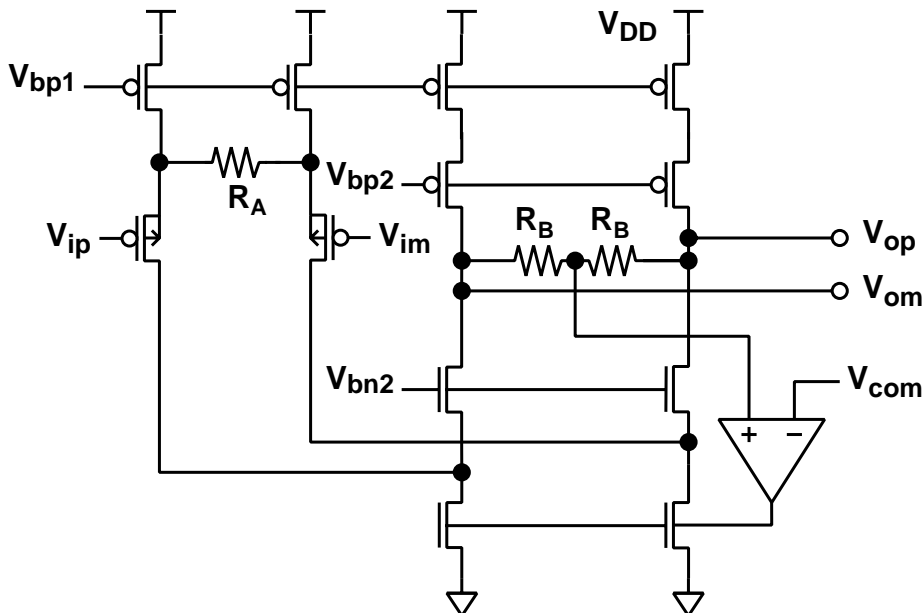


Fig. 4.21 Fully differential fixed gain amplifier used in the anti-aliasing filter

To obtain Butterworth filter characteristics (maximum passband flatness) [96], the coefficient  $4/\sqrt{A+2}$  is set to  $\sqrt{2}$  by choosing a gain of  $A = 6$  for the fixed gain amplifier. The corner frequency of the anti-aliasing filter is set to  $f_c = 450$  kHz

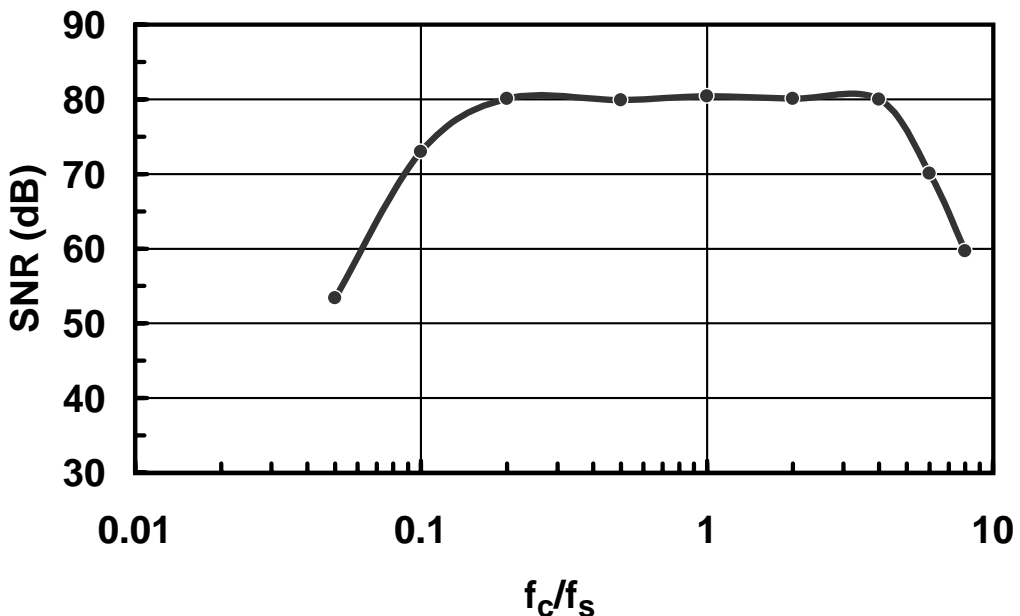


Fig. 4.22 SNR of the sensor interface with MASH  $\Sigma\Delta$  A/D converter as a function of the anti-aliasing filter cutoff frequency, obtained by MATLAB simulation.

by the choice of  $R = 100 \text{ k}\Omega$  and  $C = 10 \text{ pF}$ . The DC gain of the anti-aliasing filter is 0.75. A second fixed gain amplifier, as shown in Figure 4.21, provides additional gain for a total DC gain of 4.5.

A MATLAB behavioral simulation of the SNR of the second-order bitstream, low-pass filtered at 1/100 of the sampling frequency for different ratios  $f_c/f_s$  of the anti-aliasing filter corner frequency to the sampling frequency of the  $\Sigma\Delta$  modulator is shown in Figure 4.22. It indicates that the filter cutoff frequency can be chosen in the range of  $0.2f_s \dots 4f_s$  without degrading the SNR of the  $\Sigma\Delta$  modulator.

#### 4.4.6 Sampled-time integrators

The noise shaping in the main  $\Sigma\Delta$  modulator is performed by parasitic insensitive switched capacitor integrators, as shown in Figure 4.23.

The integrator of the cascade  $\Sigma\Delta$  modulator has three differential inputs:

1. the integrator output of the main  $\Sigma\Delta$  modulator  $e_1$ ,

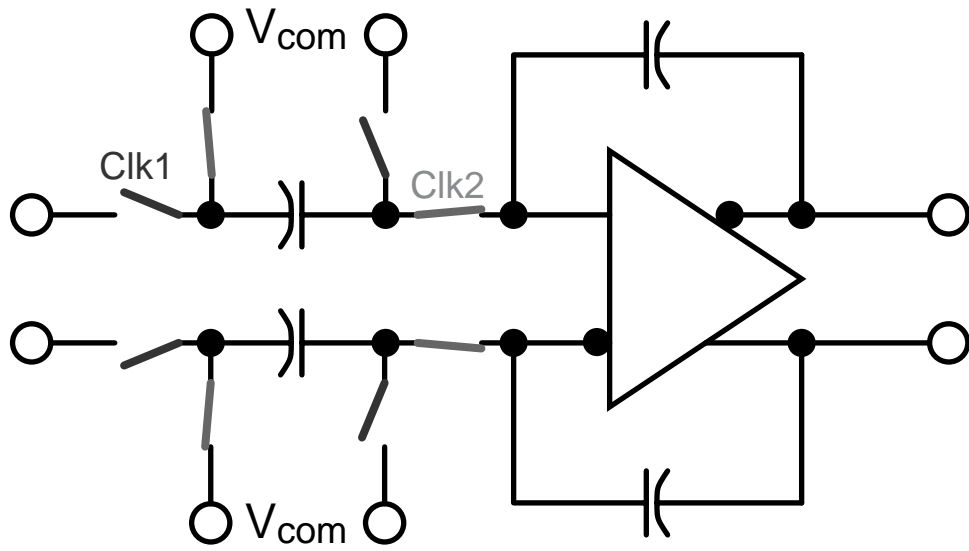


*Fig. 4.23 Switched capacitor integrator used in main  $\Sigma\Delta$  modulator*

2. the quantized output of the main  $\Sigma\Delta$  modulator  $y_1$ ,
3. the quantized output of the cascade  $\Sigma\Delta$  modulator  $y_2$ .

The amplitude of the quantized signals  $y_1$  and  $y_2$ , and thus the open loop gain of the cascade  $\Sigma\Delta$  modulator is set by a differential reference voltage  $F_2 = V_{\text{refp}} - V_{\text{refn}}$ . The polarity of these signals is inverted by reversing the switching sequence at the input of the coupling capacitors. For perfect matching of the open loop gains of the  $\Sigma\Delta$  modulators,

$$V_{\text{refp}} - V_{\text{refn}} = S \cdot k_{\text{fb}} \cdot I_{\text{fb}}, \quad (4.52)$$

with the DC sensitivity  $S$  of the fluxgate sensor plus preamplifier, demodulator and anti-aliasing filter to magnetic fields, and the feedback efficiency  $k_{\text{fb}}I_{\text{fb}}$ , which is explained in Section 4.4.8.

The amplifiers are fully differential folded cascode amplifiers with switched capacitor common mode feedback (see Figure 4.18).

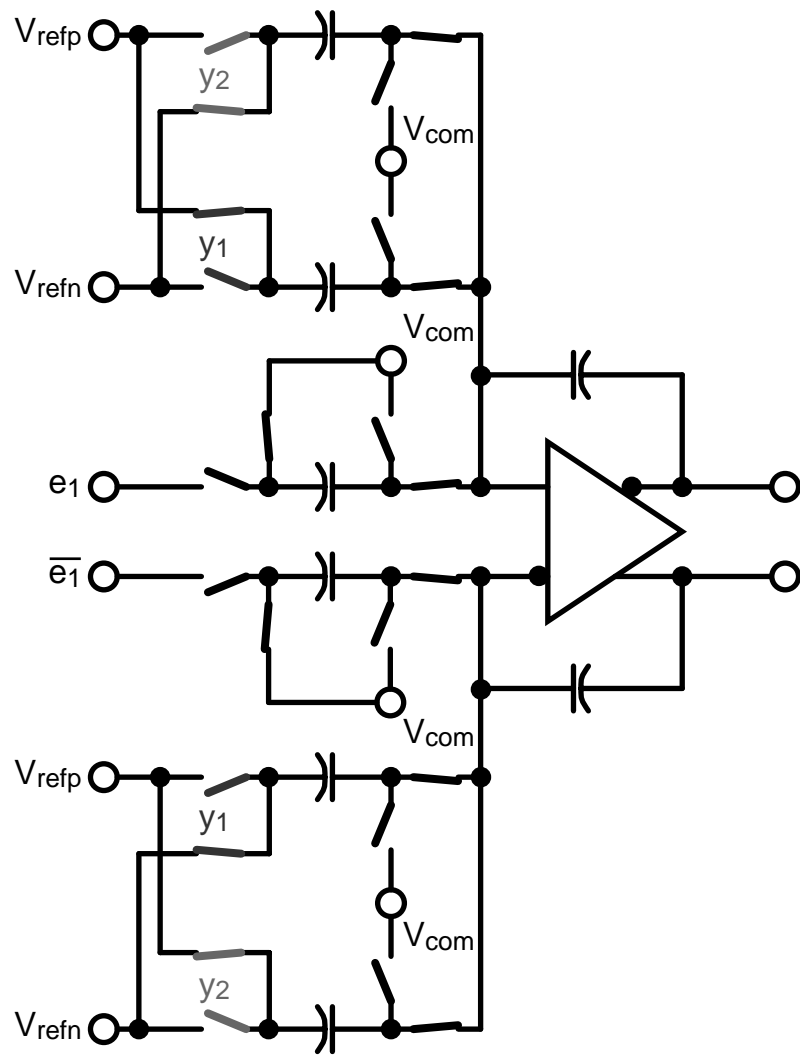


*Fig. 4.24* Switched capacitor integrator used in cascade  $\Sigma\Delta$  modulator with one analog differential input ( $e_1$ ) and two digital inputs for the quantized signals  $y_1$  and  $y_2$ . The gain of the cascade loop is set by the reference voltage  $F_2 = V_{\text{refp}} - V_{\text{refn}}$ ; the polarity of the signal is controlled by the switching sequence.

#### 4.4.7 Comparator

For the digitization of the integrated signal, a latched comparator as described in [98] is used. It is shown in Figure 4.25. The comparator consists of a differential input stage, a combination of nmos and pmos flip-flops, and a CMOS output latch. Its operation is controlled by the non-overlapping clocks Clk1 and Clk2. While Clk1 is high and Clk2 is low, the nmos and pmos flip-flops are forced to a

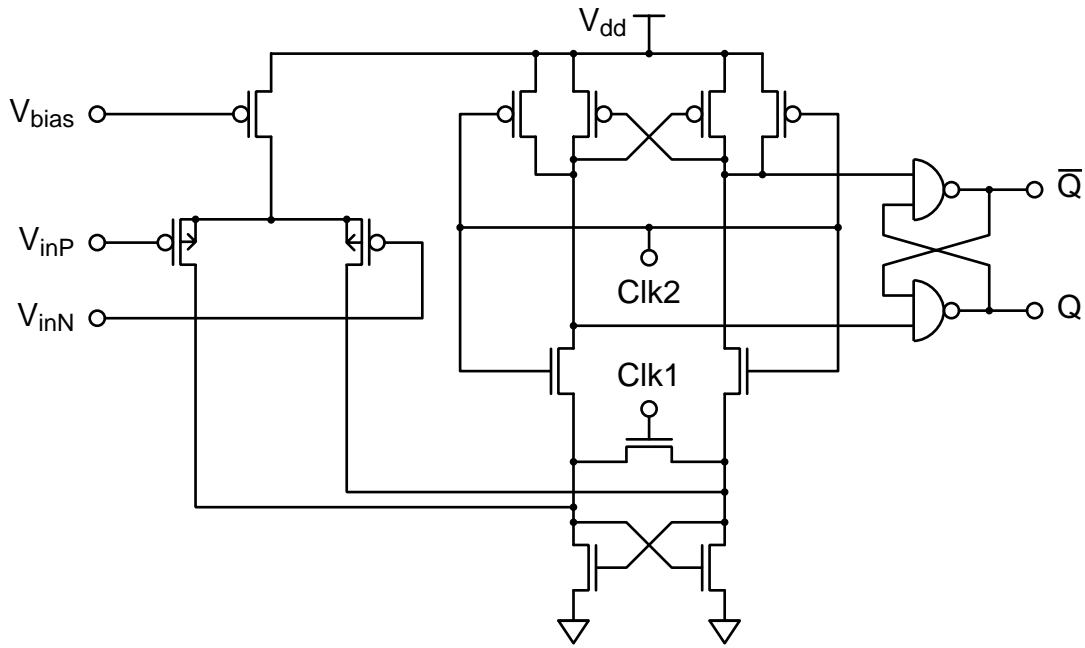


*Fig. 4.25 Schematic of latched comparator used as 1-bit quantizer*

state in which the branch currents are equal. When  $Clk2$  is high and  $Clk1$  is low, the current imbalance due to the input stage is amplified by the positive feedback of the nmos and pmos flip-flops and transferred to the output latch. The active edge for sampling the input signal is the falling edge of  $Clk2$ .

#### 4.4.8 Feedback current source

Feedback in the  $\Sigma\Delta$  modulator with the embedded fluxgate is provided by a constant current source that drives the feedback current  $I_{fb}$  through the feedback coil of the fluxgate sensor. The feedback effectivity is given by a factor  $k_{fb}$  times the feedback current, determined by the pitch of the feedback coil  $p_{fb}$  (see Table 4.1) and a factor  $\eta_{fb}$  representing the fraction of the feedback magnetic flux that is coupled into the cores:

$$F_1 \equiv \frac{H_{fb}}{y_1} = \frac{\eta_{fb}}{p_{fb}} I_{fb} \equiv k_{fb} I_{fb}. \quad (4.53)$$

The feedback current source is dimensioned for a current of up to  $I_{fb} = 2.5$  mA.

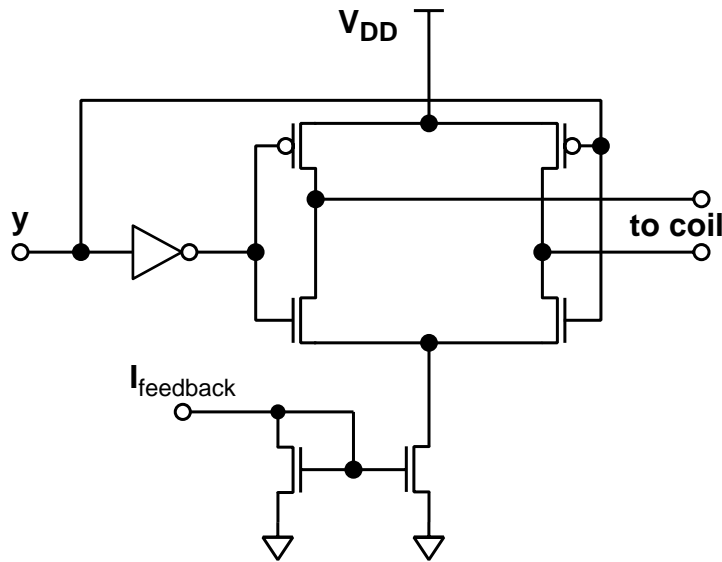


Fig. 4.26 Feedback current source

#### 4.4.9 Timing generator

The clock signals for the fluxgate sensor excitation and demodulation as well as the timing control signals for the cascade  $\Sigma\Delta$  modulator are generated by digital logic.

#### 4.4.10 Auxiliary circuit: monitor buffer

To monitor analog signals at different points in the  $\Sigma\Delta$  loop, namely

- at the input of the comparator (signal 7 in Figure 4.13)
- at the input of the integrator (signal 6)
- at the output of the front-end amplifier<sup>1</sup>,

buffered test outputs have been added

The output buffers are implemented as pair of single-ended class AB amplifiers as shown in Figure 4.27.

---

1. This positioning, instead of monitoring signal 5, was done on special request by the person responsible for the design of the sensor. The cross-coupled switch can be turned off simply by setting the charging currents in the phase shifter (see Figure 4.19) to zero.

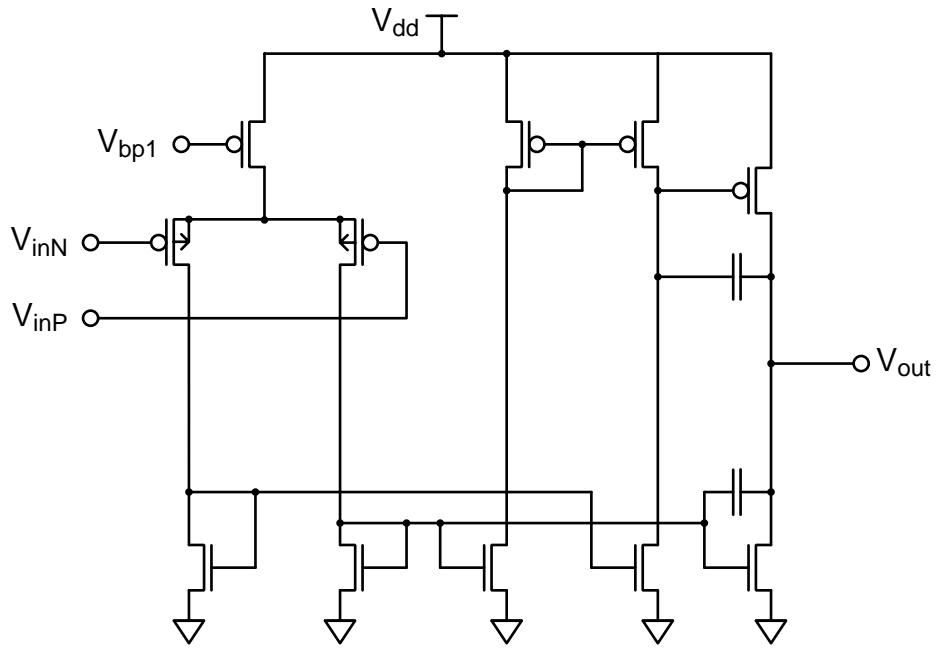


*Fig. 4.27 Buffer amplifier for analog monitor signals*

## 4.5 Measurements

The integrated microfluxgate system has been implemented in the  $0.8 \mu\text{m}$  CYE double-poly, double-metal CMOS process by Austria Mikrosysteme International AG [55]. A micrograph of the device is shown in Figure 4.28.

Measurements have been carried out at a sensor excitation frequency of 2.5 MHz, corresponding to a  $\Sigma\Delta$  modulator sampling frequency of 156.25 kHz. As none of the building blocks has been optimized for power consumption, the power consumption is relatively high (300...350 mW).

The sensitivity to magnetic induction  $S/\mu_0$ , measured at the input of the integrator (point 6 in Figure 4.13) is in the range of 400 V/T to 680 V/T, corresponding to a sensitivity of the unamplified fluxgate signal of 7...12 V/T. A cross-sensitivity of 3% to magnetic induction perpendicular to the direction of sensitivity has been measured.

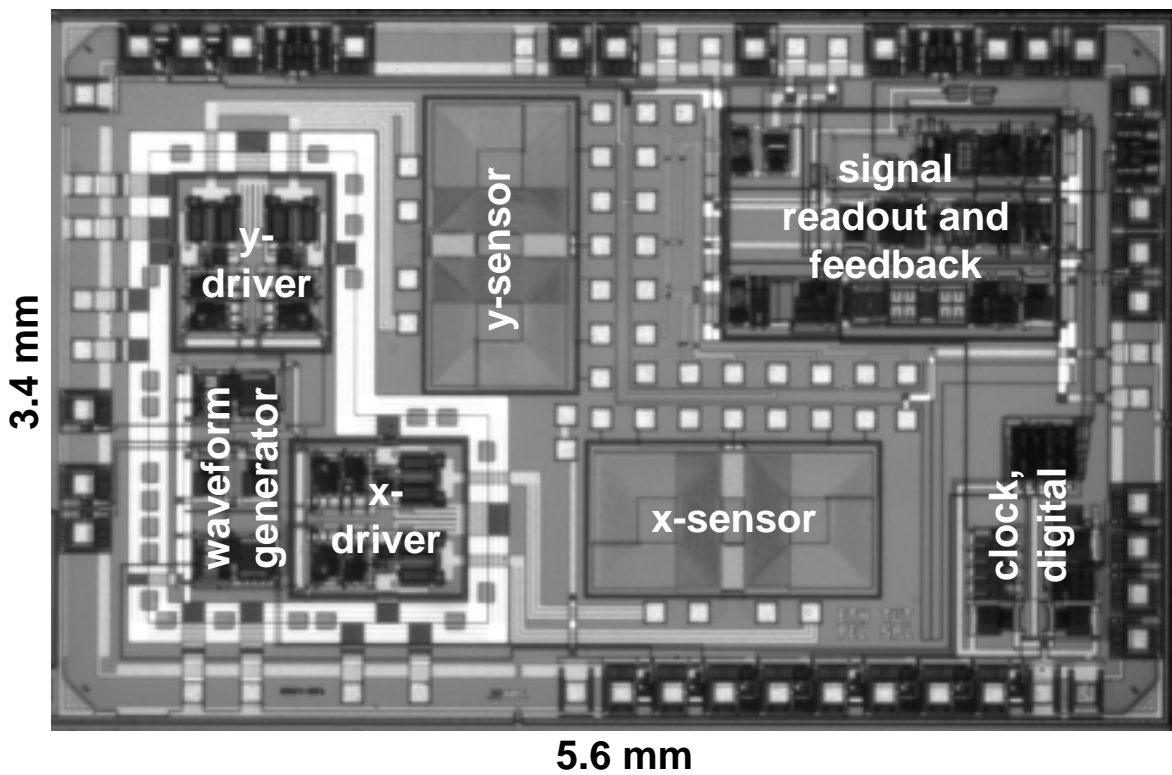


Fig. 4.28 Micrograph of implemented integrated microfluxgate system

As can be seen from (4.50) and (4.53), the sensitivity of the magnetometer is proportional to the feedback current:

$$\frac{1}{F_1} = \frac{1}{k_{fb} I_{fb}}. \quad (4.54)$$

In terms of magnetic induction, the sensitivity is characterized by

$$\frac{B_{fb}}{y_1} = \mu_0 \frac{H_{fb}}{y_1} = \mu_0 k_{fb} I_{fb} \equiv \beta I_{fb}. \quad (4.55)$$

As the output resolution of the fluxgate magnetometer depends on the choice of the decimation filter for the bitstream, the system is best characterized by the *feedback conversion factor*  $\beta$ . Even though the sensitivity varies by a factor of 1.7, the feedback conversion factor varies only by 10%, between 36  $\mu\text{T}/\text{mA}$  and 40  $\mu\text{T}/\text{mA}$ . This corresponds to a coupling efficiency of the feedback field of

<i>Quantity</i>	<i>Symbol</i>	<i>Value</i>
Supply current	$I_{\text{supply}}$	120...140 mA
Analog sensitivity (after low pass filter)	$\frac{S}{\mu_0}$	$400 \dots 680 \frac{\text{V}}{\text{T}}$
Equivalent sensitivity of the fluxgate sensor		$7 \dots 12 \frac{\text{V}}{\text{T}}$
Directional cross-sensitivity	$\frac{S_{\perp}}{S_{\parallel}}$	typ. 3%
Analog nonlinearity		4...10 $\mu\text{T}$
Analog feedback effectivity		$14.8 \dots 28.5 \frac{\text{V}}{\text{A}}$
Feedback conversion factor	$\beta$	$36 \dots 40 \frac{\mu\text{T}}{\text{mA}}$
	$k_{\text{fb}}$	$28 \dots 32 \frac{\text{A/m}}{\text{A}}$
Feedback coupling efficiency	$\eta_{\text{fb}}$	0.13...0.15
Digital full scale range		$\pm 36 \dots 40 \frac{\mu\text{T}}{\text{mA}}$
Nonlinearity		typ. 3%
Equivalent nonlinearity within $ B_{\text{ext}}  < 50 \mu\text{T}$		< 1.5 $\mu\text{T}$
Equivalent angle error for $ B_{\text{ext}}  = 50 \mu\text{T}$		4°

Tab. 4.2 Measured parameters of the integrated microfluxgate system

$$\eta_{\text{fb}} = 0.13 \dots 0.15.$$

The full scale digital output range of the loop corresponds to a digital output of  $|y_1| = 1$ , so, due to (4.49), it is given by  $\pm \beta I_{\text{fb}}$ .

The measurement results are summarized in Table 4.2.

## Acquisition and digital filtering of the bitstream

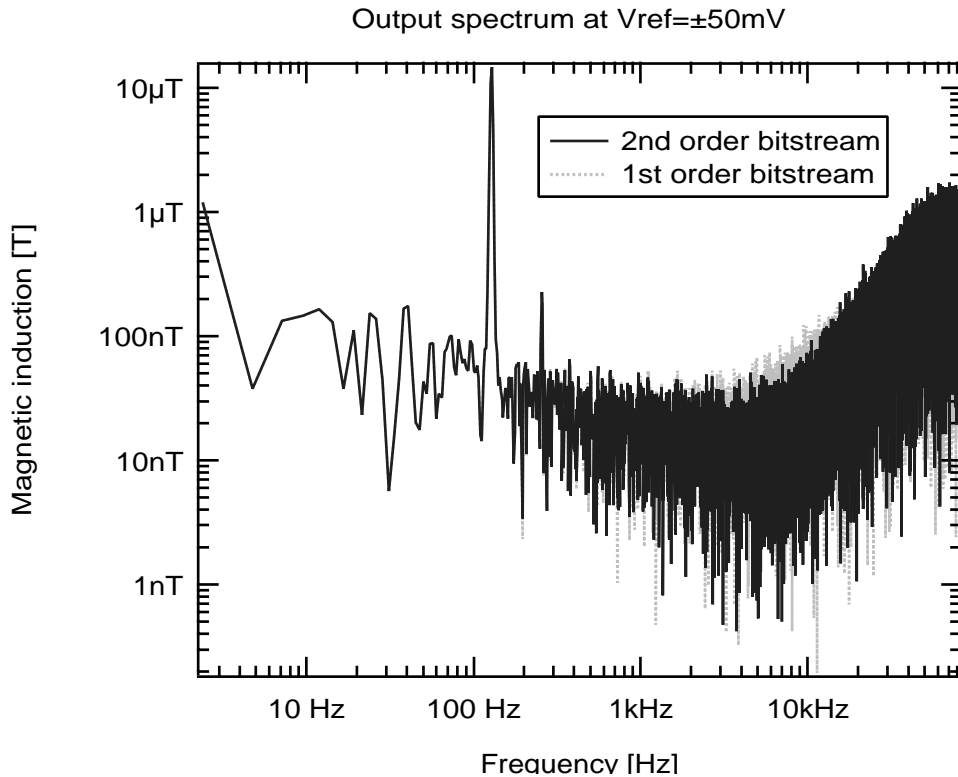


*Fig. 4.29 Spectra of the first and second order bitstream outputs in response to a sinusoidal magnetic induction of  $B_{\text{ext}} = 22 \mu\text{T}$  at a frequency of 127 Hz, measured with the sensor for y direction*

The output signal delivered by the implemented circuit is either a 1-bit first order bitstream, or a 2-bit second order bitstream. To obtain a digital number proportional to the magnetic induction, the bitstreams must be decimated. For this purpose, a versatile data acquisition program has been implemented. Long sequences ( $2^{15} \dots 2^{20}$  samples) of both the first and second order bitstream are simultaneously sampled and read into the main memory of a Macintosh 9600/200 computer by Direct Memory Access, using a National Instruments DIO 6533 digital I/O interface card [100]. Sampling is synchronized with the  $\Sigma\Delta$  modulator clock. The LabView [101] signal processing virtual instruments were used to implement a variety of decimation filters, windowing, and spectral analysis of the bitstream.

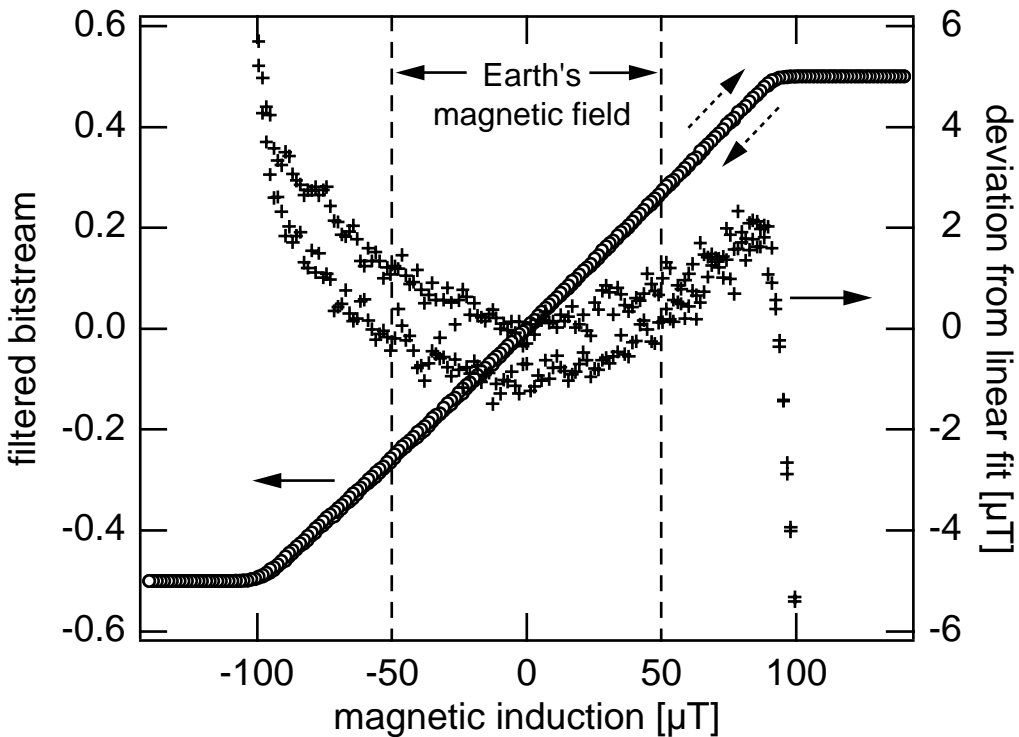


*Fig. 4.30 System response to magnetic induction parallel to the Y sensor*

A FFT spectrum of simultaneously acquired first and second order bitstreams in response to a sinusoidal magnetic induction of  $B_{\text{ext}} = 22 \mu\text{T}$  is shown in Figure 4.29. Due to an error in the simulation model used, the  $1/f$  noise in the continuous time building blocks described in sections 4.4.3 through 4.4.5 are much higher than expected (noise floor of  $3 \mu\text{V}/\sqrt{\text{Hz}}$  at the input of the integrator  $\oplus$  in Figure 4.13, with a corner frequency of  $f_{3\text{dB}} = 20 \text{ kHz}$  for the onset of  $1/f$  noise). This results in an equivalent noise level of  $880 \dots 1500 \text{ nT}/\sqrt{\text{Hz}}$  at 100 Hz.

Despite the high noise floor, the second order noise shaping of the cascade  $\Sigma\Delta$  modulator is discernible.

Eliminating the effects of the high noise floor by averaging over 50 repeated sweeps over the magnetic induction and the angle of rotation of a magnetic induction of  $50 \mu\text{T}$ , respectively, at a feedback current of  $I_{\text{fb}} = 2 \text{ mA}$ , Figures 4.30 and 4.31 have been obtained.

Within the maximum range of the Earth's magnetic field, the deviation from a linear response is less than  $1.5 \mu\text{T}$ .

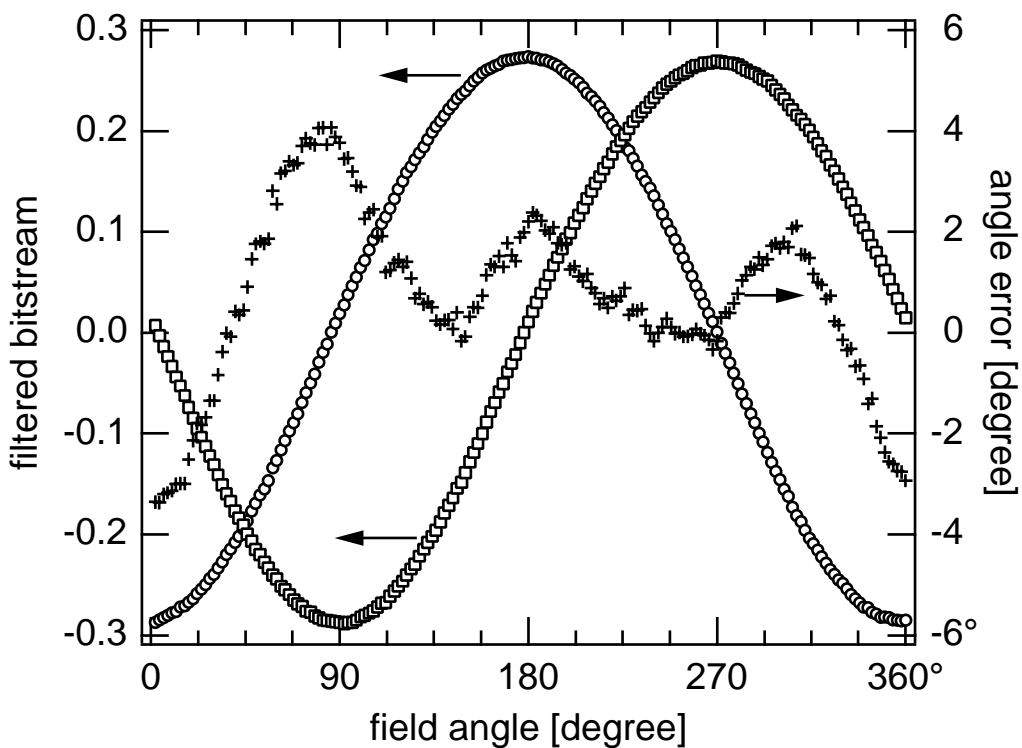


Fig. 4.31 System response to a rotating magnetic induction of  $B_{ext}=50 \mu T$

The maximal deviation of the measured angle error for a rotating magnetic induction of  $50 \mu T$  is  $4^\circ$ .

## 4 Integrated Microfluxgate System

---

---

# 5 Conclusion

In this thesis, contributions to integrate magnetic sensors together with standard industrial CMOS circuit technology have been made.

In Chapter 2, a modeling scheme to obtain compact SPICE equivalent circuit models of resistive sensors has been developed. While the primary purpose of the models is the description of Hall sensors within an integrated microsystem, functional interactions with other physical quantities can be introduced to the equivalent circuit models as well. This has been exemplified by describing the influence of mechanical stress to Hall sensors.

In Chapter 3, the Spinning Current method for offset compensated magnetic field measurements using Hall sensors has been investigated. It is shown that the Continuous Spinning method is a highly useful tool for sensor characterization using laboratory instruments. However, its usefulness for a circuit implementation is limited due to the amplification of sensor and circuit nonidealities inherent to the method. Based on these findings and on sensor models obtained by the methods developed in Chapter 2, an integrated Hall magnetometer has been developed that allows averaging of the signals a Hall sensor array. Even with only one Hall sensor, the measured residual offset of the system is equivalent to  $(43 \pm 7)\mu\text{T}$  at a linear output range of  $\pm 200$  mT.

An integrated microsystem to measure lower ranges of magnetic induction is presented in Chapter 4. It uses CMOS compatible microfluxgate sensors embedded in a  $\Sigma\Delta$  modulator to obtain digital output. The implemented system has a nonlinearity of less than  $1.5 \mu\text{T}$  in the range of  $\pm 50 \mu\text{T}$ . The angular resolution is better than  $4^\circ$ .

## 5 Conclusion

---

---

# 6 References

- [1] Shoji Kawahito, Introduction to Sensor Interface Circuits Using Oversampling Techniques, *course handout*, PEL 1996–1997
- [2] S. Kawahito, A. Yamasawa, S. Koga, Y. Tadokoro, K. Mizuno, O. Tabata, “Digital interface circuits using Sigma–Delta modulation for integrated micro–fluxgate magnetic sensors”, *Proc. 1996 IEEE International Symposium on Circuits and Systems*, vol. 4, pp. 340–343
- [3] S. Kawahito, Y. Sasaki, M. Ashiki, T. Nakamura, “Micromachined Solenoids for Highly Sensitive Magnetic Sensors, *1991 International Conference on Solid–State Sensors and Actuators (Transducers ’91)*, pp. 1077–1080
- [4] S. Kawahito, Y. Sasaki, M. Ishida, T. Nakamura, “A Fluxgate Magnetic Sensor with Micromachined Solenoids and Electroplated Permalloy Cores”, *1993 International Conference on Solid–State Sensors and Actuators (Transducers ’93)*, pp. 888–891
- [5] S. Kawahito, Y. Sasaki, H. Sato, T. Nakamura, Y. Tadokoro, “A fluxgate magnetic sensor with micro–solenoids and electroplated permalloy cores”, *Sensors and Actuators A43*, no. 1–3, pp. 128–134, May 1994
- [6] S. Kawahito, Y. Sasaki, H. Satoh, S. Choi, T. Nakamura, Y. Tadokoro, “Miniature fluxgate sensing element for high–performance integrated silicon magnetic sensors” *Sensors and Materials*, vol. 5 no. 5, pp. 241–251, 1994
- [7] S. Kawahito, H. Satoh, M. Sutoh, Y. Tadokoro, “Micro–Fluxgate Magnetic Sensing Elements using Closely–Coupled Excitation and Pickup Coils”, *1995 International Conference on Solid–State Sensors and Actuators (Transducers ’95)*, pp. 233–236
- [8] S. Kawahito, C. Maier, M. Schneider, M. Zimmermann, H. Baltes, A 2–D CMOS Microfluxgate Sensor System for Digital Detection of Weak

- Magnetic Fields, *IEEE Journal of Solid-State Circuits*, vol. 34 no. 12, pp. 1843–1851, December 1999
- [9] S. Kawahito, M. Yoshida, M. Sasaki, K. Umehara, D. Miyazaki, Y. Tadokoro, K. Murata, S. Doushou, A. Matsuzawa, “A CMOS Image Sensor with Analog Two-Dimensional DCT-Based Compression Circuits for One-Chip Cameras, *IEEE Journal of Solid-State Circuits*, vol. 32 no. 12, pp. 2030–2041, December 1997
- [10] R. P. Feynman, “There’s Plenty of Room at the Bottom”, reprinted in: *IEEE Journal of Microelectromechanical Systems*, vol. 1, no. 1, pp. 60–66, March 1992
- [11] R. P. Feynman, “Infinitesimal Machinery”, *IEEE Journal of Microelectromechanical Systems*, vol. 2, no. 1, pp. 4– March 1993
- [12] D. E. Ricken, W. Gessner (eds.), *Advanced Microsystems for Automotive Applications 99*, Springer, Heidelberg 1999
- [13] Special Issue on Integrated Sensors, Microactuators&Microsystems (MEMS), *Proceedings of the IEEE*, vol. 86, no. 8, August 1998
- [14] C. S. Smith, “Piezoresistance Effect in Germanium and Silicon”, *Physical Review*, vol. 94, no. 1, April 1954
- [15] J. J. Wortman, J. R. Hauser, R. M. Burger, “Effect of Mechanical Stress on p–n Junction Device Characteristics”, *Journal of Applied Physics*, vol. 35, no. 7, July 1964
- [16] K. Matsuda, Y. Kanda, K. Suzuki, “Second-Order Piezoresistance Coefficients of n-Type Silicon”, *Japanese Journal of Applied Physics*, vol. 28, no. 10, pp. L 1676–L 1677, October 1989
- [17] S. Middelhoek, “Quo vadis silicon sensors?”, *Sensors and Actuators A41–42*, pp. 1–8, 1994
- [18] K. E. Petersen, “Silicon as Mechanical Material”, *Proceedings of the IEEE*, vol. 70, no. 5, May 1982
- [19] A. V. Chavan, K. D. Wise, “A Batch-Processed Vacuum-Sealed Capacitive Pressure Sensor”, *The 9th International Conference on*

---

*Solid-State Sensors and Actuators (Transducers '97)*, vol. 2,  
pp. 1449–1452, Chicago, 1997

- [20] “Low Cost  $\pm 2 \text{ g}/\pm 10 \text{ g}$  Dual Axis iMEMS Accelerometers with Digital Output”, *ADXL202/ADXL210 Data Sheet*, Analog Devices, Inc., Norwood, MA, 1999
- [21] D. J. Harrison, C. Skinner, S. B. Cheng, G. Ovcirk, S. Attiya, N. Bings, C. Wang, J. Li, P. Thibault, W. Lee, “From Micro-Motors to Micro-Fluidics: The Blossoming of Micromachining Technologies in Chemistry, Biochemistry and Biology”, *The 10th International Conference on Solid-State Sensors and Actuators (Transducers '99)*, Sendai, 1999
- [22] J. Bühler, “Deformable Micromirror Arrays by CMOS Technology”, *Diss. ETH No. 12139*, ETH Zürich, 1997
- [23] C. Kuratli, “Realization of Silicon Based Ultrasound Micro-Systems”, Diss. ETH No. 13202, ETH Zürich, 1999, printed in: *Series in Microelectronics*, vol. 86, Hartung-Gorre, Konstanz 1999
- [24] D. J. Smith, *HDL Chip Design*, Doone, Madison, Alabama 1996
- [25] Field programmable gate arrays, Xilinx Inc., <http://www.xilinx.com>
- [26] K. S. Kundert, *The Designer's Guide to SPICE&SPECTRE*, Kluwer, Boston 1995
- [27] D. P. Foty, *MOSFET Modeling with SPICE: Principles and Practice*, Prentice Hall, 1996
- [28] C. Enz, F. Krummenacher, E. Vittoz, “An Analytical MOS Transistor Model Valid in All Regions of Operation and Dedicated to Low Voltage and Low Current Applications”, *Analog Circuits and Signal Processing*, vol. 8, pp. 83–114, 1995
- [29] Y. Cheng et al., *BSIM3 Version 3.0 Manual*, Electronics Research Laboratory, University of California, Berkeley 1995
- [30] SpectreHDL, *online documentation*, Cadence Design Systems, Inc.
- [31] F. V. Fernandez, A. Rodriguez-Vazquez, J. L. Huertas, G. G. E. Gielen (eds.), *Symbolic Analysis Techniques*, IEEE Press, Piscataway 1997

- [32] E. Hennig, R. Sommer, M. Wiese, “Approximate symbolic pole/zero extraction using equation-based simplification driven by eigenvalue shift prediction”, *Proc. 1998 IEEE International Symposium on Circuits and Systems*
- [33] A. Nathan and H. Baltes, *Microtransducer CAD, Physical and Computational Aspects*, Wien, New York: Springer Verlag, 1999; Chapters 6,9.
- [34] M. Mayer, O. Paul, and H. Baltes, “Complete set of piezoresistive coefficients of CMOS n<sup>+</sup>-diffusion”. *Eighth Micromechanics Europe Workshop (MME’97)*, pp. 203–206
- [35] M. von Arx, “Thermal Properties of CMOS Thin Films”, *Diss. ETH No. 12743*, ETH Zürich, 1998
- [36] ISE TCAD Manuals, vol. 14: DESSIS–ISE; *ISE Integrated Systems Engineering AG*, Zurich 1997
- [37] S. Müller, “An object-oriented approach to multidimensional semiconductor device simulation”, *Diss. ETH No. 10734*, ETH Zürich, 1994
- [38] D. J. Erdman, D. J. Rose, G. B. Nifong, R. Subrahmanyam, S. Kendal, “CAzM—Circuit Analyzer with Macromodeling”, MCNC and Duke University, Durham NC, USA, 4.1 ed., 1991
- [39] M. J. Caruso, T. Bratland, C. H. Smith, R. Schneider, “A New Perspective on Magnetic Field Sensing”, *SENSORS*, December 1998
- [40] J. E. Lenz, “A Review of Magnetic Sensors”, *Proceedings of the IEEE*, vol. 78, no. 6, pp. 673–689, 1990
- [41] K. Mohri, “Micro magnetic sensor”, *Trans. Inst. Elect. Eng.*, vol. 116E, no. 1, pp. 7–10, 1996
- [42] F. Primdahl, “The fluxgate magnetometer”, *J. Phys. E: Sci. Instrum.*, vol. 12, pp. 241–253, 1979
- [43] T. Seitz, “Fluxgate Sensor in Planar Microtechnology”, *Sensors and Actuators A21–23*, pp. 799–802, 1990

- 
- [44] B. Sauer, R. Gottfried–Gottfried, T. Haase, H. Kück, “CMOS–compatible integration of thin ferromagnetic films”, *Sensors and Actuators A41–42*, pp. 582–584, 1994
  - [45] R. Gottfried–Gottfried, W. Budde, R. Jähne, H. Kück, B. Sauer, S. Ulbricht, U. Wende, “A miniaturized magnetic–field sensor system consisting of a planar fluxgate sensor and a CMOS readout circuitry”, *Sensors and Actuators A54*, pp. 443–447, 1996
  - [46] G. W. Day, A. H. Rose, “Faraday effect sensors: the state of the art”, *SPIE Proceedings*, vol. 985, p. 138, 1988
  - [47] M. N. Baibich, J. M. Broto, A. Fert, F. Nguyen Van Dau, F. Petroff, P. Etienne, G. Creuzet, A. Friederich, J. Chazelas, “Giant magnetoresistance in (001)Fe/(001)Cr magnetic superlattices”, *Physical Review Letters*, vol. 61, pp. 2472–2475, 1988
  - [48] *Sensors, A Comprehensive Survey*, ed. W. Göpel, J. Hesse, J. N. Zemel, vol. 5, “Magnetic Sensors”, ed. R. Boll, K. J. Overshott, Weinheim: VCH, 1989
  - [49] M. Metz, “Offset in CMOS Magnetotransistors — Analysis and Reduction”, *Diss. ETH No. 13275*, ETH Zürich, 1999
  - [50] E. H. Hall, “On A New Action of the Magnet on Electric Currents”, *American Journal of Mathematics*, vol. 2, Baltimore 1879
  - [51] R. S. Popovic, J. A. Flanagan, P. A. Besse, “The future of magnetic sensors”, *Sensors and Actuators A56*, pp. 39–55, 1996
  - [52] R. Steiner Vanha, “Rotary Switch and Current Monitor by Hall-Based Microsystems”, *Diss. ETH No. 13135*, ETH Zürich, 1999
  - [53] M. Schneider, “CMOS Magnetotransistor and Fluxgate Vector Sensors”, *PhD Thesis #12746*, ETH Zurich, 1999
  - [54] R. Steiner (Vanha), F. Kroener, T. Olbrich, R. Baresch, H. Baltes, “In–plane sensitive vertical Trench–Hall device”, *Technical Digest of International Electron Device Meeting (IEDM’98)*, p. 479, San Francisco 1998
-

- [55] Austria Mikrosysteme International AG, Unterpremsätten, Österreich; <http://www.amsint.com>
- [56] S. G. Taranow et al., “Method for the compensation of the non-equipotential voltage in the Hall voltage and means for its realization”, *German patent No. 2333080*, 1973
- [57] A. Bilotti, G. Monreal, R. Vig, “Monolithic Magnetic Hall Sensor Using Dynamic Quadrature Offset Cancellation”, *IEEE Journal of Solid-State Circuits*, vol. 32, pp. 829–836, June 1997
- [58] P. J. A. Munter, “Spinning-current method for offset reduction in silicon Hall plates”, *PhD Thesis*, Delft University of Technology, 1992
- [59] P. J. A. Munter, “A Low-offset Spinning-current Hall plate”, *Sensors and Actuators A21–23*, pp. 743–746, 1990
- [60] P. J. A. Munter, “Spatial symmetry of transduction effects in Hall plates”, *Sensors and Actuators A31*, pp. 206–209, 1992
- [61] S. (A. A.) Bellekom, P. J. A. Munter, “Offset reduction in spinning-current Hall plates”, *Sensors and Materials*, vol. 5 no. 5, pp. 253–263, 1994
- [62] S. Bellekom, “Origins of offset in conventional and spinning-current Hall plates”, *PhD Thesis*, Delft University of Technology, 1998
- [63] S. Bellekom, L. Sarro, “Offset reduction of Hall plates in three different crystal planes”, *1997 International Conference on Solid-State Sensors and Actuators (Transducers '97)*, pp. 233–236
- [64] S. Bellekom, L. Sarro, “Offset reduction of Hall plates in three different crystal planes”, *Sensors and Actuators A66*, pp. 23–28, 1998
- [65] A. Häberli, M. Schneider, P. Malcovati, R. Castagnetti, F. Maloberti, H. Baltes, “Two-Dimensional Magnetic Microsensor with On-Chip Signal Processing for Contactless Angle Measurement”, *IEEE Journal of Solid-State Circuits*, vol. 31, pp. 1902–1907, December 1996
- [66] C.-W. Ho, A. E. Ruehli, P. A. Brennan, “The Modified Nodal Approach to Network Analysis”, *IEEE Transactions on Circuits and Systems*, vol. CAS-22 no. 6 pp. 504–509, June 1975

- 
- [67] B. Johnson, T. Quarles, A. R. Newton, D. O. Pederson, A. Sangiovanni-Vincentelli, “SPICE3 Version 3e User’s Manual”, University of California, Berkeley, 1991; available from  
<http://www-cad.eecs.berkeley.edu:80/Software/software.html>
  - [68] Jan G. Korvink, “Discretization Methods”, Short Course Notes, *CAD for MEMS’97 International Workshop*, Zurich, Physical Electronics Laboratory, 1997
  - [69] A. M. Winslow, “Numerical Solution of the Quasilinear Poisson Equation in a Nonuniform Triangular Mesh”, *J. Comp. Phys.* vol. 1, p. 149, 1966
  - [70] D. A. Bittle, J. C. Suhling, R. E. Beaty, R. C. Jaeger, R. W. Johnson, “Piezoresistive Stress Sensors for Structural Analysis of Electronic Packages”, *Journal of Electronic Packaging*, vol. 113, pp. 203–215, September 1991
  - [71] H. Baltes and R. Castagnetti, *Semiconductor Sensors*, edited by S. M. Sze, Wiley Interscience, New York, 1994; Chapter 5 “Magnetic Sensors”, pp. 205-270
  - [72] ISE TCAD Manuals, vol. 6: SOLIDIS, MEMDRAW, utilities; *ISE Integrated Systems Engineering AG*, Zurich 1997
  - [73] W. H. Press, B. P. Flannery, S. A. Teukolsky, W. T. Vetterling, *Numerical Recipes in C*, Cambridge University Press, 1992
  - [74] H. H. Pham, A. Nathan, “Compact MEMS–SPICE Modelling”, *Sensors and Materials* vol. 10 no. 2, pp. 63–75, 1998
  - [75] C. A. Desoer, E. S. Kuh, *Basic circuit theory*, New York: McGraw Hill, 1969
  - [76] J. G. Korvink, A. M. Häberli, R. Castagnetti, P. Malcovati and H. Baltes, “Optimization of an Novel Split Current Hall Device by Numeric Modelling”, *European Solid–State Research Conference (ESSDERC)*, Den Haag, The Netherlands, pp. 67–70, 1995
  - [77] C. Maier, R. Steiner, M. Mayer, R. Vogt, H. Baltes, “SPICE Model for Mechanically Stressed Device/Circuit Simulation”, *Proc. 1998 IEEE International Symposium on Circuits and Systems*, vol. 6, pp. 405–408.
-

- [78] S. Wolfram, *The Mathematica Book*, Cambridge University Press, 1996
- [79] R. Steiner, A. Häberli, F.-P. Steiner, and H. Baltes, “Offset Reduction in Hall Devices by Continuous Spinning Current Method”. *1997 International Conference on Solid-State Sensors and Actuators (Transducers ’97)*, pp. 381–384
- [80] C. S. Smith, “Piezoresistance Effect in Germanium and Silicon”, *Phys. Rev.*, 94, pp. 42–49, 1954
- [81] R. Steiner, F. Kroener, T. Olbrich, R. Baresch, H. Baltes, “Trench–Hall device with deep contacts”, *10th International Conference on Solid–State Sensors and Actuators (Transducers ’99)*, vol. 1, p. 80, Sendai 1999
- [82] D. Johns, K. Martin, *Analog Integrated Circuit Design*, chapter 6, “Advanced Current Mirrors and Opamps”, fig. 6.7, page 265, J. Wiley&Sons, Toronto 1997
- [83] A. Häberli, “Compensation and Calibration of IC Microsensors, *Diss. ETH No. 12090*, page 50, Zürich 1997
- [84] R. Unbehauen, A. Cichocki, *MOS Switched-Capacitor and Continuous-Time Integrated Circuits and Systems*, Springer, Heidelberg 1989
- [85] F. C. Williams, S. W. Noble, “The fundamental limitations of the second–harmonic type of magnetic modulator as applied to the amplification of small d. c. signals”, *Proc. of the Institution of Electrical Engineers*, vol. 97 part II, February 1950
- [86] J. Brophy, “Fluctuations in Magnetic and Dielectric Solids”, chapter 1 in: *Fluctuation Phenomena in Solids*, ed. J. Burgess, Academic Press, New York 1965
- [87] R. C. Foss, “Second–Harmonic Magnetic Modulator Using Ferrite Core Materials”, *IEEE Transactions*, vol. 83, pp. 561–565, September 1964
- [88] C. Menolfi, Q. Huang, “A Low–Noise CMOS Instrumentation Amplifier for Thermoelectric Infrared Detectors”, *IEEE Journal of Solid–State Circuits*, vol. 32 no. 7, pp. 968–976, July 1997

- 
- [89] C. Menolfi, Q. Huang, “A Chopper Modulated Instrumentation Amplifier with First Order Low-pass Filter and Delayed Modulation Scheme”, *Proc. ESSCIRC’99*, pp. 54–57, Duisburg, September 1999
  - [90] S. H. Ardalani, J. J. Paulos, “An Analysis of Nonlinear Behavior in Delta-Sigma Modulators”, *IEEE Transactions on Circuits and Systems*, vol. CAS-34, pp. 593–603, June 1987; reprinted in *Oversampling Delta-Sigma Data Converters*, ed. J. C. Candy, G. Temes, IEEE Press, 1992
  - [91] W. A. Geyger, “The Ring-Core Magnetometer—A New Type of Second-Harmonic Flux-Gate Magnetometer”, *AIEE Transactions*, part I, vol. 81, pp. 65–73, March 1962
  - [92] M. Schneider, S. Kawahito, H. Baltes, “High Sensitivity CMOS MicroFluxgate Sensor”, *Dig. Tech. Papers, NanoSpace’98*, 1998
  - [93] M. Rebeschini, “The Design of Cascaded  $\Delta\Sigma$  ADCs”, in *Delta-Sigma Data Converters*, ed. S. Norsworthy, R. Schreier, G. Temes, chapter 6, IEEE Press, 1997
  - [94] MATLAB, *reference manual*, MathWorks Inc.
  - [95] J. A. Fisher, “A High-performance CMOS power amplifier”, *IEEE Journal of Solid-State Circuits*, vol. 20, pp. 1200–1205, December 1985
  - [96] P. Horowitz, W. Hill, *The Art of Electronics*, 2nd ed., Cambridge University Press, 1989
  - [97] K. R. Laker, W. M. C. Sansen, *Design of Analog Integrated Circuits and Systems*, chapter 7, McGraw-Hill, 1994
  - [98] G. M. Yin, F. Op’t Eynde, W. Sansen, “A high-speed CMOS comparator with 8-bit resolution”, *IEEE Journal of Solid-State Circuits*, vol. 27, pp. 208–211, February 1992
  - [99] D. Senderowicz, R. Castello, “Off-Chip Drivers”, *course handout: Special Techniques for High-Performance Op-Amp IC Design*, EPFL Lausanne, February 1997
  - [100] National Instruments Corporation, DIO 6533 User Manual, available on the www site <http://www.ni.com>, July 1997

## 6 References

---

- [101] National Instruments Corporation, LabView version 4.0 *User Manual*, January 1996

---

# Curriculum vitae

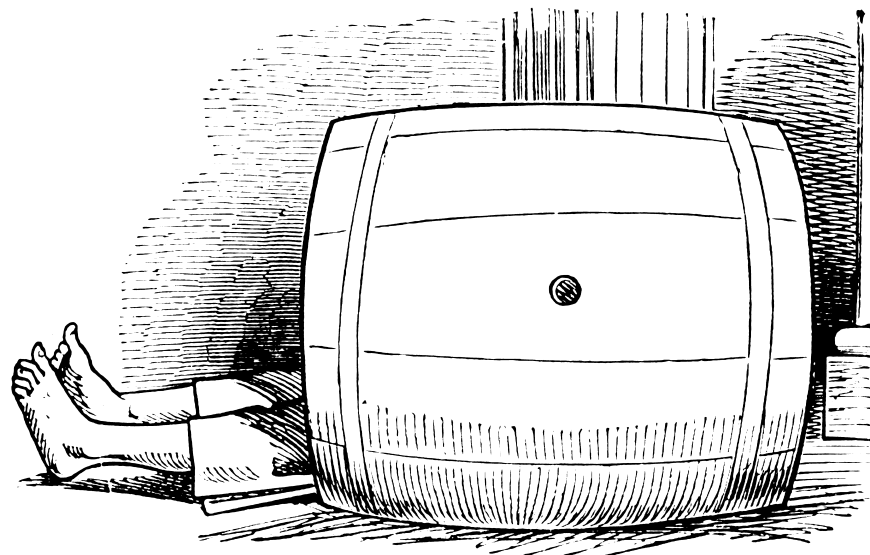
Christoph Hans Maier  
Born 06 January, 1967  
German Citizen

1985	<i>Design and implementation of an 8-bit microcomputer</i>
1986	Abitur (graduation from high school)
1986 – 1988	Civil service
1988 – 1995	Physics student at the University of Heidelberg
1989 – 1994	<i>Scholarship: Studienstiftung des deutschen Volkes</i>
1995	Diploma in physics at the University of Heidelberg
	Thesis on “Implementation of an active image tracking system for the visualization of water flow using particle tracing velocimetry”
1996 –	Doctoral work at the Physical Electronics Laboratory directed by Prof. Dr. Henry Baltes, on issues of circuit design for integrated microsensors
July 1997.	<i>Following completion of the circuit design for the integrated microfluxgate sensor, deassignment from circuit design to microsensor modeling</i>
2000	Completion of doctoral work at the Physical Electronics Laboratory.

# Curriculum vitae

---

# Quodlibet



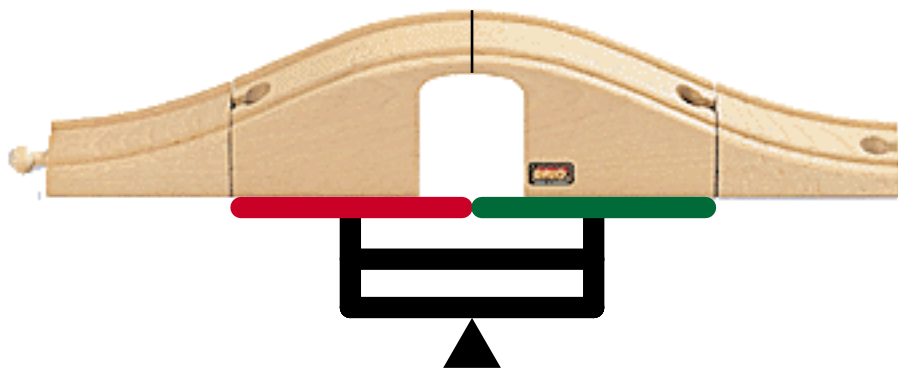


# 7 A Child's Play



Ever since about age 3, I enjoy playing with model railroads. To me, doing microsensor system and circuit design is essentially the same thing—maybe with a little fancier toys. I have been repeatedly told that this is considered Unprofessional by the standards of the Physical Electronics Laboratory. As this is just an unauthorized (*I insist*) Appendix, I invite you to join me while I indulge in a little game. Let's see where we get...

## 7.1 Balancing a bridge



Wooden toy railroads come with a lot of fancy tracks. For example, here's a bridge made of two ramps and a center piece [102]. Just for fun, let's cut the the center piece in the middle and put the halves on a scale.

## Will the scale be balanced?

— Ideally, yes.

## Why is the scale balanced?

— Because the bridge, and the center piece as well, are the *same* on the left and right sides.

Let's use a little math to tell what we mean by *same* here:

Let's go to the top of the bridge and measure how far we go from there.

We'll call the distance from the top, say,  $x$ , counting upward when we go right and downward when we go left. As we measure the height  $h(x)$  of the bridge at position  $x$  waypoint, we can put *sameness* into math as

$$h(x) = h(-x). \quad (7.1)$$

*Balancing* is also something that can be translated into math, namely an *equation*: The mass of the left half of the center piece must be the same as the mass of the right half:

$$m_{\text{left}} = m_{\text{right}}. \quad (7.2)$$

If we want, we can get even fancier and write the masses as integrals:

$$\rho \cdot w \cdot \int_{x_{\text{left}}}^0 h(x) dx = \rho \cdot w \cdot \int_0^{x_{\text{right}}} h(x) dx. \quad (7.3)$$

$\rho$  is the density of the wood,  $w$  is the width of the track, and  $x_{\text{left}}$  and  $x_{\text{right}}$  are the edges of the center piece.<sup>1</sup> These edges must be at the same distance from the top, i.e.,

$$x_{\text{left}} = -x_{\text{right}}, \quad (7.4)$$

---

1. To be exact, we should replace  $h(x)$  by  $h(x)-h_{\text{Tunnel}}(x)$ . But we're going to cheat and fill that hole, anyway...

such that

$$\int_{x_{\text{left}}}^0 h(x)dx = \int_0^{x_{\text{right}}} h(-x)dx. \quad (7.5)$$

So, if things are perfectly the same, according to (7.1), the halves balance.

Unfortunately, except in maths, things are never perfect. So, there's our next question:

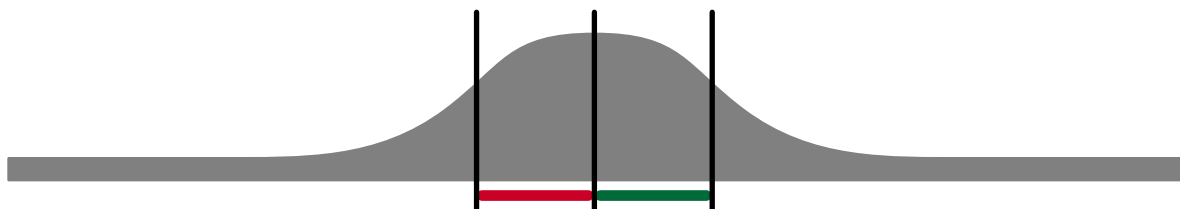
### What can cause imbalance?

—Generally, anything that causes the halves to have different weights, i.e., anything that might disturb equation (7.2).

Let's think about how we could make such a bridge. Imagine that we start with a long track, with a bump in the middle:



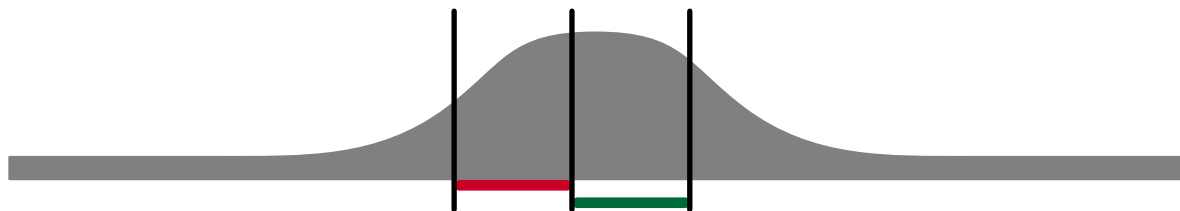
We could use a sawmill with three equally spaced blades to cut out the center pieces:



So far, everything is perfectly balanced. The middle saw blade hits the top perfectly, and the outer blades cut exactly where they belong (7.4).

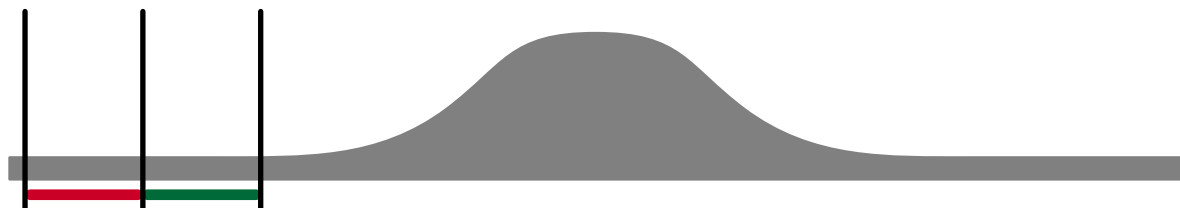
But we wanted to find out what can go *wrong*.

What happens if the saw blades don't hit exactly in the middle? Let's assume that the saw blades shift a little to the left:

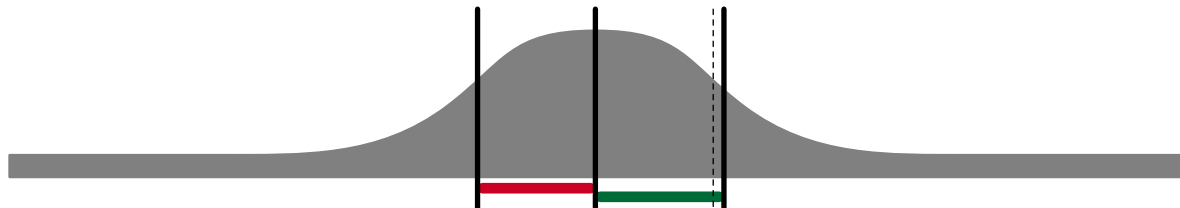


Now, the right piece we cut out is heavier!

If we miss the bump completely, the pieces are balanced again, though maybe not quite the way we wanted it:



There's yet something else that can make the pieces unbalanced. Imagine that one of the saw blades jiggles to the side a little:



So, we see that there are a few things that can cause imbalance. But we haven't yet answered the question:

### **How bad is the imbalance?**

Actually, these pictures give us a good idea how bad the imbalance is in different cases. *Try it!* Take a transparency, draw three parallel lines on it, and move it around on the first drawing of the bump. Just for fun, you can also try drawing the lines closer together or farther apart.

But eventually, to answer the question “*how bad?*” we need a number. To get numbers, we must use maths. Now, as first thing we should think about what we actu-

ally mean by “*bad*”. If we want to know how bad the imbalance is, we should look at

$$\Delta m = m_{\text{right}} - m_{\text{left}}. \quad (7.6)$$

Just for laziness, let’s measure  $w$  in units of “wooden railroad track gauge” and  $\rho$  in units of “wood density”. Thus, we get  $w \equiv 1$  and  $\rho \equiv 1$ .

After these definitions, let’s start with wiggling one of the blades. For the amount of wiggle, let’s use a fancy symbol:  $\xi$ . Then, we get for the mass of one piece

$$\int_0^{x_{\text{right}} + \xi} h(x)dx - \int_0^{x_{\text{right}}} h(x)dx \approx \xi \cdot \frac{d}{dx_{\text{right}}} \int_0^{x_{\text{right}}} h(x)dx = \xi \cdot h(x_{\text{right}}) \quad (7.7)$$

In plain words: If we always wiggle by the same amount, *the higher the bridge at the place where we cut, the worse is the imbalance*.

What happens if we move the whole grid of saw blades by the same distance? For small movements, we just apply the method we used in (7.7) on all the integration limits, to get

$$\Delta m \approx \xi(h(x_{\text{right}}) + h(x_{\text{left}}) - 2h(0)) = -2\xi(h(0) - h(x_{\text{left}})). \quad (7.8)$$

Let’s stop a moment and think about what this equation means.

The farther away we go from the top of the bridge, the farther down we go, and the greater becomes the difference  $h(0) - h(x_{\text{left}})$ . So, for a given distance  $\xi$ :

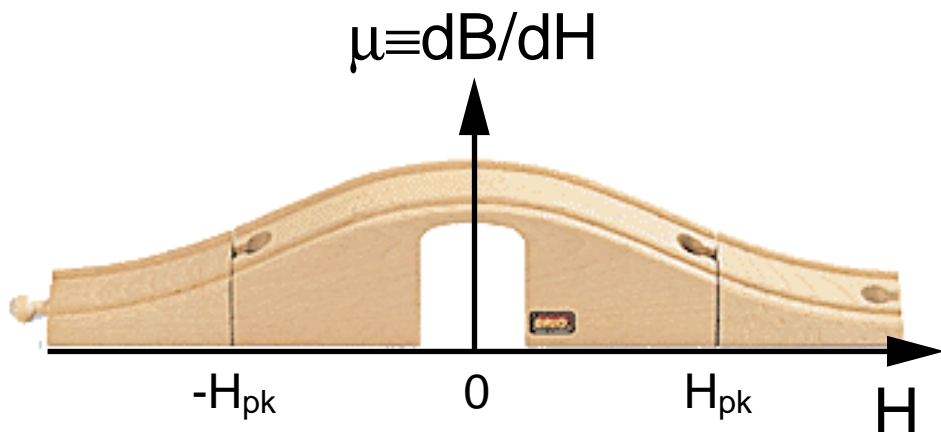
*If we put the saw blades farther apart, the imbalance becomes worse.* But once we’ve gone all the way down and off the bridge, things don’t get worse any more.

## 7.2 Balancing magnetic flux

<i>Toy bridge</i>	<i>Fluxgate sensor</i>
position $x$	magnetic field $H$
cut position $x_{\text{left}}, x_{\text{right}}$	peak magnetic field $\pm H_{\text{pk}}$
height $h(x)$	relative permeability $\mu(H) \equiv \frac{dB}{dH}(H)$
wood density $\rho$	vacuum permeability $\mu_0$
track gauge $w$	core cross-section $A_{\text{eff}}$
mass $m_{\text{left}}, m_{\text{right}}$	magnetic flux $\Phi^-, \Phi^+$
$\int_0^{x_{\text{right}}} h(x) dx$	$\int_0^{H_{\text{pk}}} \mu(H) dH$

Tab. 7.1 Matching quantities between toy bridge and fluxgate sensor

We've looked at balancing a toy bridge in considerable detail. So, what's the point? *It turns out that this toy bridge is an excellent model for a fluxgate sensor!* We just have to map the appropriate quantities. Here's how:



The *height* becomes the *relative permeability* of the ferromagnetic sensing core. The *masses* to balance are the *magnetic fluxes* for positive and negative magnetic fields. As shown in Table 7.1, other quantities can be matched as well. Let's go through the questions of our previous discussion again:

### **Is the magnetic flux for positive and negative magnetic fields balanced?**

— Ideally, that is, when there's no external magnetic field, yes.

### **Why is the magnetic flux balanced?**

— Because, like in (7.1), the relative permeability for positive and negative magnetic fields of the same magnitude is equal:

$$\mu(H) = \mu(-H), \quad (7.9)$$

and, like in (7.4), the peak positive and negative magnetic fields  $\pm H_{\text{pk}}$  used for excitation are equal.

### **What can cause imbalance of the magnetic flux?**

The magnetic flux can become unbalanced for several reasons:

- An external magnetic field shifts all integration limits by the same value. This is just like the shift of *all* the saw blades by the same distance.
- Fluctuations in the peak or zero excitation field look like a random jiggle of *one* saw blade.
- Fluctuations in the peak and zero field magnetization of the ferromagnetic core due to macroscopic or microscopic (Barkhausen noise) remanence effects *also* look like the random jiggle of one saw blade.

### **How large is the imbalance of the magnetic flux?**

Exactly like in (7.8), an external magnetic field  $H_{\text{ext}}$  causes a flux imbalance:

$$\int_{H_{\text{ext}}}^{H_{\text{pk}} + H_{\text{ext}}} \frac{d\Phi}{dH}(H) dH - \int_{-H_{\text{pk}} + H_{\text{ext}}}^{H_{\text{ext}}} \frac{d\Phi}{dH}(H) dH \approx -2H_{\text{ext}}A_{\text{eff}}\mu_0(\mu(0) - \mu(H_{\text{pk}})). \quad (7.10)$$

The math for fluctuations of the excitation magnetic field works just like (7.7):

$$\int_0^{H_{\text{pk}} + \Delta H} \frac{d\Phi}{dH}(H) dH - \int_0^{H_{\text{pk}}} \frac{d\Phi}{dH}(H) dH \approx \Delta H \cdot \frac{d\Phi}{dH}(H_{\text{pk}}) = \Delta H \cdot A_{\text{eff}} \mu_0 \mu(H_{\text{pk}}) \quad (7.11)$$

and

$$\int_{-\Delta H}^{H_{\text{pk}}} \frac{d\Phi}{dH}(H) dH - \int_0^{H_{\text{pk}}} \frac{d\Phi}{dH}(H) dH \approx -\Delta H \cdot \frac{d\Phi}{dH}(0) = -\Delta H \cdot A_{\text{eff}} \mu_0 \mu(0). \quad (7.12)$$

We see: the imbalance at zero excitation field is worse than at peak excitation field, because *the imbalance at a certain field  $H$  is proportional to the relative permeability  $\mu(H)$* . The fluctuations between zero and peak excitation don't matter!

It is a *very* remarkable fact that the imbalance *caused by magnetization fluctuations* about  $\Phi(H)$  depends on the relative permeability  $\mu(H)$  as well. It's *not* as obvious as it looks! Let's draw the analogy: The magnetization fluctuation doesn't correspond to jitter of the saw blades, but to a change of the height of the bridge. The observation that the mean square random fluctuations of magnetization  $M(H)$  about a certain magnetic field  $H$  are proportional to the magnetic susceptibility  $\chi(H)$ <sup>1</sup> was actually worth a Nobel Prize! (Onsager, 1968) [103];[104],[105]

### 7.3 Building a scale for magnetic flux

We've just found out that operating a fluxgate sensor can be compared to balancing weights. A lot of different fluxgate sensors exist [106],[107],[108],[109]. But

---

1. It's not a nice habit to introduce new names without explanation. The susceptibility is defined as

$\chi \equiv \frac{dM}{dH}$ , and we can define the magnetization by  $M \equiv B/\mu_0 - H$ .

for measuring the balance, we need a *scale*. A balance for pieces of wood is straightforward, but:

### How does a scale for magnetic flux work?

To get an answer, first we recall how a fluxgate sensor works. Fluxgate sensors are like transformers: they use a coil to make a magnetic field  $H_{\text{exc}}$  and a coil to pick up the magnetic flux  $\Phi$ .

The magnetic field is proportional to the current  $I$  that generates it:  $H_{\text{exc}} \sim I$ . So that part looks pretty straightforward. The pick-up side is more complicated, for two reasons. First, we want to measure *integrals* of the flux between zero and some maximum magnetic field  $H_{\text{pk}}$ . Second, we measure magnetic flux by an induction voltage  $V_{\text{ind}}$ . But the induction voltage is proportional to the *change* of the magnetic flux,  $V_{\text{ind}} \sim \frac{d\Phi}{dt}$ . Let's put this into math to sort it out. We want to measure the imbalance

$$\int_0^{H_{\text{pk}}} \frac{d\Phi}{dH}(H_{\text{exc}}) dH_{\text{exc}} - \int_{-H_{\text{pk}}}^0 \frac{d\Phi}{dH}(H_{\text{exc}}) dH_{\text{exc}}. \quad (7.13)$$

To do the integrals, we must sweep  $H_{\text{exc}}$  *somewhat* from 0 to  $H_{\text{pk}}$  and from 0 to  $-H_{\text{pk}}$ , by a time dependent field  $H_{\text{exc}}(t)$ , and we must integrate the induced voltage over time. So, we must change *what* we integrate:  $\frac{d\Phi}{dH} \rightarrow \frac{d\Phi}{dt}$  and *how* we integrate:  $dH_{\text{exc}} \rightarrow dt$ . Fortunately, these substitutions match perfectly:

$$\int_0^{H_{\text{pk}}} \frac{d\Phi}{dH}(H_{\text{exc}}) dH_{\text{exc}} = \int_{t(0)}^{t(H_{\text{pk}})} \frac{d\Phi}{dt}(t) dt \sim \int_{t(0)}^{t(H_{\text{pk}})} V_{\text{ind}}(t) dt. \quad (7.14)$$

One thing is remarkable: it doesn't matter *how* we sweep  $H_{\text{exc}}$  over time, as long as we start at 0 and finish at  $H_{\text{pk}}$ . *A scale for magnetic flux measures the quantity*

$$\int_{t(0)}^{t(H_{\text{pk}})} V_{\text{ind}}(t) dt - \int_{t(-H_{\text{pk}})}^{t(0)} V_{\text{ind}}(t) dt, \quad (7.15)$$

*irrespective of the detailed shape of the sweep of the magnetic field.*

### **What *exactly* do we want to measure?**

At this point, we should note that we aren't interested in the flux imbalance in itself, but in the external magnetic field  $H_{\text{exc}}$  that causes it. (In our toy bridge example, we really want to measure how far off center the sawmill cuts, not how unbalanced the bridge pieces are.) There's yet another, even more important question:

### **What do we want to *do* with the flux scale?**

The answer is obvious: Build toys, of course!!! But, what *kind* of toys? That's a difficult question. What can measuring small magnetic fields be good for? Let's think about it a little.

- We could locate small magnets: strap a *magnetized* needle to a mouse, put the mouse in a haystack, and we can always tell where it is. Or strap a little magnet to a computer mouse, and we always know where we move it, without dragging along wires or mousepads. Bigger kids with *lots* of money to spend on their toys might prefer to play cat-and-mouse with submarines. MAD?—Yes.<sup>1</sup>
- We could turn the game around and locate ourselves with respect to a large but weak magnet. Imagine that we let a little bug crawl across a slab of magnetized iron. It could find its way by seeing little cracks and irregularities of the iron by their distortion of the magnetic field. Now imagine ourselves crawling on a *huge* magnet. Wait—we're already doing this! Earth is a magnet, and we can find out where we are with a magnetic compass. What about cracks and irregularities?—Magnetized ore would do such a thing. We could even think of shooting our gadget into outer space, to map the magnetic fields of other planets.

What do a lot of these toys have in common? We want them to be small, and we want to move them around. This is important to keep in mind when we try to answer the question:

---

1. Magnetic Anomaly Detection. What did *you* think?

## What makes a *good* scale?

- A good scale is *sensitive*. That is, for a small field  $H_{\text{ext}}$ , we want to get a large signal.
- A good scale is *accurate*. That is, noise and drift must be small compared to the measurement signal.
- A good scale is *efficient*. That is, it doesn't use a lot of stuff that is unnecessarily expensive.

First, let's not look at the scale, but at the sensor itself, or, in our toy analogy, at the bridge. For a shift of the saw blades, the imbalance becomes very bad very fast if the bridge is *high*, *wide*, and *steep*. How does this translate to sensor properties?

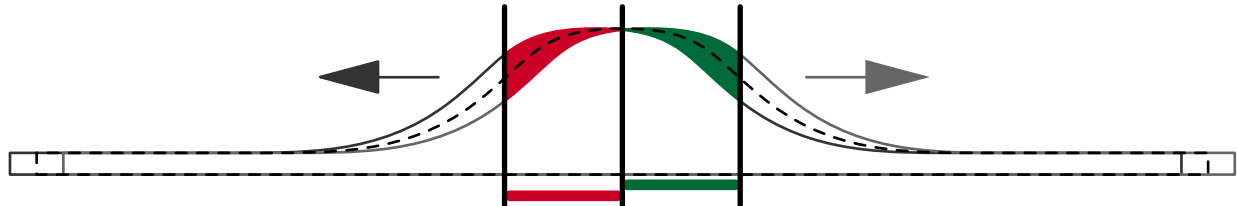
- A high bridge corresponds to a fluxgate core with *high zero field permeability*  $\mu(H=0)$ . If we start with the excitation current, a *high excitation efficiency*  $H_{\text{exc}}/I_{\text{exc}}$  also helps.
- A wide bridge corresponds to a fluxgate core with *large effective cross-section*  $A_{\text{eff}}$ . *High pick-up efficiency*  $V_{\text{ind}}/\frac{d\Phi}{dt}$  also contributes.
- A steep bridge corresponds to a fluxgate core with *low saturation magnetic field*. This is a little difficult to describe precisely: The field  $H_{\text{sat}}$  such that  $\mu(\pm H_{\text{sat}}) \approx 1$  should be low, but it isn't obvious what "almost as low as 1" means.

After these preliminaries, let's focus on the scale. How can we make it as sensitive and accurate as the sensor (or bridge) allows?

- To get a sensitive scale, equations (7.8) and (7.10) tell us to set the outer cuts all the way down the bridge, that is, we should choose the excitation field high enough to achieve saturation:  $H_{\text{pk}} \geq H_{\text{sat}}$ . If we can't quite make that, we should at least go as far down as possible. This also helps to get an accurate scale, because the influence of noise and jitter at the outer cuts, or peak magnetic fields, are reduced.
- Our height measurements as we go from the top to the outer cuts and back should be accurate. This corresponds to a low-noise measurement of the induction voltage as we sweep from zero to peak excitation field or back.

It helps a lot to use a *differential* sensor arrangement, because the dynamic range of the induction voltage (or weights) we measure is reduced significantly. With

toy bridges, it would work like this: We shift two bumps by the same distance, but in opposite directions. When we cut the bumps into pieces, we measure only the *difference* of the weights of the two pieces cut by the same pair of saw blades. This is shown in the next figure: only the areas with solid background color appear as weights on our scale.



The question remains: How do we make the scale efficient? First we must find out: *What is the expensive stuff?*

To answer that, recall that we want to build small gadgets that we can carry around. Usually, the bulkiest and heaviest part in something portable that uses electricity is the battery that stores the energy. So, the energy that our scale needs is most expensive.

Most energy is used for producing the magnetic field that drives the core: The typical excitation current  $I_{\text{exc}}$  is tens of milliamperes. The excitation current is drawn from the power supply, so the power consumption is  $V_{\text{supply}}I_{\text{exc}}(t)$ . Remembering that it doesn't matter how we get from zero field (and current) to peak excitation and back, we conclude: *For an efficient flux scale, we should go from zero to peak excitation field and back as fast as possible.*

## 7.4 Making a model for the flux scale

By now, we have found out what makes a good scale for magnetic flux with a fluxgate sensor: we must excite the core as hard as possible as fast as possible. *How fast* can we go from zero to peak excitation and back?

To answer that, we must make an *electrical* model of the fluxgate sensor and the flux balancing circuitry. A good framework for electrical models is SPICE [110]. It's public domain, so there's no risk of grown-ups allowing us to use the toys they paid for only if we do things exactly as they say. It's even available for my Macintosh toy [111]. So, with that issue settled, let's try to find an answer to the question:

```

* Brachtendorf Eck Laur coil
.subckt coil 1 2 3 4 5 6
* Nodes:
* 1,2: primary coil terminals 3,4: secondary coil terminals 5,6: external magnetic field
* h: H
* 25: delayed H field
* 28: |dH/dt|
* ma: anhysteretic magnetization
* mi: irreversible magnetization
* mt: total magnetization
* fl: magnetic flux
* Parameters: (parameters in italics must be substituted by their numerical values)
* kh1, kh2: proportionality constants to couple H to I
* kvb1, kvb2: proportionality constant to couple V to B
* mu0: vacuum permeability
* msat: saturation magnetization
* c: fraction of reversible magnetization
* a: scale factor for magnetic field
* alfa: feedback factor of magnetization
* k: hysteresis strength
* taudelay: time constant of magnetic field delay
* rser1,rser2: series resistance of coils
* cpar1,cpar2: parallel capacitance of coils

* amperemeter
v1sense    1 10  0
v2sense    3 15  0
* induction voltage source
h1ind     10 11  vb  kvb1
h2ind     15 16  vb  kvb2
* parasitics
rlseries   11  2 rser1
c1parallel 1  2 cpar1
r2series   16  4 rser2
c2parallel 3  4 cpar2
* magnetic field (in A/mm, i.e., scaled down by factor 1000)
h1          h 21 v1sense kh1
h2          21 22 v2sense kh2
ehext      22  0 5 6 0.001
* filtered derivative of magnetic field (current, scaled down by factor 1000*1000)
rhdelay    h 25 taudelay*1000/second
vhdelay    24  0 0
chdelay    25 24 1m
* sign of derivative of magnetic field (scaling by 10^-6 becomes irrelevant)
bsignhdot  0 28 i=i(vhdelay)/(abs(i(vhdelay))+1e-8)
rsignhdot  28 0 1
csignhdot  28 0 1p
* anhysteretic magnetization (normalized to [-1,1] interval)
bmanhyst   ma 0 v=(1/tanh(v(32)))-(1/v(32))
ghfield    0 32 h 0 1
gmfeedback 0 32 mt 0 alfa
rhsum      32 0 (A/mm)/a
* irreversible magnetization (normalized to [-1,1] interval)
*bmagdiff  0 41 i=uramp(v(28)*v(ma,mt))
bmagdiff   0 41 i=v(28)*v(ma,mt)
rmagdiff   41 0 1/k
bmirrdh   0 42 i=v(41)*(1+alfa*v(42))
rdmirrdh  42 0 1
* i(vhdelay) is scaled down by a factor 10^6
bmirr     0 43 i=v(42)*i(vhdelay)
vdmirrdt  43 mi 0
cmirr     mi 0 1u
rmirr     mi ma 1e12
* total magnetization
gmirr     0 mt mi 0 1-c
rmanhyst  ma mt 1/c
rmtotal   0 mt 1/(1-c)
* magnetic induction (current through vb, scaled down by 1000)
ehsum     61 0 h 0 1m
emsum     fl 61 mt 0 msat/(A/mm)
vb        fl 62 0
*cb       62 0 mu0/(V s/A m)
cb        62 0 1.25664e-6
.ends coil

```

Fig. 7.1 SPICE3 equivalent circuit model of coil with ferromagnetic core

## Is a model for flux scales available?

There's a nice model for ferromagnetic cores with hysteresis, originally developed by Jiles and Atherton [112], and extended and put into SPICE by Brachtendorf, Eck, and Laur [113]. It's a good point to start with (Figure 7.1). Unfortunately, the modeling of the hysteresis effects involves time derivative operations. Derivatives are sensitive to discretization error, so getting a correct simulation with SPICE3 is tricky. Worse yet, this model does not include DC remanence, so the situation we want to model is not modeled quite correctly: after going fast from zero magnetic field to peak magnetic field and back, the remanence decays completely. That doesn't happen in reality.

## How can we adapt the model for our purpose?

The overhead of the Brachtendorf–Eck–Laur model to describe hysteresis does us no good. It doesn't make much sense to include it in our model of the flux balance. On the other hand, we must extend the model to a differential sensor with one excitation and *two* pick-up coils. Figure 7.2 shows the equivalent circuit diagram of the adapted model. The SPICE3 netlist is shown in Figure 7.3.

To write an equivalent circuit model is one thing. To write a *useful* one is quite another. For starters, we're interested in an answer to the question:

## Can we see the bridge with our SPICE model?

Let's think a moment what we must do to get a picture of the bridge. The height of the bridge looks like  $\frac{d\Phi}{dH}$ . In the circuit model, we can observe the induction voltage across the pick-up coil  $V_{\text{ind}} \sim \frac{d\Phi}{dt}$ . So, we should see the shape of the bridge if  $\frac{dH}{dt}$  is a constant. To do this, we must apply an excitation current with constant slope. A triangle wave has constant slope, so let's apply it! Figure 7.5 shows how. The excitation current and the induction voltages are shown in Figure 7.4. If we correct for the effect of the different slopes  $\frac{dH}{dt}$ , we can see the shape of the bridge, and we also see how far from the top of the bridge we're going!

We've seen now that our SPICE model of the magnetic flux balance agrees with the toy bridge model. Of course, an important question remains...

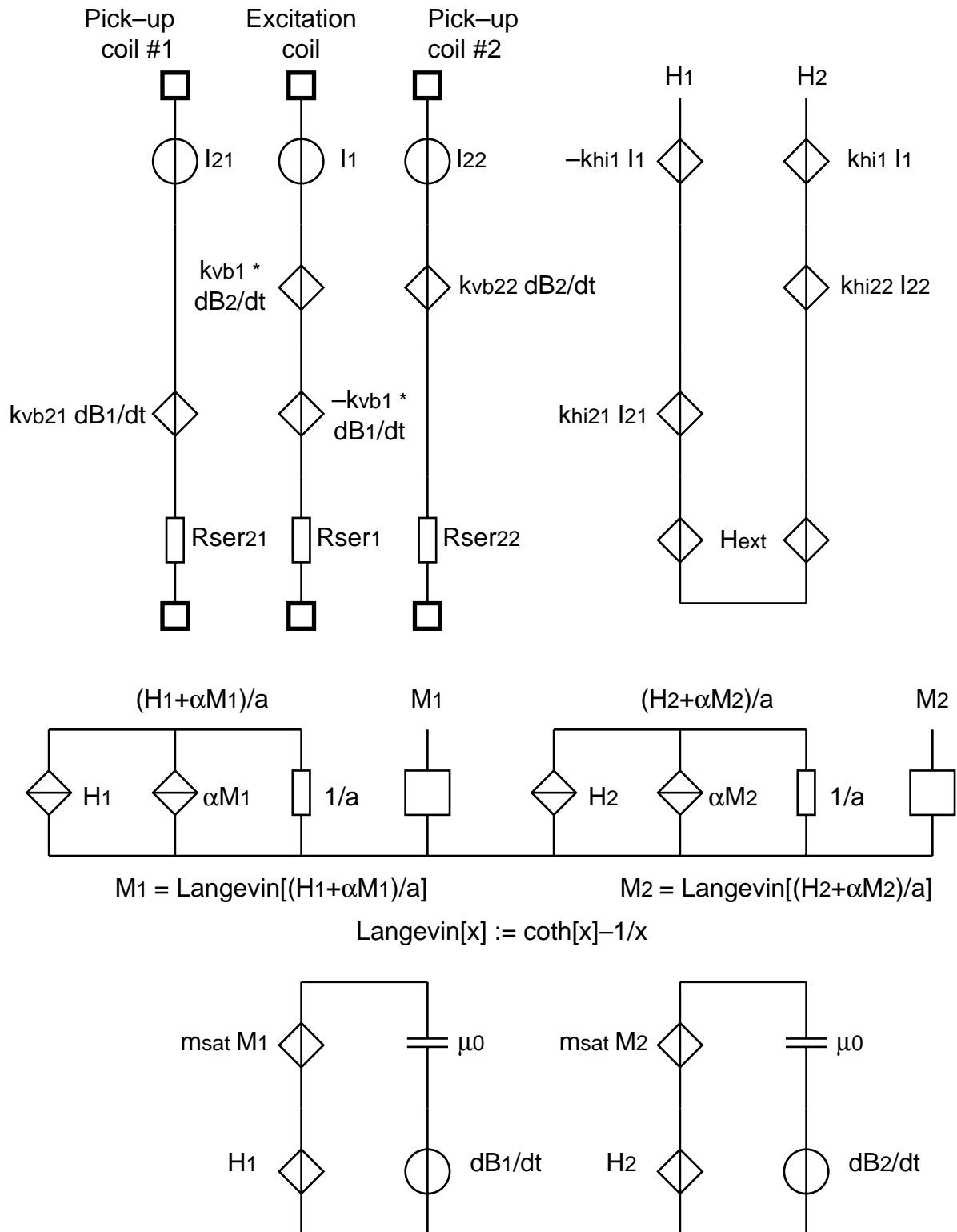


Fig. 7.2 Equivalent circuit model of differential fluxgate sensor as listed in Figure 7.3. The thick square boxes are sensor terminals; the thin square boxes are SPICE3 nonlinear controlled voltage sources.

```

* Double fluxgate coil (Langevin)
.subckt coil 1 2 3 4 5 6 7 8
* Nodes:
* 1,2: primary coil terminals      3,4: secondary coil (I) terminals
* 5,6: secondary coil (II) terminals 7,8: external magnetic field
* h1: H1
* h2: H2
* mal,ma2: anhysteretic magnetization
* mt1,mt2: total magnetization
* f11,f12: magnetic flux
* Parameters:
* kh1l, khi21, khi22: proportionality constants to couple H to I
* kvb1l, kvb21l, kvb22l: proportionality constant to couple V to B
* mu0: vacuum permeability
* msat: saturation magnetization
* a: scale factor for magnetic field
* alfa: feedback factor of magnetization
* rser1,rser21,rser22: series resistance of coils
*
* amperemeter
v1sense    1 10  0
v21sense   3 14  0
v22sense   5 18  0
* induction voltage source
h1lind    10 11  vb1 -.45u
h12ind    11 12  vb2 .45u
h21ind    14 15  vb1 1.05u
h22ind    18 19  vb2 1.05u
* parasitics
r1series   12  2 100
r21series  15  4 3182.5
r22series  19  6 3182.5
* magnetic field (in A/mm, i.e., scaled down by factor 1000)
* core I
h1l      h1 21 v1sense -25.5
h21      21 22 v21sense 59.5
eh1ext   22  0 7 8 0.001
* core II
h12      h2 26 v1sense 25.5
h22      26 27 v22sense 59.5
eh2ext   27  0 7 8 0.001
* anhysteretic magnetization (normalized to [-1,1] interval)
* core I
bm1anhyst mt1  0  v=(1/tanh(v(32)))-(1/v(32))
gh1field  0 32 h1  0  1
gm1feedback 0 32 mt1 0  0.02
rhlsum    32  0 5
* core II
bm2anhyst mt2  0  v=(1/tanh(v(36)))-(1/v(36))
gh2field  0 36 h2  0  1
gm2feedback 0 36 mt2 0  0.02
rh2sum    36  0 5
* magnetic induction (current through vb, scaled down by 1000)
* core I
eh1sum    61  0 h1  0  1
em1sum    f11 61 mt1 0  772
vbl      f11 62  0
cb1      62  0  1.25664e-6
rb1      f11 0  1e12
* core II
eh2sum    65  0 h2  0  1
em2sum    f12 65 mt2 0  772
vb2      f12 66  0
cb2      66  0  1.25664e-6
rb2      f12 0  1e12
.ends coil

```

*Fig. 7.3 SPICE3 equivalent circuit model of differential fluxgate sensor based on simplified Brachtendorf–Eck–Laur model. See Figure 7.2 for the schematic diagram.*

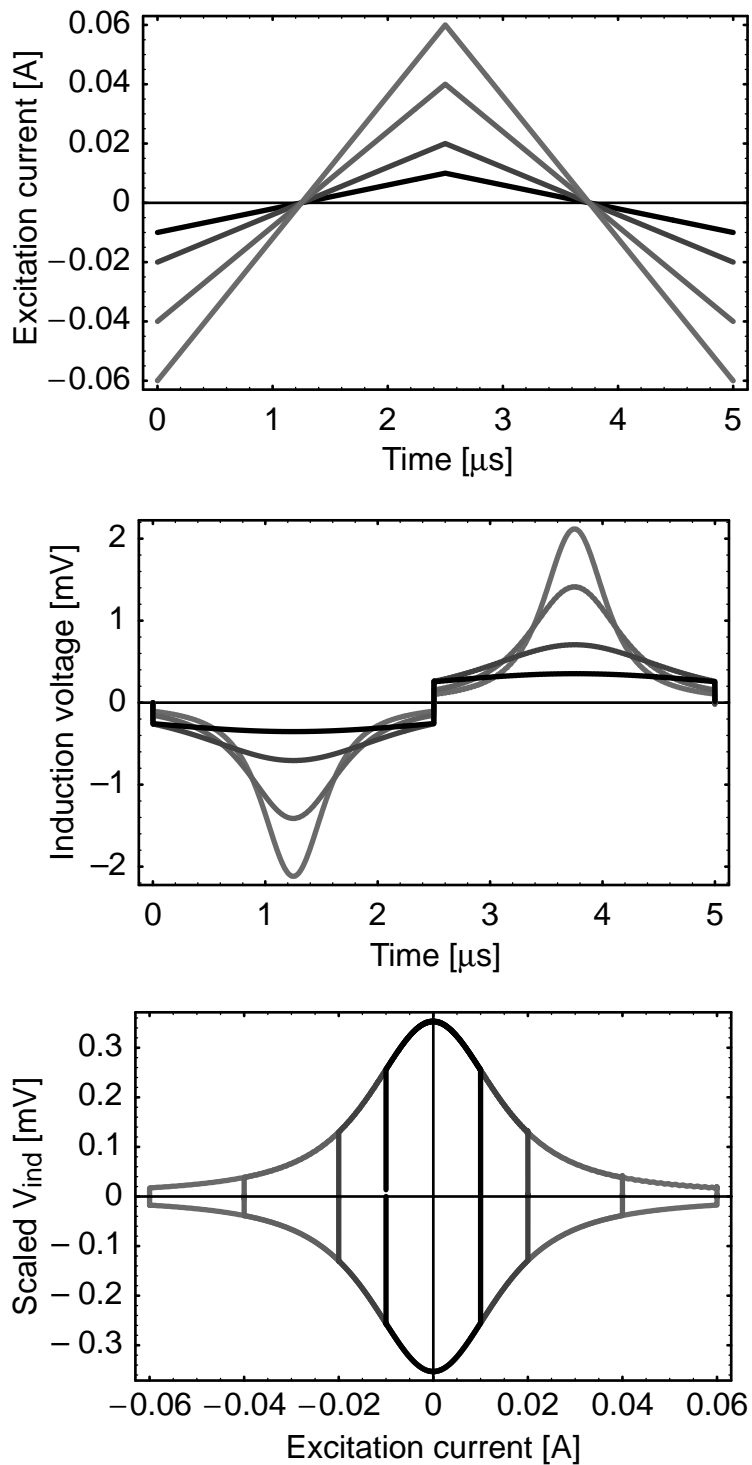


Fig. 7.4 SPICE simulation results for the induction voltage of one ferromagnetic core. The induction voltage in the lower diagram is scaled by the peak excitation voltages (1, 2, 4, and 6 V).

```

* coil
xb 4 5 10 15 15 20 hext 0 coil
*xp 4 5 10 15 15 20 parasitics
* drive source
vdrive 1 0 pulse(-1 1 0 2.499u 2.499u 1n 5u) dc -1
rdum 1 0 1meg
* drive voltage source: gain is peak voltage
edrive 3 0 1 0 6
vaux1 3 4 0
vaux2 5 0 0
* magnetic offset field (A/m); 16 A/m approx. 20uT
vhext hext 0 1
* pickup resistance
rpul 10 0 200k
rpu1 15 0 1
rpu2 20 0 200k
* pickup capacitance
cpul 10 0 5f
cpuc 15 0 5f
cpu2 20 0 5f
.tran 1n 20u 0 .016180339887u
.end
    vpeak

```

*Fig. 7.5 SPICE3 netlist for differential fluxgate excitation with triangle waveform.*

### Does our model agree with measurement?

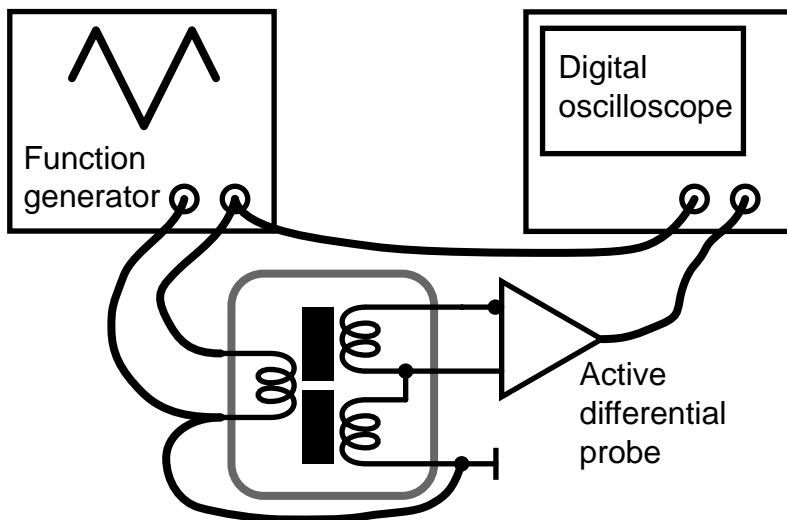


*Fig. 7.6 Measurement setup for model verification*

While working towards my thesis, I always acted Professionally and relied on the Sensor Expert's Sophisticated measurements of the behavior of the fluxgate sensor [114]. But finally, I just *couldn't* resist to do a quick measurement on my own, right *after* delivering the official examination version of the thesis *exactly* as

instructed. The measurement setup is shown in Figure 7.6. A function generator produces the triangular excitation waveform. The pick-up signal of one coil is sensed by an active differential probe *immediately* at the sensor. Both excitation and pick-up signals are recorded by a digital oscilloscope for off-line analysis. Let's have a look at the data.

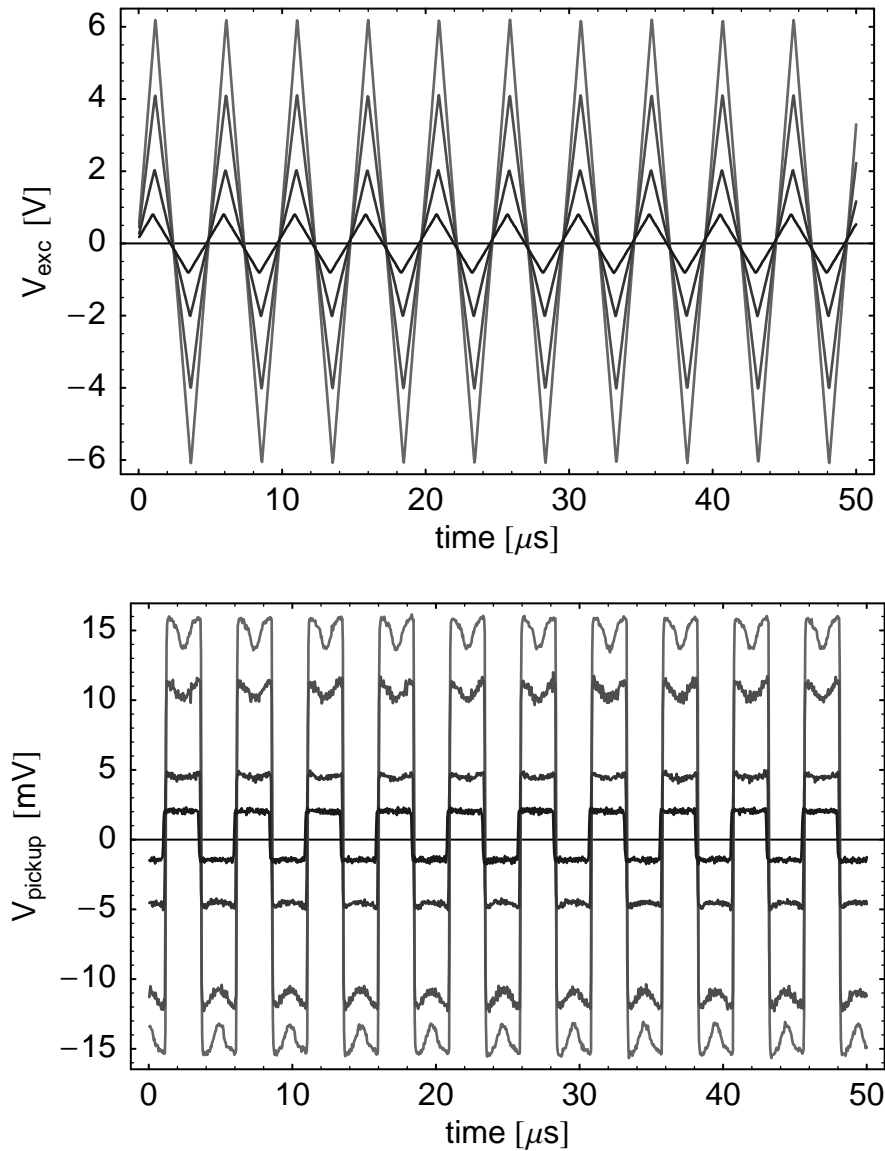


*Fig. 7.7 Measured excitation and pick-up voltages of the differential fluxgate sensor used in Chapter 4.*

Figure 7.7 shows that the data at the pick-up coil doesn't look *at all* like the model. The pick-up signal is very noisy, and a strong square wave is superimposed on the signal predicted by the model. But if we play with the data a little:

1. we determine the amplitude of the square wave by finding the maximum and minimum amplitudes of the pick-up voltage
2. we determine the frequency of the waveform by fitting a Cosine function to the excitation voltage
3. we subtract the square wave and fold a 200  $\mu\text{s}$  oscilloscope record of 5000 samples in one 5  $\mu\text{s}$  period

we get something that starts to look like our modeled signal: see Figure 7.8.

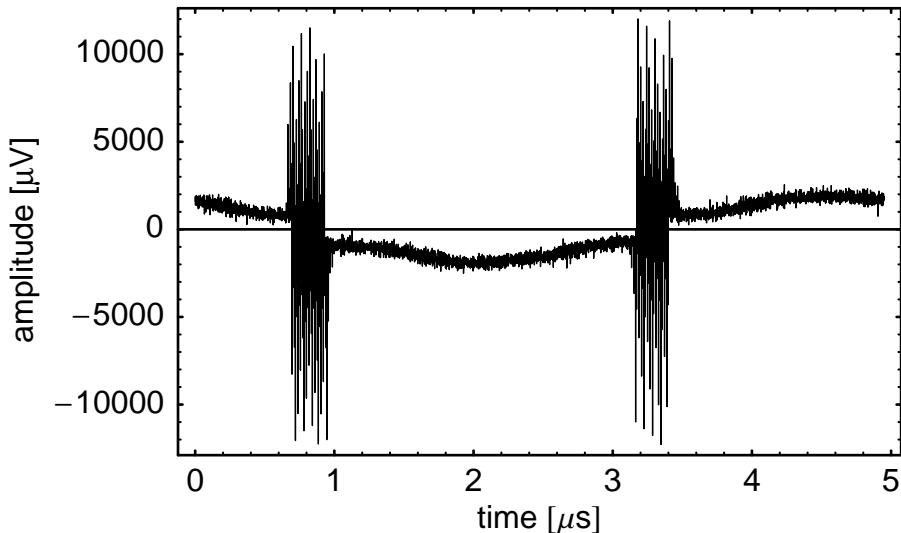


*Fig. 7.8 Pick-up coil signal for a peak excitation voltage of 4.06 V, with square wave signal subtracted, folded in one period.*

To get rid of the noise, we apply a few more steps:

4. Median filtering gets rid of the bursts of noise due to phase jitter of the oscillator
5. In a final step, the signal is smoothed and decimated repeatedly by filtering with a binomial convolution mask,  $\frac{1}{4} [1 \ 2 \ 1]$  and discarding every second sample. [115]

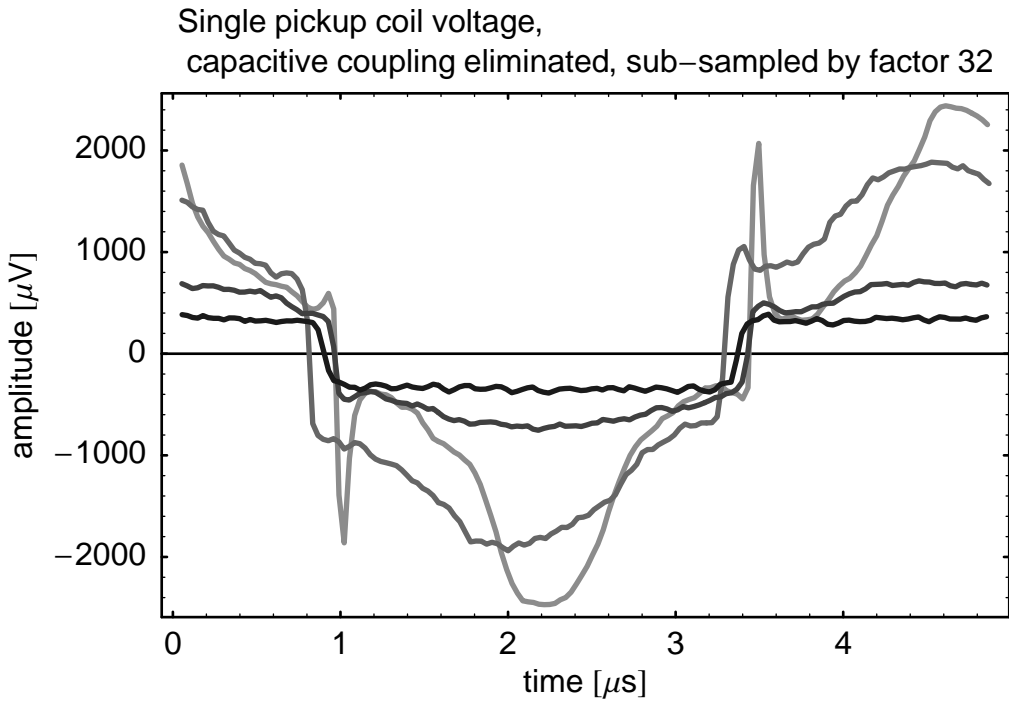


*Fig. 7.9 Single core induction voltages for 0.82 V, 2.02 V, 4.06 V, and 6.16 V triangular excitation voltage, obtained by filtering from measurement.*

The final result is shown in Figure 7.9. In the end, what you see is what you get: After a little filtering, we have extracted and visualized the permeability of the fluxgate core from the measured data. It looks very much like the data produced by our model in the middle diagram of Figure 7.4.

But that's not what we really need. The more important question is:

### **How can we get our model to agree with measured data?**

So far, our model as listed in Figure 7.3 does not explain the square wave that is superimposed on the induction voltage. How can we explain it?

In Figure 7.7, the square wave looks like the negative *time derivative* of the excitation voltage. In Figure 7.2, we have modeled a time derivative function: we've measured the current through a capacitance that was driven by a voltage. In the model, we use an ideal voltage source to measure the current. A resistor would transform the current to a proportional voltage. So, a C–R high-pass filter could produce the square wave.

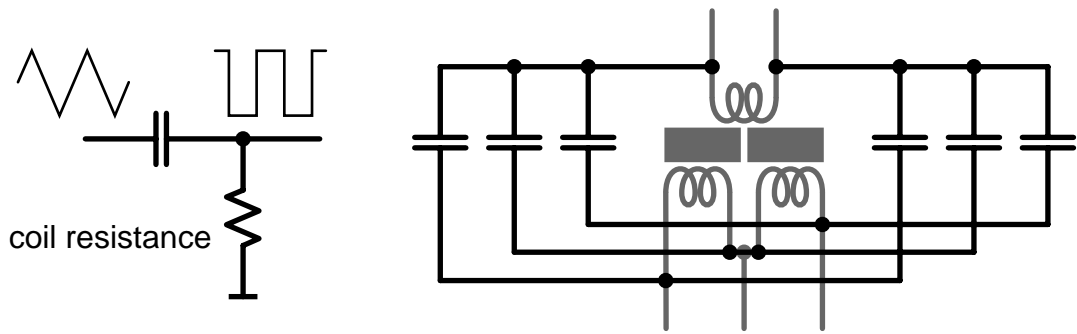


*Fig. 7.10 Parasitic C–R highpass filter producing the square wave seen in the measurement (left) and fluxgate sensor model extension (right)*

*Can we find such a high-pass filter in the fluxgate sensor?*

—Yes, we can. The capacitance is the parasitic capacitance between the windings of the excitation and pick-up coils; the resistance is the coil resistance. So, to get a realistic sensor model, we must add the parasitic capacitances. This is shown in Figure 7.10. The extension of the SPICE coil model listed in Figure 7.3 is shown in Figure 7.11.

```
* coil parasitics
.subckt parasitics 1 2 3 4 5 6
* nodes: same as coil
c12 1 2 1f
c34 3 4 1f
c56 5 6 1f
c13 1 3 1p
c14 1 4 .5p
c15 1 5 .5p
c16 1 6 1p
c23 2 3 1p
c24 2 4 .5p
c25 2 5 .5p
c26 2 6 1p
.ends parasitics
```

*Fig. 7.11 Extension of the SPICE model of the differential fluxgate sensor listed in Figure 7.3, to account for parasitic capacitances.*

**Does our revised model agree with measurement?**

To see that, let's repeat the simulation listed in Figure 7.5, but this time with parasitics added according to Figure 7.11. The result is shown in Figure 7.12: It looks very similar to our measurement in Figure 7.7!

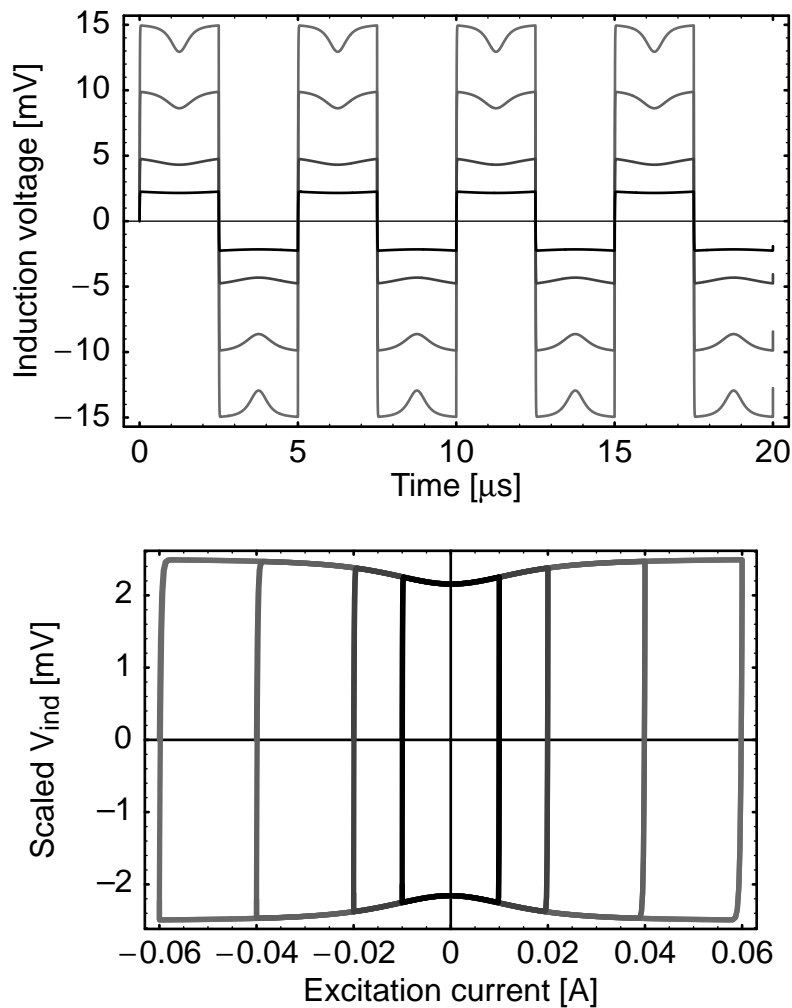


*Fig. 7.12 SPICE simulation results for the induction voltage of one ferromagnetic core with added parasitic capacitances. The induction voltage in the lower diagram is scaled by the peak excitation voltages (1, 2, 4, and 6 V).*

So what happened to the bridge shape now? It's still there, but it shows up only as a small bump on a big box caused by the parasitic capacitances.

We have now written a SPICE equivalent circuit model of the fluxgate sensor. When we compared our model with measurement, it didn't match at first. But after we added some parasitic capacitances, it matches with measurement very well.

So, now we're ready to tackle the important question:

## What do we learn from our model?

- Our model is based on drawing the analogy with balancing a toy bridge. As the model reproduces curves that we've measured, it verifies that the analogy is correct.
- For the guys who build the fluxgate sensor, it is quite tricky to predict its behavior. They must make a lot of clever measurements and assumptions to get a clue how the sensor *might* work in the end [114]. Together with the rather simple measurement we've used here to test our model, we can directly measure the *actual* shape of the bridge (or permeability profile, if you prefer) under realistic operating conditions.
- We can also see how far down the bridge we're going. So we can directly find out whether our excitation magnetic field is strong enough.
- If we got *really* serious about the kind of measurements we've used, we could fit the parameters of our model (that's the *italic* stuff in Figure 7.3) systematically. That way, we could characterize the performance of every sensor in detail. This is quite important as the sensor fabrication process doesn't appear to be too well controlled yet.
- We learn something *very* important: The sensor signal is just a small jiggle on top of something much larger that is caused by the parasitic capacitances. So, if we ever wanted to design a sensor on our own, we'd have to be very careful about the parasitic capacitances. This is *not* an obvious design criterion. For the sake of my game, I'll focus more on building the scale for the sensor output signal. But to do that, we'll have to watch the effects of the capacitances very carefully as well. They may set a limit to the overall performance of our toys.

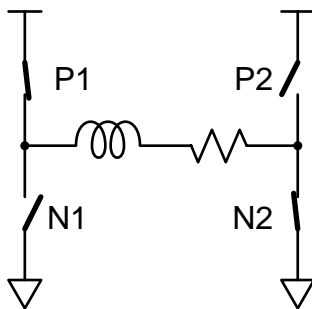
## 7.5 Designing a circuit for the flux scale

With the realistic SPICE model of the fluxgate sensor, we can now design a scale for the flux imbalance in the sensor: the CMOS excitation and readout circuit. First, let's recall what is important:

- We want to build a sensitive circuit. So, we should design for high dynamic range.
- We want to build an accurate circuit. So, we should design for low noise.
- We want to build an efficient circuit. So we should design for low power.

As we take the sensor properties for granted here, dynamic range and noise depend mainly on the amplifier for the pick-up voltage. The power efficiency, on the other hand, depends on how we put *all* the pieces together. So, we should first look how we can build an efficient circuit. Remember: to make the circuit efficient, we must go from zero to peak magnetic field and back as fast as possible.

### How do we go from zero to peak excitation and back as fast as possible?



The fastest and most power-efficient excitation is also the simplest: *Just use switches*. As the switches are either on or off, almost no power is dissipated in them. The peak excitation current is determined by the coil and switch resistances as

$$I_{\text{pk}} = \frac{V_{\text{supply}}}{R_{\text{coil}} + R_{\text{pswitch}} + R_{\text{nswitch}}}. \quad (7.16)$$

How fast we get peak excitation is determined by the time constant of the first order L-R low-pass filter

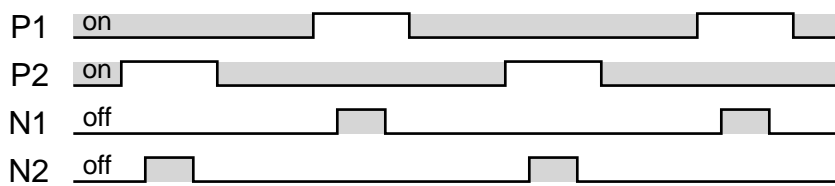
$$\tau_{\text{exc}} = \frac{L_{\text{coil}}}{R_{\text{coil}} + R_{\text{pswitch}} + R_{\text{nswitch}}}. \quad (7.17)$$

With typical inductance and resistance values of microfluxgate sensors ( $L_{\text{coil}} < 300 \text{ nH}$ ,  $R_{\text{coil}} \approx 100\Omega$ ), this time constant is a few nanoseconds.

For the switch timing sequence, we should recall what *exactly* we want to do: go from zero to maximal excitation *and back* as fast as possible. Going from zero to peak is straightforward: just connect one end of the excitation coil to  $V_{\text{supply}}$  and the other one to ground. For going back real fast, it won't just do to open the current path.

*First*, the inductance will try to keep the current flowing anyway. With larger inductances, for example those used in switched voltage regulators, we'd need to use fast flyback diodes to avoid large voltage spikes. In our case, this problem is taken care of by parasitic capacitances and diodes.

*Second*, the decay of the excitation current is slower and noisier if there is a higher resistance in the excitation current loop.



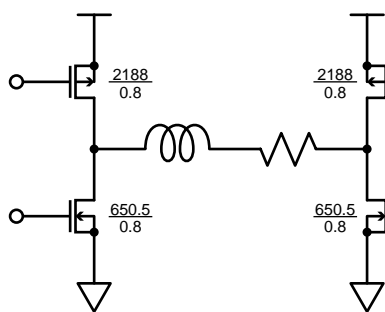
It makes best sense to short the excitation coil when we go back to zero current: We switch both its terminals to the same supply rail. Of course, we must make sure that at no time we close both switches at the same terminal of the excitation coil. So, for a short time, both these switches are open. But at no time, the excitation coil is left floating at both ends.

### Let's design the excitation switches!

We want to build a CMOS circuit for the flux scale. So, we must use MOS transistors as switches. The switches are controlled by digital signals, that is, either zero volts or the supply voltage is applied between gate and source of the switch transistors. Let's assume that we can use a digital standard cell with sufficient fan-out to get negligible switching time, so we don't need to care about gate capacitance. We *do* need to care about the switch on resistance. To dimension the switches, we use the simplified equation for MOS transistors in linear region

$$I_{ds} = k \frac{W}{L} \left( V_g - V_T - \frac{V_d + V_s}{2} \right) (V_d - V_s) \quad (7.18)$$

for  $V_g = 5$  V,  $V_s = 0$  V,  $V_d = 0.2$  V,  $I_{ds} = 50$  mA, and the Austria Mikro-systeme International CYE [116] process parameters  $V_T = 0.8$  V,  $k_{NMOS} = 100 \mu\text{A}/\text{V}^2$ ,  $k_{PMOS} = 36 \mu\text{A}/\text{V}^2$ , and  $L_{min} = 0.8 \mu\text{m}$ , to get widths of  $W_{NMOS} = 487.8 \mu\text{m}$  and  $W_{PMOS} = 1355 \mu\text{m}$ .



When we do a SPICE operating point simulation with these dimensions and the full BSIM3v3 [117] transistor model parameters [118], the voltage drops are  $V_{ds,NMOS} = 0.279$  V and  $V_{ds,PMOS} = 0.323$  V. After scaling the widths appropriately by  $\frac{0.279}{0.2}$  and  $\frac{0.323}{0.2}$  to

$W_{\text{NMOS}} = 680.5 \mu\text{m}$  and  $W_{\text{PMOS}} = 2188 \mu\text{m}$ , we get the desired voltage drop of 0.2 V across the switches.

```

* half bridge for Chiesi type fluxgate drive
* designed for 0.2V drop with 46mA at 5V gate drive
.subckt halfbridge vdd vss out gp gn
* nodes:
* vdd: positive supply
* vss: negative supply
* out: half bridge output
* gp: p-channel gate drive
* gn: n-channel gate drive
mp out gp vdd vdd p1 l=8e-7 w=2188e-6 ad=5.03n as=5.03n pd=2.19m ps=2.19m nrd=.59m nrs=.59m
mn out gn vss vss n1 l=8e-7 w=680.5e-6 ad=1.56n as=1.56n pd=685u ps=685u nrd=1.91m nrs=1.91m
.ends halfbridge

* timing generator for Chiesi type fluxgate drive
.subckt timing vdd vss n1 n2 p1 p2
* nodes:
* vdd: positive supply
* vss: negative supply
* n1: drive bridge #1 n-channel
* n2: drive bridge #2 n-channel
* p1: drive bridge #1 p-channel
* p2: drive bridge #2 p-channel
vnldrv n1 vss dc 5 pulse(0 5 20n 500p 500p 50n 500n)
vn2drv n2 vss dc 0 pulse(0 5 270n 500p 500p 50n 500n)
vp1drv vdd p1 dc 0 pulse(5 0 16n 500p 500p 58n 500n)
vp2drv vdd p2 dc 5 pulse(5 0 266n 500p 500p 58n 500n)
.ends timing

* top level circuit
*
* coil
xb 4 5 10 15 15 20 hext 0 coil
xp 4 5 10 15 15 20 parasitics
* drive source
vsupply 1 0 dc 5
xclock 1 0 51 52 53 54 timing
xdrv1 1 0 4 53 51 halfbridge
xdrv2 1 0 5 54 52 halfbridge
* excitation parasitics
cpar1n 4 0 10p
cpar1p 4 1 10p
cpar2n 5 0 10p
cpar2p 5 1 10p
* magnetic offset field (A/m); 16 A/m approx. 20uT
vhext hext 0 -1
* pickup common mode voltage
vpucom 16 0 dc 2.5
* pickup resistance
rpul 10 16 200k
rpu1 15 16 1
rpu2 20 16 200k
* pickup capacitance
cpul 10 0 5f
cpuc 15 0 5f
cpu2 20 0 5f
.tran .1n 1u 0 .4n

```

Fig. 7.13 SPICE netlist for simulation of a fluxgate sensor driven by a set of four switches.

### How does the fluxgate sensor respond to the switched excitation?

Let's take a look at how the fluxgate sensor behaves when we hook it up to this excitation circuit. For the timing, let's choose an “on” time of 50 ns, a cycle time of 500 ns, and a delay of 4 ns between turning off one switch and turning on the switch to the other supply rail.

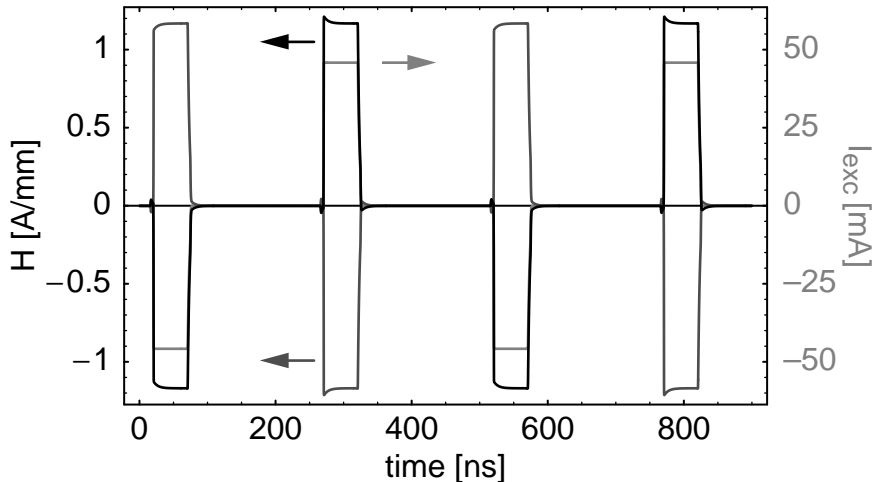


*Fig. 7.14 SPICE simulation results of the excitation current (light gray) and the magnetic fields in the ferromagnetic cores (black, dark gray).*

Figure 7.14 shows what we get from a SPICE simulation of the fluxgate sensor with the drive circuit. The SPICE netlist we’re using is listed in Figure 7.13. We see something unexpected: The excitation current stabilizes at maximum level almost immediately, but there are twitches on the waveforms of the magnetic fields! *Where do these twitches come from?* Could it be that the ferromagnetic core can’t follow the excitation current fast enough? —That could be the reason, but *we haven’t modeled that effect in our simulation*. It’s also not a good explanation for the *overshoot* of the magnetization. Something else must cause these twitches.

Let’s have a look at the signals at the pick-up coil. Maybe that gives us a clue. The voltages at the pick-up coil terminals, with the center terminal connected to 2.5 V, are shown in Figure 7.15.

We see two important features:

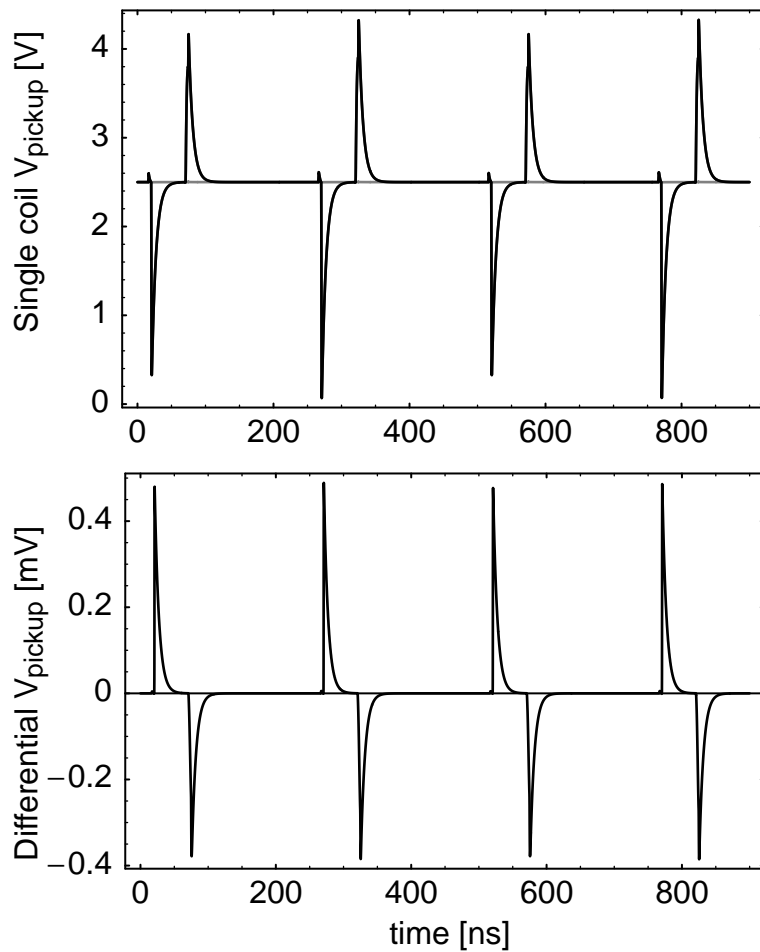


*Fig. 7.15 SPICE simulation results of terminal voltages at pick-up coils (top) and voltage difference across series connected pick-up coils (bottom), at an external magnetic field of  $H_{\text{ext}} = 1 \text{ A/m}$ .*

- The common mode voltage at the pick-up coil is 3...4 orders of magnitude larger than the flux imbalance signal that we want to measure.
- The signals at the pick-up coil decay with a time constant similar to the twitches on the magnetic field. Closer inspection (plot of  $\log |V_{\text{pu, diff}}|$  vs. time) reveals that this is the impulse response of the C-R high pass formed by the parasitic capacitances and the coil resistance ( $3.18 \text{ k}\Omega \cdot 2 \text{ pF} \approx 6.4 \text{ ns}$ ).

Figure 7.16 shows that the current through the pick-up coil causes the twitch of the core magnetic field. This current results from the charge injected through the parasitic capacitances between the excitation and the pick-up coils.

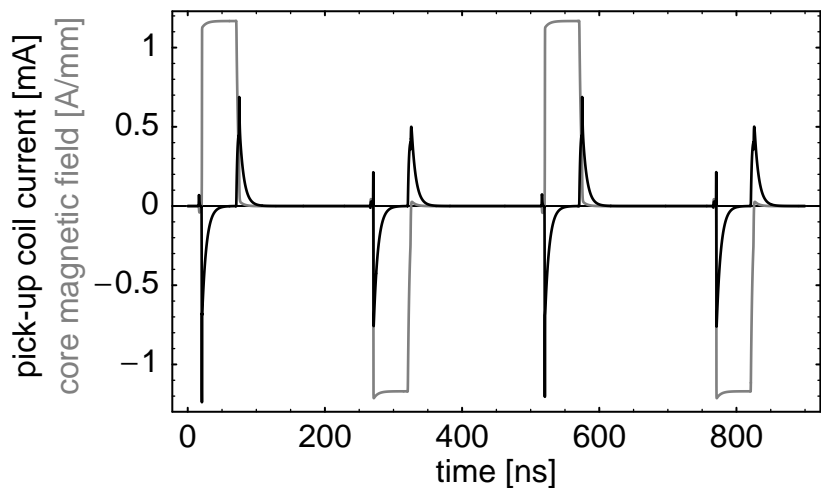


*Fig. 7.16 SPICE simulation of pick-up coil current (black) and magnetic field in the ferromagnetic core (light gray).*

If we want to make our sweeps to and from well-defined peak excitation fields, we must wait until the charge from the parasitic capacitances has drained off. *It's the parasitic capacitances that limit how fast we can go to peak excitation and back!* So, these parasitic capacitances, together with the pick-up coil resistance, set a lower limit on power consumption.

### **Can we excite the sensor faster than the parasitics would allow?**

If we can't redesign the sensor for smaller parasitic capacitances, we're left with two choices.

First, we could just decide not to care about incomplete settling of the peak excitation magnetic field. Our flux balance would still work, but we'd get very sensitive to switch timing jitter.

But if we think about what's happening, there's a second choice: It's the time we must wait when we turn *on* the current that makes trouble. We don't care if we must wait for the charge to go away after we switch *off* the current, because we don't draw any excitation current while we're waiting.

*So, how can we drain away the charge faster?*

We lower the resistance at the pick-up coil terminals.

*How can we do this?*

We *short* the pick-up coils while we switch on the excitation current!

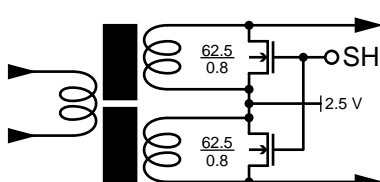
```

* timing generator for switched fluxgate drive with shunt
.subckt timing vdd vss n1 n2 p1 p2 sh
* nodes:
* vdd: positive supply
* vss: negative supply
* n1: drive bridge #1 n-channel
* n2: drive bridge #2 n-channel
* p1: drive bridge #1 p-channel
* p2: drive bridge #2 p-channel
* sh: drive for shunt transistors
vn1drv n1 vss dc 5 pulse(0 5 20n 500p 500p 20n 500n)
vn2drv n2 vss dc 0 pulse(0 5 270n 500p 500p 20n 500n)
vp1drv vdd p1 dc 0 pulse(5 0 16n 500p 500p 28n 500n)
vp2drv vdd p2 dc 5 pulse(5 0 266n 500p 500p 28n 500n)
vshdrv sh vss dc 5 pulse(0 5 12n 500p 500p 24n 250n)
.ends timing

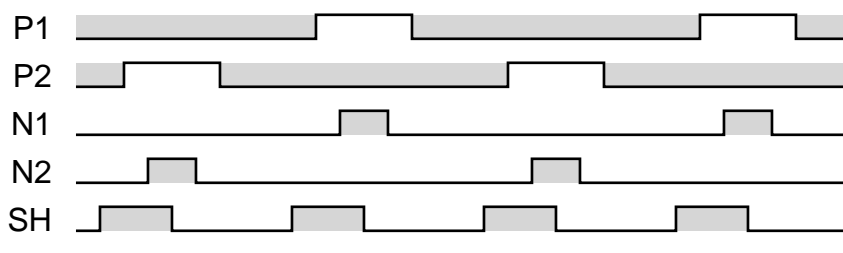
* top level circuit
*
* coil
xb 4 5 10 15 15 20 hext 0 coil
xp 4 5 10 15 15 20 parasitics
* drive source
vsupply 1 0 dc 5
xclock 1 0 51 52 53 54 55 timing
xdrv1 1 0 4 53 51 halfbridge
xdrv2 1 0 5 54 52 halfbridge
*rload 4 5 100
cparln 4 0 10p
cparlp 4 1 10p
cpar2n 5 0 10p
cpar2p 5 1 10p
* magnetic offset field (A/m); 16 A/m approx. 20uT
vhext hext 0 -1
* pickup common mode voltage
vpucom 16 0 dc 2.5
* pickup resistance
rpul 10 16 100meg
rpucl 15 16 1
rpu2 20 16 100meg
* pickup capacitance
cpul 10 0 5f
cpuc 15 0 5f
cpu2 20 0 5f
* pickup shorting switches
msh1 10 55 15 0 n1 l=8e-7 w=62.5e-6 ad=143.75p as=143.75p pd=67.1u ps=67.1u nrd=20.8m
nrs=20.8m
msh2 20 55 15 0 n1 l=8e-7 w=62.5e-6 ad=143.75p as=143.75p pd=67.1u ps=67.1u nrd=20.8m
nrs=20.8m

```

*Fig. 7.17 SPICE netlist for simulation of a fluxgate sensor driven by a set of four switches.*

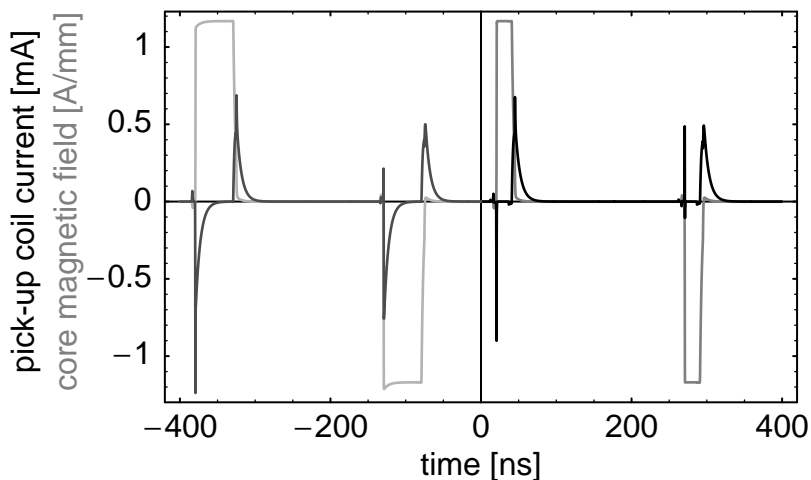


We use NMOS transistors of dimension  $\frac{62.5}{0.8}$  to lower the resistance seen by the sense terminals from the pick-up coil resistance of  $3.2 \text{ k}\Omega$  to  $75\Omega$  for a common mode voltage of  $2.5 \text{ V}$  at the center terminal.



We must switch on the shunt transistors before we turn on the current, and we must open them before we start switching it off.

The SPICE netlist to try this out is shown in Figure 7.17. Let's see what has changed now!



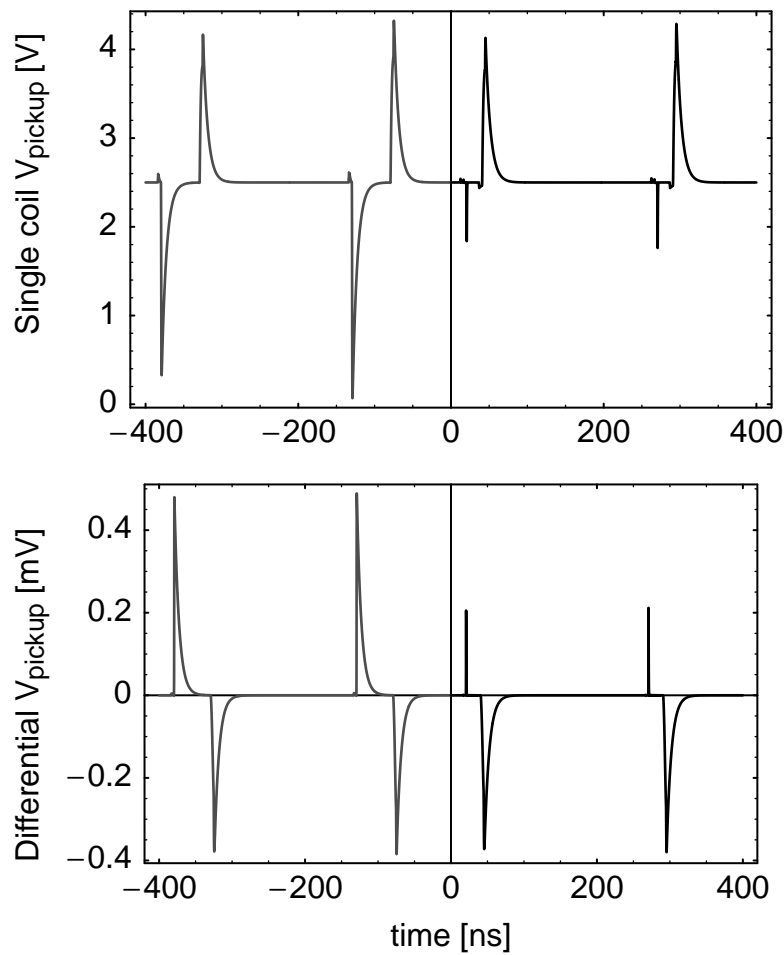
*Fig. 7.18 SPICE simulation results of the excitation current and the magnetic fields in the ferromagnetic cores without (left) and with (right) shunting switches.*

Figure 7.18 shows the pick-up coil current and the core magnetic field “before and after”, that is, with and without the short circuit switches. The magnetic field settles *much* faster now, and we can use a shorter current pulse. We've saved a lot of energy!

The pick-up coil voltages with and without short circuit switches are shown in Figure 7.19.

With the short circuit switches, the common mode voltage spike caused by switching on the excitation current is almost gone. Now, the stage that measures the differential pick-up voltage needs only half the input common mode range.

The flux imbalance signal for the transient from zero to peak excitation almost dis-



*Fig. 7.19 SPICE simulation results of terminal voltages at pick-up coils (top) and voltage difference across series connected pick-up coils (bottom), at an external magnetic field of  $H_{\text{ext}} = 1 \text{ A/m}$ , without (left) and with (right) shunting switches.*

appears as well. *We're throwing away half our signal!* But we're getting a lot in return, so it may be a worthwhile investment:

- We save *more than half* the power needed for the excitation.
- The common mode range of the pick-up coil signal is reduced by half.
- We could get away with a simple active low-pass filter as readout circuit *without any extra switches!*

With the trick to shunt the pick-up coils while we switch on the excitation current, we can build a very *efficient* scale. Now it's time to think how to build an *accurate* and *sensitive* scale. To do this, first we must answer the question:

### What does the imbalance signal of the sensor look like?

When we look at Figure 7.19, we already have *some* idea what to expect. But before we can start designing a circuit to measure the flux imbalance voltage, we need to know what can possibly happen to signal that we want to measure. We use the netlist from Figure 7.17 with different values for  $H_{\text{ext}}$  to get more data.

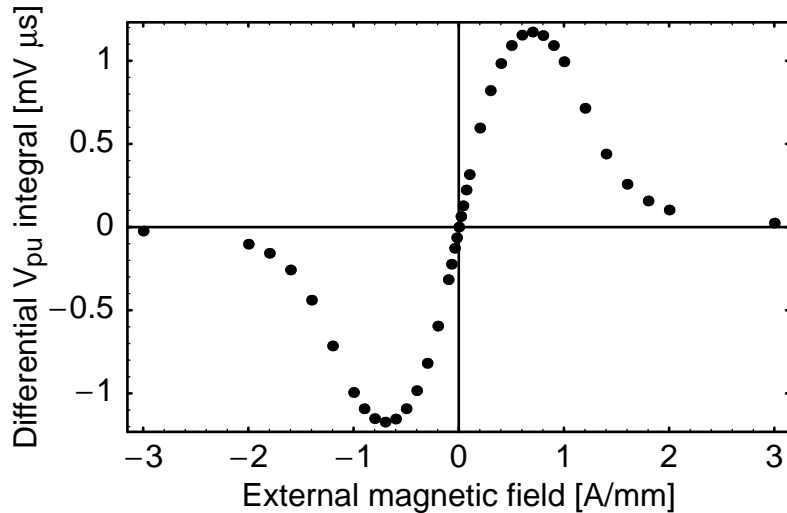


Fig. 7.20 Integral of differential pick-up voltage peak versus external magnetic field, obtained from SPICE data.

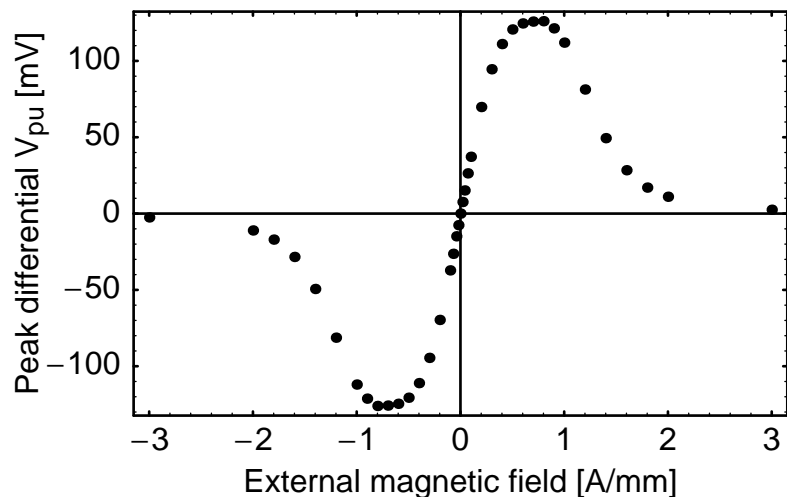


Fig. 7.21 Peak differential pick-up voltage versus external magnetic field, without capacitive loading of the pick-up coil terminals, obtained from SPICE data.

The *area* of the differential induction voltage peak as a function of the external magnetic field is shown in Figure 7.20.<sup>1</sup> This is the quantity we want to measure.

Figure 7.21 looks very similar. It shows the *height* of the differential induction voltage peak. It determines how large the linear differential voltage range of the sensor amplifier must be. Height and area are proportional only because the induction voltage pulse is shaped by the parasitic RC seen by the pick-up coil sense terminals.

It's interesting to see what happens if we change the capacitive loading at the sense terminals. We model the terminal as R–C low pass filter, with  $R$  the resistance of the pick-up coil and  $C$  the total capacitance at the terminal. The impulse response of the low pass filter,

$$h_{RC}(t) = \frac{e^{-t/RC}}{RC}, \quad (7.19)$$

is inversely proportional to  $RC$ , while the integrated impulse is independent of  $RC$ :

$$\int_0^{\infty} h_{RC}(t) dt = \int_0^{\infty} \frac{e^{-t/RC}}{RC} dt = 1. \quad (7.20)$$

When we add more capacitance to the sense terminals, we lower the height of the voltage peaks, but we don't change their area. This is true for the common mode voltage peaks (see Figures 7.15 and 7.19, upper diagram) as well. We relax the requirements on the common mode input voltage range *and* the linear differential input voltage range of the sense amplifier!

What's the price we pay for this? —It takes longer for the peaks to decay. This doesn't hurt us, because we're not drawing any excitation current while we wait.

---

1. The integrals have been calculated off line by trapezoid integration:

$\text{integral} = \langle [1 -1] \otimes \text{timesteps} | [1/2 1/2] \otimes \text{voltages} \rangle$ . The parameters of the model have not been fit to measurement systematically. I just tried to get a good match between Figure 7.7 and Figure 7.12. The simulation data does not correspond to any sensor in particular.

```

* coil parasitics
.subckt parasitics 1 2 3 4 5 6
* nodes: same as coil
c12 1 2 1f
c34 3 4 1f
c56 5 6 1f
c13 1 3 1.01p
c14 1 4 .5p
c15 1 5 .5p
c16 1 6 0.99p
c23 2 3 0.99p
c24 2 4 .5p
c25 2 5 .5p
c26 2 6 1.01p
.ends parasitics

```

Fig. 7.22 SPICE model of coil parasitics with capacitance mismatch.

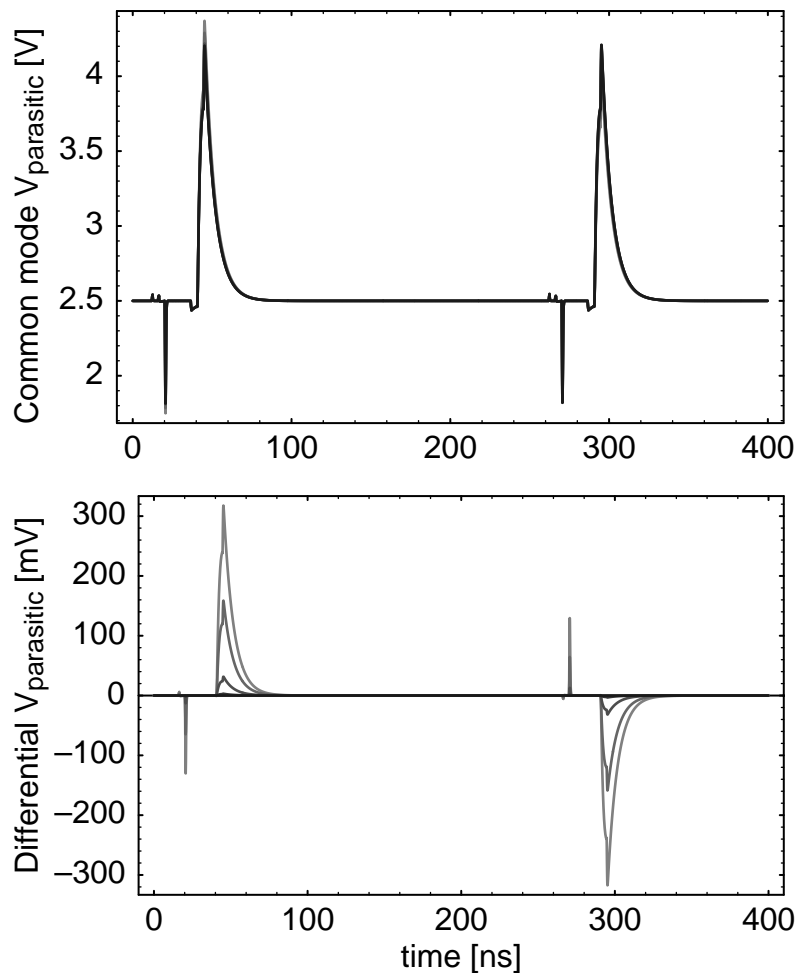
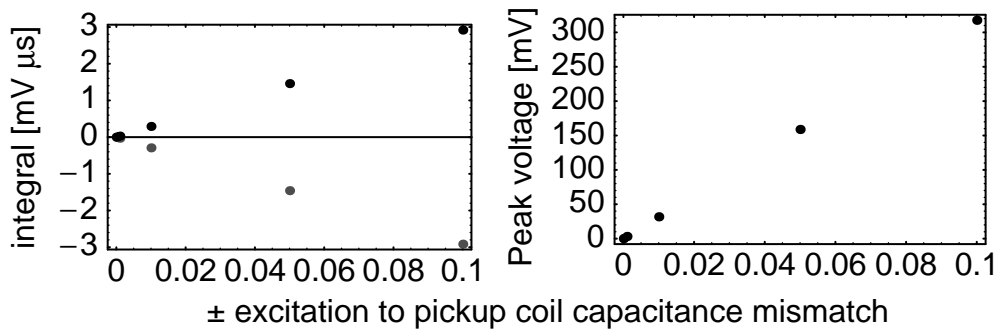


Fig. 7.23 SPICE simulation results of terminal voltages at pick-up coils (top) and voltage difference across series connected pick-up coils (bottom) caused by capacitance mismatches of 0,  $\pm 0.1\%$ ,  $\pm 1\%$ ,  $\pm 5\%$ , and  $\pm 10\%$ .

Now, we have a good enough idea what the flux imbalance signal looks like. But we've seen in Figures 7.7 and 7.12 that this imbalance signal is very small compared to the signal caused by the capacitance between the coils. This capacitive signal doesn't show up in the differential pick-up voltage because we have modeled the parasitics (see Figure 7.11) to be *exactly* the same for both pick-up coil sense terminals. Let's check what mismatch of the parasitic capacitances will do: We modify the parasitic capacitances to include mismatch, as shown in Figure 7.22, and replace the coils by its series resistances. The differential voltage that we get now is *only* caused by capacitance mismatch.



*Fig. 7.24 Integral (left) and peak voltage (right) of differential voltage spikes caused by mismatch of parasitic capacitances.*

As we can see in Figure 7.23, capacitance mismatch also produces peaks of the differential voltage, but their polarity alternates with the polarity of the excitation signal. Figure 7.24 shows the dependence of the peak area and height as a function of the capacitance mismatch. Peak area and height are proportional to the capacitance mismatch. A mismatch of  $\pm 4\%$  produces peaks as large as the maximum flux imbalance. The areas of the positive and negative peaks are equal. When we integrate over two subsequent peaks, we get rid of the signal due to capacitance mismatch. But we must make sure that the linear range of the sense amplifier isn't exceeded.

Now we have a fairly good idea what the *entire* differential signal at the pick-up coil looks like. So:

## Let's design a readout circuit for the flux scale!

To measure the time integral of a voltage, we must build a voltage integrator. First, we must define specifications for the readout circuit. There are a lot of quantities commonly used to specify an amplifier. It's very important that we pick the specifications that *really* matter to us.

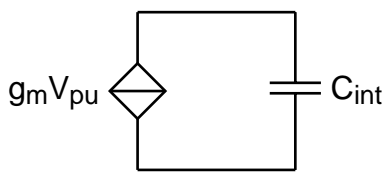
<i>Quantity</i>	<i>Symbol</i>	<i>Value</i>	<i>Unit</i>
Full scale input range	$\hat{\phi}_{\text{peak}}$	1.4	$\frac{\text{mV}\mu\text{s}}{\text{peak}}$
Sense amplifier input resistance	$R_{\text{in}}$	>300	$\text{k}\Omega$
Full scale voltage linearity error	$\epsilon_{\text{lin}}$	1	%
Linear differential input voltage range (unloaded sensor)	$\hat{V}_{\text{in}}$	$\pm 200$	$\text{mV}$
Linear common mode input range	$V_{\text{in, cm}}$	2	$\text{V}$
Full scale output voltage	$\hat{V}_{\text{out}}$	$\pm 1$	$\text{V}$
Dynamic range	$\log_2 DR$	12	bits
Total output noise	$v_{\text{onoise}}$	250	$\mu\text{V}$
Supply voltage	$V_{\text{supply}}$	5	$\text{V}$

Tab. 7.2 Basic design specifications for the flux imbalance sense amplifier

- We don't want to overload the integrator with the signal from the pick-up coil.  
So, we need to specify the largest peak area that we want to measure, the **full scale input range**.
- We want to measure the flux imbalance signal without excessive attenuation.  
So, we must make sure that the **sense amplifier input resistance** is high enough.
- The flux imbalance signal must not be distorted excessively. So, we must choose a **linearity error** we accept within the **differential input voltage range**.

- We must make sure that the **input common mode voltage range** can handle the sensor signals.
- At the back end of the circuit, we want to use, but not exceed, the **full scale output voltage**.
- To choose the sensitivity of the flux scale, we specify the **dynamic range** of the output signal. This gives us an upper limit for the **total output noise**.
- The **supply voltage** and the **power consumption** that we allow constrains how we can achieve the other specifications.

These basic specifications and their values are listed in Table 7.2. Note that we *haven't* specified the *bandwidth* of the sense amplifier. We'll choose it as good as we can within the constraints of our specifications.

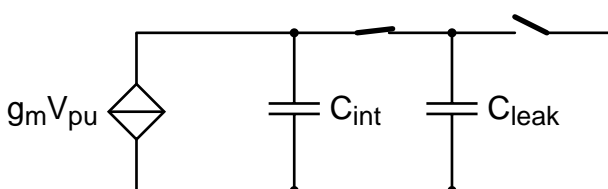


Let's choose an architecture for the voltage integrator. A  $g_m C$  integrator is a suitable topology: The transconductance provides gain and isolates the integrating capacitance from the shunt at the input. The gain is

$$S_\phi \equiv \frac{V_{\text{out}}}{\phi_{\text{peak}}} = \frac{g_m}{C_{\text{int}}} n_{\text{peak}}. \quad (7.21)$$

With just a transconductance and a capacitor, the output voltage across the capacitor grows beyond all limits with the number of peaks  $n_{\text{peak}}$ . We have several possibilities to prevent this:

- We can compensate the magnetic field to zero by a feedback coil, as in Chapter 4.
- We can discharge the integration capacitor after a certain number of excitation cycles, as in Chapter 3.
- We can build a leaky integrator:

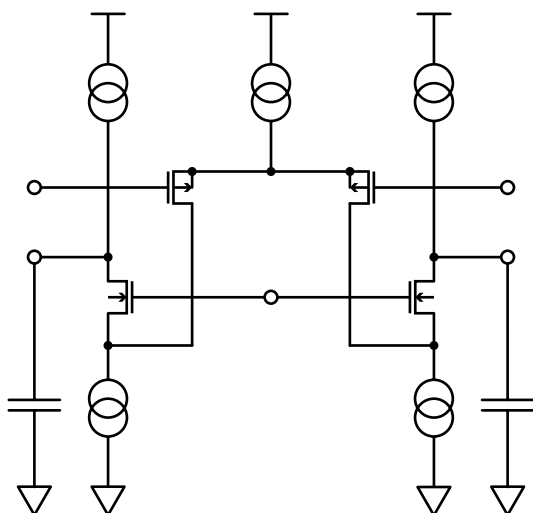


If we use a switched capacitor and synchronize the switching sequence to the shunt timing, the gain is independent of the operating frequency:

$$\frac{V_{\text{out}}}{\phi_{\text{peak}}} = \frac{g_m}{C_{\text{int}}} \sum_{n=0}^{\infty} \left( \frac{C_{\text{int}}}{C_{\text{int}} + C_{\text{leak}}} \right)^n = \frac{g_m}{C_{\text{int}}} \frac{C_{\text{int}} + C_{\text{leak}}}{C_{\text{leak}}}. \quad (7.22)$$

Now, we must translate this ideal architecture into a real CMOS circuit, with its distinctly nonideal components. For the sake of our game, we use Austria Mikro-systeme International's CYE process [116]. As this process provides poly–poly capacitors, it's no problem to get linear capacitances. But building a sufficiently linear and low–noise transconductance with MOS transistors is quite an issue.

Let's build the transconductance as PMOS differential pair.



*Why a differential pair?* —As we can see in Figures 7.15, 7.19, and 7.23, we need good common mode rejection. As we're switching large currents at the excitation side of the sensor, we should build a design immune to noise from the substrate and the power supplies. A *fully differential topology* will help here.

*Why PMOS?* —The process we're using is an n–well process. So, we can connect bulk and source of the input transistors together.

This helps with our common mode and power supply rejection. PMOS transistors also have less  $1/f$  noise than their NMOS counterparts. We want to measure low frequency signals, so this is important.

A folded topology accommodates large voltage swings both of the output and the input common mode voltages. The price we pay for this is higher current consumption and more noise due to the extra current sources. But compared with what we'd need with other topologies for a linear transconductance [120], we're still doing rather well.

Let's have a good look at the circuit diagram and play with the circuit parameters in our mind a little.<sup>1</sup>

---

1. If you don't know what *the hell* I'm talking about, you might want to look up Tom Hornak's "True Analog Circuit Design" [119].

- We've taken care of the common mode input and output swings by the topology. Maybe we must shift down the center tap voltage of the pick-up coil.
- The total thermal output noise is always proportional to  $kT/C_{\text{int}}$  [121], so we can always deal with noise by increasing the integration capacitance and slowing down the readout. We get a low proportionality factor if the transconductance of the input differential pair is much higher than of the current sources. We get high transconductance either by high drain current (*not* a good idea to draw these lines too thick) or low gate overdrive  $V_{d,\text{sat}}$ . But as we move gate and source of the input transistors closer together, we're losing linear differential input range: the drain current difference of the input pair is

$$\Delta I_d = \Delta V_{\text{in}} \frac{2I_d}{V_{d,\text{sat}}} \sqrt{1 - \left(\frac{V_{\text{in}}}{2V_{d,\text{sat}}}\right)^2} = \Delta V_{\text{in}} g_m (1 - \epsilon_{\text{lin}}). \quad (7.23)$$

When we solve for  $\epsilon_{\text{lin}}$ , we get

$$V_{d,\text{sat}} = \frac{\hat{V}_{\text{in}}}{2\sqrt{\epsilon_{\text{lin}}(2 - \epsilon_{\text{lin}})}}. \quad (7.24)$$

For an allowed nonlinearity of 1%, 1.5% and 2%, we get gate overdrive voltages of  $3.5\hat{V}_{\text{in}}$ ,  $2.9\hat{V}_{\text{in}}$ , and  $2.5\hat{V}_{\text{in}}$ , respectively.

To keep the noise low, the current sources should not get less gate overdrive than the input differential pair. Let's set the gate overdrive of the input differential pair to  $V_{d,\text{sat}} = 400$  mV. We must add capacitance to the input nodes to push down the maximum voltage of the imbalance peaks to  $\hat{V}_{\text{in}} = 100$  mV.

- The quiescent current through the output branch of the folded cascode is needed to keep the cascode transistors conducting. It doesn't need to be larger than the maximal drain current *difference* of the input transistors,

$$\Delta I_d \approx I_d \frac{2\Delta V_{\text{in}}}{V_{d,\text{sat}}} = 4I_d \sqrt{\epsilon_{\text{lin}}(2 - \epsilon_{\text{lin}})}. \quad (7.25)$$

For a nonlinearity of 1%, 1.5% and 2%, the maximum drain current difference is  $0.56I_d$ ,  $0.69I_d$ , and  $0.8I_d$ , respectively.

- With the current through the output branches of the amplifier set to  $rI_d$ , the total input referred thermal noise is, according to textbook [122] formula:

$$\begin{aligned} v_{\text{noise, thermal}}^2 &= 2 \frac{2}{3} \frac{kT}{C_{\text{int}}} \left( \frac{g_{m, \text{in}} + g_{m, \text{nsrc}} + g_{m, \text{psrc}}}{g_{m, \text{in}}} \right) . \\ &= \frac{4}{3} \frac{kT}{C_{\text{int}}} \left( 1 + (1+r) \frac{V_{d, \text{sat,in}}}{V_{d, \text{sat;nsrc}}} + r \frac{V_{d, \text{sat,in}}}{V_{d, \text{sat;psrc}}} \right) \end{aligned} \quad (7.26)$$

The total noise depends only on transconductance ratios and the size of the integration capacitance. We're getting this noise each time we sample the output voltage.

- While the total noise depends on how large we make our integrating capacitance, the measurement speed depends on the transconductance. The faster we want to get, the more power we must use for the readout integrator. On the other hand, we need a certain number of peaks for one accurate measurement. For every peak, we need the energy to excite the ferromagnetic core. So, there's an optimal transconductance that minimizes power.

Let's calculate the energy necessary for one excitation pulse. The excitation current is  $I_{\text{exc}} = 46 \text{ mA}$  from a supply voltage of  $V_{\text{supply}} = 5 \text{ V}$  for an excitation pulse width of  $t_{\text{exc}} = 20 \text{ ns}$ . We consume

$$W_{\text{exc}} = V_{\text{supply}} I_{\text{exc}} t_{\text{exc}} = 4.6 \text{ nJ/peak} \quad (7.27)$$

for the excitation. For every picofarad of parasitic capacitance that is charged to supply voltage and completely discharged, we consume

$$W_{\text{Cpar}} = V_{\text{supply}}^2 C_{\text{par}} = (25 \text{ pJ/pF}) C_{\text{par}}. \quad (7.28)$$

We need to operate the readout amplifier for the time it takes for the imbalance signal pulse to decay to the precision that we want. The decay time constant is  $\tau = R_{\text{coil}} C_{\Sigma}$ , with  $C_{\Sigma}$  the total capacitance at the pick-up coil sense nodes. For a decay to  $\epsilon$  of the peak amplitude, we need to wait  $t_{\text{int}} = \ln(\epsilon) R_{\text{coil}} C_{\Sigma}$ . A rather conservative estimate for the time would be  $t_{\text{int}} = 12 \cdot 3.2 \text{ k}\Omega \cdot 4 \text{ pF} = 154 \text{ ns}$ .

If the total current consumption of the integrator is  $I_{\text{fe}}$ , the energy required to measure and integrate one peak is

$$W_{\text{int}} = V_{\text{supply}} I_{\text{fe}} t_{\text{int}} = 5 \text{ V} \cdot 154 \text{ ns} \cdot I_{\text{fe}} = I_{\text{fe}} \cdot 0.77 \text{ nJ}/(\text{mA} \cdot \text{peak}). \quad (7.29)$$

The current required by the front-end circuit is composed of the current for the amplifier plus the current required for the bias generator

$$I_{\text{fe}} = 2(1+r)I_d + I_{\text{biasgen}} = 2(1+r)\frac{g_m V_{d, \text{sat,in}}}{2} + I_{\text{biasgen}} \equiv \gamma g_m. \quad (7.30)$$

$\gamma$  is the proportionality factor that tells how much current we need to get the transconductance we need to get the sensitivity  $S_\phi$  we want. With (7.21) we get

$$I_{\text{fe}} = \gamma g_m = \gamma \frac{S_\phi C_{\text{int}}}{n_{\text{peak}}}. \quad (7.31)$$

Let's figure out the total energy for one measurement:

$$W_\Sigma = n_{\text{peak}}(W_{\text{exc}} + W_{\text{int}}) = V_{\text{supply}}(I_{\text{exc}} t_{\text{exc}} n_{\text{peak}} + \gamma S_\phi C_{\text{int}} t_{\text{int}}). \quad (7.32)$$

The *total* energy consumption of the integrator is *independent* of the transconductance, because  $g_m n_{\text{peak}} = \gamma S_\phi C_{\text{int}} = \text{constant}$ . However, a high transconductance saves excitation peaks and the energy required for the excitation.

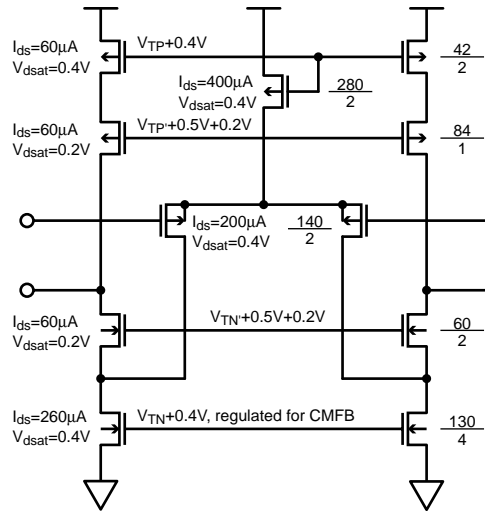
*If we want to save energy, we should spend a lot of current for the flux imbalance integrator to get our measurement with a minimum of sensor excitations.*

Let's take a look at the integration time  $t_{\text{int}}$ . It is proportional to the capacitance at the pickup node, which is inversely proportional to the peak pickup voltage. The desired input linearity is the proportionality constant between peak pickup voltage and input transistor gate overdrive voltage. Let's put this together:

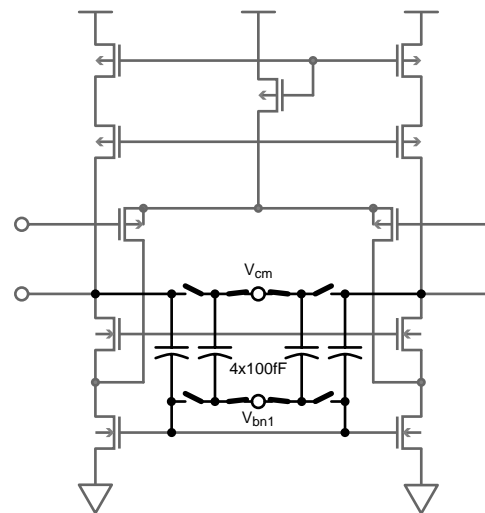
$$t_{\text{int}} \sim C_\Sigma \sim \frac{1}{\hat{V}_{\text{in}}} \sim \frac{1}{V_{d, \text{sat,in}}} \sim \frac{1}{\gamma} \Rightarrow W_{\text{int}} \sim \gamma t_{\text{int}} \sim \frac{t_{\text{int}}}{t_{\text{int}}} \equiv 1. \quad (7.33)$$

For the energy consumption, it doesn't matter how much we slow down the imbalance peak from the sensor. After these preliminaries,

## Let's dimension the transconductance amplifier!



For the sake of this little game, we don't need to get too fancy. Let's pick a transconductance of  $g_m = 1 \text{ mA/V}$  and a gate overdrive of  $V_{d, \text{sat}} = 400 \text{ mV}$  for the input transistors. According to  $I_d = g_m V_{d, \text{sat}} / 2$ , we get an input branch current of  $200 \mu\text{A}$  and an output branch current of  $rI_d = 60 \mu\text{A}$ . Compromising between thermal noise and output swing, we give the current sources a gate overdrive of  $V_{d, \text{sat}} = 400 \text{ mV}$ , and about half of this gate overdrive to the cascodes. To help with matching, output resistance, and  $\frac{1}{f}$  noise, we choose the device lengths rather conservatively:  $L_{\text{NMOS}} = 4 \mu\text{m}$  and  $L_{\text{PMOS}} = 2 \mu\text{m}$ ; half for the cascodes.



The SPICE netlist of the transconductance amplifier and a bias network is shown in Figure 7.25. Amplifier and bias block are designed for a total current of  $I_{\text{fe}} = 760 \mu\text{A}$ .

The amplifier is fully differential, so we regulate the output common mode voltage by capacitive feedback of both output voltages to the gates of the bottom sources. *This common mode feedback circuit is a leaky integrator to the differential output voltage!* The switched capacitances correspond to  $C_{\text{leak}}$  in equation (7.22).

So, we can do two things simultaneously [123] with the switched capacitors. But we can also avoid the leaky integrator behavior if we alternate between bursts of activity and quiet phases [124]: We set the common mode operating point by switching the capacitors back and forth *before* the measurement, but we don't switch *during* the measurement. Figure 7.26 lists the SPICE netlist of the common mode feedback circuit for the amplifier.

```

.include amscye.cir

.subckt fcasc vss vdd vbp0 vbp1 vbp2 vbn1 vbn2 in1 in2 out1 out2
* folded cascode amplifier
* target: 1mA/V transconductance
* 1% linear range: 100mV
mcs      vcs vbp0 vdd vdd p1 l=2u w=280u ad=644p as=644p pd=285u ps=285u nrd=4.6m nrs=4.6m
min1    vd1 in1   vcs vcs p1 l=2u w=140u ad=322p as=322p pd=149u ps=149u nrd=9.3m nrs=9.3m
mns1    vd1 vbn1   vss vss n1 l=4u w=130u ad=299p as=299p pd=135u ps=135u nrd=10m nrs=10m
mnc1    out1 vbn2   vd1 vss n1 l=2u w=60u ad=138p as=138p pd=65u ps=65u nrd=22m nrs=22m
mpc1    out1 vbp2   vp1 vdd p1 l=1u w=84u ad=193p as=193p pd=89u ps=89u nrd=15.4m nrs=15.4m
mps1    vp1 vbp1   vdd vdd p1 l=2u w=42u ad=97p as=97p pd=47u ps=47u nrd=31m nrs=31m
.ends fcasc

.subckt fcbias vss vdd iref vbp1 vbp2 vbn1 vbn2
* bias circuit for folded cascode amplifier
* nominal reference current: 40uA from vdd
mns0    vdn0 vdn0   vss vss n1 l=4u w=20u ad=46p as=46p pd=24.6u ps=24.6u nrd=65m nrs=65m
mnc0    iref iref vdn0 vdn0 n1 l=.8u w=20u ad=46p as=46p pd=24.6u ps=24.6u nrd=65m nrs=65m
mns1    vdn1 vdn0   vss vss n1 l=4u w=20u ad=46p as=46p pd=24.6u ps=24.6u nrd=65m nrs=65m
mnc1    vbp1 iref vdn1 vdn0 n1 l=.8u w=20u ad=46p as=46p pd=24.6u ps=24.6u nrd=65m nrs=65m
mps1    vdp1 vbp1   vdd vdd p1 l=2u w=28u ad=64.4p as=64.4p pd=32.6u ps=32.6u nrd=46m nrs=46m
mpc1    vbp1 vbp2   vdp1 vdd p1 l=1u w=56u ad=129p as=129p pd=60.6u ps=60.6u nrd=23m nrs=23m
mns2    vdn2 vdn0   vss vss n1 l=4u w=20u ad=46p as=46p pd=24.6u ps=24.6u nrd=65m nrs=65m
mnc2    vbp2 iref vdn2 vdn0 n1 l=.8u w=20u ad=46p as=46p pd=24.6u ps=24.6u nrd=65m nrs=65m
mps2    vbp2 vbp2   vdd vdd p1 l=5u w=24u ad=55.2p as=55.2p pd=28.6u ps=28.6u nrd=54m nrs=54m
mps3    vdp3 vbp1   vdd vdd p1 l=2u w=28u ad=64.4p as=64.4p pd=32.6u ps=32.6u nrd=46m nrs=46m
mpc3    vbn1 vbp2 vdp3 vdd p1 l=1u w=56u ad=129p as=129p pd=60.6u ps=60.6u nrd=23m nrs=23m
mnc3    vbn1 vbn2 vdn3 vss n1 l=2u w=40u ad=92p as=92p pd=44.6u ps=44.6u nrd=32.5m nrs=32.5m
mns3    vdn3 vbn1   vss vss n1 l=4u w=20u ad=46p as=46p pd=24.6u ps=24.6u nrd=65m nrs=65m
mps4    vdp4 vbp1   vdd vdd p1 l=2u w=28u ad=64.4p as=64.4p pd=32.6u ps=32.6u nrd=46m nrs=46m
mpc4    vbn2 vbp2 vdp4 vdd p1 l=1u w=56u ad=129p as=129p pd=60.6u ps=60.6u nrd=23m nrs=23m
mns4    vbn2 vbn2   vss vss n1 l=5u w=9u ad=20.7p as=20.7p pd=13.6u ps=13.6u nrd=144m nrs=144m
.ends fcbias

```

*Fig. 7.25 SPICE model of transconductance amplifier and bias block. The amplifier bias terminal vbp0 is shorted to vbp1. The vbn1 bias is used for common mode feedback.*

```
* common mode regulation
.subckt cmreg vss vdd vcm vbn out1 out2 vcmf tp tn cp cn
cout1 out1 vcmf 100f
cxf1 xft1 xbn 100f
xcmal vss vdd tp tn out1 xft1 sw2
xcmol vss vdd cp cn vcm xft1 sw2

cout2 out2 vcmf 100f
cxf2 xft2 xbn 100f
xcmal vss vdd tp tn out2 xft2 sw2
xcmo2 vss vdd cp cn vcm xft2 sw2

xbta1 vss vdd tp tn vcmf xbn sw2
xbta2 vss vdd tp tn vcmf xbn sw2
xbtol vss vdd cp cn vbn xbn sw2
xbto2 vss vdd cp cn vbn xbn sw2
* dummy resistors to ensure op convergence
rcmol vcm xft1 100g
rcmo2 vcm xft2 100g
rbto vbn xbn 100g
* common mode regulation for dc operating point (dummy)
rcmfb vcmf cmrl 100g
eout1 cmrl cmr2 out1 vcm 0.1
eout2 cmr2 vbn out2 vcm 0.1
.ends cmreg
```

*Fig. 7.26 SPICE netlist of common mode feedback network. The transmission gate switches sw2 are defined in Figure 7.34. The digital control signals for the transmission gates are tp, tn and cp, cn.*

**Let's take a look at the performance of our transconductor!**

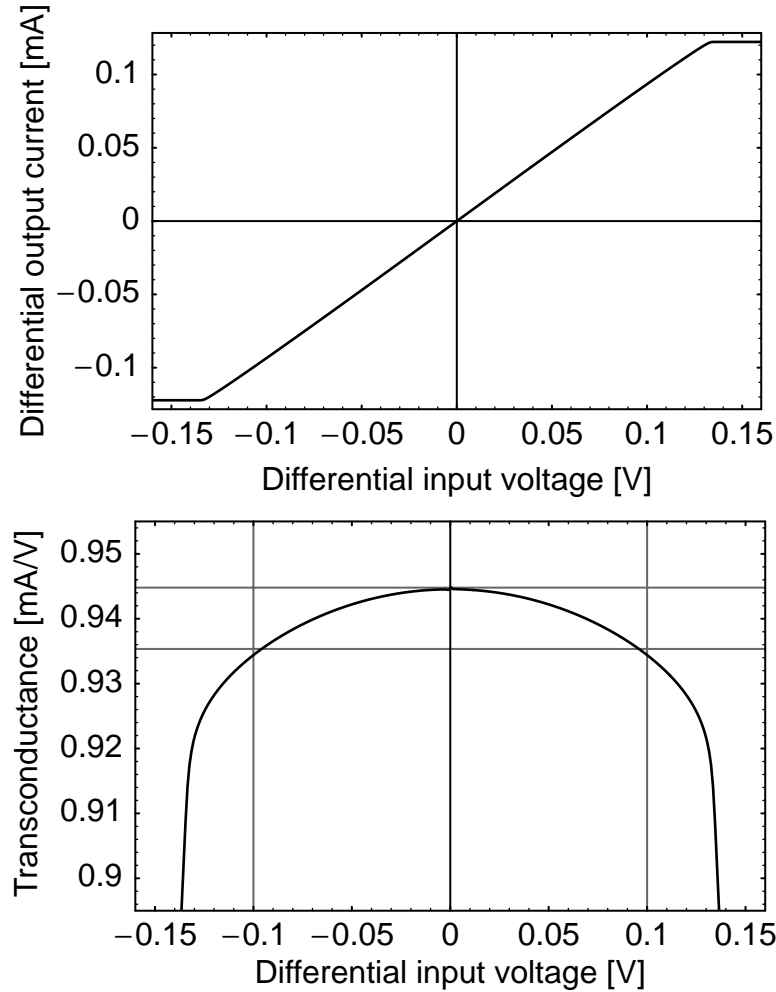


Fig. 7.27 Differential output current and DC large signal transconductance<sup>a</sup>  $\Delta I_d / \Delta V_{in}$ , obtained from the SPICE simulation of the transconductance amplifier described in Figure 7.25. The design target of 1% linearity for a  $\pm 100$  mV input voltage range is indicated by gray lines.

a. Note that the large signal transconductance is *not* equal to the small signal  $g_m$ :  $\frac{\Delta I_d}{\Delta V_{in}} \neq \frac{dI_d}{dV_{in}}$ .

The DC transconductance is simulated with the differential outputs shorted by an ammeter. Figure 7.27 confirms that the 1% linear transconductance range is  $\pm 100$  mV, as designed.

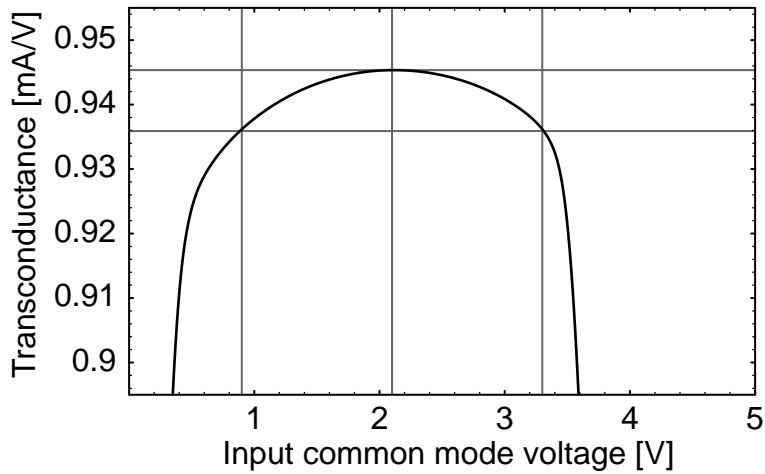


Fig. 7.28 Dependence of DC small signal transconductance  $dI_d/dV_{in}$  on the input common mode voltage. The gray lines indicate the common mode range in which the transconductance deteriorates less than 1%.

Figure 7.28 shows the dependence of the small signal transconductance on the common mode input. The maximal transconductance is obtained at an input common mode voltage of 2.1 V. Between 0.9 V and 3.3 V, the transconductance deteriorates less than 1%.

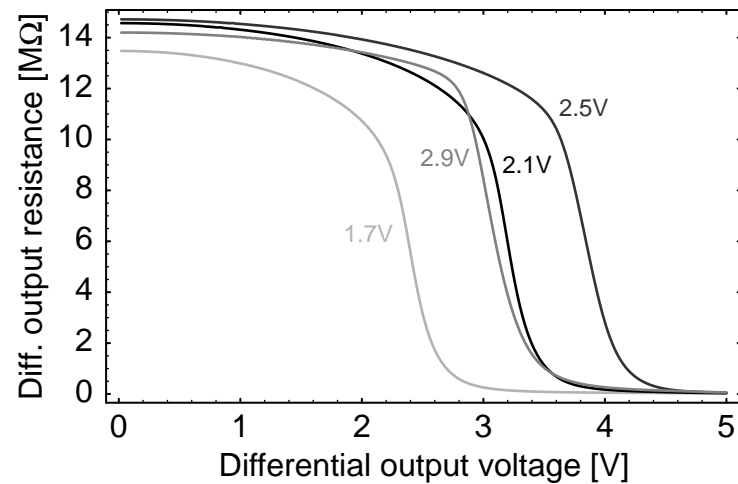
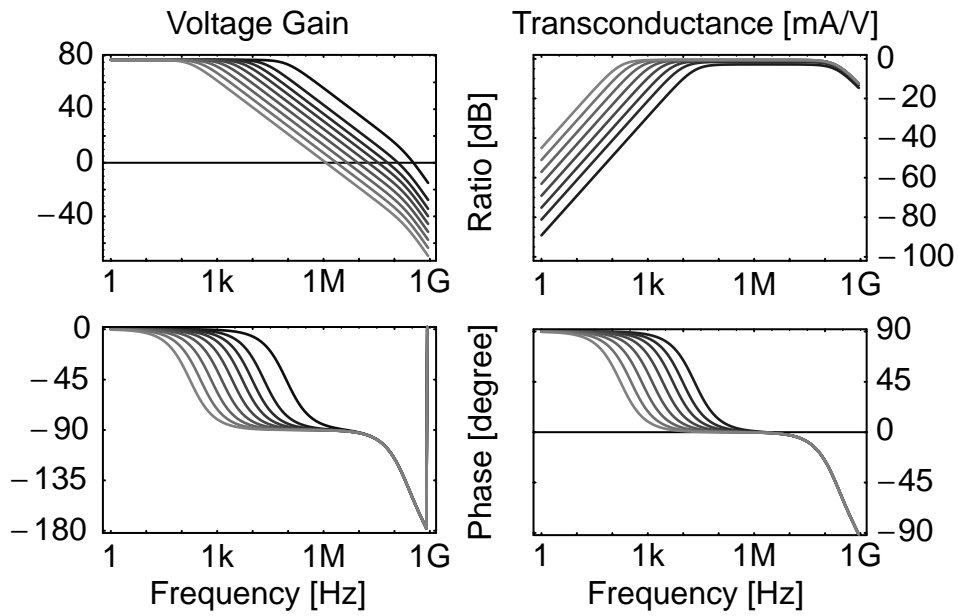


Fig. 7.29 Differential output resistance  $\Delta I_{out}/\Delta V_{out}$  for different output common mode voltages.

The large signal differential output resistance is shown in Figure 7.29. It deteriorates for differential output voltages of more than 1.5 V.



*Fig. 7.30* AC small signal voltage gain (left) and transconductance (right), with integrating capacitors of 64 pF, 32 pF, 16 pF, 8 pF, 4 pF, 2 pF, 1 pF, and 400 fF between the output terminals (light to dark gray). The voltage gain with no integrating capacitor is shown in black in the left diagrams.<sup>a</sup>

- a. The transconductance shown is the transconductance of one of the input transistors. The ratio of differential output current to input differential current is only half as large.

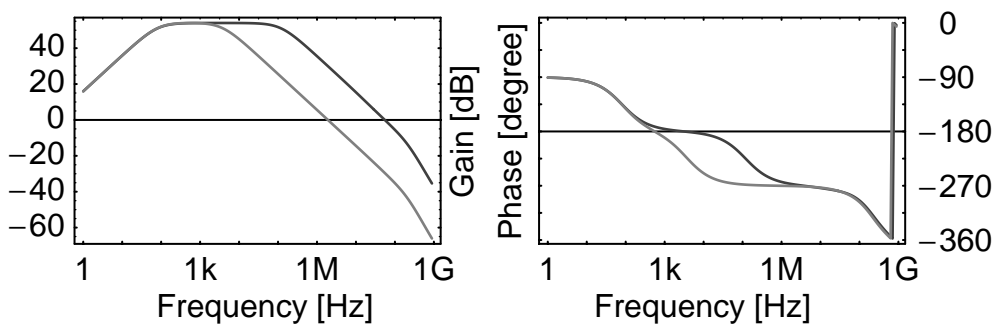


*Fig. 7.31* Open loop small signal gain of the common mode feedback loop with no additional load capacitance (black) and 8 pF capacitance at each output (gray). The roll-off and phase lead at low frequencies are artefacts of the dummy resistor that sets the DC operating point.

It's standard design procedure to simulate the AC voltage gain. But as we might be more interested in the transconductance, I've simulated it, too; see Figure 7.30.

It's *not* just standard procedure to simulate the AC common mode gain: we need a stable common mode operating point. The simulation result in Figure 7.31 confirms that the common mode regulation is stable with and without load capacitance at the output.

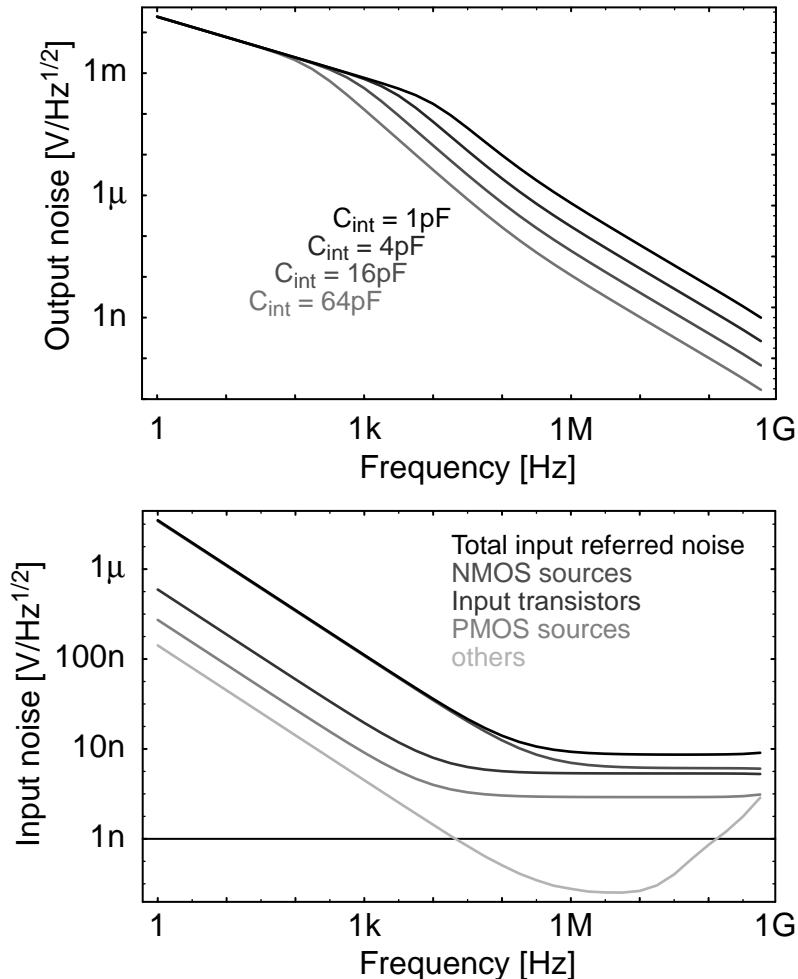


Fig. 7.32 SPICE3 noise simulation of differential output noise density (top) for different integration capacitances, and of input referred noise with contributions of the major noise sources (bottom). The input referred noise is independent of the load capacitance.

Finally, let's have a look at the noise. Simulations for different integration capacitances (Figure 7.32) show that the input referred noise spectral density is independent of the capacitance, while the output noise scales with  $1/C_{int}$ . When we trace back the origin of the noise, we see that it is justified to consider only the

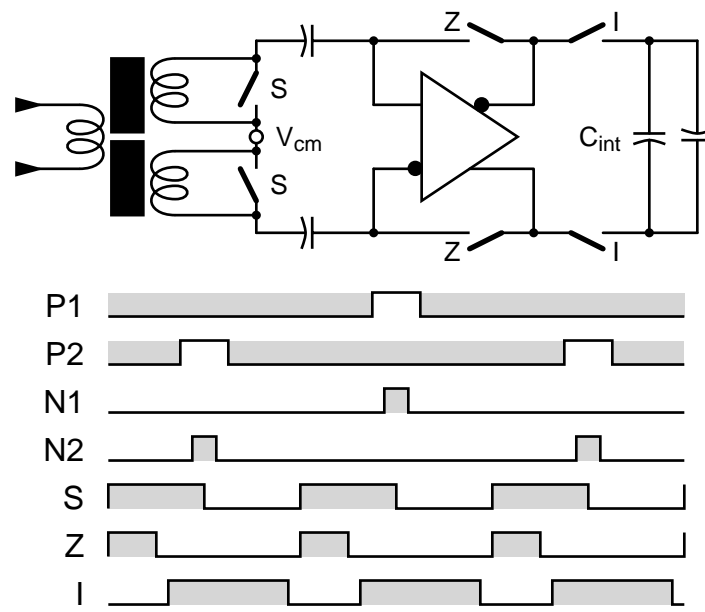
input transistors and the current sources, as in (7.26). The total thermal noise of  $8.3 \text{ nV}/\sqrt{\text{Hz}}$  is  $\sqrt{6.8}$  times the noise for a transconductance of  $1 \text{ mA/V}$ . This is somewhat more than the theoretical value from (7.26) of 5.2.

The thermal noise performance of the transconductor is ok, but the  $\frac{1}{f}$  noise and worse yet, offset, can deteriorate our measurement seriously.

### Let's get rid of offset and $1/f$ noise!

There are two methods to eliminate offset and  $\frac{1}{f}$  noise (which we can think of as offset drift):

- *Chopper amplifier*: The polarity of the signal is reversed before and after the offset-ridden amplifier by two sets of cross-coupled switches. This is the usual choice for a fluxgate readout amplifier, because the flux imbalance signals to and from peak excitation have alternating polarities. A cross-coupled switch is needed only at the output.<sup>1</sup>
- *Correlated double sampling*: In a first measurement, only the offset is measured. It is subtracted from the second measurement of signal plus offset.



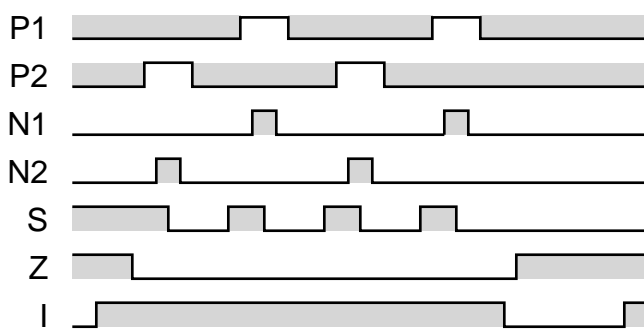
While the pick-up coils are shorted (**S** switches closed), the input voltage is zero. The amplifier offset is stored on the coupling capacitors between the pick-up coil and the integrator amplifier when the auto zero (**Z**) switches are closed. The integration (**I**) switches are opened to speed up the settling of the transconductance amplifier in closed loop configuration. The autozero cycle is terminated before the sensor is excited.

1. A flux scale using the chopper principle and an *excellent* planar 2D fluxgate sensor has been developed at EPFL and presented at Transducers'99. [125]

If the **Z** and **I** switches are closed simultaneously, the integrating capacitors are discharged to the amplifier offset voltage, and the integrator is reset. If the **Z** and **I** switches are switched on in a non-overlapping sequence, the integrator can be auto-zeroed once per sensor excitation.

For every auto-zero cycle, we pay two penalties:

- We sample  $kT/C$  noise on both the coupling and the integration capacitances.
- Part of the integrated signal charge leaks to the output capacitances of the transconductance amplifier.



But we can choose a timing that leaves the integrating capacitance connected to the transconductance in open loop configuration (**Z** open, **I** closed) for several sensor excitation cycles. In this mode, the short-circuit (**S**) switches act as half-wave shunt rectifier for the flux imbalance signal.

We can use the same trick to speed up settling of the transconductance amplifier common mode voltage: by closing all switches simultaneously, we precharge the output terminals and the feedback transistor gate to approximately correct voltages. Doing this, we're shorting the amplifier outputs. But this doesn't hurt if we do it at the *beginning* of a measurement cycle, when we want to start from zero differential voltage and charge, anyway.

## 7.6 Putting It All Together

We have now covered a lot of issues:

- We started with a *very* simple model of a balance for a toy bridge, which just *happens* to be rather useful to understand a sensor that measures magnetic flux imbalance.
- We have adapted an equivalent circuit model of nonlinear inductances to get a model for a flux imbalance sensor.

- We have compared this model to measurement and found a significant difference between model and measurement. We have extended our model to conform with measurement.
- We have devised an excitation and readout scheme with a trick that throws away half our imbalance signal, but saves a lot of energy.
- We have designed the circuits needed to excite the flux imbalance sensor and to measure the flux imbalance signal. We've even found a nice way to eliminate noise and offset.

So, now it's time to put together the scale for flux imbalance that we want!

### Toy Box Design

The nice thing about a toy train is that “*Its timeless design and modular construction provide children with endless ways to create new layouts and endless ways to play*” [102]. Generally, any good toy box contains a lot of rather simple bits and pieces that fit together easily for a lot of different layouts. I’ve started to make such a toy box for sensor circuits in section 3.5. Now we can use these bits and pieces, and *in particular the way they fit together*, for our flux balance. The principle schematic of the circuit is shown in Figure 7.33.

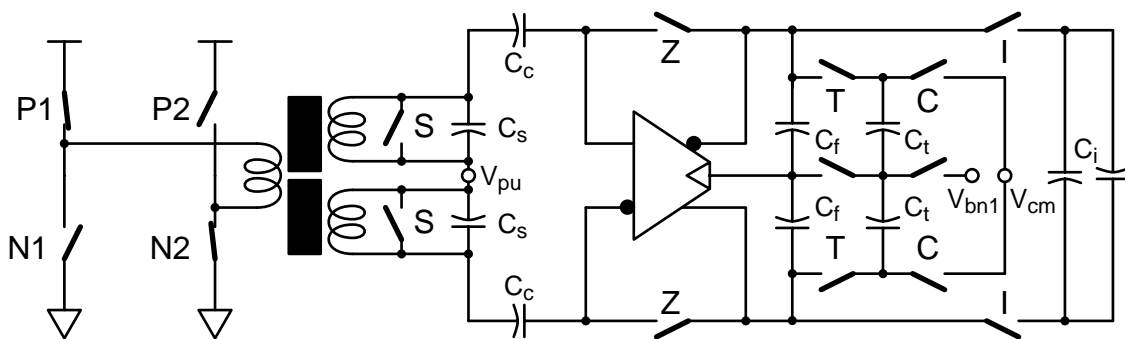


Fig. 7.33 Principle schematic of the flux balance circuit.

The excitation away from the top of the permeability bump is done by the MOSFET switches that we have discussed earlier. While the excitation field is turned on, shunt (**S**) switches ensure that the magnetization of the cores is not delayed by currents through the pick-up coils. The pick-up coils of the fluxgate sensor are *deliberately* loaded with shunt capacitances  $C_s$  to reduce the peak differential voltage of the flux imbalance pulse caused by the *decay* of the magneti-

zation. The peak common mode voltage due to the parasitic capacitance between excitation and pick-up coils is reduced as well. The imbalance signal itself is not reduced, but flattened and spread in time. The flux imbalance integral  $\int V dt$  doesn't change. The differential voltage of the pick-up coils is coupled to the input of the transconductance amplifier by capacitors  $C_c$ . After the flux imbalance pulse has decayed, the offset and  $\frac{1}{f}$  noise of the transconductance amplifier are stored on these capacitors by simultaneously closing the **S** and **Z** switches. The instantaneous noise and offset is sampled when the **Z** switches are opened. That's why  $C_c$  should be at least as large as the capacitors  $C_i$  for the integration of the flux imbalance signal. As the coupling capacitors and the gate capacitance of the input transistors form a capacitive divider,  $C_c$  should also be larger than the input capacitance of the transconductance amplifier. The flux imbalance signal is integrated on a capacitance  $C_i$  between the output terminals of the fully differential transconductance amplifier. The **I** switches connect the integration capacitor to the amplifier. They are opened when an offset compensation cycle is necessary during an ongoing measurement. Part of the integrated signal charge is diverted to the capacitors  $C_f$  that close the common mode feedback loop. When the common mode feedback capacitors  $C_t$  are switched during measurement, they act as leakage capacitors: the effective number of peaks in equation (7.21) is set by the capacitor ratio  $(2C_i + C_f + C_t)/C_t$ . When the transconductor is auto-zeroed, this ratio is  $(2C_i + C_f)/C_f$ . In both cases, the sensitivity of our flux balance does not depend on the operating frequency.

The schematic of the flux balance circuit contains a lot of switches. They are small but nonetheless important bits of our toy box. For the sake of our game, let's use CMOS transmission gate switches as provided by the foundry [116], and an additional design with  $W = 4 \mu\text{m}$ . They have already been used in the Hall magnetometer. SPICE design parameters for the switches are listed in Figure 7.34.

For the toy box concept to make any sense, we should be able to build different toys from the same set of bits and pieces. With the basic design shown in Figure 7.33, we can build a variety of flux scales. We just orchestrate the switch timing in different ways.

```

.subckt sw10 vss vdd gn gp a b
* complementary switch, w=10.4u
mp      a   gp      b   vdd p1 l=.8u w=10.4u ad=24p as=24p pd=15u ps=15u nrd=125m nrs=125m
mn      a   gn      b   vss n1 l=.8u w=10.4u ad=24p as=24p pd=15u ps=15u nrd=125m nrs=125m
.ends sw10

.subckt sw4 vss vdd gn gp a b
* complementary switch, w=4u
mp      a   gp      b   vdd p1 l=.8u w=4u ad=9.2p as=9.2p pd=8.6u ps=8.6u nrd=325m nrs=325m
mn      a   gn      b   vss n1 l=.8u w=4u ad=9.2p as=9.2p pd=8.6u ps=8.6u nrd=325m nrs=325m
.ends sw4

.subckt sw2 vss vdd gn gp a b
* complementary switch, w=2.7u
mp      a   gp      b   vdd p1 l=.8u w=2.7u ad=6.2p as=6.2p pd=7.3u ps=7.3u nrd=481m nrs=481m
mn      a   gn      b   vss n1 l=.8u w=2.7u ad=6.2p as=6.2p pd=7.3u ps=7.3u nrd=481m nrs=481m
.ends sw2

```

*Fig. 7.34 SPICE netlists of the switches used in the assembly of the flux balance systems.*

### Continuous Mode Flux Scale

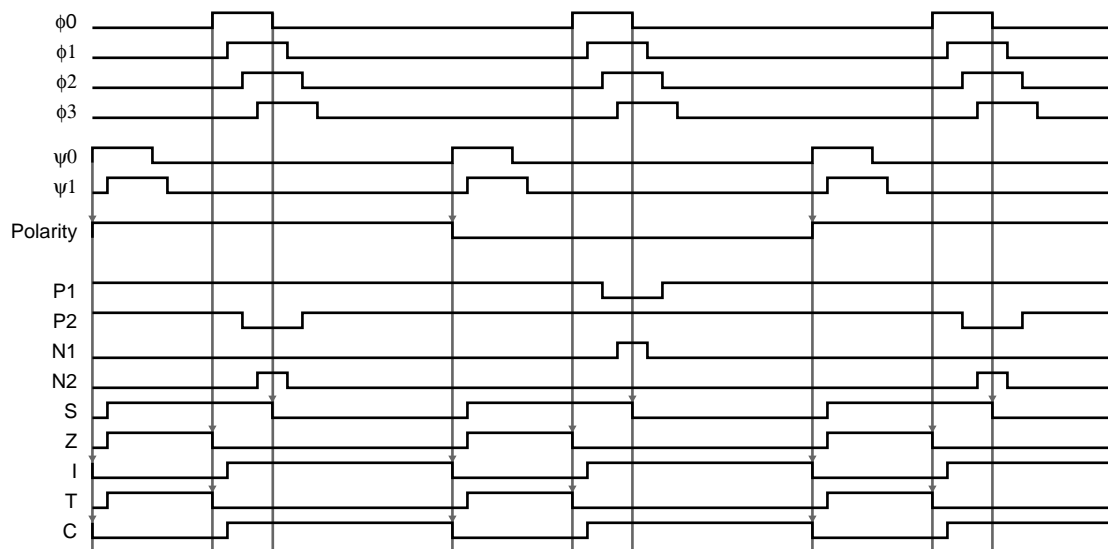


*Fig. 7.35 Switching sequence for continuous operation as leaky integrator.  
For the switch names see Figure 7.33. The top signals show how to derive the switch timing from two external clocks.*

If we want to measure magnetic fields continuously, it makes sense to operate the flux scale as leaky integrator. The switch timing to do this is shown in Figure 7.35: Before the core is magnetized, the transconductance amplifier is auto-zeroed. Immediately before the core magnetization pulse, the auto-zero phase is terminated and the integrating capacitance is connected to the open loop transconduc-

tor. When the core is fully magnetized, the pick-up coil shunt switches are opened. After the flux imbalance voltage caused by the falling magnetization slope has decayed, the integration phase ends and a new auto-zero phase starts.

## Burst Mode Flux Scale

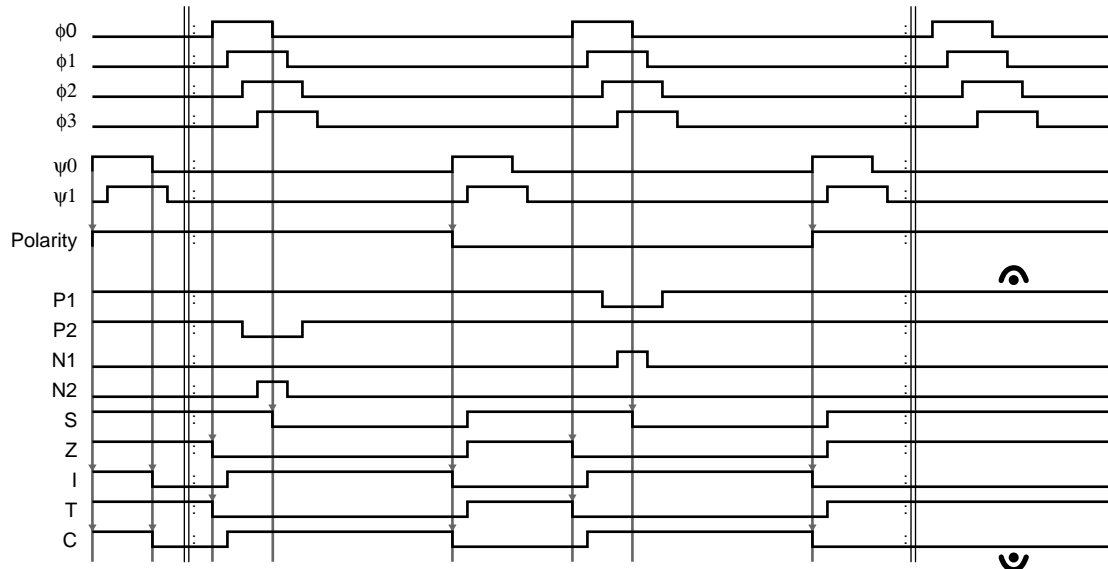


*Fig. 7.36 Switch timing for burst mode. The leftmost up beat resets the integrator differential and common mode voltages. The holding time is limited only by the leakage current of the opened **I** switches.*

*For the switch names see Figure 7.33. The top signals show how to derive the switch timing from two external clocks.*

In many cases, the weak magnetic fields that we can measure with our flux balance don't change much over time. As each magnetization of the sensor cores needs a lot of energy, it makes sense to take a measurement every once in a while and power down the flux scale for the remainder of the time. Figure 7.36 shows how it's done: at the beginning of our measurement, we precharge the output to the common mode voltage by closing both the **T** and **C** switches simultaneously during the first auto-zero phase. Thus, lengthy settling of the output common mode voltage is avoided and the transconductance amplifier works right away. After a certain number of core excitation pulses, we simply freeze the switches in auto-zero state, with the accumulated flux imbalance signal stored as voltage on the integrating capacitor. The capacitor can then be connected to an output buffer

or a data converter. For a continuous analog output voltage, we can switch two identical integration capacitors back and forth between our flux balance and an output buffer.

*Let's take a look how this flux scale behaves when we simulate it!*

```

* timing generator for fluxgate drive, leaky integrator mode
.subckt leaky vss vdd n1 n2 p1 p2 sh zp zn ip in tp tn cp cn
* nodes:
* vdd: positive supply
* vss: negative supply
* n1: drive bridge #1 n-channel
* n2: drive bridge #2 n-channel
* p1: drive bridge #1 p-channel
* p2: drive bridge #2 p-channel
* sh: drive for shunt transistors
* zp,zl: drive for autozero switches (active H,L)
* ip,il: drive for output switches (active H,L)
* tp,tl: drive for cmfb charge transfer switches (active H,L)
* cp,cn: drive for cmfb precharge switches (active H,L)

* reset state flag
vres res 0 dc 1 pulse(0 1 0 500p 500p 40n 20u)

vn1drv n1 vss dc 0 pulse(0 5 80n 500p 500p 20n 500n)
vn2drv n2 vss dc 0 pulse(0 5 330n 500p 500p 20n 500n)
vp1drv vdd p1 dc 5 pulse(5 0 76n 500p 500p 28n 500n)
vp2drv vdd p2 dc 5 pulse(5 0 326n 500p 500p 28n 500n)
vsdrv sh vss dc 5 pulse(0 5 4n 500p 500p 86n 250n)
vzpdrv zp vss dc 5 pulse(0 5 4n 500p 500p 64n 250n)
vzndrv vdd zn dc 5 pulse(0 5 4n 500p 500p 64n 250n)
vipdrv ip vss dc 5 pulse(0 5 72n 500p 500p 178n 250n)
 vindrv vdd iin dc 5 pulse(0 5 72n 500p 500p 178n 250n)
 bipdrv vdd ip v=(1-v(res))*v(vdd,iip)
 bindrv in vss v=(1-v(res))*v(iin,vss)
 vtpdrv ttp vss dc 5 pulse(0 5 4n 500p 500p 64n 250n)
 vtndrv vdd ttn dc 5 pulse(0 5 4n 500p 500p 64n 250n)
 btpdrv vdd tp v=(1-v(res))*v(vdd,ttp)
 btndrv tn vss v=(1-v(res))*v(ttn,vss)
 vcpdrv ccp vss dc 5 pulse(0 5 72n 500p 500p 178n 250n)
 vcndrv vdd ccn dc 5 pulse(0 5 72n 500p 500p 178n 250n)
 bcpdrv vdd cp v=(1-v(res))*v(vdd,ccp)
 bcndrv cn vss v=(1-v(res))*v(ccn,vss)
.ends leaky

```

*Fig. 7.37 SPICE3 netlist for the auto-zero/leaky integrator timing mode shown in Figures 7.35 and 7.36.*

The netlist to implement the timing is shown in Figure 7.37. But before we can start the simulation, we have to choose values for the capacitors.

- The shunt capacitance  $C_s$  must scale down the pick-up coil peak voltages by a factor of 2, so it should be about the same as all the parasitic capacitances at the pick-up coil in parallel.
- We've already picked a small but arbitrary value for the common mode feedback capacitances.

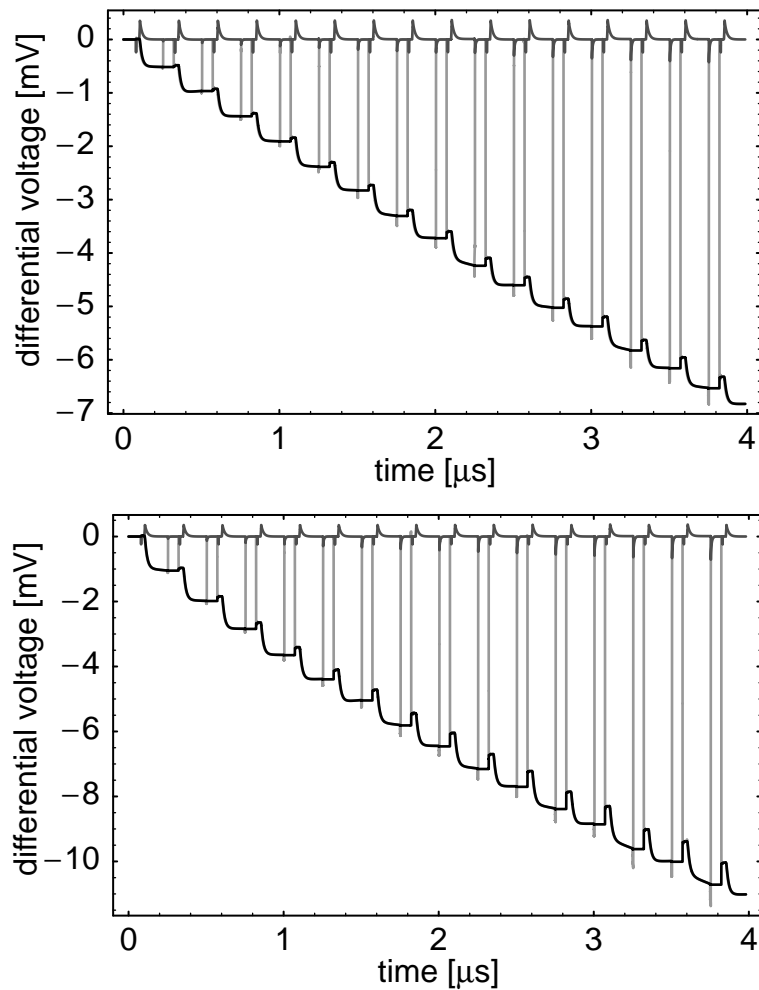


*Fig. 7.38 SPICE simulation of differential voltage at the integrating capacitor (black), differential input voltage (dark gray), and differential output voltage at the transconductor outputs (light gray), for an integration capacitance of  $C_i = 5\text{ pF}$  (top) and  $C_i = 2.5\text{ pF}$  (bottom). The circuit is operated in leaky integrator mode.*

- The coupling capacitances  $C_c$  should be about the same or slightly larger than the integration capacitance  $C_i$ .

So, the integration capacitance is the difficult part.

According to our specs in Table 7.2, we're aiming at a full scale output voltage in the  $\pm 1\text{ V}$  ballpark, at a dynamic range of 12 bits. So, we're aiming for a total noise

of about  $250\mu\text{V}$ . With a conservative estimate of the thermal noise excess factor of  $\text{NEF} = 7$  and the formula for the total thermal noise we get:

$$v^2 = \text{NEF} \frac{8kT}{3C_i} \text{ and thus}^1 \quad (7.34)$$

$$C_i = \frac{56kT}{3v^2} = 18.7 \cdot \frac{4142(\text{pF} \cdot \mu\text{V}^2)}{v^2} = \frac{77500(\text{pF} \cdot \mu\text{V}^2)}{(250\mu\text{V})^2} = 1.24\text{pF}. \quad (7.35)$$

Let's be conservative and try two values for the integration capacitor:  $C_i = 5\text{pF}$  and  $C_i = 2.5\text{pF}$ . My choice of the other capacitance values are  $C_s = 2\text{pF}$ ,  $C_c = 5\text{pF}$ , and  $C_f = C_t = 100\text{fF}$ .

Figure 7.38 shows the transient simulation of the flux balance system, operated in leaky integrator mode. For the first input flux imbalance peaks, the sensitivity is  $S_\phi = 0.88 \text{ V}/(\text{mV} \cdot \mu\text{s})$  and  $S_\phi = 1.70 \text{ V}/(\text{mV} \cdot \mu\text{s})$ , respectively. Some 10% of the input signal amplitude is lost across the coupling capacitors  $C_c$ . The integrator leakage is clearly visible as spikes towards zero when  $C_i$  is reconnected to  $C_f$  after the auto-zero phase. Unfortunately, the numerical roundoff errors of SPICE3 [110] prevent us from extracting a reliable figure for the effective number of peaks. I'm pushing SPICE and my computer to their very limits to get any reasonable simulation at all! Nevertheless, they *do* confirm that a flux scale as shown in Figure 7.33 and operated with the switch timing shown in Figure 7.36 works just fine.

### Fast and Efficient Flux Scale with Pre-Initialization

If we want to build a *very* efficient flux scale, we can do even better. *We don't even need to change the circuit in Figure 7.33!* We only need to change the switch timing sequence according to Figure 7.39: Instead of interleaving auto-zero and common mode adjustment cycles with our measurement, we adjust the common mode and compensate the offset in advance. Only then we take the measurement under conditions as ideal as possible. Let's have a look at the SPICE simulation.

---

1. Never mind some factors of 2 that might pop up because of the differential topology...

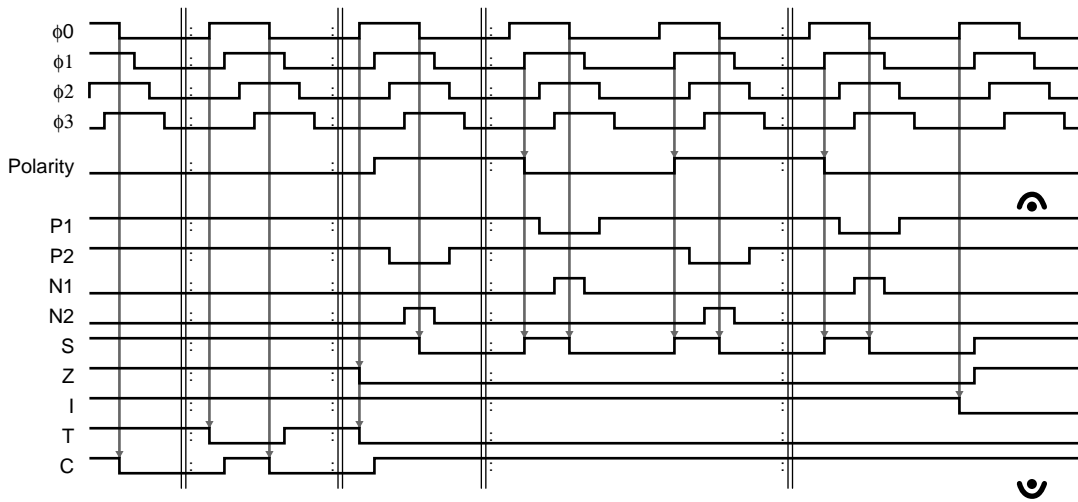


*Fig. 7.39* Switch timing for pre-initialized burst mode. The upbeat preinitializes the common mode voltage. The first loop tunes the common mode voltage while the integration capacitor is reset. The second loop accumulates the flux imbalance signal without leakage. The holding time is limited only by the leakage current of the opened **I** switches.  
For the switch names see Figure 7.33. The top signals show how to derive the switch timing from a single external clock.

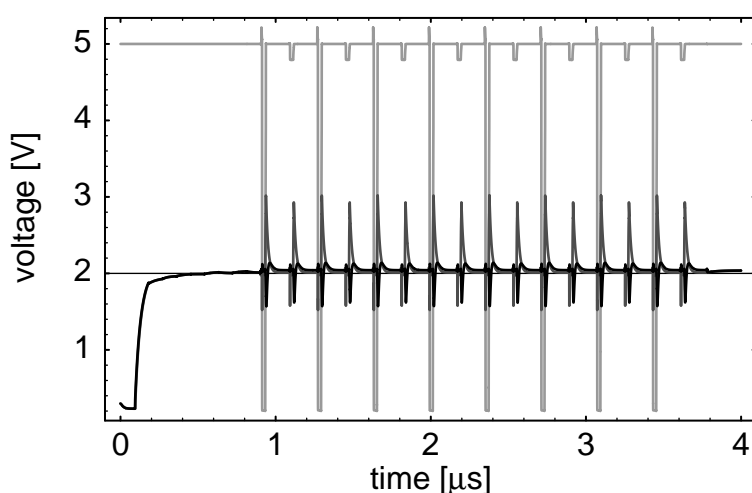


*Fig. 7.40* SPICE simulation of common mode voltages at the output (black) and input (dark gray) of the transconductor of the circuit shown in Figure 7.33, operated in burst mode with preinitialization (see Figure 7.39). The light gray signal is the voltage at one excitation coil terminal.

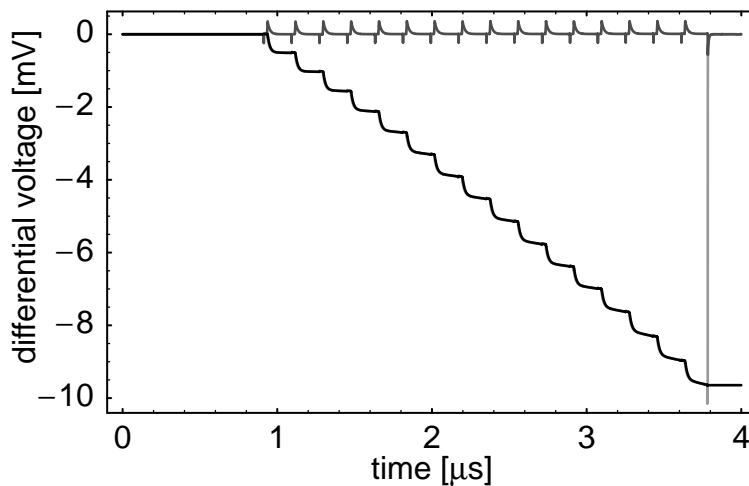


*Fig. 7.41 SPICE simulation of differential voltage at the integrating capacitor (black), differential input voltage (dark gray), and differential voltage at the transconductor outputs (light gray), for an integration capacitance of  $C_i = 5\text{pF}$ . The circuit as shown in Figure 7.33 is operated in burst mode with preinitialization (see Figure 7.39).*

Figure 7.40 shows that the common mode output voltage of the transconductor settles quickly to an *almost* correct value at the end of the reset phase. During the preinitialization phase, it converges further towards the correct operating point. This operating point is then retained during the burst of sensor excitations.

In Figure 7.41 we see that we have no more leakage at the integrator, because no switching occurs at the output of the transconductor during the entire measurement burst. Only at the end of the measurement, the integration capacitance is disconnected and the transconductor returns to auto-zero mode. We have implemented an almost ideal integrator! The increasing slope of the steps in the output voltage is an artefact of SPICE. The numerical error of the simulation is integrated at the input of the transconductor and causes offset.

For extended measurement bursts, offset drift might become a real problem. This problem can be solved by inserting an autozero refresh cycle as in Figures 7.35 and 7.36 into the second cyclic sequence in Figure 7.39. This works just like dynamic RAM refresh by cycle stealing. We lose signal charge and sample  $\frac{kT}{C}$  noise *only* when we need to.

Figure 7.42 shows the netlist to implement the timing of Figure 7.39.

## Quodlibet7 A Child's Play

---

```
* timing generator for fluxgate drive, burst mode
.subckt burst vss vdd n1 n2 p1 p2 sh zp zn ip in tp tn cp cn
* nodes:
* vdd: positive supply
* vss: negative supply
* n1: drive bridge #1 n-channel
* n2: drive bridge #2 n-channel
* p1: drive bridge #1 p-channel
* p2: drive bridge #2 p-channel
* sh: drive for shunt transistors
* zp,zl: drive for autozero switches (active H,L)
* ip,il: drive for output switches (active H,L)
* tp,tl: drive for cmfb charge transfer switches (active H,L)
* cp,cn: drive for cmfb precharge switches (active H,L)

* reset state flag
vres res 0 dc 1 pwl(0 1 180n 1 180.5n 0 10m 0)
* precharge state flag
vpre pre 0 dc 1 pwl(0 1 904n 1 904.5n 0 10m 0)
* integration state flag
vint int 0 dc 0 pwl(0 0 904n 0 904.5n 1 3780n 1 3780.5n 0 10m 0)

vn1drv nn1 vss dc 0 pulse(0 5 12n 500p 500p 20n 360n)
vn2drv nn2 vss dc 0 pulse(0 5 192n 500p 500p 20n 360n)
vp1drv vdd pp1 dc 5 pulse(5 0 8n 500p 500p 28n 360n)
vp2drv vdd pp2 dc 5 pulse(5 0 188n 500p 500p 28n 360n)

bn1drv n1 vss v=v(int)*v(nn1,vss)
bn2drv n2 vss v=v(int)*v(nn2,vss)
bp1drv p1 vss v=v(int)*v(pp1,vss)
bp2drv p2 vss v=v(int)*v(pp2,vss)

vsdrv ssh vss dc 5 pulse(0 5 8n 500p 500p 18n 180n)
bsdrv vdd sh v=v(int)*v(vdd,ssh)

vzpdrv zp vss dc 5 pwl(0 5 900n 5 900.5n 0 3780n 0 3784.5n 5 10m 5)
vzndrv vdd zn dc 5 pwl(0 5 900n 5 900.5n 0 3780n 0 3784.5n 5 10m 5)

vipdrv ip vss dc 5 pwl(0 5 3780n 5 3780.5n 0 10m 0)
 vindrv vdd in dc 5 pwl(0 5 3780n 5 3780.5n 0 10m 0)

vtpdrv ttp vss dc 5 pulse(0 5 94n 500p 500p 86n 180n)
vtndrv vdd ttn dc 5 pulse(0 5 94n 500p 500p 86n 180n)
btpdrv tp vss v=v(pre)*v(tp,vss)
btndrv vdd tn v=v(pre)*v(vdd,ttn)

vcdrv ccp vss dc 5 pulse(0 5 4n 500p 500p 86n 180n)
vcndrv vdd ccn dc 5 pulse(0 5 4n 500p 500p 86n 180n)
bcdrv vdd cp v=v(pre)*(1-v(res))*v(vdd,ccp)
bcndrv cn vss v=v(pre)*(1-v(res))*v(ccn,vss)
.ends burst
```

Fig. 7.42 SPICE3 netlist for the ideal integrator/burst timing mode shown in Figure 7.39.

### We're done!!!

Starting from our very simple toy model, we've designed a very efficient and accurate scale to measure the imbalance signal of a fluxgate sensor. Just by applying different digital timing sequences, we can use the flux scale in different modes: The continuous mode would come in handy when energy consumption is not an issue, for example for sensor characterization, or to build a *very* simple demonstrator to impress your boss. The highly optimized preinitialized burst mode cuts energy consumption down to a minimum. If you *really* wanted to get serious about putting such a toy into a watch, that might come in handy.

## 7.7 Some Notes on the Tools and Equipment Used

### You Don't Need a Lot of Expensive Toys to Play!

For this *Quodlibet*, I have used only a minimum of equipment:

- my own 400 MHz Macintosh PowerBook G3 running Mac OS 9, with
- my own Mathematica 4.0 [126] and
- Anthony Wilson's public domain MacSpice3f4 for the Macintosh [111].

I have taken recourse to Physical Electronics Laboratory resources only twice:

1. To get a minimal measurement data base for the sensor model verification, I have done the measurement of the flux gate signal waveforms with a left over plated microfluxgate sensor,<sup>1</sup> a digital oscilloscope with active differential probe, the waveform generator, and LabView [127] for GPIB based data acquisition and logging. On this occasion, I also built a driver circuit with my own stuff: a pair of 2N3904 and 2N3906 each, plus one 7406 TTL driver to verify that the excitation scheme described herein works in principle.<sup>2</sup> I used the National Instruments DIO6533 board [128] and LabView to generate a digital timing sequence and the digital oscilloscope to look at the waveforms. I did these measurements during the last week of 1999, *after* handing in the examination version of my thesis.
2. To get realistic device models, I extracted the BSIM3v3 MOS model parameters for the CYE process of Austria Mikrosysteme International AG [116] from one of my unpublished circuit designs for the Physical Electronics Laboratory.

It has been my principal objective to demonstrate my ability to do useful circuit design with my own resources only.

### But isn't it crazy not to use all the expensive Professional equipment at PEL?

—*Though this be madness, yet there is method in't.* [131][132][133]

---

1. after breaking its perspex coffin to wire bond the “uninteresting” center tap of the pick-up coil...  
2. However, the diffusion capacitance of the bipolar transistors was a nuisance.

# 8 References

- [102] BRIO AB, Viaduct Bridge, *order #33351*,  
<http://www.brio.se/eng/toy/railway.html>
- [103] D. Chandler, *Introduction to Modern Statistical Mechanics*, Oxford University Press, 1987
- [104] F. Reif, *Fundamentals of Statistical and Thermal Physics*, McGraw–Hill, Singapore, 1965
- [105] L. D. Landau, E. M. Lifschitz, Lehrbuch der Theoretischen Physik, *Bd. VIII: Elektrodynamik der Kontinua*, 5. Aufl., Akademie Verlag Berlin, 1990
- [106] S. Kawahito, H. Satoh, M. Sutoh, Y. Tadokoro, “Micro–Fluxgate Magnetic Sensing Elements Using Closely–Coupled Excitation and Pickup Coils”, *Proc. Transducers’95*, pp. 233–236
- [107] H. Luz, “Magnetic Field Measurements with Foerster–Probes”, *Elektronik*, vol. 8, pp. 247–250, August 1968
- [108] T. Seitz, “Fluxgate Sensor in Planar Microtechnology”, *Sensors and Actuators A21–23*, pp. 799–802, 1990
- [109] M. Schneider, S. Kawahito, H. Baltes, “High Sensitivity CMOS MicroFluxgate Sensor”, *Dig. Tech. Papers, NanoSpace’98*
- [110] T. Quarles, A. R. Newton, D. O. Pederson, A. Sangiovanni–Vincentelli, *SPICE3 Version 3f3 User’s Manual*, University of California, Berkeley 1993, <http://cvs.sourceforge.net/cgi-bin/cvsweb.cgi/macspice3f4/documentation/?cvsroot=macspice3f4>
- [111] Reto Ambühler, Anthony Wilson, *MacSpice3*,  
<http://home.earthlink.net/~wilsona/macspice.html>
- [112] D. C. Jiles, D. L. Atherton, “Theory of ferromagnetic hysteresis”, *Journal of Magnetism and Magnetic Materials*, vol. 61, pp. 48–60, 1986

- [113] H. G. Brachtendorf, C. Eck, R. Laur, “Macromodeling of Hysteresis Phenomena with SPICE”, *IEEE Transactions on Circuits and Systems II*, vol. 40 no. 5, May 1997
- [114] M. Schneider, “CMOS Magnetotransistor and Fluxgate Vector Sensors”, *DISS. ETH No. 12746*, ETH Zürich, 1999
- [115] H. Gröning, “Mehrgitterbewegungssegmentierung und Messungen am großen Simulationstank zur Bestimmung von Sedimentverlagerungen”, *Diploma thesis*, Fakultät für Physik und Astronomie, Universität Heidelberg, August 1996
- [116] Austria Mikrosysteme International AG, <http://www.amsint.com/>
- [117] W. Liu, X. Jin, J. Chen, M.-C. Jeng, Z. Liu, Y. Cheng, K. Chen, M. Chan, K. Hui, J. Huang, R. Tu, P. K. Ko, C. Hu, BSIM3v3.2.2 MOSFET Model, *User’s Manual*, Dept. of EECS, University of California, Berkeley, 1999, <http://www-device.EECS.Berkeley.EDU/~bsim3/>
- [118] SpectreS BSIM3v3 MOS device models for the CYE technology, Austria Mikrosysteme International AG, <http://www.amsint.com/>
- [119] T. Hornak, “True Analog Circuit Design”, in: *Analog Circuit Design, Art, Science, and Personalities*, ed. Jim Williams, Butterworth–Heinemann, 1991
- [120] C. Yoo, S.–W. Lee, W. Kim, “A  $\pm 1.5$ -V, 4-MHz CMOS Continuous-Time Filter with a Single-Integrator Based Tuning”, *IEEE Journal of Solid-State Circuits*, vol. 33 no. 1, January 1998, pp. 18–27
- [121] R. Sarpeshkar, T. Delbrück, C. Mead, “White Noise in MOS Transistors and Resistors”, *IEEE Circuits and Devices*, November 1993, pp. 23–29
- [122] K. R. Laker, W. M. C. Sansen, *Design of Analog Integrated Circuits and Systems*, chapter 6.4, McGraw–Hill, Singapore 1994
- [123] J. S. Bach, The Art of Fugue: Contrapunctus VIII, Contrapunctus XI, *BWV 1080*
- [124] J. S. Bach, Double Violin Concerto, *BWV 1043*

- [125] L. Chiesi, P. Kejik, B. Janossy, R. S. Popovic, “CMOS Planar 2D Micro-Fluxgate Sensor”, *Proc. Transducers’99*, Sendai 1999
- [126] S. Wolfram, *The Mathematica Book*, 4th edition, Cambridge University Press, 1999
- [127] National Instruments Corporation, *LabView 4.0 User Manual*, January 1996
- [128] National Instruments Corporation, *DIO 6533 User Manual*, available from <http://www.ni.com/>
- [129] R. Russell, “The Process of Analog Design”, in: *Analog Circuit Design, Art, Science, and Personalities*, ed. Jim Williams, Tchebycheff–Heinemann, 1991
- [130] Niccolo Machiavelli, *The Prince*, Penguin Books, London 1995,  
<http://www.constitution.org/mac/prince00.htm>  
<http://207.250.124.106/intellex/home/pstm/prince/pstmbpri.htm>
- [131] R. P. Feynman, Appendix F: Personal Observations on the Reliability of the Shuttle, in “*What do you care what other people think?*”, Bantam Books, 1989, <http://www.vitalschool.edu/mon/SocialConstruction/FeynmanChallengerRpt.html>
- [132] R. P. Feynman, Afterthoughts, in “*What do you care what other people think?*”, Bantam Books, 1989
- [133] F. McGillivray, A. Smith, “*Cooperating Democrats, Defecting Autocrats*”, Paper presented at the Peace Science Society meeting, Rutgers NJ October 1998. [http://wizard.ucr.edu/cps/working\\_papers98/mcgillavry98.html](http://wizard.ucr.edu/cps/working_papers98/mcgillavry98.html)
- [134] Wilhelm Busch, “Diogenes und die bösen Buben von Korinth”, in: *Lustige Wilhelm Busch Sammlung*, Braun & Schneider, Munich 1955.  
<http://gutenberg.aol.de/wbusch/diogen/diogen.htm>
- [135] Antoine de Saint Exupery, *Le Petit Prince*, Reynal & Hitchcock, New York 1943. <http://www.geocities.com/Athens/Rhodes/1916/index2.html>

### SPICE3 Netlist of the Flux Balance Circuit

```

* Childs Play Flux Balance

.control
set sourcepath = ( ChristophMaierG3 :CVS :macspice3f4 )
.endc
.include amscye.cir

.subckt fcasc vss vdd vbp0 vbp1 vbp2 vbn1 vbn2 in1 in2 out1 out2
* folded cascode amplifier
* target: 1mA/V transconductance
* 1% linear range: 100mV
mcs    vcs vbp0 vdd vdd p1 l=2u w=280u ad=644p as=644p pd=285u ps=285u nrd=4.6m nrs=4.6m
min1   vd1 in1  vcs vcs p1 l=2u w=140u ad=322p as=322p pd=149u ps=149u nrd=9.3m nrs=9.3m
mns1   vd1 vbn1 vss vss n1 l=4u w=130u ad=299p as=299p pd=135u ps=135u nrd=10m nrs=10m
mnc1   out1 vbn2 vd1 vss n1 l=2u w=60u ad=138p as=138p pd=65u ps=65u nrd=22m nrs=22m
mpc1   out1 vbp2 vp1 vdd p1 l=1u w=84u ad=193p as=193p pd=89u ps=89u nrd=15.4m nrs=15.4m
mps1   vp1 vbp1 vdd vdd p1 l=2u w=42u ad=97p as=97p pd=47u ps=47u nrd=31m nrs=31m
.ends fcasc

.subckt fcbias vss vdd iref vbp1 vbp2 vbn1 vbn2
* bias circuit for folded cascode amplifier
* nominal reference current: 40uA from vdd
mns0 vdn0 vdn0 vss vss n1 l=4u w=20u ad=46p as=46p pd=24.6u ps=24.6u nrd=65m nrs=65m
mnc0 iref iref vdn0 vdn0 n1 l=.8u w=20u ad=46p as=46p pd=24.6u ps=24.6u nrd=65m nrs=65m

mns1 vdn1 vdn0 vss vss n1 l=4u w=20u ad=46p as=46p pd=24.6u ps=24.6u nrd=65m nrs=65m
mnc1 vbp1 iref vdn1 vdn0 n1 l=.8u w=20u ad=46p as=46p pd=24.6u ps=24.6u nrd=65m nrs=65m
mps1 vdp1 vbp1 vdd vdd p1 l=2u w=28u ad=64.4p as=64.4p pd=32.6u ps=32.6u nrd=46m nrs=46m
mpc1 vbp1 vdp1 vdd p1 l=1u w=56u ad=129p as=129p pd=60.6u ps=60.6u nrd=23m nrs=23m

mns2 vdn2 vdn0 vss vss n1 l=4u w=20u ad=46p as=46p pd=24.6u ps=24.6u nrd=65m nrs=65m
mnc2 vbp2 iref vdn2 vdn0 n1 l=.8u w=20u ad=46p as=46p pd=24.6u ps=24.6u nrd=65m nrs=65m
mps2 vbp2 vbp2 vdd vdd p1 l=5u w=24u ad=55.2p as=55.2p pd=28.6u ps=28.6u nrd=54m nrs=54m

mp3 vdp3 vbp1 vdd vdd p1 l=2u w=28u ad=64.4p as=64.4p pd=32.6u ps=32.6u nrd=46m nrs=46m
mpc3 vbn1 vbp2 vdp3 vdd p1 l=1u w=56u ad=129p as=129p pd=60.6u ps=60.6u nrd=23m nrs=23m
mnc3 vbn1 vbn2 vdn3 vss n1 l=2u w=40u ad=92p as=92p pd=44.6u ps=44.6u nrd=32.5m nrs=32.5m
mns3 vdn3 vbn1 vss vss n1 l=4u w=20u ad=46p as=46p pd=24.6u ps=24.6u nrd=65m nrs=65m

mps4 vdp4 vbp1 vdd vdd p1 l=2u w=28u ad=64.4p as=64.4p pd=32.6u ps=32.6u nrd=46m nrs=46m
mpc4 vbn2 vbp2 vdp4 vdd p1 l=1u w=56u ad=129p as=129p pd=60.6u ps=60.6u nrd=23m nrs=23m
mns4 vbn2 vbn2 vss vss n1 l=5u w=9u ad=20.7p as=20.7p pd=13.6u ps=13.6u nrd=144m nrs=144m
.ends fcbias

* common mode regulation
.subckt cmreg vss vdd vcm vbn out1 out2 vcmf tp tn cp cn
cout1 out1 vcmf 100f
cxfl1 xft1 xbn 100f
xcmal vss vdd tp tn out1 xft1 sw2
xcmol vss vdd cp cn vcm xft1 sw2

cout2 out2 vcmf 100f
cxfl2 xft2 xbn 100f
xcmal2 vss vdd tp tn out2 xft2 sw2
xcmol2 vss vdd cp cn vcm xft2 sw2

xbta1 vss vdd tp tn vcmf xbn sw2
xbta2 vss vdd tp tn vcmf xbn sw2
xbto1 vss vdd cp cn vbn xbn sw2
xbto2 vss vdd cp cn vbn xbn sw2
* dummy resistors to ensure op convergence
rcmol vcm xft1 100g
rcmo2 vcm xft2 100g
rbto vbn xbn 100g
* common mode regulation for dc operating point (dummy)
rcmfb vcmf cmr1 100g
eout1 cmrl cmr2 out1 vcm 0.1
eout2 cmr2 vbn out2 vcm 0.1
.ends cmreg

```

## 7.7 Some Notes on the Tools and Equipment Used

---

```

.subckt diffin inp inn com
* circuit to center a differential voltage
ediff com inn inp inn 0.5
.ends diffin

.subckt sw10 vss vdd gn gp a b
* complementary switch, w=10.4u
mp      a   gp     b   vdd p1 l=.8u w=10.4u ad=24p as=24p pd=15u ps=15u nrd=125m nrs=125m
mn      a   gn     b   vss n1 l=.8u w=10.4u ad=24p as=24p pd=15u ps=15u nrd=125m nrs=125m
.ends sw10

.subckt sw4 vss vdd gn gp a b
* complementary switch, w=4u
mp      a   gp     b   vdd p1 l=.8u w=4u ad=9.2p as=9.2p pd=8.6u ps=8.6u nrd=325m nrs=325m
mn      a   gn     b   vss n1 l=.8u w=4u ad=9.2p as=9.2p pd=8.6u ps=8.6u nrd=325m nrs=325m
.ends sw4

.subckt sw2 vss vdd gn gp a b
* complementary switch, w=2.7u
mp      a   gp     b   vdd p1 l=.8u w=2.7u ad=6.2p as=6.2p pd=7.3u ps=7.3u nrd=481m nrs=481m
mn      a   gn     b   vss n1 l=.8u w=2.7u ad=6.2p as=6.2p pd=7.3u ps=7.3u nrd=481m nrs=481m
.ends sw2

.subckt coil 1 2 3 4 5 6 7 8
*
* Nodes:
* 1,2: primary coil terminals
* 3,4: secondary coil (I) terminals
* 5,6: secondary coil (II) terminals
* 7,8: external magnetic field
* 10,11,12: nodes in primary coil branch
* 14,15: nodes in secondary coil branch I
* 18,19: nodes in secondary coil branch II
* h1: H1
* h2: H2
* 21,22: nodes in H field assembly branch
* mal,ma2: anhysteretic magnetization
* 32: (H1+alfa M1)/a
* 36: (H2+alfa M2)/a
* mt1,mt2: total magnetization
* f11,f12: magnetic flux
*
* Parameters:
* kh11, kh121, kh122: proportionality constants to couple H to I
* kvb1, kvb21, kvb22: proportionality constant to couple V to B
* mu0: vacuum permeability
* msat: saturation magnetization
* a: scale factor for magnetic field
* alfa: feedback factor of magnetization
* rser1,rser21,rser22: series resistance of coils
* cpar1,cpar21,cpar22: parallel capacitance of coils
* cl3,c14,c23,c24: cross-coupling capacitances
*

* amperemeter
v1sense    1 10  0
v21sense   3 14  0
v22sense   5 18  0
* induction voltage source
*h11ind    10 11  vbl -kvb1
h11ind    10 11  vbl -.45u
*h12ind    11 12  vb2 kvb1
h12ind    11 12  vb2 .45u
*h21ind    14 15  vbl kvb21
h21ind    14 15  vbl 1.05u
*h22ind    18 19  vb2 kvb22
h22ind    18 19  vb2 1.05u
* parasitics
*rlseries   12  2 rser1
rlseries   12  2 100
*c1parallel 1  2 cpar1
*r21series  15  4 rser21
r21series  15  4 3182.5
*c21parallel 3  4 cpar21
*r22series  19  6 rser21
r22series  19  6 3182.5
*c22parallel 5  6 cpar21
* magnetic field (in A/mm, i.e., scaled down by factor 1000)

```

## Quodlibet8 References

---

```
* core I
*h11      h1 21 vlsense -khil
*h11      h1 21 vlsense -89.2857
h11      h1 21 vlsense -25.5
*h21      21 22 v2lsense khi21
*h21      21 22 v2lsense 208.333
h21      21 22 v2lsense 59.5
eh1ext   22  0  7  8  0.001
* core II
*h12      h2 26 vlsense khil
*h12      h2 26 vlsense 89.2857
h12      h2 26 vlsense 25.5
*h22      26 27 v22sense khi22
*h22      26 27 v22sense 208.333
h22      26 27 v22sense 59.5
eh2ext   27  0  7  8  0.001
* anhysteretic magnetization (normalized to [-1,1] interval)
* core I
bmlanhyst mt1  0  v=(1/tanh(v(32)))-(1/v(32))
gh1field  0 32 h1  0  1
*gmlfeedback 0 32 mt1 0  alfa
gmlfeedback 0 32 mt1 0  0.02
*rh1sum    32  0  (A/mm)/a
*rh1sum    32  0  0.02k
rh1sum    32  0  5
* core II
bm2anhyst mt2  0  v=(1/tanh(v(36)))-(1/v(36))
gh2field  0 36 h2  0  1
*gm2feedback 0 36 mt2 0  alfa
gm2feedback 0 36 mt2 0  0.02
*rh2sum    36  0  (A/mm)/a
*rh2sum    36  0  0.02k
rh2sum    36  0  5
* magnetic induction (current through vb, scaled down by 1000)
* core I
eh1sum    61  0 h1  0  1
*em1sum    f11 61 mt1 0  msat/(A/mm)
em1sum    f11 61 mt1 0  772
vb1       f11 62  0
*cb1       62  0  mu0/(V s/A m)
cb1       62  0  1.25664e-6
rb1       f11 0  1e12
* core II
eh2sum    65  0 h2  0  1
*em2sum    f11 65 mt2 0  msat/(A/mm)
em2sum    f12 65 mt2 0  772
vb2       f12 66  0
*cb2       66  0  mu0/(V s/A m)
cb2       66  0  1.25664e-6
rb2       f12 0  1e12
.ends coil

* coil parasitics
.subckt parasitics 1 2 3 4 5 6
* nodes: same as coil
c12 1 2 1f
c34 3 4 1f
c56 5 6 1f
c13 1 3 1p
c14 1 4 .5p
c15 1 5 .5p
c16 1 6 1p
c23 2 3 1p
c24 2 4 .5p
c25 2 5 .5p
c26 2 6 1p
.ends parasitics

* half bridge for Chiesi type fluxgate drive
* designed for 0.2V drop with 50mA at 5V gate drive
.subckt halfbridge vss vdd out gp gn
* nodes:
* vdd: positive supply
* vss: negative supply
* out: half bridge output
* gp: p-channel gate drive
* gn: n-channel gate drive
mp  dp  gp vdd vdd  p1 l=8e-7 w=2188.3e-6 ad=5033.2p as=5033.2p pd=2193u ps=2193u nrd=.594m
nrs=.594m
```

## 7.7 Some Notes on the Tools and Equipment Used

---

```

vp    dp out dc 0
vn    out dn dc 0
mn    dn gn vss vss n1 l=8e-7 w=680.5e-6 ad=1565.1p as=1565.1p pd=685.1u ps=685.1u nrd=1.91m
nrs=1.91m
.ends halfbridge

* timing generator for fluxgate drive, leaky integrator mode
.subckt leaky vss vdd n1 n2 p1 p2 sh zp zn ip in tp tn cp cn
* nodes:
* vdd: positive supply
* vss: negative supply
* n1: drive bridge #1 n-channel
* n2: drive bridge #2 n-channel
* p1: drive bridge #1 p-channel
* p2: drive bridge #2 p-channel
* sh: drive for shunt transistors
* zp,zl: drive for autozero switches (active H,L)
* ip,il: drive for output switches (active H,L)
* tp,tl: drive for cmfb charge transfer switches (active H,L)
* cp,cn: drive for cmfb precharge switches (active H,L)

* reset state flag
vres   res   0 dc 1 pulse(0 1   0   500p 500p  40n 20u)

vn1drv  n1 vss dc 0 pulse(0 5   80n 500p 500p  20n 500n)
vn2drv  n2 vss dc 0 pulse(0 5   330n 500p 500p  20n 500n)
vp1drv  vdd  p1 dc 5 pulse(5 0   76n 500p 500p  28n 500n)
vp2drv  vdd  p2 dc 5 pulse(5 0   326n 500p 500p  28n 500n)
vsdrv   sh vss dc 5 pulse(0 5   4n 500p 500p  86n 250n)
vzpdrv  zp vss dc 5 pulse(0 5   4n 500p 500p  64n 250n)
vzndrv  vdd  zn dc 5 pulse(0 5   4n 500p 500p  64n 250n)
vipdrv  iip vss dc 5 pulse(0 5   72n 500p 500p  178n 250n)
vindrv  iin vdd dc 5 pulse(0 5   72n 500p 500p  178n 250n)
bipdrv  vdd  ip v=(1-v(res))*v(vdd,iip)
bindrv  in vss v=(1-v(res))*v(iin,vss)
vtpdrv  ttp vss dc 5 pulse(0 5   4n 500p 500p  64n 250n)
vtndrv  vdd  ttn dc 5 pulse(0 5   4n 500p 500p  64n 250n)
btndrv  vdd  tp v=(1-v(res))*v(vdd,tp)
btndrv  tn vss v=(1-v(res))*v(ttn,vss)
vcpcdrv ccp vss dc 5 pulse(0 5   72n 500p 500p  178n 250n)
vcndrv  vdd  ccn dc 5 pulse(0 5   72n 500p 500p  178n 250n)
bcpcdrv vdd  cp v=(1-v(res))*v(vdd,ccp)
bcndrv  cn vss v=(1-v(res))*v(ccn,vss)
.ends leaky

* timing generator for fluxgate drive, burst mode
.subckt burst vss vdd n1 n2 p1 p2 sh zp zn ip in tp tn cp cn
* nodes:
* vdd: positive supply
* vss: negative supply
* n1: drive bridge #1 n-channel
* n2: drive bridge #2 n-channel
* p1: drive bridge #1 p-channel
* p2: drive bridge #2 p-channel
* sh: drive for shunt transistors
* zp,zl: drive for autozero switches (active H,L)
* ip,il: drive for output switches (active H,L)
* tp,tl: drive for cmfb charge transfer switches (active H,L)
* cp,cn: drive for cmfb precharge switches (active H,L)

* reset state flag
vres   res   0 dc 1 pw1(0 1 180n 1 180.5n 0 10m 0)
* precharge state flag
vpre   pre   0 dc 1 pw1(0 1 904n 1 904.5n 0 10m 0)
* integration state flag
vint   int   0 dc 0 pw1(0 0 904n 0 904.5n 1 3780n 1 3780.5n 0 10m 0)

vn1drv nn1 vss dc 0 pulse(0 5   12n 500p 500p  20n 360n)
vn2drv nn2 vss dc 0 pulse(0 5   192n 500p 500p  20n 360n)
vp1drv  vdd  pp1 dc 5 pulse(5 0   8n 500p 500p  28n 360n)
vp2drv  vdd  pp2 dc 5 pulse(5 0   188n 500p 500p  28n 360n)

bn1drv  n1 vss v=v(int)*v(nn1,vss)
bn2drv  n2 vss v=v(int)*v(nn2,vss)
bp1drv  p1 vss v=v(int)*v(pp1,vss)
bp2drv  p2 vss v=v(int)*v(pp2,vss)

vsdrv   ssh vss dc 5 pulse(0 5   8n 500p 500p  18n 180n)
bsdrv   vdd  sh v=v(int)*v(vdd,ssh)

```

## Quodlibet8 References

---

```
vzpdrv zp vss dc 5 pwl(0 5 900n 5 900.5n 0 3780n 0 3784.5n 5 10m 5)
vzndrv vdd zn dc 5 pwl(0 5 900n 5 900.5n 0 3780n 0 3784.5n 5 10m 5)

vipdrv ip vss dc 5 pwl(0 5 3780n 5 3780.5n 0 10m 0)
 vindrv vdd in dc 5 pwl(0 5 3780n 5 3780.5n 0 10m 0)

vtpdrv ttp vss dc 5 pulse(0 5 94n 500p 500p 86n 180n)
vtndrv vdd ttn dc 5 pulse(0 5 94n 500p 500p 86n 180n)
btpdrv tp vss v=v(pre)*v(ttp,vss)
btndrv vdd tn v=v(pre)*v(vdd,ttn)

vcdrv ccp vss dc 5 pulse(0 5 4n 500p 500p 86n 180n)
vcndrv vdd ccn dc 5 pulse(0 5 4n 500p 500p 86n 180n)
bcdrv vdd cp v=v(pre)*(1-v(res))*v(vdd,ccp)
bcndrv cn vss v=v(pre)*(1-v(res))*v(ccn,vss)
.ends burst

*** top level circuit

* master timing
xtmg 0 vdd n1 n2 p1 p2 s zp zn ip in tp tn cp cn burst

* amplifier
xa 0 vdd vbpl vbp1 vbp2 vcmf vbn2 inol in2 out1 out2 fcasc
* input offset
voft in1 inol dc 0
* bias
xb 0 vdd iref vbpl vbp2 vbn1 vbn2 fcbias
* common mode feedback
xcmfb 0 vdd vcm vbn1 out1 out2 vcmf tp tn cp cn cmreg

* supply
vcc vdd 0 dc 5
* common mode voltage
vcm vcm 0 dc 2
* bias current
ib vdd iref dc 40u

* input voltage for ac and dc simulations
*vin in1 in2 dc 0 ac 1
*xicm in1 in2 vcm diffin

* load
cload col co2 2.5p
xos1 0 vdd ip in out1 col sw10
xos2 0 vdd ip in out2 co2 sw10
* for dc op (dummy)
ros1 col vcm 100g
ros2 co2 vcm 100g

* reset switches
*vresp resp 0 dc 0 pulse(0 5 0n 500p 500p 40n 4u)
*vresn vdd resn dc 0 pulse(0 5 0n 500p 500p 40n 4u)
*vresp resp 0 dc 5 pwl(0 5 10n 5 10.5n 0 10m 0)
*vresn vdd resn dc 5 pwl(0 5 10n 5 10.5n 0 10m 0)
*vresp resp 0 dc 5 pwl(0 5 40n 5 40.5n 0 10m 0)
*vresn vdd resn dc 5 pwl(0 5 40n 5 40.5n 0 10m 0)

*xrs1 0 vdd resp resn col vcm sw10
*xrs2 0 vdd resp resn co2 vcm sw10

*xro1 0 vdd resp resn out1 vcm sw4
*xro2 0 vdd resp resn out2 vcm sw4
*xrb 0 vdd resp resn vcmf vbn1 sw4

*gres iref 0 resp 0 4u

* common mode test
*vexc exc 0 dc 0 ac 1
*cexc exc vcmf 200f
*cld1 out1 0 100f
*cld2 out2 0 100f

* structure for autozero
msh1 pul s vcm 0 n1 l=8e-7 w=62.5e-6 ad=143.75p as=143.75p pd=67.1u ps=67.1u nrd=20.8m
nrs=20.8m
cin1 pul in1 5p
xaz1 0 vdd zp zn out1 in1 sw10
```

## 7.7 Some Notes on the Tools and Equipment Used

---

```
raz1 out1 in1 100g
msh2 pu2 s vcm 0 n1 l=8e-7 w=62.5e-6 ad=143.75p as=143.75p pd=67.1u ps=67.1u nrd=20.8m
nrs=20.8m
cin2 pu2 in2 5p
xaz2 0 vdd zp zn out2 in2 sw10
raz2 out2 in2 100g

* input
*vin vs1 vs2 dc 0
*pulse(0 2m 150n 500p 500p 5n 250n)
*xicm vs1 vs2 vcm diffin

* coil
xc exc1 exc2 pul vcm vcm pu2 hext 0 coil
xp exc1 exc2 pul vcm vcm pu2 parasitics

* slow down pickup
cpul pul vcm 2p
cpu2 pu2 vcm 2p

* excitation driver
xdrv1 0 vdd exc1 p1 n1 halfbridge
xdrv2 0 vdd exc2 p2 n2 halfbridge
cpar1n exc1 0 10p
cpar1p exc1 vdd 10p
cpar2n exc2 0 10p
cpar2p exc2 vdd 10p
* magnetic offset field (A/m); 16 A/m approx. 20uT
*vhext hext 0 1e-3
vhext hext 0 dc 2

* node set to ensure op convergence
.nodeset v(iref) = 2.1 v(b:vdn0) = 1.28 v(b:vdn1) = 1.28 v(b:vdn2) = 1.28
* initial conditions for transient convergence
.ic v(iref) = 2.1 v(b:vdn0) = 1.28 v(b:vdn1) = 1.28 v(b:vdn2) = 1.28

* simulations
.options reltol=20u
*.options chgtol=1e-15
.tran .8n 4.2u 0
*.op
*.ac dec 20 1 lg
*.noise v(out1,out2) vin dec 4 1 lg 1
*.dc vin -300m 300m 1m vcm 0.5 4.5 1

.control
set nobreak
*set width=255
run
.endc
```



---

# Acknowledgments

First of all, I want to express my deepest gratitude to Professor Dr. Shoji Kawahito. While he was Visiting Professor at the Physical Electronics Laboratory, he taught me the How and Why of analog circuit design not only by patiently answering a lot of dumb questions, but first and foremost by giving an example of outstanding technical excellence, ingenuity, determination, and personal integrity. I am particularly indebted to Professor Dr. Shoji Kawahito for his trust to accept to co-examine this thesis.

I owe thanks to Professor Dr. Jan G. Korvink for co-examining the thesis, and for an abundance of highly useful and inspiring hints and advice how to do scientific work.

It has been a great pleasure to meet and work with Professor Arokia Nathan!

I am most indebted to Martin Zimmermann. His exemplary competence, professionalism, and steadfast reliability have been crucial for every circuit design to which I have contributed, and a lot more.

My wholehearted thanks goes to Dr. Oliver Brand, who successfully got me through difficult times at PEL.

I wish to thank Dr. Ralph Steiner Vanha for providing the Hall sensors used for this thesis and for quite a few inspiring discussions.

My thanks go to Dr. Michael Schneider for providing the integrated microfluxgate sensors *just in time*. I also wish to mention the advice on circuit design issues he gave to the best of his ability.

I thank Dr. Michael Mayer for providing measurements of Hall sensors under stress and for many inspiring discussions.

I owe special thanks to Dr. Andreas Häberli for providing me with a good start to a new job at PEL.

Thanks to my fellow IC designer Christoph Hagleitner for a lot of useful discussions and sanity checks of circuits.

## Acknowledgments

---

I thank Stefano Taschini and Dr. Markus Emmenegger for their help with simulation issues and their assistance with quite a few computer hiccups. They made my temporary exile to the simulation group at the Technopark a rather pleasant stay.

Special thanks to the system administrators Igor Levak, Dr. Niklaus Schneberger, Max Schlapfer, and Christoph Kolb, for keeping the computers up and running despite all the strange things I did with them.

Thanks to Erna Hug and Yelena von Allmen for keeping everything well organized.

I sincerely thank Dr. sc. techn. (ETH) Rolf Vogt for his faithful and loyal representation of Prof. Baltes's appreciation of circuit design to staff and collaborators of PEL.

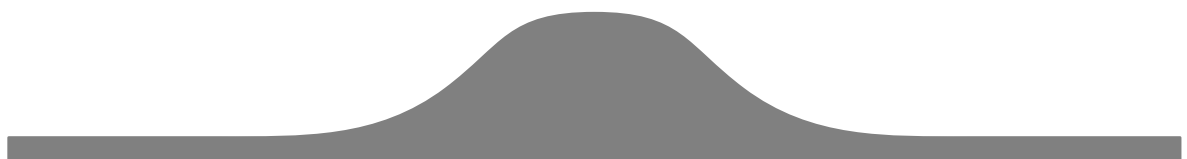
I want to thank all the other colleagues at PEL who all did their part to make the institute an ok place to be: Dr. M. von Arx, Dr. M. Bächtold, Dr. D. Bolliger, Dr. J. Bühler, M. Graf, Dr. A. Hierlemann, Dr. M. Hornung, Dr. D. Jäggi, N. Kerness, Dr. A. Koll, Dr. S. Koller-Lucae, D. Lange, Dr. F. Mayer, Dr. M. Metz, Dr. T. Müller, U. Münch, Prof. Dr. O. Paul, L. Plattner, Dr. B. Rogge, A. Schaufelbühl, D. Scheiwiller, S. Trautweiler, Dr. M. Wälti, and Dr. V. Ziebart.

---

*“Now, wait a moment!”*

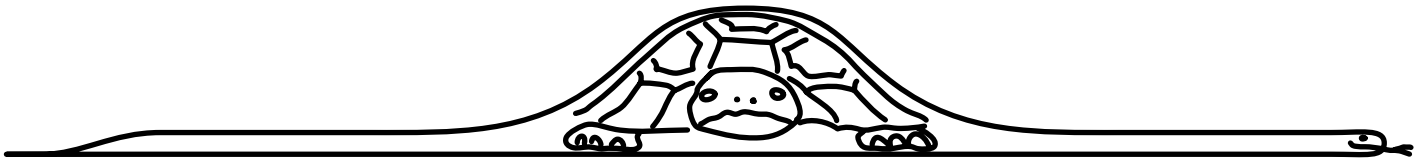
I hear somebody say.

*“Those strange bumps in Section 7.1 aren’t pieces of wood.  
That’s a snake that has eaten something!!!”*



## Acknowledgments

---



You're *absolutely* right, Franz–Peter.